**Synthesis and Support Shape Effects on the Catalytic Activities
of CuO$_x$/CeO$_2$ Nanomaterials**

by

Elizabeth Theresa Zell

Submitted in Partial Fulfillment of the Requirements

for the Degree of

Doctor of Philosophy

in the

Materials Science and Engineering Program

YOUNGSTOWN STATE UNIVERSITY

May, 2018

Synthesis and Support Shape Effects on the Catalytic Activities
of CuO$_x$/CeO$_2$ Nanomaterials

Elizabeth Theresa Zell

I hereby release this dissertation to the public. I understand that this dissertation will be made available from the OhioLINK ETD Center and the Maag Library Circulation Desk for public access. I also authorize the University or other individuals to make copies of this thesis as needed for scholarly research.

Signature:

_____
Elizabeth Theresa Zell, Student   Date

Approvals:

_____
Dr. Ruigang Wang, Thesis Advisor   Date

_____
Dr. Timothy Wagner, Co-advisor   Date

_____
Dr. Sherri Lovelace Cameron, Committee Member   Date

_____
Dr. Tom Oder, Committee Member   Date

_____
Dr. Clovis Linkous, Committee Member   Date

_____
Dr. Salvatore A. Sanders, Dean of Graduate Studies   Date

For Bill

Abstract

In this dissertation, the research focused on the preparation of shape-controlled cerium oxide (CeO_2), a known active catalyst support, to investigate the structure-property relationship for CO oxidation reaction. The use of surfactants during synthesis of shape-controlled oxide supports can have an adverse effect on the catalytic activity. Thus, CeO_2 of different morphologies (nanorods, nanocubes, and nano-octahedra) were synthesized using a hydrothermal method without an addition of surfactants in the solution. Since the size has a strong effect on differences in geometric and/or electronic properties of catalyst supports effects on the adsorption and activation of CO (carbon monoxide) and molecular oxygen are also known to take place. We strive to understand if there is a correlation with the nano-catalyst's shapes with different termination planes and the catalytic activity. Furthermore, the research focused on the impregnation of cost-effective metal catalysts with a higher known abundance on the planet. The different morphologies of CeO_2 supports were impregnated with copper oxide (CuO) at varying wt.% (1, 5 and 10 wt.%) using a wet incipient method. The samples were oxidized and reduced in order to garner a better understanding of the reducibility effect. The catalysts were then investigated to correlate the increased catalytic activities with the various shapes and defects. CuO/CeO_2 and CuO_x/CeO_2 were characterized using Raman spectroscopy, X-ray Photoelectron Spectroscopy (XPS), X-ray Diffraction (XRD) and Transmission Electron Microscopy (TEM). The catalytic activities were measured using Temperature Programmed Reduction (TPR), Temperature Programmed Oxidation (TPO), Temperature Programmed Desorption (TPD), and CO oxidation reaction. The results showed that CeO_2 nanorods were the superior shape regarding enhancing the catalytic

activity due to its increased surface area and surface defects. CuO catalyst impregnated on CeO_2 nanorods with increased surface defects demonstrated improved CO oxidation and low reduction temperatures. Additionally, a systematic study of various bimetal oxides and bimetallic nano-catalysts (Fe-CuO, Ni-CuO, Mn-CuO and $Ag-CuO_x$) impregnated on shape-controlled CeO_2 was investigated to understand the effects of the binary catalyst system on the catalytic efficiencies. This was done while keeping copper as one of the binary metal catalysts, since CuO catalysts showed enhanced catalytic activity. The collected data determined that each of the bimetallic catalyst systems showed an improvement in catalytic activity and an enhancement of the stability as compared to CuO/CeO_2 catalysts. To make an in-depth investigation of the interfacial interaction and structure of the CuO_x/CeO_2, TEM and HRTEM techniques were to characterize CuO_x/CeO_2 nanorods. The H_2-TPR profiles were re-evaluated and offered information on the possible structural analysis as well as indicating reduction temperatures.

Acknowledgements

I would like to thank several people who helped me while I was working through my Ph.D. at Youngstown State University. First and foremost, I would not be in this position if it was not for the dedication and patience of my advisor, Dr. Ruigang Wang. He had faith in me, and when I needed his expertise he was always there to help. I have a much richer understanding because he gave all he knew to help me better understand. I also want to express my gratitude to Dr. Timothy Wagner; your advice and positive attitude has given me so much. I have a better understanding and a much greater appreciation for the chemistry professor and the people we work with. I would also like to acknowledge and thank Dr. Sherri Lovelace-Cameron, when I needed a woman's perspective you were there to listen and encourage me through my time at YSU. Not to mention, we share an affinity for Pittsburgh sports. When talking science was too much, I could always ask you "how about that #84"? Dr. Clovis Linkous and Dr. Tom Oder I would like to thank you for all you help and guidance on my research and through my dissertation. Dr. Virgil Solomon, where would I have been without your help? Your dedication to students is unmeasurable and your understanding of the electron microscope was always so helpful. So, thank you to all of my advisors, committee members and professors that help shape me into a better scientist and a better person.

I would love to thank two very special people, Shaikh "Tofa" Hossain and Matt Caputo for their help in every situation I faced. Without you two, I would not be finishing this degree. So, thank you, thank you, thank you! Lisa Devore, I am unsure how to thank you. I am just so blessed and thankful for your friendship. Dr. Tracy Olin, Jaydah Wilson and Josie Allen thank you. I love you guys and am so fortunate to have you as my friends but

Table of Contents

List of Figures

xi

List of Tables

Chapter 1: Introduction

1.1. Background

Ceria-based materials are one of the most studied active heterogeneous catalyst supports for structural and chemical properties, reduction behavior and non-stoichiometry, oxygen storage capacity and metal-ceria interactions.[1,2,3,4] These properties demonstrate beneficial applications in environmental concerns. Figure 1.1 illustrates the prominent role that ceria has for many of its key applications: H_2 production, glass-polishing materials, ultraviolet absorbent, heat resistant alloy coatings, buffer layers for superconductors, reducing harmful emissions from manufacturing and transportation fields, nano-catalyst and many more.[5]
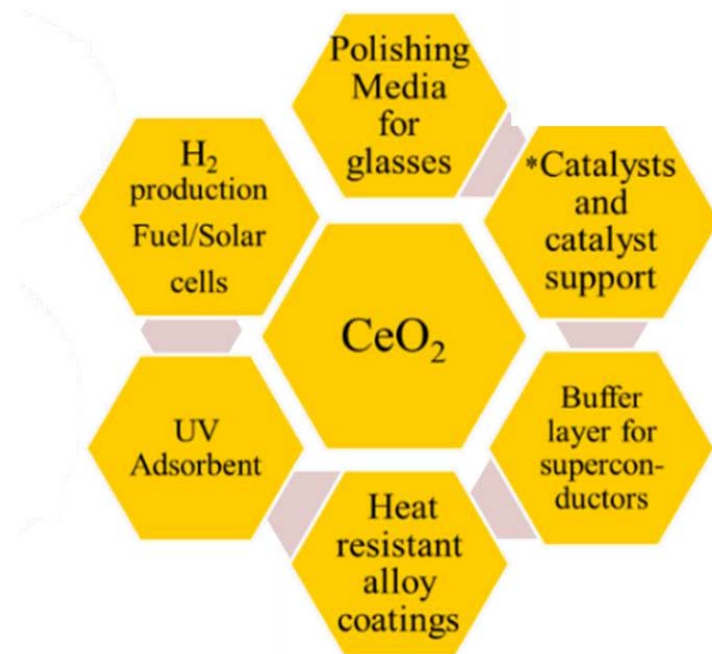
Figure 1.1. The key applications of CeO_2.

Originally invented in the early 50's by Eugene Houdry, the first catalytic converters were considered a two-way catalytic system.[6] Unburned hydrocarbons (HC_x) and carbon monoxides (CO) were converted to water (H_2O) and carbon dioxide (CO_2). In the late 70's the three-way catalytic converter "TWC" was introduced, which allowed nitric oxides (NO_X) to convert to nitrogen gas (N_2). Ceria (CeO_2) can store excess oxygen under fuel lean conditions and release it under fuel rich conditions for the oxidation of CO and hydrocarbons.[7] This happens due to its ability to switch between Ce^{4+} and Ce^{3+} oxidation states depending on the temperature and oxygen partial pressure in the exhaust gas composition.[8] Ceria can undergo many reactions by exchanging oxygen with gas molecules in the exhaust environment.[9]

The catalytic converter reactions are as follows:

Under fuel lean conditions (or oxygen rich conditions)

$$2CO + O_2 \rightarrow 2CO_2 \tag{1.1}$$

$$4HC_x + (4x + 1)O_2 \rightarrow 4xCO_2 + 2H_2O \tag{1.2}$$

$$CeO_2 \leftrightarrow CeO_{2-x} + x/2\, O_2 \tag{1.3}$$

Under fuel rich conditions (or oxygen lean conditions)

$$2NO_x + 2xCO \rightarrow N_2 + 2xCO_2 \tag{1.4}$$

$$CeO_{2-x} + x/2\, O_2 \leftrightarrow CeO_2 \tag{1.5}$$

In addition, ceria also helps in maintaining the dispersion and stability of the noble metals and enhances the thermal stability to the γ-alumina phase in the commercial catalytic converters. In water gas shift reaction, it appears that a redox mechanism in ceria by releasing and storing oxygen could promote CO oxidation during the transient oscillations in the exhaust.[10,11,12]

Water gas shift reaction:

$$CO + H_2O \rightarrow H_2 + CO_2 \qquad\qquad (1.6)$$

CO adsorbed reaction:

$$CO_{ad} + O_{surface\ or\ lattice} \rightarrow CO_2(g) \qquad\qquad (1.7)$$

In CeO$_2$-supported Pt catalyst, it was proposed that the reaction occurs between CO adsorbed on noble metals and the oxygen derived from the CeO$_2$ lattice at the noble metal and CeO$_2$ interface.[13] Due to the use of the costly noble metals, the current catalysts used in these catalytic reactions mentioned above require non-noble metal alternatives. Catalyst based on combinations between copper and CeO$_2$ constitute a highly attractive alternative from an economical point of view and very low light off temperatures for CO oxidation.[14,15] Both CuO/CeO$_2$ and CuO$_x$/CeO$_2$ have been reported to have high catalytic activity to promote carbon monoxide oxidation, water-gas shift reaction, and methanol steam reforming. This can be attributed to the quick reversible Ce^{4+}/Ce^{3+} redox couple, Cu^{2+}/Cu^{+}/Cu^{0} redox triple, and the CuO$_x$($0 \leq x \leq 1$)-CeO$_{2-x}$($0 \leq x \leq 0.5$) interactions. The redox functionality of both catalyst and support are vital components for gas adsorption, oxygen migration at the metal-support interface and in the catalytic reactions.

Understanding how to improve catalytic efficiencies at lower temperature is important for remediation of environmental issues; the goal of this dissertation research was motivated by the desire to explore fundamental interfacial structure-catalytic activity relationships in shape-controlled CeO_2 supported monometallic and bimetallic transitional metal catalysts. Engineering these nanomaterials to perform in a particular way is also important therefore, there is more to just synthesizing nanomaterials and characterizing them. In the literature, there is a limited understanding of cerium oxides' the overall structural defects contribution on catalytic activity. Further investigation was conducted to increase catalytic activities.

1.2. Problem Statement

Environmental cleanup has not only become a way of life but an industry. Cleaning up the toxic emissions from automobiles has been a main focus of many major scientific inquires. The "three-way catalyst" (TWC), is used to reduce these pollutants. The problem lies in that these current catalysts have a number of disadvantages and potential issues. Metal catalysts commercially used, platinum (Pt), rhodium (Rh) and palladium (Pd), are quite expensive, in limited supply and require high operating temperatures. Depicted in Figure 1.2, approximately 4 to 9 grams of precious metals are used in each catalytic converter.[16] These noble metals performance are also dependent on temperature. Since, these catalysts operate at temperatures in the range of 400 ^{o}C to 650 ^{o}C there are still environmental consequences of which remain unclear.[6] For example automobiles utilizes the catalytic converter to convert toxic emissions from the combustion engine, however all emissions are not converted until operating temperatures are reached (so-called cold start problem). Therefore, lowering these oxidation and reduction conversion

temperatures will greatly benefit the environment and utilizing a more cost-effective catalyst to replace the noble metals currently used is of great interest.
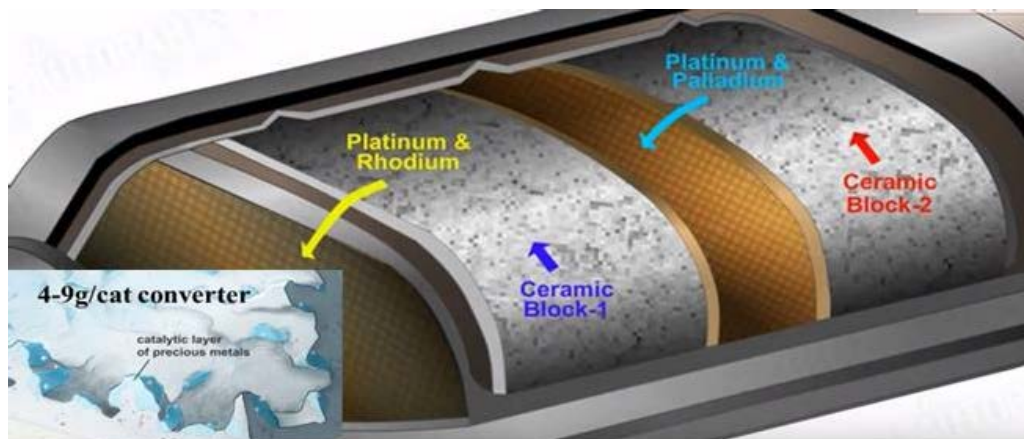
Figure 1.2. Inside a catalytic converter showing two ceramic honeycomb blocks with washcoat materials containing the precious metals platinum, rhodium, and palladium. Reprinted with permission by The Royal Society of Chemistry [16]

Another problem stems from the catalyst supports. In oxide-supported heterogeneous catalysts, commercially used are silica (SiO_2) and alumina (Al_2O_3), which are "inactive supports". This means that the support that the catalyst is impregnated upon does not supply or exchange any oxygen to help with the simultaneous remediation of toxic emissions such as NO_x, CO and unburned hydrocarbons. Also, some forms of ceria (CeO_2) are being used commercially for supports which are in fact an "active" support system, as opposed to inactive supports. However, these active supports are an octahedral morphology, possessing the most compact and stable CeO_2 (111) surface lattice plane. The octahedral shape CeO_2 support still allows for surface and lattice oxygen to be utilized in the conversion of these toxic emissions, but the amount of oxygen remains low and the operating temperature is considerably high.[17] The generation of CeO_2 nanoparticles in shapes other than octahedra, such as nanorods, nanotubes, or nanocubes,

presents an opportunity for the synthesis of support materials with more reactive surfaces such as (110), (100), (211) etc. and mobile oxygen species accessible on the crystal surface for catalysis applications. These model systems offer a great opportunity to carry out an interfacial interaction study and kinetic investigation, and are invaluable for fundamental understanding of the support reducibility and geometric/electronic/surface defect effects of support and possible transport phenomena between catalysts and supports. In addition, understanding the surface structure effect has not been investigated at great length, it is still not understood how the interfacial structure affects catalytic activities. Therefore, the objective of this dissertation focuses on elucidating the effect of CeO_2 support shape in CuO_x-CeO_2 catalysis on low-temperature CO oxidation. The outcome of the project will be a detailed understanding of the formation and properties, including those of catalytic importance, of metal/oxide interfaces at the atomic level.

1.3. Literature Review

1.3.1. Cerium Oxide

The growing number of academic publications on ceria research in the past two decades has shown how significant CeO_2 is as a catalyst or catalyst support, seen in Figure 1.3. Since 1995, the number of published ceria topics has quadrupled, and a steady increase on ceria based in catalyst based the application of ceria in TWCs and novel technologies for the treatment of emissions from diesel and spark-ignited internal combustion engines.[18]
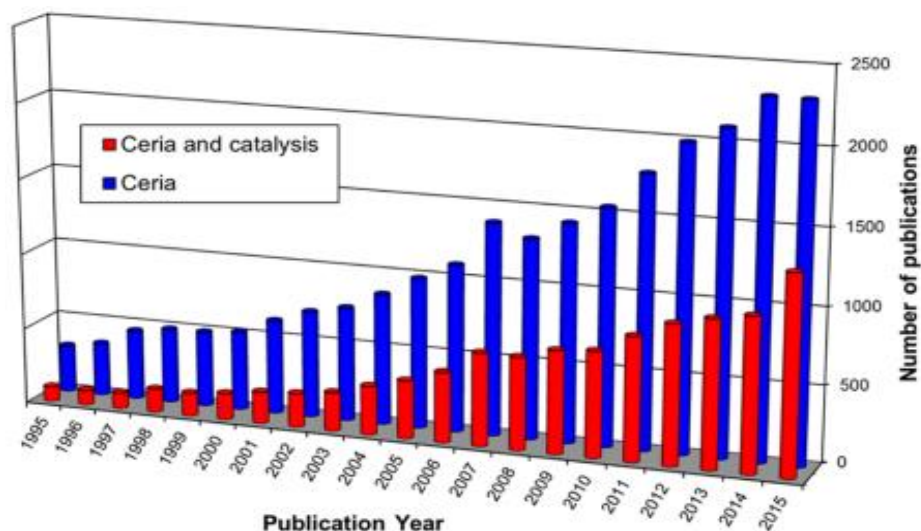
Figure 1.3. Number of publications on CeO₂-based materials in catalysis. Reprinted with permission from American Chemical Society [18]

The crystal structure of ceria (CeO_2) is a face centered cubic (FCC) structure with a space group of Fm3m and has a lattice constant of 5.410 Å.[19] On the periodic table the rare-earth metals (REMs) are in the lanthanide family (14 elements). Cerium, a REM that is soft, silvery and ductile that easily oxidizes in air to cerium oxide (ceria, CeO_2). It is one of the most abundant REM's with 0.0046 wt.% present in the Earth's crust.[20] This high abundance of cerium oxide (CeO_2) makes this compound of technological importance due to its wide range of industrial applications. The most interesting properties of ceria happen on the nanoscale. Since, nanoscale ceria materials can be transformed easily from Ce^{3+}/Ce^{4+} in a redox reaction, this transformation is beneficial in many industrial applications.[21] These microscopic properties ($CeO_2 \leftrightarrow CeO_{2-x} + x/2\,O_2$) have a wide variety of applications that are related to the rapid formation and elimination of oxygen vacancies. Some of these applications aid in the three-way catalysts (TWCs) for the elimination of toxic auto-exhaust gases, low-temperature water–gas shift (WGS) reactions, oxygen sensors, among many others.[22]

Synthetic procedures for catalyst and catalyst support systems depend on a wide variety of parameters. This research of shaped controlled CeO_2 nanostructures has consisted of many referenced works on the active catalyst support systems. Important parameters revealed that shape controlled metal oxides are an important parameter when dealing with catalysts. The heterogeneous catalysts and their support systems are often evaluated depending on their applications.

1.3.2. Structural Properties

Cerium's electronic configuration is $4f^2 5d^0 6s^1$ and has two valence states cerium (III) and cerium (IV). As seen in Figure 1.4, the catalytic activity of ceria (CeO_2) is governed by this ability to absorb and release oxygen. This is dependent upon the oxygen partial pressure and temperature in the surrounding atmosphere which causes a change in the oxidation state of cerium (Ce) between Ce^{3+} and Ce^{4+} ($Ce^{4+} + e^- \leftrightarrow Ce^{3+}$ or $CeO_2 \leftrightarrow CeO_{2-x} + x/2\, O_2$).[23]

Ceria (CeO_2) has three low index planes are as follows (100), (110) and (111). Theoretical calculations can show that a (111) surface is the most stable surface and has the highest oxygen vacancy formation energy among the low index planes of CeO_2.[24] The (100) plane is the less stable because of the alternating charged planes.[25] This introduces a dipole moment that is perpendicular to the plane. The stabilization of the (100) planes is due to the surface defects which allow a compensation of charges. However, the stoichiometrically neutral plane is the (110) plane, where the anions and cations are proportional and results in no dipole moment perpendicular to the plane.[26] Published lattice parameter values of bulk cerium oxides are typically 0.5410 nm. Confirming the nanocrystallinity as a fluorite structure can be done by obtaining the ring patterns using

8

the selected area electron diffraction. This is necessary in understanding the lattice parameters of cerium oxide nanoparticles because each plane has different properties and these planes show different catalytic characteristics.
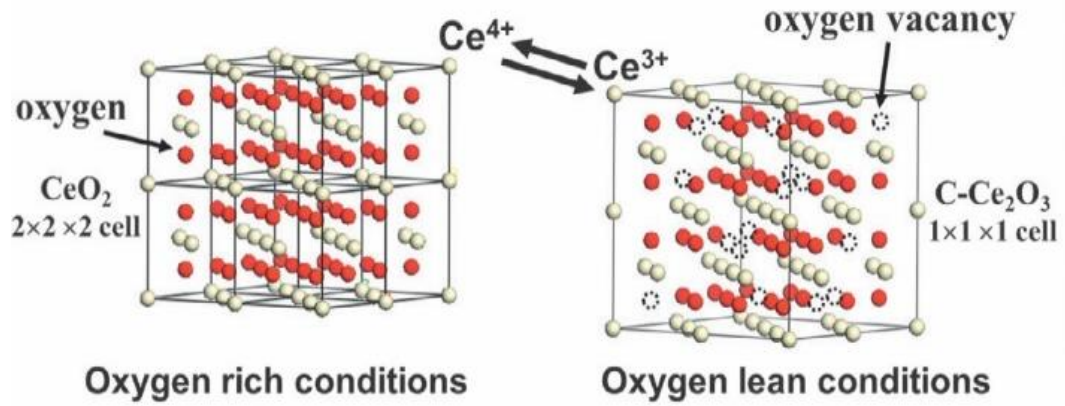
(a)
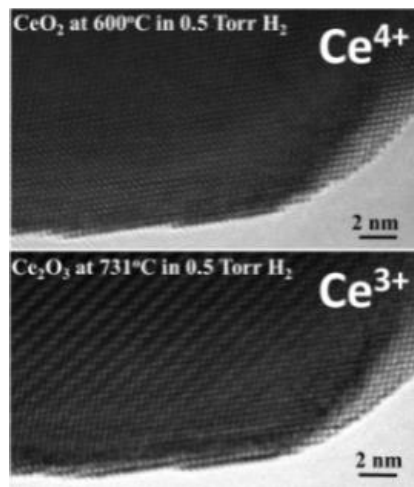
(b)
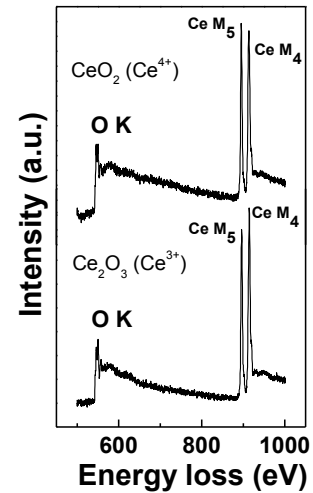
(c)

Figure 1.4. Structural change during redox processes exhibiting the lattice oxygen release/storage capacity in CeO_{2-x} ($CeO_2 \leftrightarrow CeO_{2-x} + x/2O_2$): (a) schematic – the dotted circles represent oxygen vacancies after reduction, (b) in situ high resolution transmission electron microscopy (HRTEM) images - note the emergence of superstructure after in situ reduction, and (c) electron energy loss spectra (EELS) of ceria before and after reduction – note the reversed relative Ce $M_{4,5}$ white-line intensity after reduction indicating the transformation from Ce^{4+} to Ce^{3+}. [23]

1.3.3. Morphology

Catalysts involve reactions that play an important role in the chemical and physical processes which is why they are investigated. Recent years, the research on CeO_2 morphologies has developed quite a set of strong synthetic approaches toward size/shape-controlled nanostructures. Since, the atomic structure can be indexed through microscopy these varying shapes can be determined and further understood. Seen in Figure 1.5, is a TEM image of the various morphologies of CeO_2.[27] As aforementioned and well documented the nano-octahedral morphology is the most stable, and has a (111) surface lattice plane.[28] This is followed by nanocubes and finally nanorod. These various morphologies play a crucial role in lowering the reduction temperatures and aiding in the catalytic efficiencies for automotive exhaust control systems. Therefore, it is crucial to have the ability to control the shape of ceria. It is also scientifically important to incorporate bimetallic alloy nano-catalysts because of the combination of properties that are associated with the two constituent metals, which potentially can lower reduction temperatures and improve catalytic activities. For example, Li et al. worked on improving the catalytic efficiencies through a simple hydrothermal synthesis to CeO_2 nanorods.[29] Yan et al. work on the controlled synthesis and assembly of ceria-based nanomaterials, in which his group was able to show that how that using the coordination chemistry principle it was possible to manipulate the morphology of metal oxides including CeO_2 nanocrystals and control such parameters as: structure/microstructure/texture, surface/interface, particle size, and morphology.[30,31] Therefore, making it possible to nano-engineer the next series of active ceria-based catalysts to produce desired morphologies and microstructures with controlled oxygen vacancies.
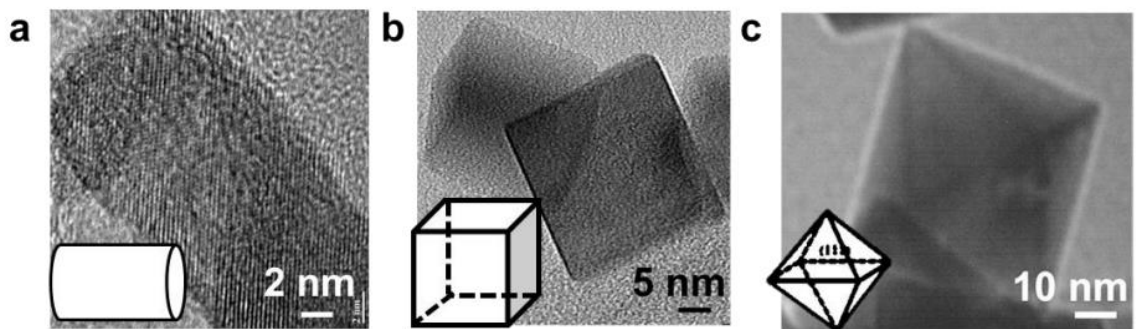
Figure 1.5. Typical TEM images of various morphologies of CeO₂ nanomaterials (a) rod, (b) cube, and (c) octahedron. Reprinted with permission from Scientific Publishing and Remittance Integration services [25]

1.3.4. Shape-controlled Synthesis of CeO₂

Nanomaterials may be synthesized in many ways via solvothermal/hydrothermal procedures, two-phase routes, microwave, co-precipitation, microemulsions, and thermal decomposition.[32] Shapes of nanomaterials range in the dimension they are placed in, such as zero dimensional for nanocubes, and nano-octahedra; 1D for nanorods and nanowires; and 2D for thin films and platelets.[33] To control the size and shape many methods can be implemented such as oriented attachment, surface energy and selective adhesion, control of growth regime, and doping-induced shape evolution shape.[34] Since, the size and shape of nanoparticles are governed by adjusting thermodynamic and kinetic parameters. The goal of this research will focus on how to control the shape of CeO₂ nanomaterials using those parameters.

Nanocrystal growth that occurs through a colloidal solution, based on their interactions between thermodynamics and kinetics, size and shape can be controlled. Through modifications of the synthetic routes such as relative concentration of molecular precursors, PH value, catalysts, and organic stabilizers, in combination with a suitable

growth temperature, the size and shape controlled metal oxide nanomaterials can be achieved.[35] Controlled nanomaterials such as cerium oxide are well known for its ability to be tuned for particular morphologies, which is a focus of this dissertation. CeO_2 nanomaterials synthesized through precipitation and hydrothermal methods have demonstrated to be vital in the investigation for enhancing catalytic performance. For example, Mai et al.[36] evaluated the various precursors, NaOH, H_2O_2, and NH_4OH, for the oxidizing agent in their research in synthesizing CeO_2 nanoplates, nanocubes and nanorods. Like this research cerium nitrate solution was used as the cerium source and they characterized these CeO_2 nanopowders with different shapes using transmission electron microscopy (TEM), BET specific surface area, X-ray diffraction (XRD) and X-ray photoelectron spectroscopy (XPS).[36] Research by Vantomme et al. suggested that using the hydrothermal method to control the shape and particle size of CeO_2 it is difficult without incorporating a surfactant to improve the morphological properties.[37] Using cetyltrimethylammonium bromide (CTAB), Vantomme established a simple synthesis for crystalline ceria nanorods with diameters ranging from 10- 25 nm and lengths ranging from 150 – 400 nm.[37] Liu et al. demonstrated that the strongest catalytic activity occurred between the interactions of CuO and CeO_2 on the nanorods supports and then, nano-polyhedra, and nanocubes respectively. This demonstrates that the morphology of CeO_2 plays a crucial role in catalytic properties.[38]

1.3.5. Surface Defects and Oxygen Vacancies

The lattice parameter of cerium oxide nanoparticles can be measured using X-ray diffraction (XRD). Understanding the structural and electronic properties of ceria nanoparticles (<3 nm) is not typically easy. These nanoparticles deviate from the bulk

fluorite structure of CeO_2.[39] Slightly larger particles (4-7 nm) can be examined using Raman and XRD. Depending on preparation methods, this could suggest the local distortions are caused by the defects in the oxide lattice. The fluorite crystal structure of CeO_2 can have several types of defects such as voids, lattice distortion, bending, steps, and twinning.[40] Defects like these are able to contribute to oxygen vacancy formation, due to the mobility of oxygen on the surface. This process aids in causing changes in the stoichiometric ratio of ceria, from CeO_2 to CeO_{2-x} ($0 < x \leq 0.5$) which the charge on the Ce adjusts by altering the charge of two cerium atoms, hence Ce^{+4} to Ce^{+3}.[41] Along with redox property and vast number of surface defects on CeO_2 aids in the ability to storage oxygen under the oxygen-rich conditions and to release oxygen under oxygen-lean conditions, seen again in Figure 1.4. Overbury et al. investigated CO oxidation over ceria nanocrystals with well-defined surface crystal planes including rods (110) and (100). Figure 1.6, illustrations various morphologies of CeO_2, the research continues explaining that the ceria nanorods demonstrate the most active of the various morphologies, followed by nanocubes and nano-octahedra.[42]
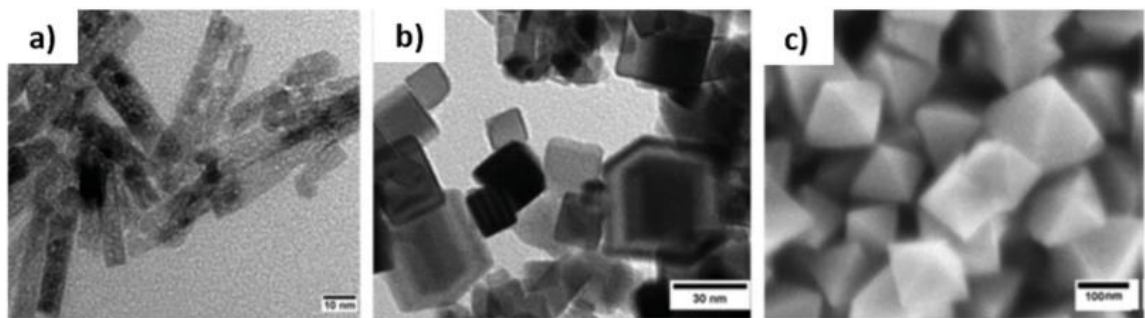
Figure 1.6. TEM images of ceria rods (a, scale bar 10 nm), cubes (b, scale bar 30 nm) and SEM image of octahedra (c, scale bar 100 nm) after CO oxidation to 673 K. Reprinted with permission from Scientific Publishing [42]

Ceria has exceptional abilities to utilize surface and lattice oxygen in various environments. The three-way catalyst is often first thought of when considering converting toxic emissions from automobile exhaust. Ceria's exceptional reversible redox properties of Ce^{4+} and Ce^{3+} are one of the main reasons oxygen in gas phase infiltrate the solid surface so the chemical reaction occurs. The three low index planes (111), (110), and (100) of ceria are well known, and it is well known that the stability of these planes follow the order of (111) > (110) > (100).[43] Where the (111) plane is the most stable of the three index planes. As such, the surface energy required to create oxygen vacancies is lower for the (110) and (100) planes. CeO_2 is considered to possess excellent oxygen storage capacity (OSC). Take for example the work of Sayle et al, the group determined that the (100) plane was more reactive and influenced the catalytic activity more compared to the (110) or the (111) plane of CeO_2.[44] Their computer modeling showed that less energy was required to create oxygen vacancies on the (100) plane, hence the (100) plane proved to be the preferred sample set.[44] The fluorite structure of CeO_2 shows that the Ce^{4+} cation is surrounded by eight equivalent O_2^- ions. This forms the corner of a cubic structure. Each O_2^- is than coordinated to four Ce^{4+}. The reduction of the coordination number of Ce^{4+} introduces Ce^{3+} ions into the crystal lattice, since the Ce^{3+} ionic radii is larger (1.034 Å) then the Ce^{4+} ions (0.92 Å), this allows oxygen vacancies to become more prominent.[45] The Ce^{3+} ions show that distortion to the local symmetry is possible. This causes defects which are due to the change in the Ce–O bond length, that alter the overall lattice parameter.[46] As stated earlier, these defects cause a change in the surface energy and the oxygen partial pressure of the surrounding

atmosphere, which in turn, changes the oxidation state of Ce between Ce^{3+} and Ce^{4+}. This allows CeO_2 to be an excellent active oxide support for use in catalytic applications.

1.3.5. Oxygen Mobility

The mobility of oxygen is thought of as "oxygen storage capacity". Oxygen storage capacity (OSC) is the mechanism that drives the catalytic activity on ceria (CeO_2) as well as the large amount of oxygen vacancies found on the surface.[47] Recall ceria has a redox ability that alters as the environment surrounding the atoms changes. When there is a shift from Ce^{3+} to Ce^{4+} states the mobility of oxygen is increased. CO and O_2 adsorb and desorb to CeO_2 surface and the mobility across the surface. This increased oxygen mobility causes a change in surface energy, which can lead to increased catalytic activities.[48] Therefore, controlling the morphologies to increase the surface energy, which is governed by OSC and other defects, is thought to increase the catalytic activities and lowering the reduction temperature. Figure 1.7 shows a schematic of the reaction that allows oxygen vacancy generation. First, shown is how the carbon monoxide is adsorbed to the CeO_2 surface; second, the surface oxygen interacts and reacts to form CO_2, which then desorbs from the surface. In addition, oxygen present in the system interacts with the void of oxygen. Since, oxygen vacancies exist, O_2 bonds are weakened and bonds are able to break and utilize the O_2 present in the system. Studies have indicated the OSC is a bulk and surface property for nanocubes and nanorods but that for the nano-octahedra the OSC is limited to the surface.[49] Since, the OSC property is shape dependent, the particle size and surface energies play crucial roles in increases catalytic parameters. Therefore, the surface of the support catalyst is significant in the catalyst and support catalyst interactions of catalytic behaviors.[50]

16
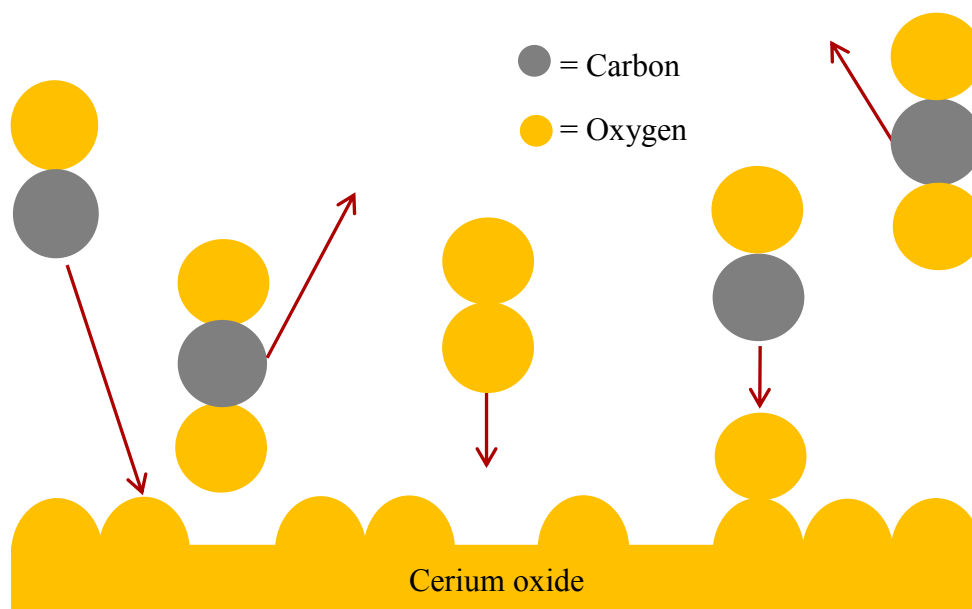
Figure 1.7. Schematic showing how CO and O_2 adsorb and desorb on the surface of CeO_2.

1.4. Oxide supported Catalyst

1.4.1. Heterogeneous Catalyst

Catalysts are a very important part of chemical and materials synthesis, fuel production, power generation and conversion, and environmental remediation.[51] Understanding of the structure–activity relationship of catalysts is necessary in the development of highly selective catalysts. There are two main types of catalysts: homogeneous and heterogeneous catalysts. Homogeneous catalysts are reactions in which the reactants and the products are in the same phase. Heterogeneous catalysts, on the other hand, involve reactants and the products that are in different phases. The surface of the heterogeneous catalyst is where the reaction occurs and this determines its catalytic property. The surface composition is controlled by the chemical make-up and its exposed crystal planes. According to Wulff's rule the electronic properties of a nanomaterial is understood by the structure and size.[52] The morphology controls the orientation of the crystal planes exposed on the surface.[53] Thus; the catalytic properties of a material can be

manipulated with their composition, size, and morphology. When looking at multicomponent catalysts, it is important to understand that the interfacial structure between adjacent components plays a crucial role in the catalytic properties and its size/morphology-surface structure and its catalytic properties. Figure 1.8, illustrations a schematic of a generalized overview of the mechanisms taking place on the surface of a heterogeneous catalyst and CeO_2 support.[54] Even though, these properties: catalyst surface structure, surface adsorbates/intermediates and catalytic property can be investigated. Investigation is limited and still remains one of the biggest challenges and discovering the relationship between the heterogeneous catalyst and the support shape effects remains to be completely understood.
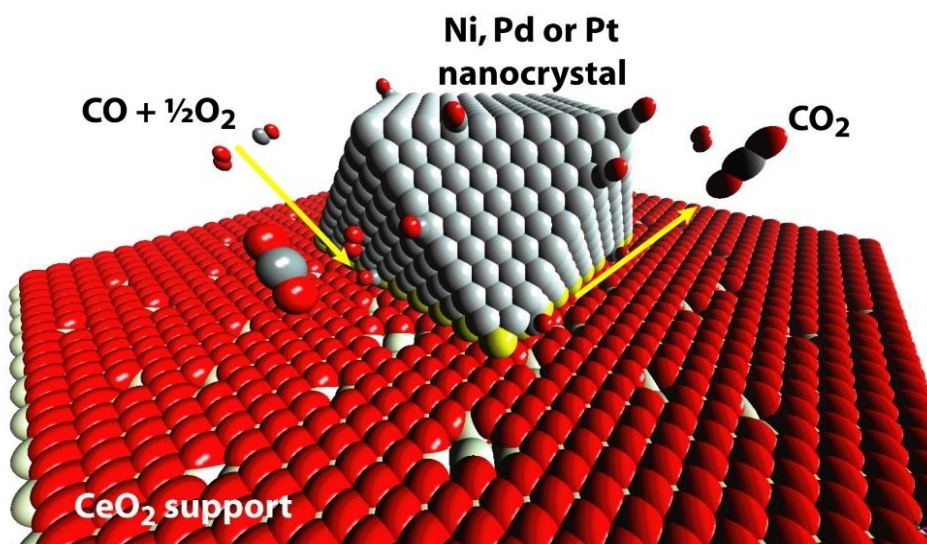
Figure 1.8. Schematic of CeO₂-supported metal heterogeneous catalyst. Reprinted with permission by Wiley Publishing [55]

1.4.2. Activation Energy

Heterogeneous catalyst take part in a multistep process seen in Figure 1.9, the first step showed the reactants diffuse through the gas phase and adsorb on the catalyst surface. During this step it is possible for the reactants to re-adsorb as the original

18

compound. It is also possible that the reactants may diffuse on the surface prior to the reaction taking place. Inevitably, the product desorbs and diffuses away from the surface into the gas phase. Surface structures are the backbone to the catalytic process and the activity of the catalyst is found in the atoms located at this interface. It is understood that these atoms do not behave as bulk material and that the atoms coordination with neighboring atoms is different. Since, the atoms at the interface are not coordinated with neighboring atoms there is a termination end that leaves free bonds available to react the reactants in the reaction that are to be oxidized or reduced. In addition to the available bonding sites interacting with reactants, these sites provide allowable pathways for the reaction to occur. Illustrated in Figure 1.9, these pathways lower the activation energy required for the reaction to take place. Since, these are gas phase reactions, lots of energy is required to break bonds and create intermediates as well as new bonds. Therefore, the use of a catalyst aids in the reduction of the energy needed. The schematic in Figure 1.9, also demonstrates the energy barriers associated with the different steps in the catalytic process. Where E_h is the activation energy for the homogeneous gas phase reaction, E_a represents the activation energy for adsorption, E_r is the activation energy for the catalytic surface reaction and E_d is the activation energy for desorption of products.
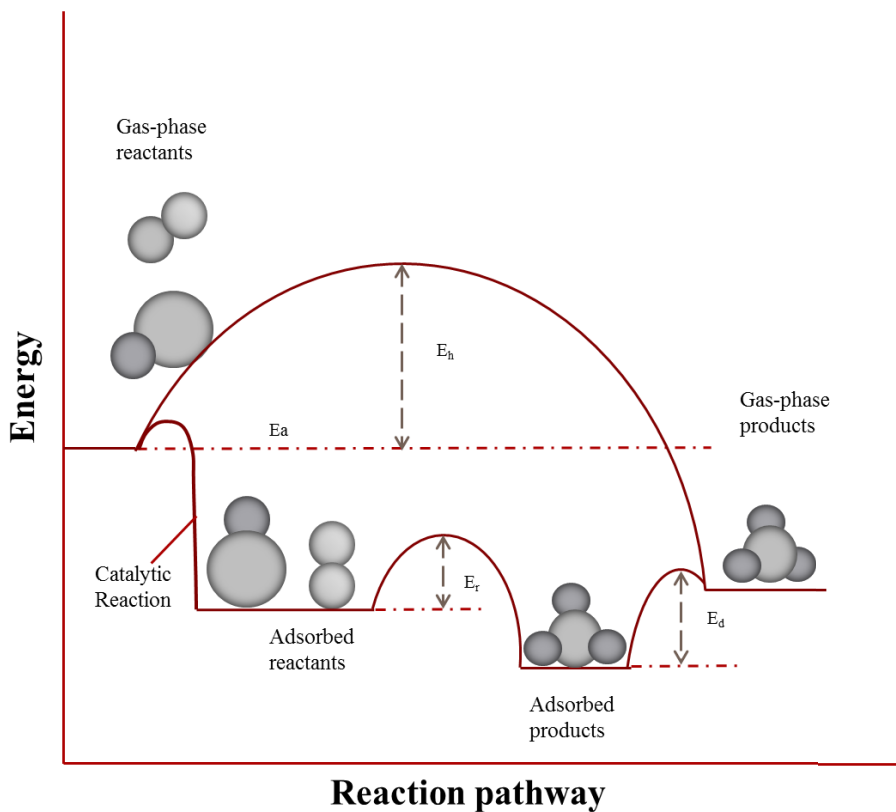
Figure 1.9. Energy barriers involved in homogeneous uncatalyzed gas phase reactions and catalytic reactions.

1.4.2. Copper Oxide

The key factors in choosing a catalyst that would complement CeO_2 and its ease of the Ce^{3+} to Ce^{4+} redox cycle and the very high oxygen mobility in the crystal structure was cost and abundance. This is because those are the factors hinder the current catalysts. Precious metals are costly and only in limited quantities. Whereas, CuO would accommodate the key factors as well as assist in increase the catalytic efficiencies that are of concern. Recall, CeO_2 has significant properties that result adsorbing and releasing oxygen. We referenced the example of the three-way catalytic converter that is assembled in automobiles to convert toxic emission to non-toxic emissions created from the combustion engines. When utilizing CuO_x as the catalyst and CeO_2 as the support the

increased activity of the CuO/CeO_2 system can be credited to the synergetic relationship between CuO_x and the CeO_2 support. What occurs is the reduction temperatures are greatly reduced from the incorporation of small CuO_x clusters and the CeO_2.
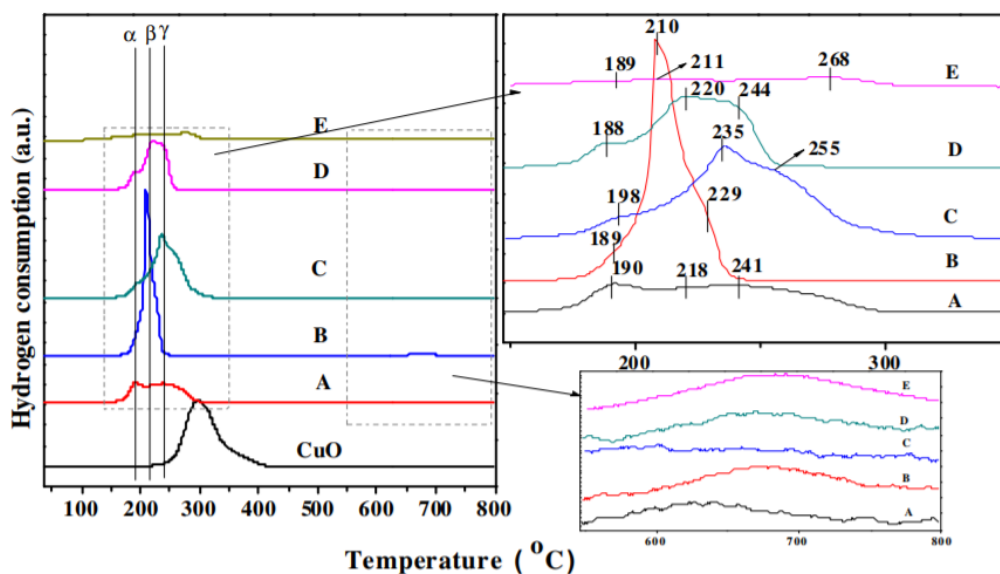
Figure 1.10. H_2-TPR profiles by Zeng et al on the catalytic performance of CuO/CeO_2 and CeO_2/CuO. Reprinted with permission from American Chemical Society [53]

In a study by Zeng et al reported, CuO/CeO_2 self-assembled rods using hydrothermal methods improve catalytic performance were due to the contact interface between highly dispersed CuO and bulk CeO_2 supplied the active sites not only for CO oxidation but also for H_2 oxidation, but that the inverse catalyst and support actually improved performance.[56] Figure 1.10 demonstrates some H_2-TPR catalytic work on Zeng's CuO/CeO_2 samples.

1.4.3. Bimetal Oxides and Bimetallic Nano-catalyst

Supported bimetallic oxides and bimetallic nano-catalysts play an increasingly major part for conversion of automobile exhaust. As well as a myriad of other applications: sensors, optical markers, and filters, fuel and oil additives for energy enhancement and

surface modifications and several other studies that focus on the design and development of metal-cluster based heterogeneous catalysts with high activity, selectivity, and stability.[57] Bimetallic catalyst studies often times show superior properties to pure metal catalysts. These metal clusters are a hybrid offering improvements in catalytic performance and are optimized through various structural elements like metal to metal ratios, geometric and electronic effects as an example; certain metals bind more strongly to oxygen. Gaining knowledge into these properties will aid in designing better catalysts. A number of influences also can be attributed to the increased catalytic activities of a bimetallic nano-catalyst system; such as the approximate dimensions of the metal nanoparticles, their interfacial interaction with the metal-oxide support, or how the additional metal interacts as an oxygen promoter.[58] Other ways that the bimetallic nano-catalysts may show preferential catalytic properties over the pure metal catalysts are when the electronic interactions between the two metals can cause direct bonding to intermediates. As for mentioned, bimetallic metal clusters can be effective catalyst for methane dehydrogenation, dehalogenation and CO oxidation reactions.[59] In this study, the CO oxidation will be studied in–depth to show superior catalytic properties of bimetal oxide and bimetallic catalysts over pure metals and/or metal oxide catalysts. Many researchers are exploring the use of bimetallic systems: Guan et al. prepared bimetallic nano-catalysts of Au/Ag deposited on TiO_2 with using photodeposition-galvanic replacement method,[60] and Cheng et al. used a wet chemical technique along with hydrazine hydrate as reducing agent to synthesis bimetallic Ni/Ag nanocomposite.[61]

22

1.6. Scope of this Dissertation

The following chapters will address the synthesis, characterization and catalysis of cerium oxide catalyst supports with an emphasis on correlating the catalyst support interface and its exposed crystal planes, and to catalytic performance. In addition a systematic study into bimetal oxides and bimetallic nano-catalysts was conducted. Although there are several synthetic methods to prepare nanostructured support cerium oxide catalysts, hydrothermal and precipitation methods, were the main routes of synthesis. To better analyze catalytic performance surfactants were not used. Also, when choosing a catalyst, nitrate compounds were mainly used to avoid extra steps to remove of unwanted compounds. The physical and chemical properties of the catalysts and catalyst supports were investigated using techniques such as X-ray diffraction, Raman Spectroscopy, electron microscopy, X-ray photoelectron spectroscopy, H_2-TPR, CO-TPD, OSC and CO oxidation. CeO_2 nanostructures with high density of oxygen vacancy defects have the ability to increase high catalytic activity and regenerative ability towards H_2-consumption and carbon monoxide oxidation.

Shape controlled nanomaterials is one of the focuses of this research and TEM is the only technique for investigation of the various morphologies. Also, this research included a study on the the catalyst-support interface and its crystal defects. This will be completed using HRTEM, as will a complete understanding of the chemical make up of the as synthesized catalyst-supports. Hussain et al looked into the irregular shaped crystallites dispersed onto an alumina supported catalyst system.[62] Understanding the work of others like Datye, A.K. & Smith, D.J.,[63] who evaluated heterogeneous catalysts with high-resolution electron microscopy, helped catapult our HRTEM research which

will help us gain a deeper understanding and breadth of this research. Additionally, a systematic study on bimetal oxides and bimetallic nano-catalysts using shape-controlled CeO_2 nanorods was conducted in order to increase catalytic performance. Bimetallic nano-catalysts are thought to possess new properties that stem from the grouping of different metals on the nanoscale, which have shown superior catalytic properties compared to their monometallic counterparts.

Table 1.1. Shape controlled synthesis of CeO₂.

CeO₂	Shapes	Sizes Length/ Diameter	Synthesis method	Remarks	Refs
CeO₂	Nanooctahedra	5-10 nm	Hydrothermal	0.1 M Ce(NO₃)₃·6H₂O Product yield is very low	64
CeO₂	Nanocubes	20-50 nm	Hydrothermal	0.1 M Ce(NO₃)₃·6H₂O	
CeO₂	Nanorods	50-200 nm	Hydrothermal	0.1 M Ce(NO₃)₃·6H₂O	64
CeO₂	Nanospheres	200 nm	Hydrothermal	Not single crystal	65
CeO₂	Nanorods, nanotubes	10-120 nm	Hydrothermal	45 days aging	66

1.7. Objectives

The main objective of this research program is to investigate the shape effects of CeO_2 and understand the interfacial relationship between the catalyst and the support.

Additional specific objectives are to:

- Synthesize ceria and impregnate CuO_x and investigate catalytic activities

- Characterize the interfacial relationship of various morphologies of CeO_2.

- Increase the catalytic efficiencies using bimetallic nano-catalysts.

Organization

This study is divided into 7 Chapters:

- Chapter 1 presents the literature review of cerium oxide, copper oxide and the bimetallic nano-catalysts. Along with the problem statement.

- Chapter 2 describes the experimental procedure used synthesizing and fully characterizing the catalyst and catalyst support systems.

- Chapter 3 presents the shape control of cerium oxide.

- Chapter 4 includes the results and discussion for the oxidized samples of CuO/CeO_2 reduced CuO_x/CeO_2 samples.

- Chapter 5 presents the bimetal oxides and bimetallic nano-catalysts/CeO_2 and how they enhance the overall catalytic performance. Using $Ag-CuO_x$, $Mn-CuO$, $Fe-CuO$ and $Ni-CuO$ as the catalysts.

- Chapter 6 shows how interfacial structures of various CeO_2 morphologies effect the catalytic performance using TEM and HRTEM.

- Chapter 7 summary and future work.

1.8. References

1. Yuan, Q.; Duan, H.; Li, L.; Sun, L. D.; Zhang, W.; Yan, H. Controlled synthesis and assembly of ceria-based nanomaterials. *J. Colloid Interface Sci*., **2009.** 335, 2, 151-167.

2. Chunwen, S.; Hong L.; Liquan, C. Nanostructured ceria-based materials: synthesis, properties, and applications. *Energy Environ. Sci*., **2012,** 5, 9, 8475-8505.

3. Ahrens, T. J., Global Earth Physics: A Handbook of Physical Constants. American Geophysical Union: Washington, D.C., **1995**.

4. Umar, A.; Kumar, R.; Akhtar, M.S.; Kumar, G.; Growth and properties of well-crystalline cerium oxide (CeO$_2$) nanoflakes for environmental and sensor application. *J. Colloid Interface Sci*., **2015,** 454, 61-68.

5. Chorkendorf, I., Niemantsverdriet, J. W., *Concepts of modern catalysis and kinetics*. Second ed.; Wiley-VCH. **2007,** 435.

6. Csere, C., 10 Best Engineering Breakthroughs. *Car and Driver*. **1988,** 33,7, 63.

7. Pei, J.; Tan H.; Boothroyd, C.; Foo, L.; He, B.; Lin, M.; Three-dimensional structure of CeO$_2$ nanocrystals. *J. Phys. Chem. C.,* **2011,** 115, 9, 3544–3551.

8. Ke, W.; Ling-Dong, S.; Chun-Hua, Y. Recent progress in well-controlled synthesis of ceria-based nano-catalysts towards enhanced catalytic performance. *Adv. Energy Mater.,* **2016,** 6, 17.

9. Yang, R.; Guo L.; Synthesis of cubic fluorite CeO$_2$ nanowires. *J. Mater. Sci*., **2005**, 40, 5, 1305-1307.

10. Zhang, D.; Du, X.; Shi, L.; Shape-controlled synthesis and catalytic application of ceria nanomaterials. *J. Chem. Soc.,* **2012,** 41, 48, 14455-14475.

11. Kumar, P.; Kumar, P.; Kumar, A.; Meena, R.C.; Structural, morphological, electrical and dielectric properties of Mn doped CeO_2. *J. Alloys Compd.,* **2016**, 672, 5, 543-548.

12. Bo, L.; Bingbing, L.; Quanjun, L.; Zepeng, L.; High-pressure Raman study on CeO_2 nanospheres self-assembled by 5 nm CeO_2 nanoparticles. *Phys. Status Solidi B.*, **2011,** 248, 5, 1154-1157.

13. Zhou, Y.; Lawrence, N.; Wu, T.; Liu, J.; Kent, P.; Soo, Y.; Cheung, C.; Pd/CeO_{2-x} nanorod catalysts for CO oxidation: insights into the origin of their regenerative ability at room temperature. *ChemCatChem.,* **2014,** 6, 10, 2937-2946.

14. Liu, W. and Flytzani-Stephanopoulos, M. Transition metal-promoted oxidation catalysis by fluorite oxides: A study of CO oxidation over $Cu-CeO_2$. *J.Chem. Eng.,* 1**996**, 67, 283.

15. Li, Y.; Fu, Q. and Flytzani-Stephanopoulos, M. Low-temperature water-gas shift reaction over Cu- and Ni-loaded cerium oxide catalysts. *Appl. Catal. B. Environ.,* **2000**, 27, 179.

16. Are There Precious Metals in Catalytic Converters? **2016**, Retrieved September 30, 2017, from https://www.thermofisher.com/blog/metals/platinum-group-metal-recovery-from-spent-catalytic-converters-using-xrf/

17. Tang, C.; Zhang, H. and Dong, L. Ceria-based catalysts for low-temperature selective catalytic reduction of NO with NH_3. *Catal. Sci. Technol*., **2016,** 6, 1248-1264.

18. Montini, T.; Melchionna, M.; Monai, M. and Fornasiero P. Fundamentals and Catalytic applications of CeO_2 based materials. *Chem. Rev.,* **2016,** 116, 10, 5987-6041.

19. Kümmerle, E. A. and Heger, G. The Structures of $C-Ce_2O3_{+\delta}$, Ce_7O_{12}, and $Ce_{11}O_{20}$.

J. Solid State Chem., **1999,** 147, 485–500.

20. Hu, Z.; Haneklaus, S.; Sparovek, G and Schnug, E. Rare earth elements in soils. *Commun Soil. Sci. Plan.,* **2006,** 37, 1381-1420.

21. Trovarelli A. Structural and oxygen storage/release properties of CeO_2-based solid solutions. *Comments Inorg. Chem.*, **1999,** 20, 4-6, 263-284.

22. Trovarelli A. Catalytic properties of ceria and CeO_2-containing Materials. *Cat. Rev. Sci.,* **1996,** 38, 4, 439-520.

23. Wang, R.; Crozier, P.A. and Sharma, R. Structural transformation in ceria nanoparticles during redox processes, *J. Phys. Chem. C.*, **2009,** 113, 14 5700-5704.

24. Mai, H. X.; Sun, L. D.; Zhang, Y. W.; Si, R.; Feng, W.; Zhang, H. P.; Liu, H. C. and Yan, C. H. Shape-selective synthesis and oxygen storage behavior of ceria nanopolyhedra, nanorods, and nanocubes. *J. Phys. Chem. B.,* **2005**, 109, 24380−24385.

25. Vyas, S.; Grimes, R.W.; Gay, D.H. and Rohl, A.L. Structure, stability and morphology of stoichiometric ceria crystallites. *J. Chem. Soc., Faraday Trans.,* **1998**, 94, 427-434.

26. Skorodumova, N.V.; Baudin, M. and Hermansson, K. Surface properties of CeO_2 from first principles. *Phys. Rev. B.,* **2004,** 69, 75401- 75409.

27. Wang, S. P.; Zhao, L. F.; Wang, W.; Zhao, Y. J.; Zhang, G. L.; Ma X. B, and Gong, J. L. Morphology control of ceria nanocrystals for catalytic conversion of CO_2 with methanol. *Nanoscale*, **2013,** 5, 5582-5588.

28. Zhao1, E.W.; Zheng, Haibin.; Zhou1, R.; Hagelin-Weaver, H. E. and Bowers, C.R. Shaped Ceria Nanocrystals Catalyze Efficient and Selective Para-Hydrogen-Enhanced Polarization. *Angew. Chem. Int. Ed.,* **2015,** 54, 14270-14275.

29. Li, Y. D.; Liao, H. W.; Ding, Y.; Fan, Y.; Zhang, Y. and Qian, Y. T. Solvothermal elemental direct reaction to CdE (E = S, Se, Te) semiconductor nanorod. *Inorg. Chem*., **1999**, 38, 1382–1387.

30. Feng, W.; Sun, L. D.; Zhang Y. W. and C. H. Yan, Synthesis and assembly of rare earth nanostructures directed by the principle of coordination chemistry in solution-based process. *Coord. Chem.Rev*., **2010,** 254, 1038–1053.

31. Yuan, Q.; Duan, H. H.; Li, L. L.; Sun, L. D.; Zhang Y. W. and Yan, C. H. Controlled synthesis and assembly of ceria-based nanomaterials. *J. Colloid Interface Sci*., **2009**, 335, 151–167.

32. Avgouropoulos, G.; Ioannides, T. Effect of synthesis parameters on catalytic properties of CuO-CeO$_2$. *Appl. Catal. B Environ.*, **2006,** 67, 1-11.

33. Putna, E.; Stubenrauch, J.; Vohs, J. and Gorte, R. Ceria-based anodes for the direct oxidation of methane in solid oxide fuel cells. *Langmuir,* 1995, **11,** 4832-4837.

34. Cao, G. *Nanostructures & Nanomaterials*. Imperial College Press. **2004**.

35. Trovarelli, A. (Ed.), *Catalysis by ceria and related materials in: Catalytic Science Series*. vol. 2, Imperial College Press, London, **2002**.

36. Mai, H.X; Sun, L.D; Zhang, Y.W.; Feng, W.; Si, R; Zhang, H.P; Liu, H.C. and Yan, C.H. Shape-selective synthesis and oxygen storage behavior of ceria nanopolyhedra, nanorods, and nanocubes. *J. Phys. Chem. B*., **2005,** 109, 24380-24385.

37. Vantomme, A.; Yuan, Z. Y.; Du G. H. and Su, B. L. Surfactant-assisted large-scale preparation of crystalline CeO_2 nanorods. *Langmuir*, **2005,** 21, 1132-1135.

38. Liu, L.; Yao, Z.; Deng, Y.; Gao, F.; Liu, B. and Dong, L. Morphology and crystal-plane effects of nanoscale ceria on the activity of CuO/CeO_2 for NO reduction by CO. *ChemCatChem.,* **2011,** 3, 978-989.

39. Trovarelli, A. *Catalysis by ceria and related materials.* London: Imperial College Press. **2005.**

40. Mock, S.; Sharp, S.; Stoner, T.; Radetic, M.; Zell, E. and Wang, R. CeO_2 nanorods-supported transition metal catalysts for CO oxidation, *J. Colloid. Interface Sci*., **2016**, 466, 261-267.

41. Rao G. R. and Mishra B. G. Structural, redox and catalytic chemistry of ceria based materials. *Bull Catal Soc.,* **2003**, 2, 122-134.

42. Wu, Z.; Li, M. and Overbury, S. H. On the structure dependence of CO oxidation over CeO_2 nanocrystals with well-defined planes. *J. Catal.,* **2012,** 285, 61–73.

43. Yang, Q.; Fu, X.; Jia, C.; Ma, C.; Wang, X.; Zeng, J.; Si, R.; Zhang, Y. and Yan, C. Structural determination of catalytically active subnanometer iron oxide clusters. *ACS Catal.,* **2016,** 6, 3072−3082.

44. Sayle, D. C.; Maicaneanu, S. A. and Watson, G. W. Atomistic models for CeO_2 (111), (110), and (100) nanoparticles, supported on yttrium-stabilized zirconia. *J. Am. Chem. Soc*., **2002**, 124, 38, 11429–11439.

45. Hendriksen, B. L. M.; Ackermann, M. D.; Van Rijn, R.; Stoltz, D., Popa, I.; Balmes, O.; Resta, A.; Wermeille, D.; Felici, R.; Ferrer, S. and Frenkenjoost, W. M. The role

of steps in surface catalysis and reaction oscillations. *Nature Chem.*, **2010**, 2, 730-734.

46. Deshpande, S.; Patil, S.; Kuchibhatla, S. and Seal S. Size dependency variation in lattice parameter and valency states in nanocrystalline cerium oxide. *Appl. Phys. Lett.,* **2005,** 87, 13, 13311- 133113.

47. Zhang, C. J.; Michaelides, A.; King, D. A. and Jenkins, S. J. Oxygen vacancy clusters on ceria: decisive role of cerium of electrons. *Phys. Rev. B.,* **2009,** 7, 79.

48. Conesa, J. C.; Martinez-Arias, A.; Fernandez-Garcia, M. and Soria, J. Surface structure and redox chemistry of ceriac automotive catalytic systems. *Res. Chem. Intermed.,* **2000,** 26, 1, 103-111.

49. Sayle. T.; Parker, C. and Catlow, A. The role of oxygen vacancies on ceria surfaces in the oxidation of carbon monoxide. *Surf Sci.,* **1994,** 316, 329-336.

50. Trovarelli A. *Catalysis by Ceria and Related Materials*. In: Hutchings G J Ed. Catalytic Science Series. London: Imperial College Press, **2002.**

51. Ma, X.; Sun, H.; Sun, Q.; Feng, X.; Guo, H.; Fan, B.; Zhao, S.; He, X. and Lv, L. Catalytic oxidation of CO and o-DCB over CuO/CeO_2 catalysts supported on hierarchically porous silica. *Catal. Commun.*, **2011,** 12, 6, 426-430.

52. Han, W.Q.; Wu, L.; Zhu, Y.; Formation and oxidation state of CeO_{2-x} nanotubes. *J. Am. Chem. Soc.,* **2005**, 127, 37, 12814–12815.

53. Mai, H.X.; Sun, L.D.; Zhang, Y.W.; Feng, W.; Si, R.; Zhang, H.P.; Liu, H.C. and Yan, C.H. Shape-selective synthesis and oxygen storage behavior of ceria nanopolyhedra, nanorods, and nanocubes. *J. Phys. Chem. B.,* **2005,** 109, 24380 – 24385.

54. Gordon, T.; Cargnello, M.; Paik, T.; Mangolini, F.; Weber, R.; Fornasiero, P. and Murray, C. Nonaqueous synthesis of TiO_2 nanocrystals using TiF_4 to engineer morphology, oxygen vacancy concentration, and photocatalytic activity. *J. Am. Chem. Soc.,* **2012,** 134, 6751-6761.

55. Cargnello, M.; Fornasiero, P.; Gorte, R.J.; Playing with structures at the nanoscale: designing catalysts by manipulation of clusters and nanocrystals as building blocks. *ChemPhysChem.,* **2013,** 14, 3869-3977.

56. Han, J.; Kim, H-J.; Yoon, S. and Lee, H. Shape effect of ceria in Cu/ceria catalysts for preferential CO oxidation. *J. Mole. Catal. A: Chem.,* **2011,** 335, 82–88

57. Sinfelt, J.H. Catalysis by alloys and bimetallic clusters. *Acc. Chem. Res.,* **1977.,**10, 1, 15–20.

58. Tang, W.; Zhang, L. and Henkelman, G. Catalytic activity of Pd/Cu random alloy nanoparticles for oxygen reduction. J. *Phys. Chem. Lett.,* **2011,** 2,1, 1328–1331.

59. Weidlich, T. and Prokeš, L. Facile dehalogenation of halogenated anilines and their derivatives using Al-Ni alloy in alkaline aqueous solution. *Cent EUR J Chem.,* **2011**, 9, 4, 590–597.

60. Jia, Q.; Zhao, D.; Tang, B.; Zhao, N.; Li, H.; Sang, Y.; Bao, N.; Zhang, X.; Xu, X and Liu, H. Synergistic catalysis of Au–Cu/TiO2-NB nanopaper in aerobic oxidation of benzyl alcohol *J. Mater. Chem. A.,* **2014**, 2, 16292-16298.

61. Manoj, K.; Gayathri, S.; Jayabal, P. and Ramakrishnan, V. Synthesis and characterization of Ni/Ag nanocomposite for surface enhanced Raman scattering measurement. *Mater. Mater. Res. Lett.,* **2015,** *2*, 6, 065003.

62. Hussain, T.; Zia, F.; Mazhar, M.; Modified nano supported catalyst for selective catalytic hydrogenation of edible oils. *Eur. Food Res. Technol.,* **2009**, 228, 5, 799-806.

63. Datye, A.K.; Smith, D.J.; The study of heterogeneous catalysts by high-resolution transmission electron microscopy. *Cat. Rev. Sci. Eng.,* **1992,** 34, 1-2, 129-178.

64. Wang, R. and Dangerfield, R.; Seed-mediated synthesis of shape-controlled CeO_2 nanocrystals. *RSC Adv.,* **2014**, 4, 7, 3615-3620.

65. Pan, C.; Zhang, D.; Shi, L. CTAB assisted hydrothermal synthesis, controlled conversion and CO oxidation properties of CeO_2 nanoplates, nanotubes, and nanorods. *J. Solid State Chem.,* **2008**, 181, 1298–1306.

66. Masek, K.; Beran, J.; Matolin V.; RHEED study of the growth of cerium oxide on Cu(111). *Appl. Surf. Sci.,* **2012,** 9, 34-38.

Chapter 2: Experimental Section

2.1. Synthesis

The simplicity of preparing ceria based nanomaterials is condensed into four main parts: synthesis of precursors, treatment of precursors before conversion to oxides, conversion of precursors to mixed oxides, and post treatment of mixed oxide material. Some synthetic routes include soft template, co-precipitation, and precipitation & aging and hydrothermal, other techniques include: hard template, sol-gel, solvothermal surfactants and polymers.[1] All these techniques have a focus on improving the physical and chemical properties of the various morphologies of ceria nanomaterials. This research will investigate the co-precipitation and hydrothermal synthesis of CeO_2.

The hydrothermal synthesis has been extensively researched because this synthetic route has shown to reduce reaction times, temperatures in the range of room temperature to 200 °C and pressures at <1.5 MPa in the nucleation process of crystal growth.[2] In addition, the hydrothermal synthesis is more cost effective for commercially engineered materials. Safety also plays a role in using the hydrothermal route because this reaction does not require sophisticated reactors. The conditions are less severe than typical chemical industrial processes used today.

2.1.1. Co-Precipitation

Co-precipitation method involves the simultaneous occurrence of nucleation, growth, coarsening and/or agglomeration. The products are typically insoluble materials formed under conditions of high supersaturation. The nucleation is the primary step in this method. Where a large number of small particles are formed and then the secondary step

involves the mechanism of Ostwald ripening page and aggregation. This step dramatically affects the size, morphology and properties of the samples. The supersaturation conditions are extremely necessary for the precipitation process which allows the chemical reaction to take place.[3] Yang et al. was able to synthesize the fluorite-type CeO_2 nanotubes with an outer diameter of 10–20 nm and inner diameter of 5–6 nm.[4] The precipitation method typically performed in conjugation with other methods such as hydrothermal method. Where $Ce(NH_4)_2(NO_3)$, octadecylamine is used as a surfactant template, and urea as the precipitation agent.[4]

2.1.2. Hydrothermal Technique

Figure 2.1 is a schematic of the autoclave used in the hydrothermal technique, which is becoming a formidable tool for advancement of materials processing.[5] In Figure 2.2, are images of the Teflon-line autoclave and box furnace used in the hydrothermal synthesis. The process of that uses the heterogeneous phase reaction in an aqueous solution with controlled thermodynamic variables parameters i.e. temperature (> 25 ^{o}C) and pressure (~100 kPa) is known as the hydrothermal synthesis.[6] This type of solution chemistry utilizes specific parameters to include the ability to create crystalline phases which are not stable at the melting point directly.[7] The process takes advantage of the vapor pressures that are built up above the solution at particular temperatures in order to assist in the crystallization process.[8] The precursors or reactants used in this type of synthesis are often suspensions and mineralizers, which are an additive that controls the solubility of the nutrient solid,[9] are typically used in high concentration and help to control the pH and increase solubility.[5] In certain situations these mineralizers will assist in particle size and aid in the creation of various morphologies.[10] In the formation of

single crystals increased pressures are utilized to control single crystal growth, and help to regulate solubility and the growth rate.[11]
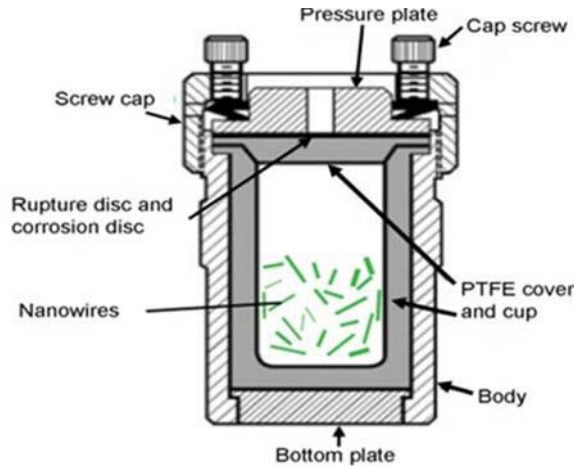
Figure 2.1. Autoclave schematic used in hydrothermal syntheses. Reprinted with permission open access [12]

(a) Teflon-lined autoclave   (b) Box furnace

Figure 2.2. Pictures of Teflon-line autoclave and box furnace for hydrothermal synthesis.

Moreover, the ability to precipitate the powders directly from solution regulates the rate and uniformity of nucleation, growth and aging, which affords size, morphology and aggregation control that is not possible with many synthetic processes.[13] Figure 2.3 showed several examples of the various morphologies possible with hydrothermal

process. This research will explore many of the synthetic routes to synthesize various morphologies, such as; dwell time temperature concentration.
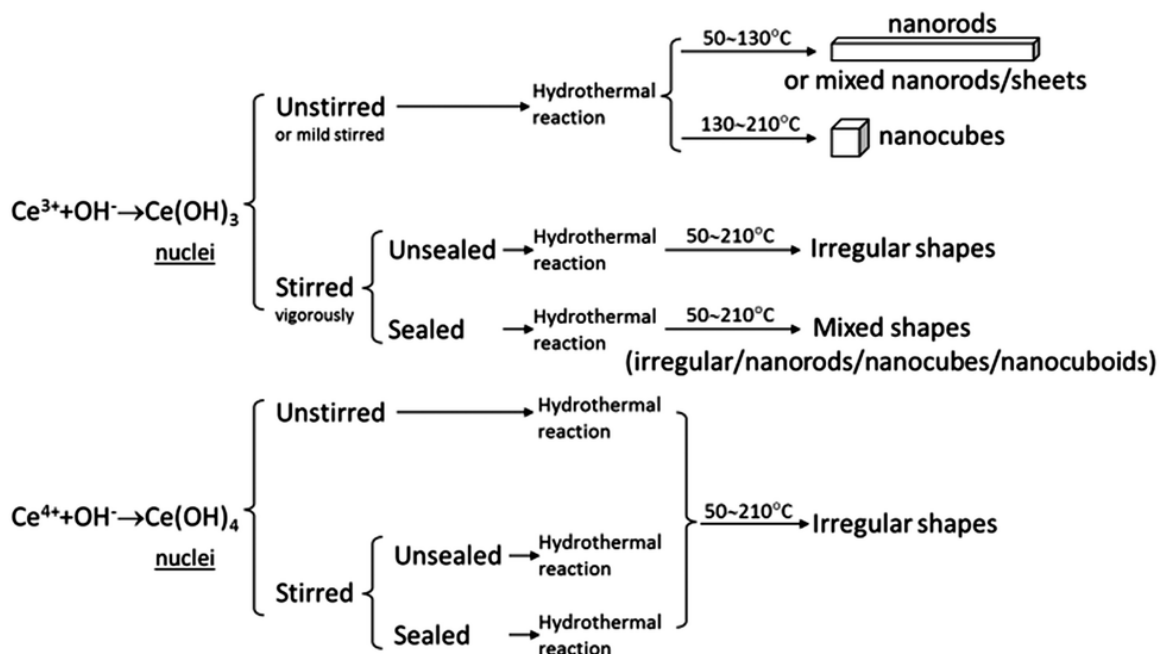
Figure 2.3. CeO₂ morphology road map. Reprinted with permission by The Royal Society of Chemistry [14]

Take for example, CeO_{2-x} nanorods that were synthesized by Mai et al. These CeO_2 nanoshapes were engineered at temperatures ranging from 100-180 $^{\circ}$C using the hydrothermal method.[15] This method dissolves and recrystallizes materials that are generally insoluble under ordinary conditions. The reaction temperatures and pressures are the primary cause for crystal nucleation and growth.[4] Mai et al. used differing concentrations of sodium hydroxide and $Ce(NO_3)_3$ as the cerium source. They determined that during the nucleation process hexagonal $Ce(OH)_3$ intermediate species were formed and higher concentration of NaOH attributed to the various morphologies.

38

2.1.3. Incipient Wetness Impregnation

Incipient wetness impregnation is a technique used to synthesis heterogeneous catalysts. A dissolved is metal used as the catalyst that is connected to a support, typically an oxide. This process is done via an aqueous or organic solution. The metal is dissolved in the solution and is then added to the metal oxide support. These two solutions typically contain the same pore volume.[16] This causes the capillaries to draw into the pores. Then the extra pore volume allows the solution transport to diffusion as opposed to a capillary process.[16] As the solvents are dried off the metal is deposited on to the oxide support. Loading of the metal is limited by the solubility of the precursor in the solution. Hence, the concentration is therefore dependent upon mass transfer within the pores during impregnation and drying.[16]

2.2.   Instrumentation

The instrumentation used in this research has the capability to determine surface, atomic structural properties and catalytic performance. Techniques like; X-ray diffraction, Raman spectroscopy, XPS, transmission electron microscope and BET surface area characterized physical properties whereas, catalytic investigations were done using H_2-TPR, CO-TPD, OSC and CO oxidation. Understanding the principles behind these techniques will help shed valuable information on environmental issues and help in engineering nanomaterials used in catalytic performance for the remediation of toxic emissions.

2.2.1. X-ray Diffraction (XRD)

Figure 2.4 is an image of the Rigaku Miniflex used for X-ray diffraction (XRD) and is an analytical technique that is used to determine the atomic and molecular structure of

a crystal. The Miniflex diffractometer uses aluminum sample holders that allow for small amounts of powder to be analyzed, the powders and/or solid samples do not exceed a one-millimeter height. Seen in Figure 2.6 is a schematic of the mechanism that takes place within the XRD machinery. The beam of incident X-rays interacts with the crystalline sample and then diffracts into various directions. Then by measuring the angles and intensities of the diffraction patterns, a three-dimensional picture of the density of electrons within the crystal is created.[7] Therefore, a better understanding of the crystal lattice can be extracted from the positions of the atoms within the crystal, such as chemical bonds, their disorder and other information.

W. H. Bragg, who was an English physicist in the 1900's, along with his son W. L Bragg observed X-ray wave interferences, which are now referred to as X-ray diffraction patterns (XRD). Bragg's derived equation, noted here as Equation 1, known as Bragg's law, is undeniable proof for the periodic atomic structure of crystals.[17] This equation goes on to explain how cleaved faces of crystals reflect X-ray beams at particular angles of incidence (theta, θ). They noted that d would refer to the variable distance between atomic layers in a crystal, and that variable λ is the wavelength of the incident X-ray beam and n is an integer. This technique can be used to investigate various states of matter using different energy sources, e.g. ions, electrons, neutrons, and protons, where the wavelength λ, is comparable to the distance between the atomic structures of interest.

$$n\lambda \ = \ 2d \ sin \ \theta \qquad\qquad\qquad\qquad (2.1)$$

Figure 2.4. Rigaku Miniflex XRD equipment.

2.2.1.1. Unit cell

The unit cell is described by three parameters, a, b, and c, which describe the length of three conjoined edges of the unit cell as well as three angles denoted α β and γ which describe the angular relationship between the edges. These unit cell parameters define and describe the crystalline systems. In a simple cubic crystal system, the conjoined edges are equivalent in length and the angles are orthonormal, which is to say a = b = c, and 90°.[18] Unit cells are the smallest possible unit of the crystal which features all the symmetry elements of the crystalline structure. In possessing all the symmetry elements of the long-range structure, a collection of unit cells, through some combination of symmetry operations such as translation, rotation, reflection and inversion, create the long-range order of macromolecular crystalline solids. This understanding of the unit cell is frequently all that is required to explain many physical properties of crystalline solids.[18]

2.2.1.2. Classification

The most important property of a crystal is its intrinsic symmetry. What is meant by symmetry is that under certain 'operations' the crystal remains unchanged.[18] Crystals have translational symmetry. This is where a move of one cell in each of three axis directions restores the structure, but some crystals have other symmetry elements as well. For example, rotational symmetry is rotation of specific angle like; 90°, 120°, and 180° that restores the structure. Mirror symmetry is the reflection across a plane that restores the structure. If all the intrinsic symmetries are discovered a complete classification of the crystal is said to be made.[18]

2.2.1.2 Lattice Systems

The way to describe the lattice system in a crystal structure is through the grouping of the axial systems. As mentioned earlier, α β and γ describe the angular relationship between the edges of the crystal system. These angles will represent the three axes in the geometrical arrangement of a crystal. There are seven lattice systems and six crystal families. The cubic system is the most straightforward of the systems and has the symmetry of a cube. This means that the rotational axes are orientated such that all four threefold rotational axes which lie along the body diagonals of the cube are 109.5° with respect to each other. The other six lattice systems are hexagonal, tetragonal, rhombohedral, orthorhombic, monoclinic and triclinic.[18]

2.2.1.3. Point groups

The crystallographic point group of a system is a shorthand notation which reflects the relevant symmetry elements of a crystalline system. Where the mathematical group comprising of the symmetry operations leaves at least one point unmoved and that leave

the appearance of the crystal structure unchanged. These symmetry operations include •

Reflection, which reflects the structure across a reflection plane • Rotation, which rotates

the structure a specified portion of a circle about a rotational axis • Inversion, which

changes the sign of the coordinate of each point with respect to a center of symmetry or

inversion point • Improper rotation, which consists of a rotation about an axis followed

by an inversion. 14 rotation axes (proper and improper), reflection planes, and centers of

symmetry are collectively called the symmetry elements. Figure 4 shows the 32 possible

crystal classes. Each one can be classified into one of the seven crystal systems.[18]

In this work, XRD is used to determine the structure and lattice parameters of cerium

oxide synthesized. The nanoceria materials are multicrystalline and are of a fluorite phase

of CeO_2. The broad peaks demonstrated the nanocrystalline nature of ceria particles.

There are three low index lattice planes within the cubic fluorite structure and XRD

analysis can show these crystal phases. Investigating these planes could contribute to a

more in-depth understanding of the different catalytic properties arising from their

morphologies and sizes. In CeO_2 the crystal plane heavily influences the CO oxidation

activity due to their different abilities of creating oxygen vacancies. Studies have been

done to model these attributes of ceria and the results showed that less energy is required

to form oxygen vacancies on (111) than on (100) and (110).[19] Thus, the nano-octahedra

with the (111) surface exposed are less active than nanocubes and nanorods surface

exposed.[20]
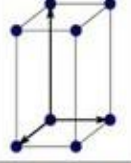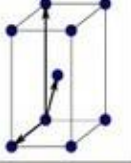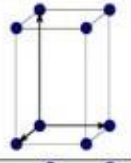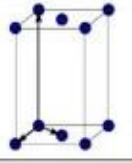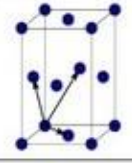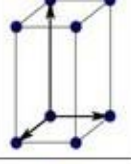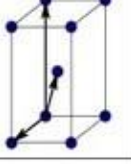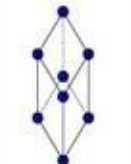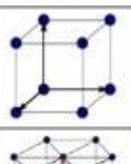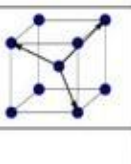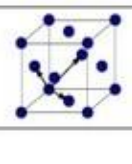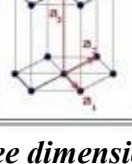
Bravais lattice	Parameters	Simple (P)	Volume centered (I)	Base centered (C)	Face centered (F)
Triclinic	$a_1 \neq a_2 \neq a_3$ $\alpha_{12} \neq \alpha_{23} \neq \alpha_{31}$				
Monoclinic	$a_1 \neq a_2 \neq a_3$ $\alpha_{23} = \alpha_{31} = 90°$ $\alpha_{12} \neq 90°$				
Orthorhombic	$a_1 \neq a_2 \neq a_3$ $\alpha_{12} = \alpha_{23} = \alpha_{31} = 90°$				
Tetragonal	$a_1 = a_2 \neq a_3$ $\alpha_{12} = \alpha_{23} = \alpha_{31} = 90°$				
Trigonal	$a_1 = a_2 = a_3$ $\alpha_{12} = \alpha_{23} = \alpha_{31} < 120°$				
Cubic	$a_1 = a_2 = a_3$ $\alpha_{12} = \alpha_{23} = \alpha_{31} = 90°$				
Hexagonal	$a_1 = a_2 \neq a_3$ $\alpha_{12} = 120°$ $\alpha_{23} = \alpha_{31} = 90°$				

Figure 2.5. Bravais lattice table in three dimensions. Reprinted with permission open access.
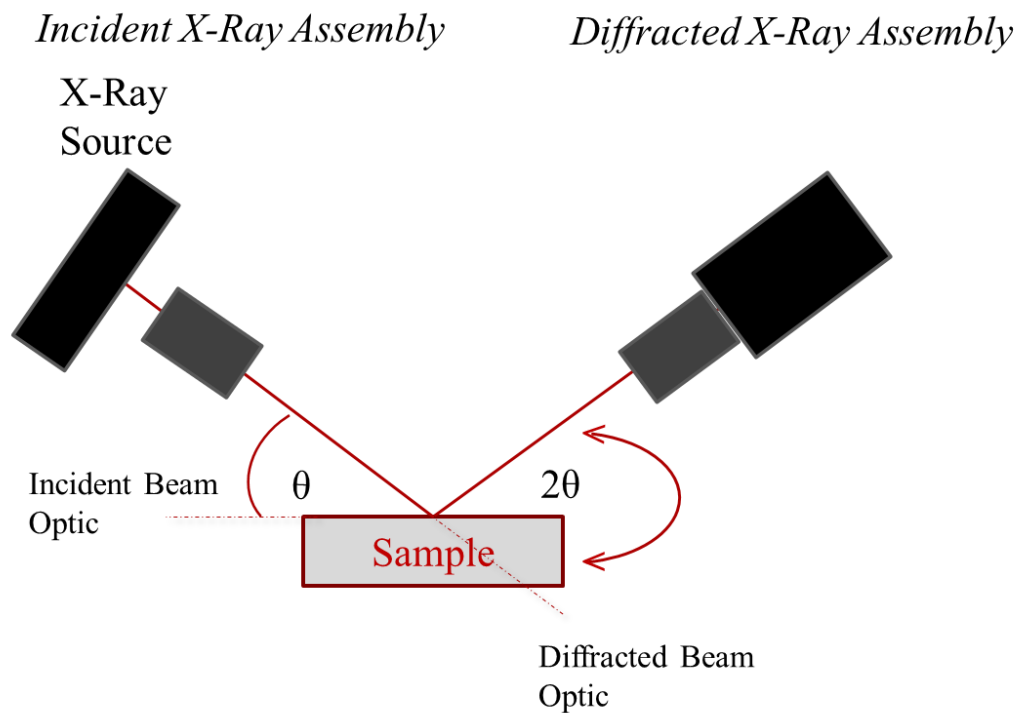
Figure 2.6. Braggs analysis for X-ray diffraction by crystal planes.

2.2.2. Raman Spectroscopy

Raman spectrometry is a technique that is well founded on the inelastic scattering of light where an analyte sample is irradiated with intense monochromatic laser light after which the scattered light is analyzed for frequency shifts. The intensity of the scattered light is usually proportional to the amount of material present, therefore making it possible to perform both qualitative and quantitative measurements. Elastically scattered photons are created when light interacts with a molecule or crystal. Incident photons interact, and scattered photons are emitted with the same frequency (energy) and wavelength as the incident photons. Approximately, 1 in 10^7 photons are scattered optically and typically lower and at different frequencies.[21] When photons are scattered at a different frequency that the incident photon it is known as inelastic scattering and the

Raman effect. Changes in vibrational, rotational or electronic energy of a molecule will cause the energy changes within the crystal lattice due to the Raman scattering. Rayleigh scattering occurs when the scattering is elastic and if it is not elastic it is Raman scattering.[22] Raman analysis can provide direct evidence of oxygen vacancies and defects owing to changes in the vibrational structure of the CeO_2 lattice. In 1928 the Nobel prize was awarded to V. C. Raman, for his efforts on the Raman effect.[23] He discovered that when monochromic light interacted with a substance light scattered. The spectrum of this light consisted of a strong excited line of that same frequency as the incident light with fringes on either side but shifted from the excited lines ranging up to 3500 cm^{-1}.[24] The lines with less energy (frequency) than that the excited lines are referred to as Stokes lines and the other lines are anti-Stokes lines. Seen in Figure 2.6 the arrows indicate the energy differences between the incident and the scattered photons. Equation 2 represents the Raman shift, in wave numbers (cm^{-1}), mathematically where the λ's are the wavelengths (in cm) of the incident and Raman scattered photons, respectively.[25]

$$\bar{v} = \frac{1}{\lambda_{incident}} - \frac{1}{\lambda_{scattered}} \tag{2.2}$$

Raman analysis of phonon softening provides a direct and versatile way of quantitatively assessing oxygen vacancy levels in catalyst-type material. The rates of CO oxidation and ceria reduction correlate to the Raman shift and the increase in the oxygen defects. The different reaction pathways of CO oxidation are confirmed by oxygen vacancy levels from the Raman shift.[26]
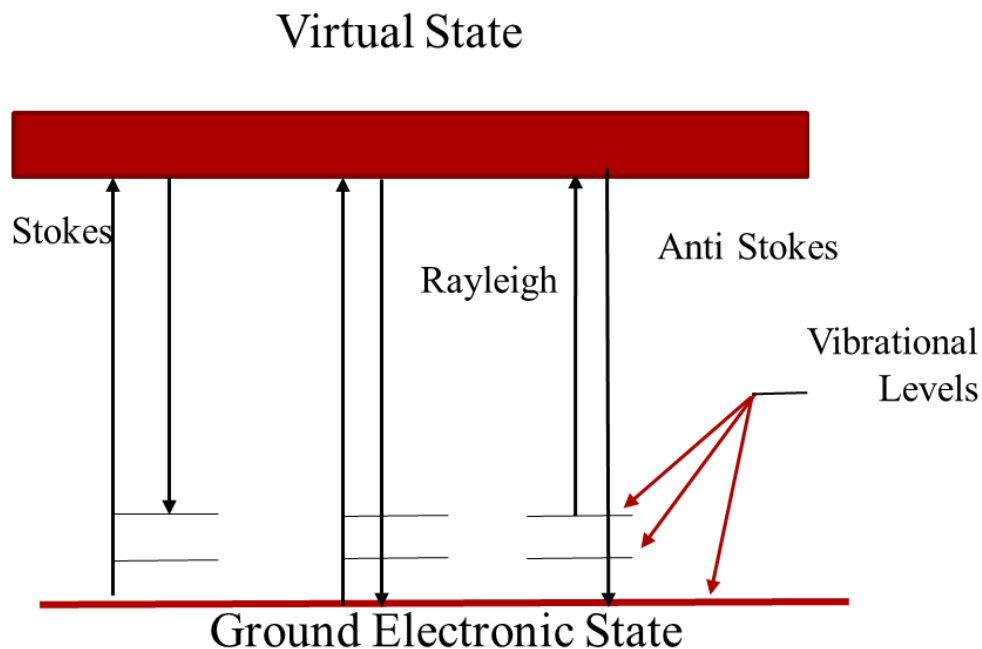
Figure 2.7. Jablonski Diagram of quantum energy transitions for Rayleigh and Raman scattering.

Recall that the Raman effect occurs during the interaction of incident photons with a electric dipole molecule. In quantum mechanics excitation from scattering occurs at a virtual state lower in energy than a real electronic transition. If the post excitation is almost equivalent excitations a change in vibrational energy occurs. This phenomenon occurs in 10^{-14} seconds or less. The virtual state description of the scattering is shown in Figure 2.7.

2.2.3. Temperature Programmed Reduction (TPR)

Temperature Programmed Reduction (TPR) is a characterization method used to determine reduction properties of various cataylsts. This chemisorption technique gives a clear look into temperatures of catalysts as they become reduced. Catalysts can be characterized using the hydrogen temperature programmed reduction (H_2-TPR).[12] Using H_2-TPR, data is collected to understand how much hydrogen adsorbs and consumes onto

the catalyst as a function of temperature. H_2-TPR analysis is done on a Micrometerics AutoChemII 2920 instrument, seen in Figure 2.8. Typically, performed using a catalyst sample (80~100 mg) at a rate of 50 mL/min with a stream of 5% H_2 and 95%He. The samples are heated from RT to 900 °C with a 10 °C/min ramp during analysis. Deconvolution of recorded TPR profiles can be performed on Origin 8.1 software using Gaussian and Lorentzian functions. This deconvolution can give a deeper understanding of how CuO_x interacts with ceria. To ensure accurate hydrogen consumption amounts are tabulated, the equipment was calibrated using a standard sample. Cu_2O was used as the known standard and a multiple of different masses were run to construct a calibration curve. The reaction that occurs in Equation 3, between Cu_2O and H_2 were used to obtain reference data for these calibrate curves, seen in Figure 2.9.[27]

Temperature programmed reduction (TPR) is a technique for the characterization of solid materials and is often used in the area of heterogeneous catalysis to establish the most efficient reduction conditions. John Ward Jenkins developed the TPR technique while working for the Shell Oil Company on heterogeneous catalysts.[28] This method allows researchers to probe catalysts and unearth their reduction conditions. The characterization goes as follows, the catalyst or sample is oxidized then placed in a reducing environment, typically a gas mixture of 3-17% hydrogen and some other inert gases (argon), as the gas passes over the sample the temperature is incrementally raised. This yields quantitative information of the reducibility of the oxide's surface, as well as the heterogeneity of the reducible surface.[29] Since the temperature is being raised, a thermal conductivity detector (TCD) is used to measure changes in the thermal conductivity of the gas stream.[30] Through particular programs the signal converted to

concentration of active gas using a level calibration. Finally, mathematical models calculate the area under the concentration vs. temperature yields total gas consumed.[29] In addition to reduction temperature and total gas consumed the TPR garners other valuable techniques. One technique is the pulse chemisorption analysis, which determines active surface area, percent metal dispersion, oxygen storage capacity and active metal particle size by applying measured doses of reactant gas to the sample. In this research, chemisorption has been a staple characterization tool and areas of study were examined such as: various TPR cycling, oxygen storage capacity and BET surface area.

Figure 2.8. Micrometrics AutoChemII 2920.

$$Cu_2O \text{ (solid)} + H_2(\text{gas}) \rightarrow 2Cu(\text{solid}) + H_2O(\text{gas}) \tag{2.3}$$
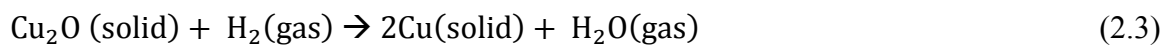
It is worth noting, no intermediate phase is observed during the reduction, such as a direct

transformation from Cu^+ to Cu^0. The H_2-consumption was then calculated using equation 4, in which 85 mg of Cu_2O was used and the calculations obtained were µmol per gram per peak area. The resultants obtained for H_2-consumption amounts were (22.1 mol/peak area).

$$H_2\text{-consumption (mmol/g)} = \frac{22.1 \ \frac{\mu mol}{peak \ area} \times peak \ area \ of \ catalyst}{mass \ of \ catalyst \ (mg)} \qquad (2.4)$$
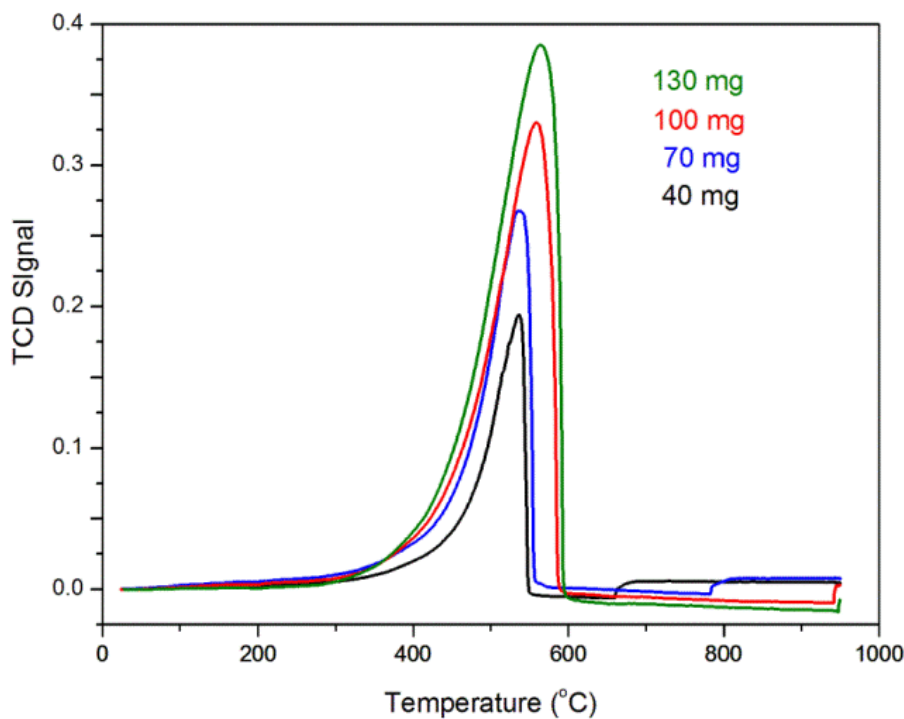
Figure 2.9. TPR calibration curves for Cu₂O.

Figure 2.10 displays the three different ways CuO_x can interact with ceria. Firstly, the alpha peak indicates copper is strongly interacting with the surface of ceria. This means Cu has created a solid solution, whereas the copper has incorporated into the lattice of

50

CeO$_2$. Secondly, the beta peak indicates loosely interactive copper to the surface of ceria. Lastly, the gamma peak depicts the bulk copper on the surface of ceria.
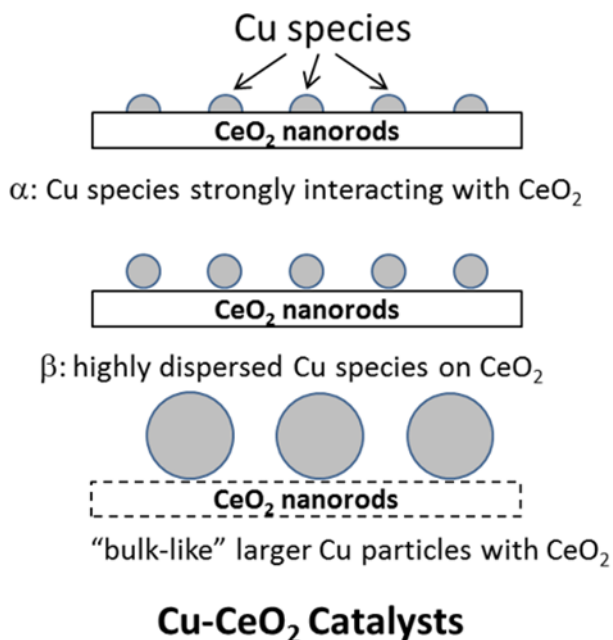
Figure 2.10. Schematic of the catalyst interaction with the support. Reprinted with permission by Wiley Publishing [31]

2.2.4. Brunauer Emmett and Teller surface area (BET)

Figure 2.8 illustrations the Micrometerics AutoChemII used to determine H$_2$-TPR and Brunauer-Emmet-Teller (BET), which is a technique that allows for valuable surface information from a catalyst to be determined. The single point BET surface area is also used to estimate total pore volume and pore size distribution of the catalysts. A material`s surface area is measured as a function of its ability to physisadsorb gas molecules. Figure 2.11 demonstrates the adsorption and desorption process used to determine BET surface area. BET uses a method that is based on the physisorption of N$_2$ molecules. N$_2$ molecules will physisadsorb on the surface at cryo-temperatures and form a monolayer. It is known that the atomic structure of one single N$_2$ molecule occupies 0.162 nm^2 and

nitrogen molecules will line up independent of the surface structure. Multilayers will begin to form, causing the calculation to vary. This is then corrected by only measuring at low absorbent pressures.[32] Brunauer, Emmett and Teller determined the monolayer volume using their derived BET equation,[33] where the Vm in turn will give the surface area, SA. The BET equation:

$$\frac{1}{V[(\frac{P_O}{P})-1]} = \frac{C-1}{V_m}\left(\frac{P}{P_O}\right) + \frac{1}{V_m C}$$

(2.5)

P = Equilibrium pressure for a particular surface coverage.

P_0 = The saturated vapor pressure of the liquid adsorbate at the adsorption temperature.

V = The volumetric uptake of gas at pressure P.

C = constant
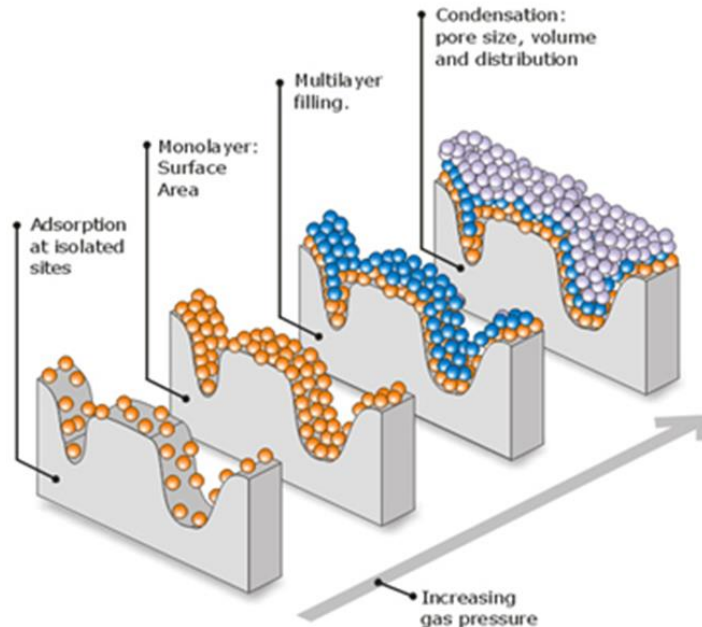
Figure 2.11. Mechanism used in BET surface area calculations. Reprinted with permission open access. [34]

2.2.5. Carbon monoxide temperature programmed desorption CO-TPD

Temperature programmed desorption is an essential method in determining gas desorption from a solid. Typically, in a temperature programmed desorption experiment the catalyst that is being evaluated is a small amount, in order to stay consistent, all samples evaluated were 85mg. The sample is place inside a U-tube that is surrounded by the furnace. The sample is heated while immersed in an inert carrier gas, typically argon, nitrogen or helium. A chromatographic detector is employed to analyze the differences in the carrier gas output, which is located after from the reactor. As the carrier gas flows over the catalyst sample gas molecules will be adsorbed on the catalyst surface. The adsorbate is typically injected into the carrier prior to the reactor. A suitable amount of time is allowed to pass evacuate the gas that has not adsorbed onto the catalyst's surface. Then the sample is heated again, this generates a linear rise in temperature with time. Now instead of the gas molecules adsorbing onto the surface gas molecules are desorbing from the surface into the carrier gas to the detector. The measurements of the carrier gas' flow rate and heating rate correspond to the catalyst temperature. Therefore, as the sample is heated and temperatures are increased the rate at which the gas molecules desorb also increases. Many parameters factor into the spectra being acquired such as the rates at which the sample is heated, the general make-up of the catalyst and surface coverage. Desorption of the gas molecules could involve several stepped mechanisms and/or other binding sites   for each species. Therefore, desorption spectra may show more than one peaks. Desorption data that is collected and analyzed is found on that of the absorbed species and its surface concentration. Since this is all geared on rate, a kinetics study is also obtainable. The kinetic process includes the surface reaction after

desorption and catalytic mechanisms can be inferred. As the products are formed it is important to understand that the main factors in creating these products is reactants surface chemistry and the surface of the adsorbed species   In order to calculate the surface coverage from the desorption spectrum equation 5 is employed:[35]

$$n_o = \int \left(-dn/dt \right) dt = \int ct \cdot p \cdot dt \qquad (2.6)$$

Where n_o is the initial coverage prior to the commencement of desorption, and ct is the proportionality factor relating the partial pressure (p) to the desorption rate. Atypical experimental set up would be as such: Micromeritic AutoChem II 2920 chemisorption analyzer, the same instrument employed in the H_2-TPR experiments, was used to conduct the CO temperature programmed desorption (CO-TPD). Each new sample was placed in a U-tube and heated from room temperature to 400 ^{o}C under He gas to remove residual moisture. Next the sample was cooled to room temperature and 5%CO-95%He gas was flowed at 50 mL/min through the sample for 30 min. Finally, the sample was heated up to 400 ^{o}C under He gas and data was collected to determine the desorption peaks of CO at certain temperatures.

2.2.6. X-ray photoelectron spectroscopy

Figure 2.12, is a pictorial representation of principles of x-ray photoelectron spectroscopy. Surface chemistry plays a vital role in understanding the principles of solid catalysts because of the based on its exceptional ability of investigating the surface geometric and electronic structure. X-ray photoemission spectroscopy (XPS) was used to examine these particular surface compositions and the chemical state of the elements present in the catalysts. The reason XPS has the capability in determining such

properties, listed above, is due to the short mean free path of photoelectrons in solid,[36] The detectable region on the solid for XPS is just a few atomic layers deep, this is within the measurable area for dependent kinetic energy of the electrons being used. Typically, XPS the analysis pertains to the chemical states and the valence band electronic structure of the materials.[37] XPS is able to detect and measure elemental configurations in the parts per thousand, as well as determine empirical formulas chemical formulas, all due to the unique surface sensitivity. When a material in bombarded with X-rays while the kinetic energy and number of electrons that escape from the few layers deep on the surface, 0-10 nm, a spectrum can be constructed. The XPS system must be maintained under ultra-high vacuum ($p\sim10^{-9}$ millibar) which allows for the surface chemistry to be measured.[36,37] The XPS spectrum is constructed by plotting the number of electrons detected versus the binding energy of the electrons detected. Since, every element is unique, a characteristic set of peaks for that element is generated and correlates to that elements binding energy that exists in or on the surface of that material. The known electron configuration within the atoms, e.g., 1s, 2s, 2p, 3s, etc. of each element then parallel the spectral peaks generated by the number of detected electrons in each of the characteristic peaks and then is directly related to the amount of element within the XPS sampling volume.[38]
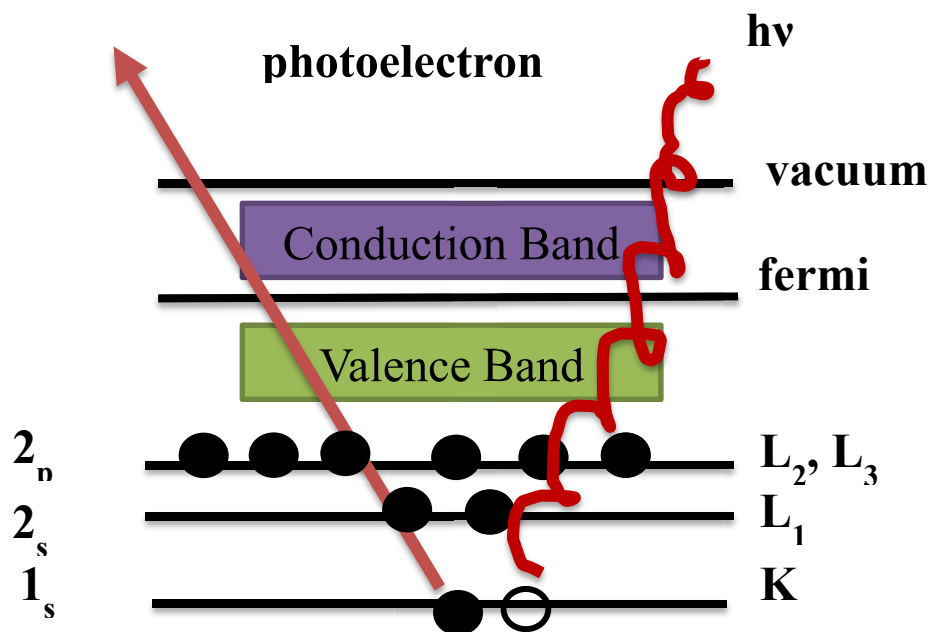
Figure 2.12. An XPS scheme showing the principles of x-ray photoelectron spectroscopy.

The energy of an Al K_α X-ray is known for that wavelength (E_{photon} = 1486.7 eV), and in Equation 2.7, a work by Ernest Rutherford in 1914, showed if the electrons emitted are measured for the value of their kinetic energies, the electron binding energy of each of the emitted electrons is then determined.[39]

$$E_{binding} = E_{photon} - (E_{kinetic} + \Phi) \tag{2.7}$$

2.2.7. CO Oxidation

To determine the percentage of carbon monoxide (CO) converted to carbon dioxide (CO_2) a characterization method called CO Oxidation is used. The catalytic activity of a material is then measured by its CO oxidation.[40,41]
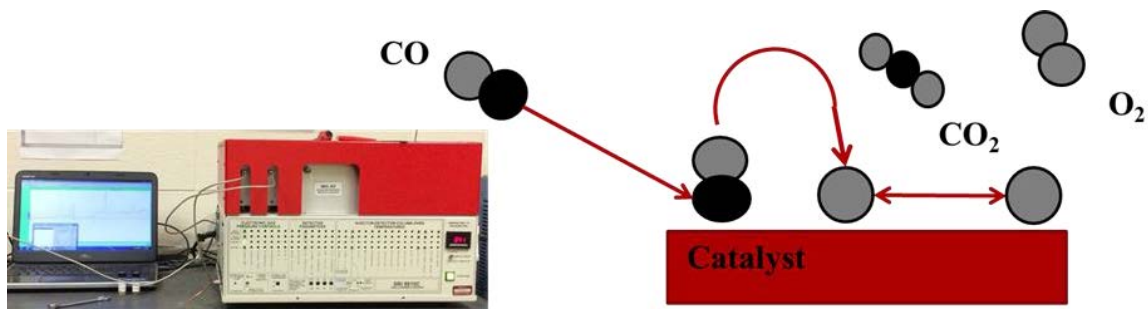
Figure 2.13. (a) Fixed bed plug flow reactor system with on-line gas chromatograph system SRI multiple gas analyzer GC 8610C Chassis. (b) Mechanism used in CO oxidation analysis.

This is technique is performed by using a fixed bed plug flow reactor system. 1 vol%CO/20 vol%O_2/79 vol%He with a 70 mL/min flow rate which is supplied by a mass flow controller and passed through the catalyst bed. Typically, a sample (30 mg) is held in place with quartz wool (coarse, 9 μm) and placed centrally in a quartz tube reactor. Figure 2.13 (b), demonstrates the mechanism that is carried out using, shown in Figure 2.13 (a), SRI multiple gas analyzer GC, 8610C chassis system. A K type thermocouple is used to monitor the reaction temperatures between 30 °C and 350 °C. The on-line gas chromatograph records the reactant CO and product CO_2 and the conversion is calculated using the simple % CO equation.[42]

$$\%CO \text{ conversion} = \left(1 - \frac{CO_{peak\ area}}{CO_{peak\ area} + CO2_{peak\ area}}\right) \times 100\% \qquad (2.8)$$

Langmuir's original work with Pt wires propelled experimentation of catalytic oxidation of CO on surfaces of noble metal clusters.[43] The molecular rearrangement of the reaction is essential in investigations of catalysis and automotive exhaust remediation as well as many other CO removal endeavors i.e. CO from H_2-containing streams by

preferential CO oxidation. With this technique our studies were able to gain deeper understanding into the thermal stability of our catalyst and active catalyst support, activation energy and amount of CO conversion. As shown in work by Tang et al.,[44] who demonstrated how catalyic activities were improved using the wet incipient impregnation method of copper nitrate and copper carbonate onto CeO_2 catalyst supports.

2.2.8. Oxygen Storage Capacity (OSC)

Determining the OSC for catalysts and catalyst supports requires an H_2 pulse chemisorption technique which uses dynamic conditions from a pulse chromatograph.[45] The technique was first introduced by Yao and Yu Yao, where they looked at the reactive oxygen species of CeO_2 and the oxygen atoms that are accessible easily.[46] This technique is done because CeO_{2-x} ($0 \leq x \leq 0.5$) helps form various types of oxygen vacancies and contributes to increase the oxygen storage capacity (OSC). Since, the subsurface oxygen vacancies can be created easily on different surfaces, depending on the surface structure, this causes the diffusion of lattice oxygen vacancies to migrate, increasing oxygen mobility.[47] Before the measurements are taken approximately 50 mg of sample is loaded in U-tube, which are pre-treated at 350 $^{\circ}C$ in 5%O_2-95%He environment for 30 min. The sample is then brought to room temperature and He gas was flowed for 30 min, this removes excess amounts of oxygen from the system and allows for a more accurate determination. The sample will then be reheated to 350 $^{\circ}C$ and 5%H_2-95%He gas is injected into the sample tube in three-minute intervals awaiting an equilibrium in the intensity of the hydrogen consumption peaks. The amount of OSC will be determined from the quantity of CO_2 created after the first CO pulse during the while alternating

pulses of CO or O_2 that are injected. The OSC is expressed as μmol of O_2 per gram of catalyst.

2.2.9. Transmission Electron Microscopy (TEM)

Transmission electron microscopy is a very sophisticated scientific imaging technique and operates on the same basic theory as the light microscope but uses electrons instead of light. Light microscope is limited by the wavelength of light whereas; electron microscopy technique passes a beam of electrons through the sample to create an image. Typically, the sample is <100 nm thick or a grid with the sample suspended on a grid. As stated earlier the beam of electrons, created by an electron gun, interacts with the sample to create an image. This method of obtaining information from a sample gives information about the topography (surface features), morphology (shape and size), composition (both qualitative and quantitative) and crystallographic information[48] Recall the section on XRD, which is an analytical technique that is used to determine the atomic and molecular structure of a crystal.
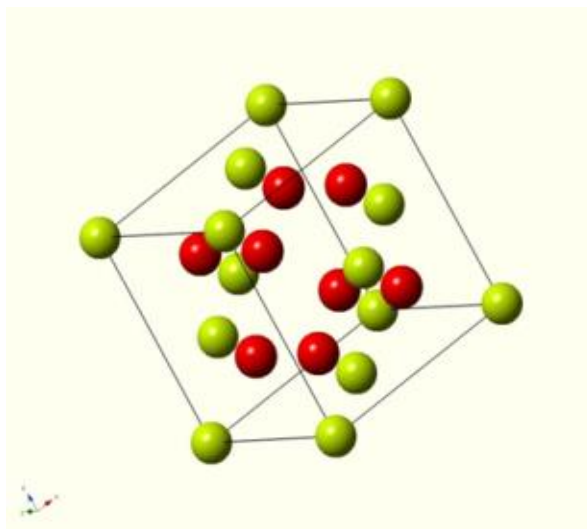
Figure 2.14. Atomic structure of CeO$_2$ unit cell.

The atomic structure of CeO_2 can be seen in Figure 2.14. The resolution of typical HRTEMs is roughly at a 0.2 nm or slightly better resolution.[49] Compared to X-rays the electron interaction is stronger and electron diffraction. When working on the nanoscale, conventional X-ray diffraction methods are too small and would require synchrotron analysis to study the sample. Equation 2.9, Bragg's law, is undeniable proof for the periodic atomic structure of crystals. Electron diffraction is available within the constructs of the TEM such imaging is made possible and is complemented with other techniques such as imaging and/or spectroscopy. Since, electrons are scattered by light atoms more intensely the resolution is beyond that of x-rays and reflections can correspond to that of the intensity. And this is due to the smaller de Broglie wavelength of electrons.[50] Louis de Broglie worked on a theory in quantum mechanics where it is possible for all matter to exhibit wave-like behavior.[51] So, a beam of light which is similar to a beam of electrons displays wave-like characteristics. Equation 2.9, expresses the wavelength, λ, known as the de Broglie wavelength corresponds to a particle's momentum, p, through the Planck constant, h:

$$\lambda_{de\ Broglie\ wavelength} = \frac{h}{p} \qquad (2.9)$$

The TEM, has the ability to obtain high resolution images, thousands of times smaller than light microscopes.[52] Through HRTEM resolutions that are so small, single atom detail is possible. In Figure 2.15, a schematic of a TEM shown from the top down. The electron source, called the electron gun, is positioned at the top it is typically equipped with a tungsten filament or a lanthanum hexaboride (LaB_6) single crystal source.[48] A high voltage source provides the gun with enough current to deliver voltage in the range of

~100–300 kV. In the thermionic electron gun direct current is used to create the beam of electrons in this process a cathode is heated and the beam of electrons are created. These electrons then need focused in order to continue down the column, this is done using an electric field, such as a Wehnelt cylinder and additional acceleration is required to continue to focus the beam of electrons.

Once the electrons are produced, by thermionic emission or field emission, and travel into the vacuum. The electron beam is then further focused through magnetic lenses on the upper section of the TEM. Electromagnetism is the phenomenon that is used in order to control and adjust the focusing of the electron beam. The electromagnetism effects allow for deflection of the electron beam in opposing direction, thus aligning the beam for TEM operation. The electromagnetic lenses, and are used to help to align the beam which causes the interaction of electrons with the magnetic field to change their alignment using the left-hand rule. In addition, the magnetic field has a variable focusing power.[53] There are different ways in the TEM to collimate beam, these consists of three of lensing stages. Figure 2.15 also shows the various stages are as such; the condenser lenses, the objective lenses, and the projector lenses. The condenser lenses, magnetic lenses, are used to initially form the electron beam, as the objective lenses are used to focus the beam that hits the specimen. Finally, the projector lenses, forms the beam onto the imaging device, such as the phosphor screen. The ratio of the distance measured between the objective lens plane and the sample is how the magnification is determined.[54] Other magnetic lenses such as stigmators are utilized to correct astigmatism and custom lenses used to correct spherical aberrations.[55]
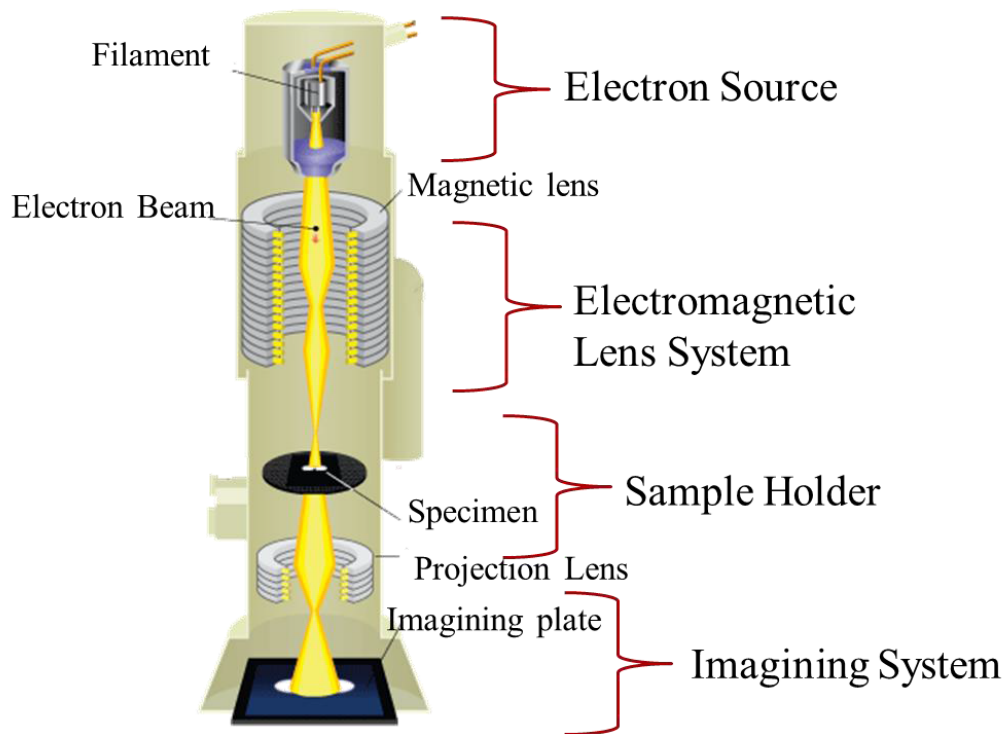
Figure 2.15. Schematic of a transmission electron microscope (TEM). Reprinted with permission open access.

In Figure 2.16, a magnified image of CeO_2 nanorods using HRTEM with SAED (selected-area electron diffraction), is shown, the parallel beam interacts with sample and the aperture used defines the area of interest. In the TEM this aperture is often located in the below the sample and the diffracted area in around a few hundred nanometers. The diffraction patterns are of a single spot that represents a single crystal diffraction pattern or ring patterns of polycrystalline samples. This technique can be used to determine phase identification, determination of structural intergrowth, determination of growth directions.[56] In addition to SAED and the conventional TEM, Energy Dispersive X-ray (EDS) Spectroscopy, is a technique used to obtain valuable information pertaining to the sample such as elemental composition. Most elements can be determined but in theory, element atomic numbers from 4 (Be) to 92 (U) can only be quantitatively analyzed.[57]

However, not all instruments are furnished to obtain chemical analysis on light elements, where the $Z < 10$.[58] An energy-dispersive X-ray spectrometer (EDS) works so that each pulse of the voltage is relative to the energy of the incoming x-ray photon. Most TEMs with EDS capabilities, qualitative analysis is done with an on-board software package, EDAX. These analyses are done using known standards and measuring the intensities of each element. Surface topography is also employed in order to determine the mean atomic differences between each element present within the sample. This is done by rastering the beam across the sample and determining the intensities of individual selected X-ray lines.

In this dissertation, outlined in detail is the synthesis, characterization and catalytic performance of various CeO_2 morphologies impregnated with CuO_x nanomaterials, as well as bimetallic alloy catalyst systematic study of the structure-activity relationship and catalytic performance. Two typical synthetic methods, hydrothermal and co-precipitation methods, are used to synthesized all cerium oxide supports. Instrument techniques were employed to gain a better understanding of the physical and chemical properties of catalysts. These characterization techniques include electron microscopy, X-ray diffraction, Raman spectroscopy, X-ray photoemission spectroscopy, BET surface area and catalytic experiments such as: CO-TPD, OSC, CO oxidation. The morphologies of the cerium oxide and their surface defects are investigated to correlate physical properities with with their catalytic performance.
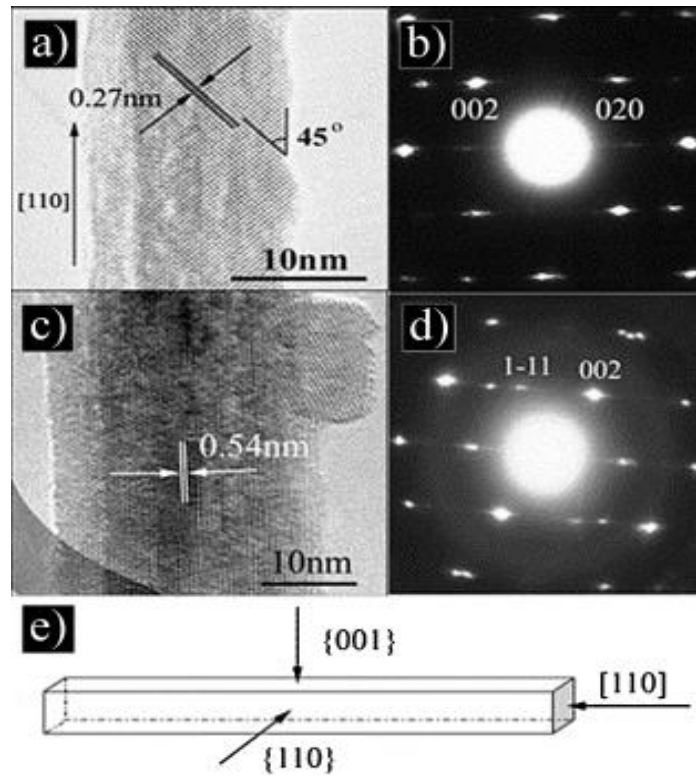
Figure 2.16. Magnified HRTEM of a typical rod view along [001]; (b) the SAED pattern of (a); (c) magnified HRTEM of a typical rod view along [110]; (d) the SAED pattern of (c); (e) the structural models of CeO₂ rod. Reprinted with permission by Wiley Publishing [59[59]]

2.3. References

1. Wang, S. P.; Zhao, L. F.; Wang, W.; Zhao, Y. J.; Zhang, G. L.; Ma, X. B. and Gong, J. L. Morphology control of ceria nanocrystals for catalytic conversion of CO_2 with methanol. *Nanoscale,* **2013,** 5, 5582-5588.

2. Roy, R. Accelerating the kinetics of low-temperature inorganic syntheses. *J. Solid State Chem.,* **1994,** 111, 11-17.

3. Karakoti, A. S.; Monteiro-Riviere, N. A.; Aggarwal, R.; Davis, J. P.; Narayan, R. J.; Self, W. T.; McGinnis, J. and Seal, S., Nanoceria as antioxidant: synthesis and biomedical applications. *JOM.,* **2008,** 60, 33-37.

4. Yang, Q.; Fu, X.; Jia, C.; Ma, C.; Wang, X.; Zeng, J.; Si, R.; Zhang, Y. and Yan, C. Structural determination of catalytically active subnanometer iron oxide clusters. *ACS Catal.*, **2016**, 6, 3072-3082.

5. Laudise, R. A. Hydrothermal Synthesis of Crystals, *Chem. Eng. News*, **1987**, 65 39, 30-43.

6. Yoshimura, M.; Suchanek, W. L. and Byrappa, K. Soft solution processing: a strategy for one-step processing of advanced inorganic materials. *MRS Bull.,* **2000,** 25, 17-25.

7. Kolb, E. D.; Barns, R. L. and Laudise, R. A. Solubility, crystal growth and perfection of aluminum orthophosphate. *J. Crystal Growth,* **1980,** 50, 404-418.

8. Sugimoto, T. *Fine Particles, Synthesis, Characterization, and Mechanisms of Growth*, Marcel-Dekker, Inc., NY, **2000**.

9. Riman, R. E. *High Performance Ceramics: Surface Chemistry in Processing Technology*, edited by Pugh and Bergstrom, Marcel-Dekker, NY, **1993,** 29.

10. Trovarelli, A. Structural and oxygen storage release properties of CeO_2 based solid solutions. *Comments Inorg. Chem.,* **1999,** 20, 263-284.

11. Ring, T. A. *Fundamentals of ceramic powder processing and synthesis,* Academic Press, San Diego, CA **1996**.

12. Grange, R.; Dutto, F. and Radenovic, A., *Nanotechnology and Nanomaterials Nanowires Implementations and Applications*, edited by Abbass Hashim, **2011.**

13. Haberko, K. and Pyda, W. *In Science and Technology of Zirconia II, Advances in Ceramics*, edited by Claussen, Ruhle and Heue, **1984,** 12, 774.

14. Wang, R. and Dangerfield, R.; Seed-mediated synthesis of shape-controlled CeO_2 nanocrystals. *RSC Adv.,* **2014**, 4, 7, 3615-3620.

15. Mai, H.X.; Sun, L.D.; Zhang, Y.W.; Feng, W.; Si, Rui.; Zhang, H.P.; Liu, H.C. and Yan, C.H. Shape-selective synthesis and oxygen storage behavior of ceria nanopolyhedra, nanorods, and nanocubes. *J. Phys. Chem. B.*, **2005,** 109, 24380.

16. Knö̈inger, H., et al. *Preparation of Solid Catalysts*. Wiley-VCH, **1999**.

17. Bragg, W.H. and Bragg, W.L. The reflection of X-rays by crystals. *Proc. R. Soc. Lond. A.*, **1913**, 88, 428.

18. Massa, W. *Crystal structure determination*. Berlin: Springer. **2000.**

19. Housecroft and Sharpe. *Inorganic chemistry*. Upper Saddle River, N.J: Pearson Prentice Hall. **2005.**

20. Sasaki, K.; Zhang, L. and Adzic, R. R., Niobium oxide-supported platinum ultra-low amount electrocatalysts for oxygen reduction. *Phys. Chem. Chem. Phys.*, **2008,** 10, 159-167.

21. Harris, Daniel C., and Bertolucci Michael D. *Symmetry and Spectroscopy an Introduction to Vibrational and Electronic Spectroscopy*. Dover, **2014**.

22. Raman, C. V. A new radiation. *J. Phys*., **1928,** 2, 387-398.

23. Singh, R., C. V. Raman and the discovery of the Raman effect. *Physics in Perspective*. **2002,** 4, 399-420.

24. Settle, Frank A. *Handbook of Instrumental Techniques for Analytical Chemistry*. Prentice Hall, **1997**.

25. Schrader, Bernhard, and Bougeard. *Infrared and Raman spectroscopy: methods and applications*. Wiley, **2008**.

26. Lee, Y.; He, G.; Akey, A.; Si, R.; Flytzani-Stephanopoulos, M. and Herman, I. Raman analysis of mode softening in nanoparticle $CeO_{2-\delta}$ and $Au-CeO_{2-\delta}$ during CO oxidation. *J. Am. Chem. Soc.,* **2011**, 133, 12952-12955.

27. Dwivedi, R. K. and Kay, D. A. R. Determination of the standard free energies of formation of Ce_2O_2S and Y_2O_2S at high temperatures. *J. Less-Common Met.* **1984,** 102, 1-7.

28. Robertson, S. D.; McNicol, B. D.; de Baas, J. H.; Kloet S.C. and J. W. Jenkins, Determination of reducibility and identification of alloying in copper nickel on silica catalysts by temperature-programmed reduction. *J. Catal*., **1975,** 37, 3, 424.

29. Temperature-Programmed Reduction using the AutoChem [Application Note]. **1999**. Http://www.micromeritics.com/, Norcross, Georgia.

30. AutoChem 2920 Automated Catalyst Characterization System [Operator's Manual]. **2009**. Http://www.micromeritics.com/, Norcross, Georgia.

31. Mock, S.; Zell, E.; Hossain, S.T.; Wang, R.; Effect of reduction treatment on CO. oxidation in CeO_2 nanorods supported CuO_x Catalysts, *ChemCatChem.*, **2017**, 10, 1, 311-319.

32. Bowker, M. *Basis and applications of heterogeneous catalysis*. Oxford Science Publications, **1998**.

33. Chorkendorff, I., and J.W Niemantsverdriet. *Concepts of modern catalysis and kinetics*. Wiley-VCH, **2003.**

34. "Surface Area." *Micromeritics Analytical Services*, particletesting.com/surface-area/.

35. Cvetanović, R.J. and Amenomiya, Y. Application of a temperature-programmed desorption technique to catalyst studies. *Adv. Catal*., **1967,** 17, 103-149.

36. Carlson, T.A. and McGuire, G.E. Study of the x-ray photoelectron spectrum of tungsten-tungsten oxide as a function of thickness of the surface oxide layer. *J. Electron Spectrosc. Relat. Phenom*., **1972**, 1, 161-168.

37. Strohmeier, B.R. An ESCA method for determining the oxide thickness on aluminum alloys. *Surf. Interface Anal.,* **1990,** 15, 51-56.

38. Reinert, F. Hüfner, S., Photoemission spectroscopy from early days to recent applications. *New J of Phy.,* **2005**, 7. 97.

39. Einstein, A., Concerning a heuristic point of view toward the emission and transformation of light. *Annalen der Physik*, **1905**, 17.

40. Bensaid, S.; Piumetti, M.; Novara, C.; Giorgis, F.; Chiodoni, A.; Russo, N. and Fino, D.; Catalytic oxidation of CO and soot over Ce-Zr-Pr mixed oxides synthesized in a multi-inlet vortex reactor: effect of structural defects on the catalytic activity. *Nanoscale Res Lett.*, **2016**, 11, 494. 1-14.

41. Wu, C.; Brescia, R.; Prato, M.; Marras, S.; Mannaa, L. and Colombo, M. Tuning the CO oxidation catalytic activity of supported metal–metal oxide heterostructures by an aqueous phase post-treatment process. *J. Mater. Chem. A.,* **2016,** 4, 18075-18083.

42. Hossain, S.T.; Almesned, Y.; Zhang, K.; Zell, E.; Bernard, D.; Balaz, S.; and Wang, R.; Support Structure Effect on CO Oxidation: A Comparative Study on SiO_2 Nanospheres and CeO_2 Nanorods Supported CuO_x catalysts. *Appl. Surf. Sci*., **2018**. 428, 598-608.

43. Langmuir, L. The mechanism of the catalytic action of platinum in the reactions $2Co + O_2 = 2Co_2$ and $2H_2 + O_2 = 2H_2O$. *Trans. Faraday Soc.,* **1922**, 17, 621-654.

44. Tang, C.; Bando, Y.; Liu, B.; Golberg, D.; Cerium oxide nanotubes prepared from cerium hydroxide nanotubes. *Adv. Mater.,* **2005**, 17, 3005–3009.

45. Kummer, J. T. Proceedings of Energy Combustion Science, Vol. 6, 177. Pergamon, Ltd, Great Britain, **1980**.

46. Yao H. C. and Yu Yao, Y. F. Ceria in Automotive Exhaust Catalysts. *J Catal.*, **1984,** 86, 254-265.

47. Perrichon, V.; Laachir, A.; Bergeret, G.; Frety R. and Tournayan, L., Reduction of cerias with different textures by hydrogen and their reoxidation by oxygen. *J. Chem. Soc. Faraday Trans.,* **1994**, 90, 773-781.

48. Egerton, Ray F. *Physical principles of electron microscopy: an introduction to TEM, SEM and AEM*. Springer, **2016**.

49. Keyse, Robert J. *Introduction to scanning transmission electron microscopy.* BIOS Scientific Publishers, **1998**.

50. MacKinnon, E. De Broglie's thesis: A critical retrospective. *Am. J. Phys.,* **1976,** 44, 1047.

51. Feynman, R. QED: The strange theory of light and matter, Penguin, **1990.** Ed. 84.

52. Gianfrancesco, D.A. *Materials for ultra-supercritical and advanced ultra-supercritical power plants.* Woodhead Publishing, **2017**.

53. Honglong, S.; Guling, Z.; Bin, Z.; Minting, L. and Wenzhong, W. A method for structure analysis of nanomaterials by electron diffraction: phase identification and unit cell determination. *Microsc. Res. Tech.,* **2013,** 76, 6, 641-647.

54. Amelinckx, S. *Electron microscopy: principles and fundamentals*. VCH, **1997.**

55. Haider, M.; Rose, H.; Uhlemann, S.; Kabius, B. and Urban, K. Towards 0.1 nm resolution with the first spherically corrected transmission electron microscope. *J. Electron. Microsc.,* **1998,** 47, 395-405.

56. Zhang, Q.; Wang, H-Y.; Jia, X.; Liu, B. and Yang, Y. One-dimensional metal oxide nanostructures for heterogeneous catalysis. *Nanoscale,* **2013,** 5, 7175-7183.

57. Sun, C.; Li, H. and Chen, L. Nanostructured ceria-based materials: synthesis, properties, and applications. *Energy Environ. Sci*., **2012,** 5, 8475-8505.

58. Goldstein, J. I., et al. Scanning Electron Microscopy and X-ray Micronalysis, 3rd ed, Plenum Press, New York. **2003.**

59. Qiao, Z.; Wu, Z. and Dai, S. Shape-Controlled Ceria-based Nanostructures for Catalysis Applications. *ChemSusChem.,* **2013**, 6, 1821 – 1833.

Chapter 3: Shape-Controlled Synthesis of the Application of CeO$_2$ Nanostructures for Catalyst Support

The results presented in this chapter will focus on the first objective of this dissertation, namely, the synthesis of size/shape-controlled CeO$_2$ using co-precipitation and the hydrothermal methods. Various molar concentrations of sodium hydroxide (NaOH) will be used. The molarity of the cerium precursor, cerium nitrate (Ce(NO$_3$)$_3$·6H$_2$O), will be approximately 0.1 M. The hydrothermal reaction temperature is a major factor and will be varied from 90-210 °C. The dwell time for crystal growth will vary between 24-96 h. In this work, it is crucial to find the proper parameters to optimize the shape controlled nanostructures.

3.1. Introduction

The fast-growing field of nano-catalysts is becoming very important in heterogeneous catalysis and materials science. This is because the properties of certain nano-catalysts are dependent upon the shape. The simplicity of fabrication of catalytic nanomaterials is making it easier for scientists to engineer materials for specific catalytic properties. Properties of heterogeneous catalysts such as, single or twinned crystals with an average size of 10-100 nm can work to scientists' advantage. This is because the sensitivity increased due to the surface structural and/or electronic properties on the nano-level.[1,2] These nano-catalysts have high surface-to-volume ratios which equates to more active sites and therefore consist of low-coordinated atoms that are located at the defect sites. For example, in a study by Haruta et al., gold was investigated for its specific properties at the nano-level.[3] It is known that bulk gold is catalytically inert but nanometer areas

have shown to become highly active for low-temperature CO oxidation.[4,5] This understanding on nano-level properties leads researchers to dig deeper into other properties. Since the size has a strong effect on differences in geometric and/or electronic properties, effects on the adsorption and activation of CO and molecular oxygen are also known to take place.[6] In addition, we strive to understand if there is a correlation with the nano-catalyst's shapes with different termination planes and the catalytic activity.[7,8] The total energy of the system i.e. surface-planes/facets heavily effects the catalytic activity. Anisotropic shape dependent nanoparticles aid in the catalytic efficiencies by exposing more reactive crystal planes.[7] Reactive planes like (111) for Co_3O_4 nanorods are noted for being some of the first documented nanoparticles to show a shape dependent effect.[9] These nanorods show superior catalytic behavior due to their coordinated Co^{3+} species as the active sites for CO oxidation. In addition, certain Fe_2O_3 nanomaterials that contain the reactive (110) planes show lower CO oxidization temperatures compared to other random morphologies.[10] Exposed crystal planes affect catalytic reactivity at far greater than properties like surface area or particle size. Recall the (100) plane of ceria is less stable because of the alternating charged planes. This introduces a dipole moment that is perpendicular to the surface plane.[11] The stabilization of the (100) planes of ceria are due to the surface defects which allow a compensation of charges. However, the stoichiometrically neutral plane of ceria is the (110) plane, where the anions and cations are proportional and results in no dipole moment perpendicular to the surface plane.[12] These properties, structural and electronic components are essential to utilizing the heterogeneous catalyst and ceria to the fullest possibilities. Extensive research on heterogeneous catalysts and ceria as a support has been a primary focus and tends to be

one of the most important research components. Since ceria has exceptional abilities to utilize oxygen in various environments, it is obvious to investigate the size/shape effects on catalytic properties. The three-way catalyst is often first thought of when considering converting toxic emissions from automobile exhaust. It is known that there is a relationship between the oxygen storage capacity and crystal plane surface of CeO_2. This relationship may be due to ceria's exceptional reversible redox properties of Ce^{4+} and Ce^{3+}. There are three well established, low index planes of ceria; (111), (110), and (100). Shown in Figure 3.1, is a modeling schematic of ceria's the low index planes. It is well known that the stability of these planes follows the order of (111) > (110) > (100).[13] Where the (111) plane is the most stable of the three index planes.
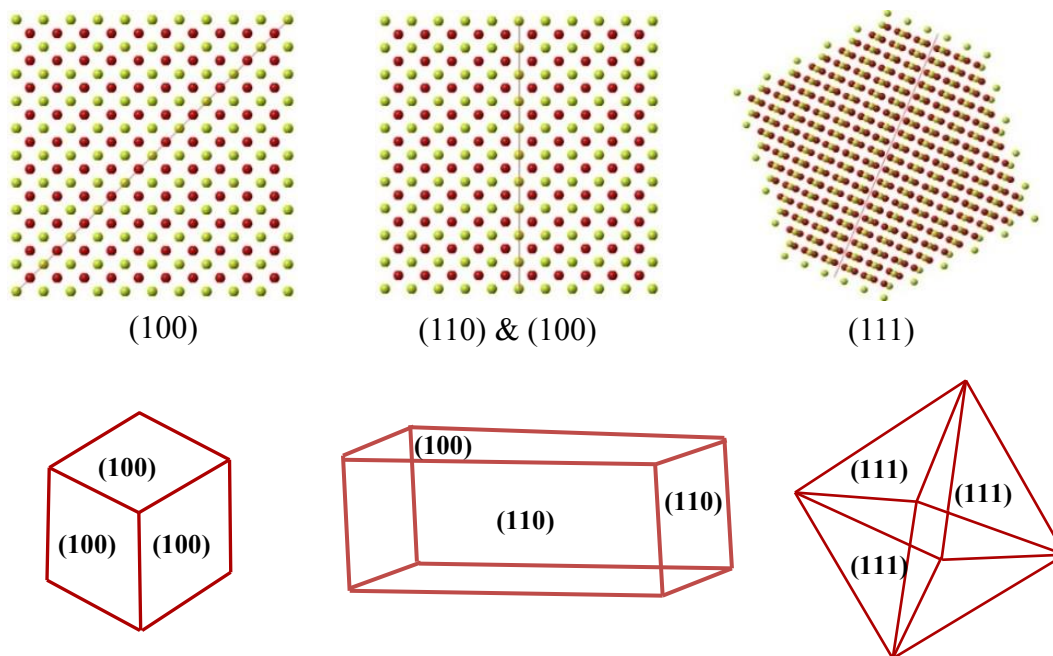
Figure 3.1. Crystal Maker models of ceria's three low index planes and shape diagrams with termination planes denoted.

Research by Wang et al. studied the morphology control of ceria nanocrystals.[14] All samples were synthesized using a hydrothermal method and cerium nitrate $(Ce(NO_3)_3 \cdot 6H_2O)$ was used as the Ce precursor.[14] However, the octahedral samples were sodium phosphate (Na_3PO_4) as the promoter and for the nanocube and nanorod samples sodium hydroxide NaOH was used. This differs from this work, where NaOH was used for all samples. In addition, all samples prepared by Wang et al., were calcinated at 600˚C for 5 h. Calcination of ceria nanocrystals at temperatures above 500˚C is known to significantly decrease the specific surface area which can be attributed to the increased surface diffusing, ultimately reducing surface area and surface roughness.[15] Noted by Mai et al. changing the concentration of the promoter, NaOH, would change the shape.[16] Mai et al synthesized various morphologies of ceria using different concentrations of NaOH, from 3 molar to 9 molar. The other experimental parameter that was changed was the temperature, where the nanorods synthesized using 6 M NaOH and were heated at 140˚C and the samples using 3 M NaOH and 9 M NaOH were only heated to 100˚C, the dwell time remained constant for all Mai's samples.[16] In addition, Mai calcinated all samples at 1000 °C in air, and was able to demonstrate that elevated temperatures and base concentration were the main factors in shape-controlled synthesis of CeO_2. In this chapter, CeO_2 nano-octahedra, nanocubes, and nanorods with different termination crystal planes have been synthesized using co-precipitation and hydrothermal methods with concentration of NaOH, dwell time and hydrothermal temperatures altered. It is also well known that high temperatures thermal treatments above 800˚C may alter the morphology and surface of CeO_2. Since, surface structure and defects play a role in effecting the catalytic performance of CeO_2, this research did not perform any high

temperature calcination on the catalysts or the supports during the experimental procedures. Additionally, the knowledge gained in the shape-controlled synthesis of CeO_2 will be used to further increase catalytic activities of supported catalysts in subsequent chapters.

3.2. Experimental

3.2.1. Catalyst Support Synthesis

In this work, a typical synthesis procedure for CeO_2 nanomaterials, involved the hydrothermal reaction, included 8 mL of 6 M NaOH solution added dropwise into 88 mL of 0.1 M $Ce(NO_3)_3$ solution with vigorous stirring. The stirring was done in order to homogenize the two reactants and facilitate the reaction. Figure 3.2 shows the flow chart of the morphological and synthetic routes of various ceria nanomaterials in our group. However, temperature is not the only factor a factor in the shape-size control of the CeO_2 nanoparticles. They can also be tuned by changing the concentration of the reactants, which will also be a focus of this chapter.
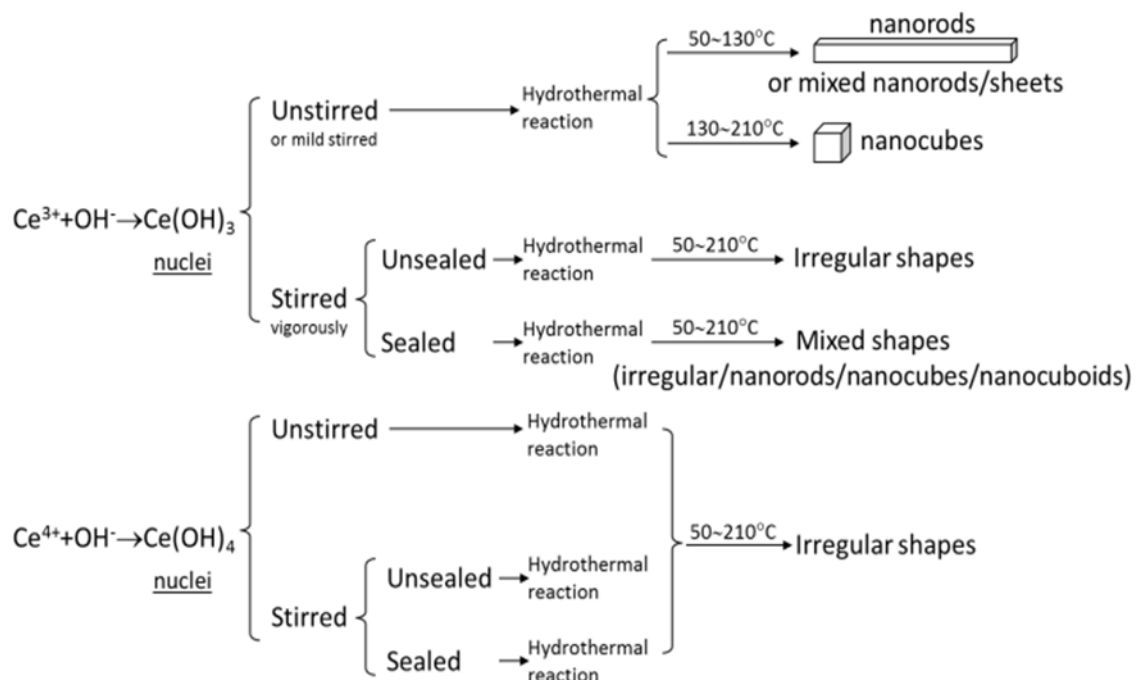
Figure 3.2. Schematic showing the shape-controlled synthesis of CeO$_2$ nanocrystals.
[17]

All techniques for characterization of the catalysts and catalytic activity, such as;

X-ray diffraction (XRD), Raman spectroscopy, X-ray photoelectron spectroscopy (XPS),

transmission electron microscopy (TEM), BET surface area measurement, temperature

programmed reduction (TPR), temperature programmed oxidation (TPO), temperature

programmed desorption (TPD), pulse chemisorption to calculate oxygen storage capacity

(OSC), and CO oxidation can be found in Chapter 2.

Table 3.1. Experimental parameters with calculated lattice constant and crystalline sizes.

CeO$_2$ Structure	Temp T (˚C)	Conc NaOH (M)	Dwell Time (h)	Ce/NaOH Ratio	Crystalline Size (nm)	Lattice Constant (Å)	BET (m^2/g)
Nano-Octa	Co-precip	6 M	N/A	11:1	10.2	5.38	38.2
Nanocubes	210	6 M	24	11:1	15.32	5.422	-
Nanocubes	170	6 M	24	11:1	17.73	5.425	-
Nanocubes	150	6 M	24	11:1	20.5	5.401	48.5
Nanorods	90	6 M	48	6:6	5.61	5.432	-
Nanorods	90	6 M	48	9:3	5.64	5.431	-
Nanorods	90	6 M	48	11:1	5.5	5.454	56.4
Nanorods	90	6 M	24	11:1	5.5	5.431	-
Nanorods	90	6 M	96	11:1	6.9	5.342	-
Nanorods	90	12 M	48	11:1	7.2	5.439	-

3.3. Results and Discussion

3.3.1. Synthetic Approach

Table 3.1 shows a systematic approach to prepare shape/size-controlled CeO_2 nanopowders for the application of catalyst supports. For the CeO_2 nano-octahedra samples, using sodium hydroxide as the precursor and cerium nitrate as the Ce source, a co-precipitation method was used. All samples were washed thoroughly with distilled water to remove any co-precipitated salts and residual ions, then washed with ethanol to avoid hard agglomeration in the nanoparticles, and dried in air at 70 °C for 12 h. Nano-octahedra samples were excluded in the systematic study, since previous work showed less than average catalytic activities. However, in the overall evaluation of the various morphologies, nano-octahedra will be considered. The first study was to explore altering the temperatures of the hydrothermal reaction experiments. This was the only parameter that was changed, using an 11:1 volume ratio of 0.1 M $Ce(NO_3)_3 \cdot 6H_2O$ (99.9% purity, Alfa Aesar) and a 6 M NaOH (>98% purity and obtained from Sigma–Aldrich), and the two were added into a 250 mL beaker on a hotplate-stirrer under slight stirring.[17] The suspension was then transferred into a Teflon-lined stainless-steel autoclave. All samples were made in a bulk solution, to maintain consistent comparable data. The hydrothermal reaction temperature was varied in the range of 90 to 210 °C. After the reaction, the autoclave was cooled to room temperature before the solid products were recovered by filtration.

The nanorods that were synthesized were studied with more rigor because of many hypotheses to consider, as nanorods possess greater surface area and superior low temperature reducibility. Firstly, the volume ratio of Ce^{3+}: OH was evaluated. The

cerium nitrate and NaOH volume ratios were set to 6:6, 9:3 and 11:1. All experimental procedures mimicked the procedures of the earlier experiments, where the two were added into a 250 mL beaker on a hotplate-stirrer under slight stirring.[17] The suspension was then transferred into a Teflon-lined stainless-steel autoclave for the hydrothermal reactions at different temperatures. All samples were made in a bulk solution, to maintain consistent comparable data. Then the autoclave was cooled to room temperature before the solid products were recovered by filtration. Next the nanorods were studied with various dwell times where all other parameters were held constant. Finally, the concentration of NaOH was altered using 6 M, 10 M and 12 M, noted in Table 3.1.

3.3.2. Structural Characterization of CeO_2

3.3.2.1. XRD and TEM

Phase purity of the CeO_2 samples was evaluated using Powder X-ray diffraction. Figure 3.3 (a) shows the typical XRD results for CeO_2 nanocubes and nanorods synthesized at 90°C and 150 °C for 48 h using the hydrothermal method, respectively and for CeO_2 nano-octahedra sample using the co-precipation route. All diffraction peaks were indexed to the cubic fluorite structure (JCPDS 81-0792, space group Fm3m) of CeO_2 for the nano-octahedral, nanocube and nanorod samples, which were observed at 2θ of 28.85°, 33.08°, 47.48°, 56.34°, 59.09°, 69.41°, 76.70° and 79.07°. These reflections can be indexed to (111), (200), (220), (311), (222), (331), (400), and (420) crystal planes. The Scherrer equation was used to estimate the crystalline size of the samples, while the (hkl) Miller indices and d-spacing information were used to compute the lattice constants of the samples and are summarized in Table 3.1 above. The crystalline size decreased as temperature increased, indicating that the growth kinetics slows as temperature is

increased, but not at 90 °C. Figure 3.3 (b), shows the XRD data for the samples synthesized at 90 $^{\circ}$C for 48 h with all three volume ratio proportions, and the XRD result indicates limited change as well. It can be seen that peak broadening occurred at all volume ratio changes which is not the case for the various morphologies. In Figure 3.3 (a), there is a clear crystalline size alteration occuring with the growth kinetics. This broadening is an indication of smaller crystalline sizes, which is consistent with the crystalline size data collected and shown in Table 3.1. This observation indicates that hydrothermal reaction temperature is the major factor in shape control of CeO_2. Seen in Figure 3.4 (a-f), it is noted that as temperature increased the shape control was altered. In Figures 3.4 (a & b), it is clear that nanorods are synthesized and as temperature is increased to 110°C, seen in Figure 3.4 (c), there becomes a mixture of nanocubes and nanorods. Figures 3.4 (d-f) predominately show that nanocubes were synthesized. However, as indicated in Table 3.1, the crystallite size does change, indicating an edging effect. Increasing the concentration of NaOH also played a role in the particle size and lattice constant, as both increased with concentration. Figure 3.5 (a-f) shows the TEM images of CeO_2 nanorod, taken at magnifications of 50 and 100 kx, which documented the alterations in NaOH concentration with all other parameters held constant. The nanorods shape was unaltered, indicating that the concentration of promoter does not change the shape and that temperature is the main factor that alters the shape of CeO_2. Figure 3.5 (a & b) represent the TEM images of CeO_2 nanorods samples with the addition of 6 M NaOH and clearly show shorter length rods and a much rough surface plane, indicating that with increased concentration of NaOH, the growth kinetics can be influenced greatly. Figure 3.5 (c & d) represent the TEM images of CeO2 nanorods

samples with the addition of 10 M NaOH concentration. It is noted that thee nanorods are growing in length, as well as displaying a smoother surface.

(a)   *(b)*
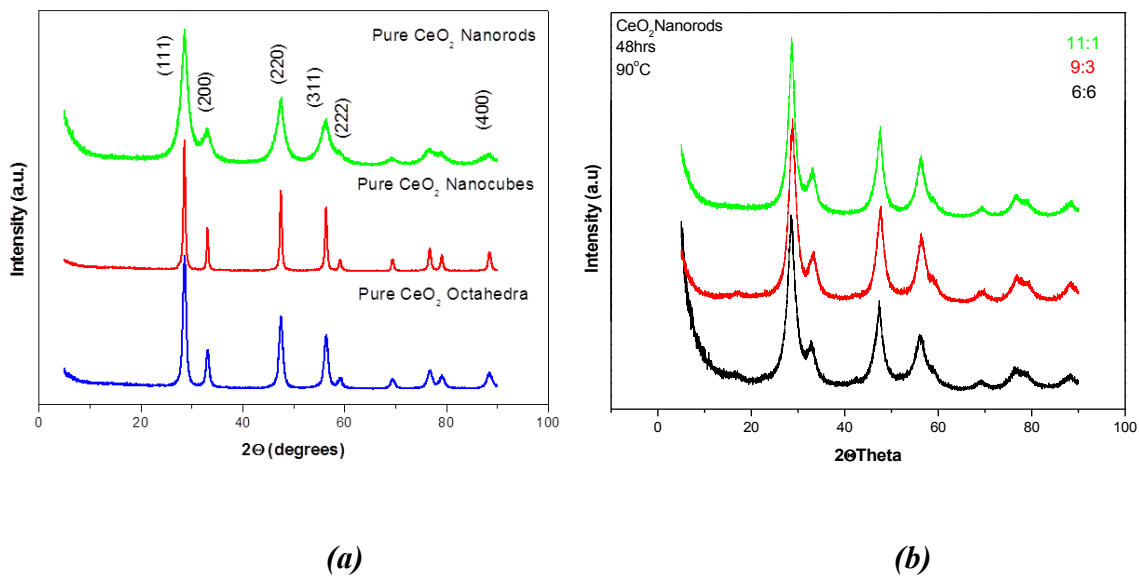
Figure 3.3. (a) XRD patterns of pure CeO₂ nano-octahredra, nanocubes and nanorods (b) XRD patterns of CeO₂ nanorods synthesized at 90 ᵒC for 48 h with various volume ratios.

Figure 3.5 (e & f) shows that CeO_2 shape is not altered even though the concentration of NaOH was doubled. The increased concentration allows the growth kinetics to occur in a particular plane, as demonstrated in the lengthening of the nanorods. CeO_2 nanorods with 12 M NaOH addition were typically 250-300 nm in length, whereas CeO_2 nanorods with 6 M NaOH addition also were shorter in length where a representative sampling indicated lengths between 50 and 100 nm. However, while there is a smooth exterior plane, these nanorods still possess many surface defects. To reiterate, the uncalcined samples all possess surface defects and as the concentration of NaOH increased so did the length of the nanorods. However, it was also noted that with increased concentration of NaOH there were significantly smoother areas, and the overall surface roughness of CeO_2 nanorods seems to vanish. Unlike the sample with 6 M NaOH addition, these nanorods,

although shorter in length, showed high levels of surface roughness. Increasing catalytic performance depends on surface defects, because they are thought to increase the oxygen vacancy creation and the numbers of active sites. Figure 3.6 (a) shows a high resolution TEM image of CeO_2 nanorods that displays the 3.11 Å and 2.7 Å lattice fringes corresponding to the (111) and (100) lattice planes of cubic fluorite-structure. Samples made with 12 M NaOH also had a 48 h dwell time. It is apparent that defects do still exist and that the two low index planes are present. Also noted, but not shown, is the (111) surface plane found at the end of the nanorod samples synthesized in this research. The surface energy required to create oxygen vacancies is lower for the (110) and (100) planes. CeO_2 is considered to possess excellent oxygen storage capacity (OSC). Studies have indicated the OSC is a bulk and surface property for nanocubes and nanorods but that for the nano-octahedra, the OSC is limited to the surface.[18] Since the OSC property is shape dependent, the particle size and surface energies play crucial roles in increasing catalytic parameters. Therefore, the surface structure of the catalyst support is significant in the catalyst support interactions of catalytic behaviors.[19] OSC will be discussed in greater depth in subsequent chapters. 3.7 (b) shows the myriad of surface defects that CeO_2 nanorods possess such as; bending, steps, voids and lattice distortion.
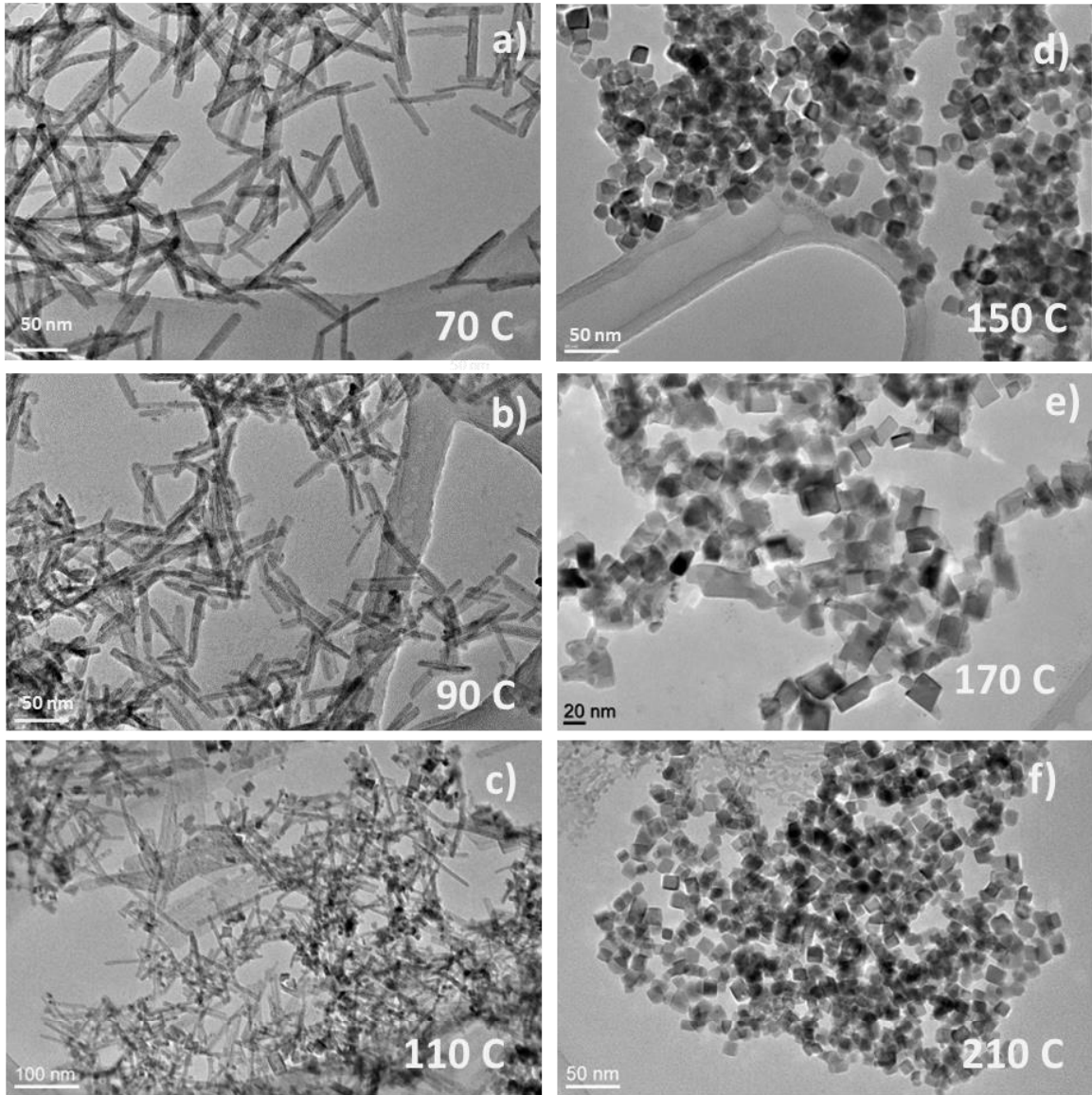
Figure 3.4. TEM images of CeO₂ (a) nanorods synthesized at 70 ˚C (b) nanorods synthesized at 90 ˚C (c) nanorods and nanocubes synthesized at 110 ˚C (d) nanocubes synthesized at 150 ˚C (e) nanocubes synthesized at 170 ˚C (f) nanocubes at 210 ˚C.
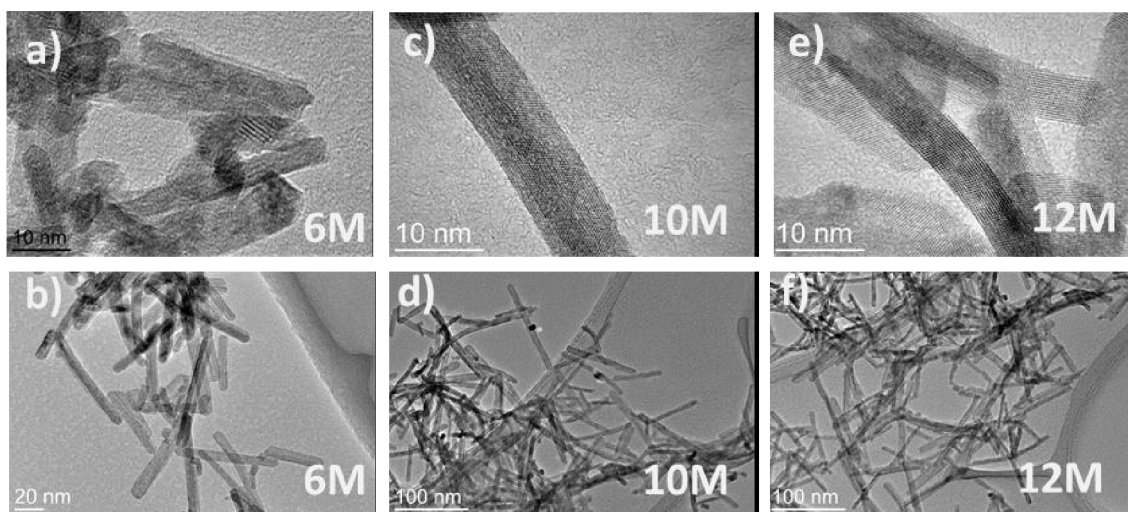
Figure 3.5. TEM Images of CeO₂ nanorods with the concentration of NaOH at (a) 6 M (100 kx) (b) 6 M (50 kx) (c) 10 M (100 kx) (d) 10 M (50 kx) (e) 12 M (100 kx) and (f) 12 M (50 kx).
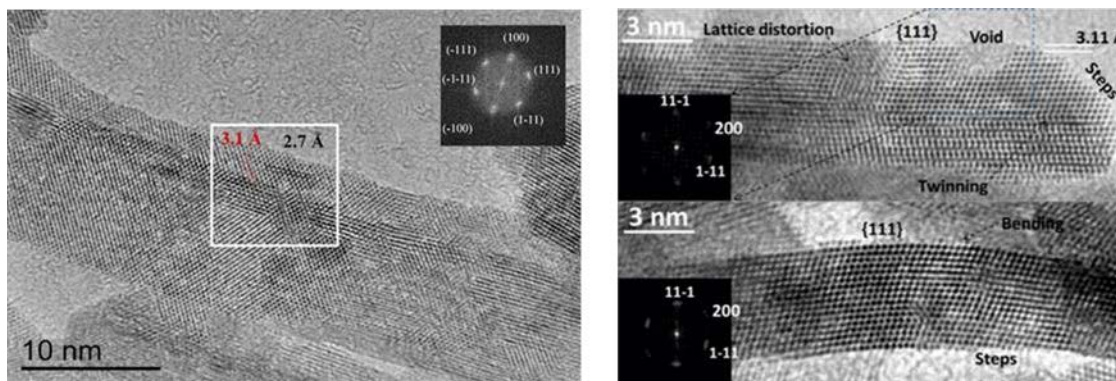
Figure 3.6. (a) High resolution TEM image and diffractogram (inserted) of CeO₂ nanorod sample synthesized using 12 M NaOH (b) TEM image of CeO₂ nanorods with various surface defects.

3.3.2.2. Raman Spectroscopy

Small changes in the vibrational structures of the CeO₂ lattice show up through Raman spectroscopy. CeO₂ has a Raman peak that is typically observed at 460 cm^{-1} which corresponds to the strong F_{2g} vibrational mode and is representative of the Ce-O stretch vibrational mode. Displayed is the typical synthesis for all three morphologies. In Figure 3.7, the nanorod samples show two peaks that are on the low and high energy

sides of F_{2g} peak, observed at ~276 cm^{-1} and ~605 cm^{-1}, which shows a slight shift in peak positions. This can be attributed to increased lattice alterations, e.g., particle size, oxygen vacancies and surface defects occur because each oxygen vacancy creates a need to maintain the electrostatic balance. The lattice expansion occurs when two Ce^{3+} ions (1.143 Å) must be replaced by two Ce^{4+} ions (0.907 Å) for each oxygen vacancy generated. An inset of a closer look at the side peak at ~ 605 cm^{-1} is shown to give a better understanding of how the nano-octahedal and nanocube samples create a far lower level of oxygen vacancy concentrations. Raman and XRD data are in agreement with each other and CeO_2 nanorods were found to have higher oxygen vacancies as well as high concentration of surface defects e.g. voids, lattice distortion, bending, steps and twinning. In a better understanding of the performance of the various morphologies of ceria, it is known that the intensity of the Raman peaks can be correlated to the amount oxygen vacancies present in a sample.[20] For instance, the intensity of the Raman peak on the high energy side, 605 cm^{-1}, of the F_{2g} peak, 460 cm^{-1}, has been associated with oxygen vacancies in CeO_2 and impregnated CeO_2. Figure 3.7 shows the peak ratio of 605/460 with their relative oxygen vacancy amounts. This ratio is unitless and demonstrates the amount of oxygen vacancies within the sample. The amounts are as such, 1.00E-5, 3.50E-6 and 0.04 nano-octahedra, nanocubes and nanorods, respectively. Nevertheless, indicating that nanorods possess more oxygen vacancies and appear to be the preferred morphology and catalytically beneficial. The objective of this portion of the research is to indicate if certain morphologies with particular well-defined planes could demonstrate low temperature reducibility and increased catalytic activity. CeO_2 nanoparticles with high crystallinity and smaller particle sizes showed higher

concentration of defects which demonstrates the existence of the oxygen vacancy in CeO_2 nanocrystals. It is noted here that the nanocubes shows almost no side peaks, an indication of oxygen vacancy defects, and the octahedra sample shows small peaks, which was in agreement with the peak comparison.
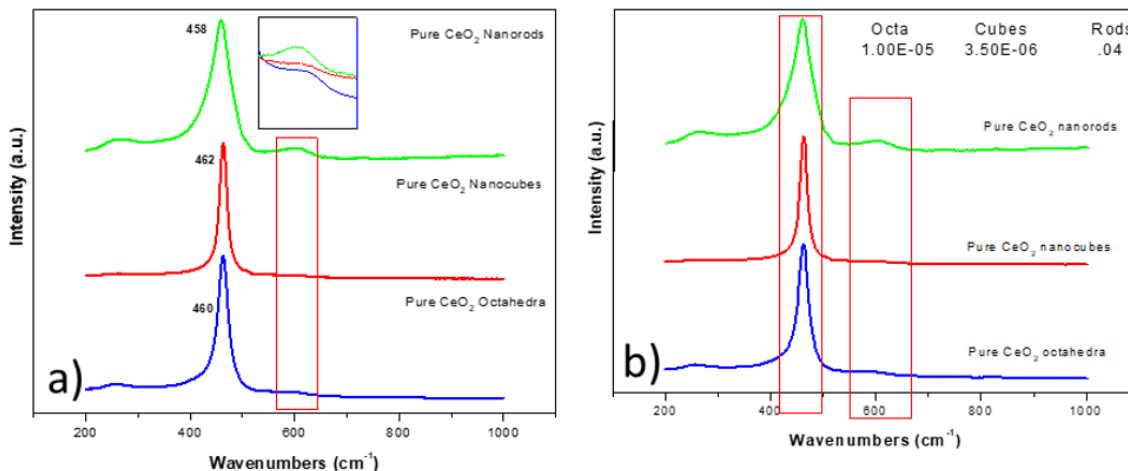
Figure 3.7. (a) Raman of pure CeO_2 octahedra, nanocubes and nanorods (b) demonstrates the amount of O_2 vacancies present within the samples.

3.3.3. Catalytic Activity Characterization

CO oxidation is a model reaction for probing the redox properties of ceria-based catalysts.[21] CO oxidation over these ceria nanoparticles with defined planes was investigated using H_2-TPR and CO oxidation technique were used to reveal how CO interacts with the different ceria surfaces.

3.3.3.1 H_2-TPR

The H_2-TPR results show that all three morphologies have the characteristic surface and bulk reduction peaks. H_2-TPR studies were conducted on the CeO_2 samples in order to compare how the morphology and oxygen vacancies affected their surface and bulk

reduction. In order to compare quality data, sample size was kept at a similar sample weight (~90 mg). H_2-TPR is one way of identifying the overall low-temperature performance of the material as an oxidation reduction catalyst. Figure 3.8 shows the intensities and positions of the surface and bulk reduction bands and those samples are dependent on the well-defined plane which indicates a particular morphology and particle size. CeO_2 nanorod samples displayed lower reduction temperature profiles for the surface and higher reduction peaks for the bulk reduction bands at 467 and 826 °C, respectively, while CeO_2 nanocubes and nano-octahedra showed lower reduction profiles for the bulk and higher temperature profiles for the surface reduction bands. These temperature profiles indicate that it is not only the surface structure but, also the defect sites of a ceria support that are controlling the catalytic behavior.[22] Denoted in Table 3.1 are the BET surface areas for the three different morphologies. The nano-octahedral, nanocube and nanorod samples show a linear correlation between the surface areas and the hydrogen consumption in the low temperature region, and the nanorods show superior H_2 consumption over all three samples. This may be due to increases in the surface area of the ceria sample. It is expected that the hydrogen consumption would be greater because of the increased defects that are present on the nanorod samples. Surface oxygen is readily available and positioned at different areas and with different coordination numbers on small crystallites   areas of ceria. Within the nanorods samples the various defects may generate defects such as steps, kinks, and corners projecting O^{2-} ions of with various coordination numbers, causing the surface area to increase due to the surface oxygen.[23] In addition to understanding the reduction temperatures, hydrogen consumption can be calculated by determining the area under the curve. Figure 3.10

showed the amount of hydrogen consumed. It is clear that the CeO_2 nanorods have the

highest amount of hydrogen consumption, 3.29 µmol/g. This is in agreement to XRD and

Raman spectroscopy.
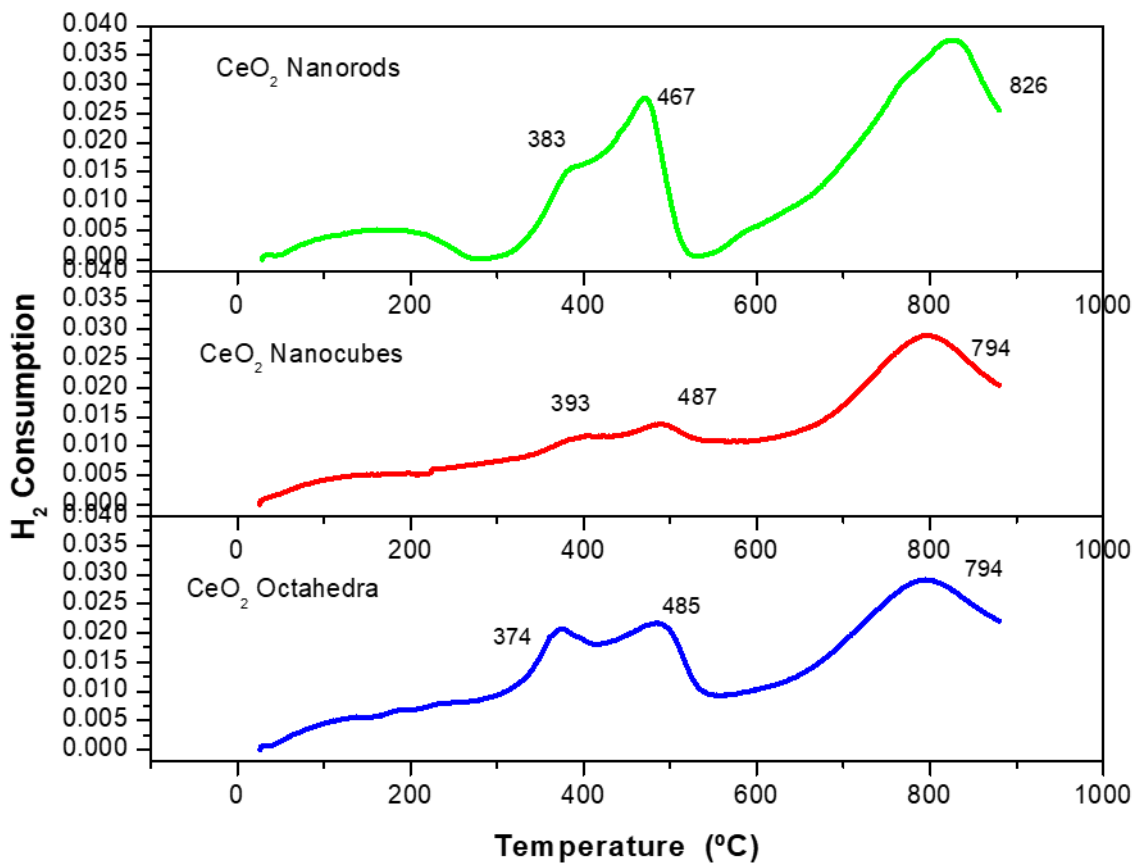
Figure 3.8. H_2-TPR of pure CeO_2 nano-octahredra, nanocubes and nanorods.
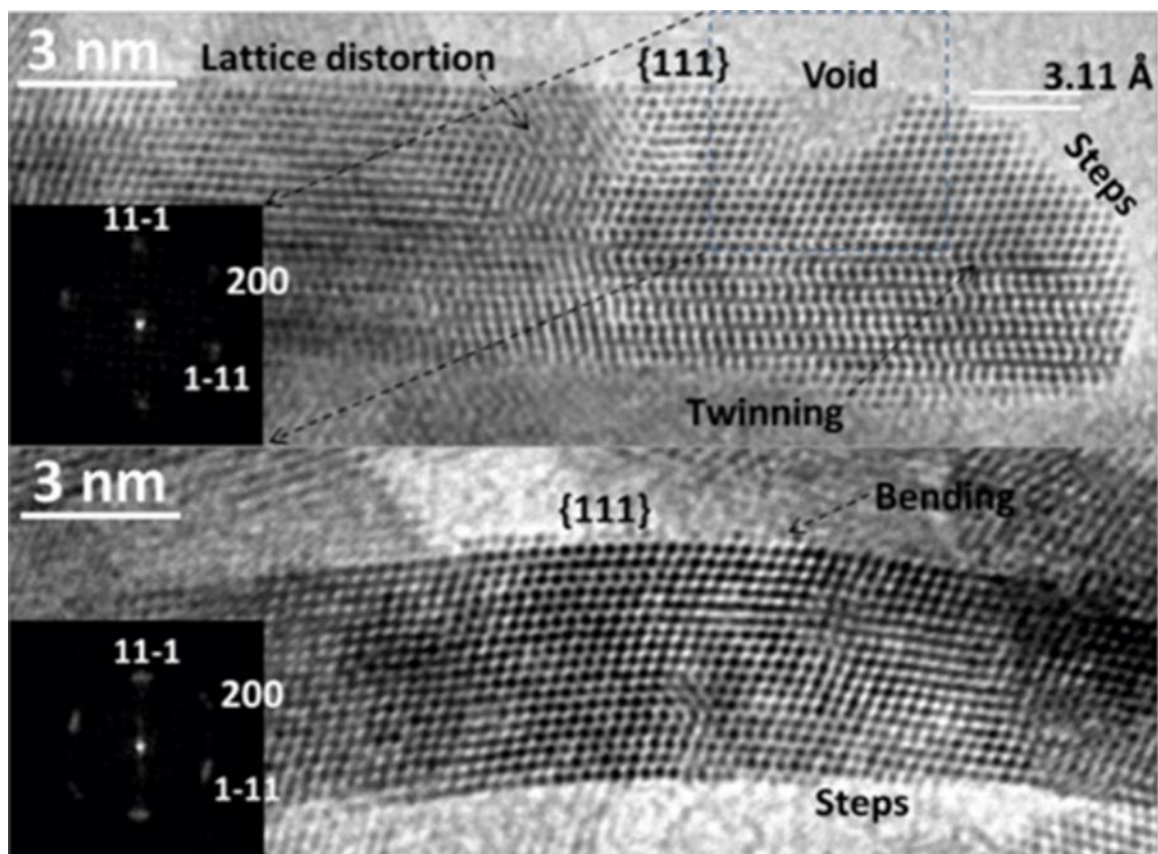
Figure 3.9. HRTEM image of CeO$_2$ nanorods. And the various surface defect
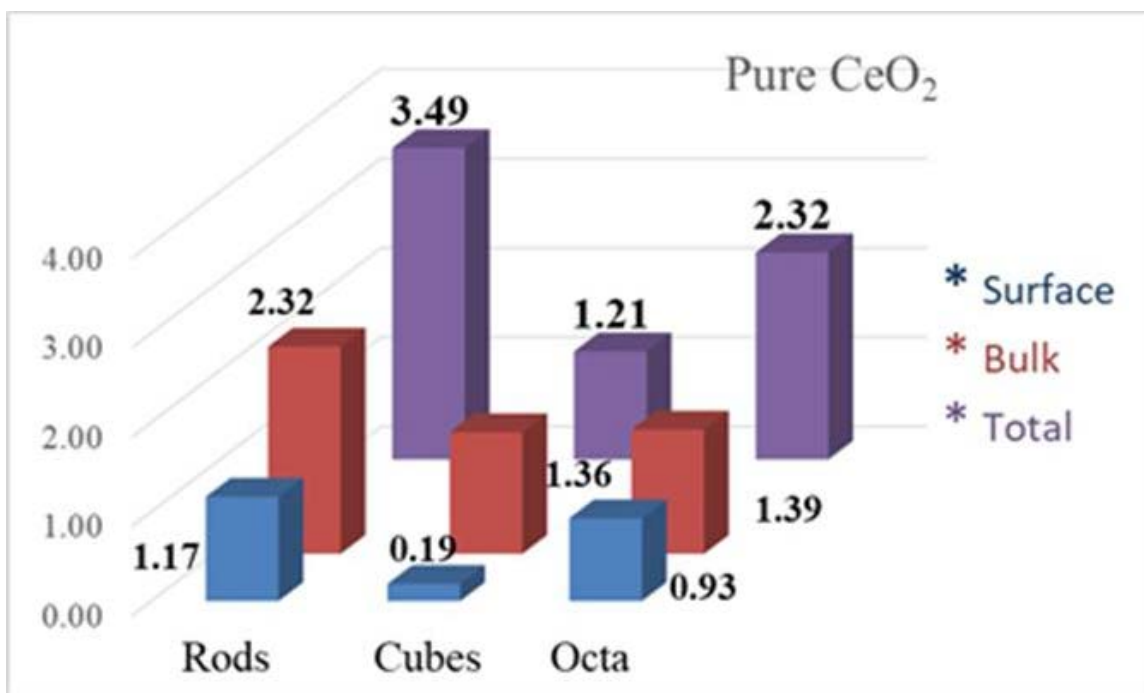
Figure 3.10. Hydrogen consumption amounts for various CeO$_2$ morphologies.

3.3.3.3. CO Oxidation

CO oxidation experiments were conducted to demonstrate the catalytic activity of the CeO$_2$ support and shed light on how the oxygen mobility within the catalyst support can aid in the enhancement of catalyst. Figure 3.11 displays all the CO conversion profiles of CeO$_2$ nano-octahedra, nanocubes and nanorods. CO conversion by CeO$_2$ nano-octahedra showed the highest T$_{50}$, at ~228 ˚C, nanocubes next highest 177 ˚C and the lowest at 155 ˚C was the nanorod sample, which showed superior conversion amongst the three morphologies. T$_{Max}$, the maximum CO conversion up to 350 ºC was 87%, 77% and 70% for nanorods, nanocubes and nano-octahedra samples, respectively. This, along with the H$_2$-TPR data, indicates that the nanorod sample is the preferred morphology for future experiments with various catalysts.
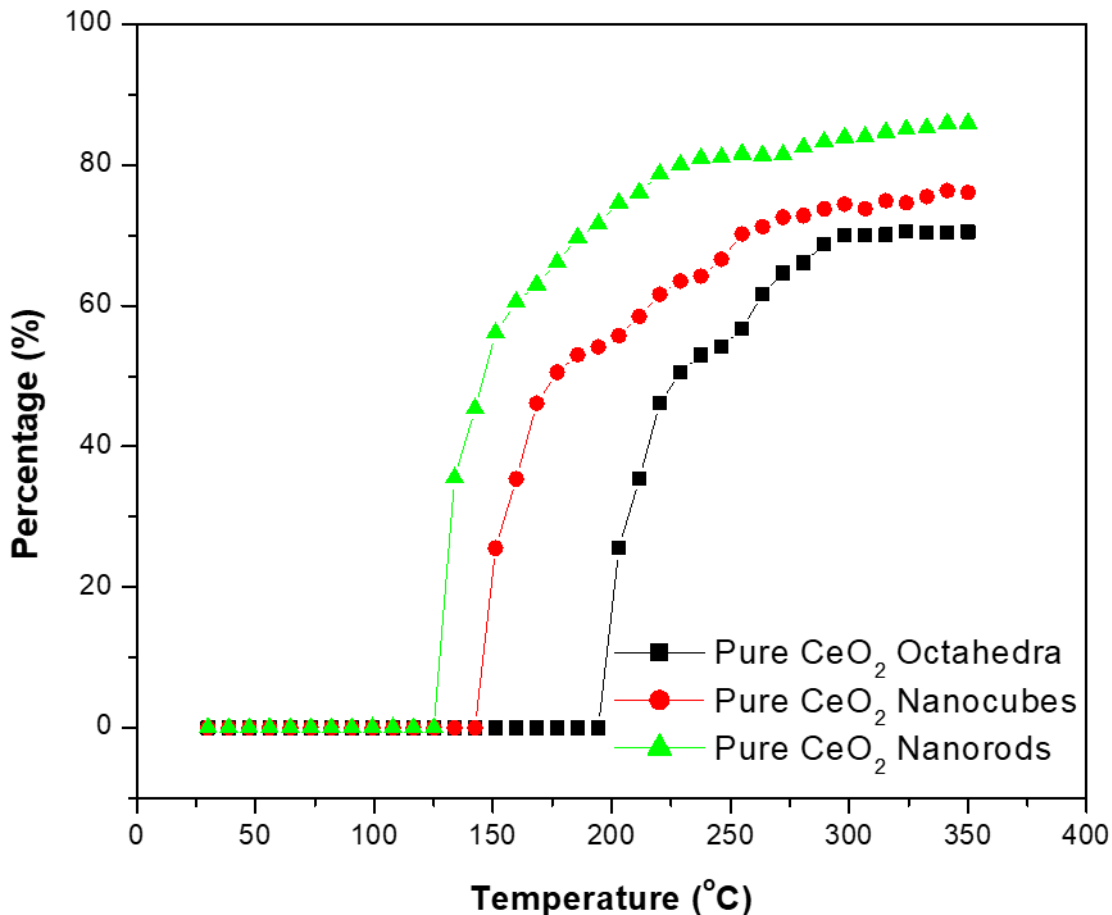
Figure 3.11. CO-Oxidation on CeO$_2$ nano-octahedra, nanocubes and nanorods.

3.4. Conclusion

This study concluded that nanorods are preferred in the synthesis of CeO$_2$ nanomaterials because of their increased catalytic properties. This is due to the increased surface defects which give rise to increased OSC, lower surface reduction temperatures and increased CO conversions. Figure 3.7 shows an increase in the number of defects on the CeO$_2$ nanorods, which exposed the more reactive (110) and (100) crystalline planes, and in this research, the (111) plane. These defect planes will aid in the performance using more cost-efficient catalysts, which will be further discussed in subsequent chapters of this dissertation. The nanorod samples have demonstrated that these samples possess

91

increased catalytic efficiencies as opposed to the nano-octahedra and nanocubes samples. Those samples only exposed stable (111) facets and (100) facets, respectively and did not show superior increased activities. In addition, all samples were investigated with the TEM in order to determine the actual morphology. Temperature played the biggest role in the synthesis of the various morphologies. Furthermore, samples that are not calcined at high temperatures are equally as catalytically active compare to samples produced by researchers such as Mai.

3.5. References

1. Somorjai, G A.; and Li, Y M.; Major successes of theory and experiment combined studies in surface chemistry and heterogeneous catalysis. *Top. Catal.,* **2010**, 53, 311-325.

2. Valden, M.; Lai, X. and Goodman, D W. Onset of catalytic activity of gold clusters on titania with the appearance of nonmetallic properties. *Science,* **1998**, 281, 1647-1650.

3. Haruta, M. Catalysis of gold nanoparticles deposited on metal oxides. CATTECH, **2002**, 6, 3, 102-115.

4. Haruta, M.; Kobayashi, T.; Sano, H. and Yamada, N. Novel gold catalysts for the oxidation of carbon monoxide at a temperature far below 0 °C. *Chem. Lett.,* **1987**, 405-408.

5. Haruta, M.; Yamada, N.; Kobayashi, T. and Iijima, S. Gold catalysts prepared by co-precipitation for low-temperature oxidation of hydrogen and of carbon monoxide. *J. Catal.,* **1989**, 115, 301-309.

6. Haruta, M. Spiers Memorial Lecture: Role of perimeter interfaces in catalysis by gold nanoparticles. *Faraday Discuss*, **2011**, 152, 11-32.

7. Ertl, G. Reactions at surfaces: from atoms to complexity. *Angew. Chem., Int Ed*, **2008**, 47, 3524-3535.

8. Zaera, F. Regio-, Stereo-, and enantioselectivity in hydrocarbon conversion on metal surfaces. *Acc. Chem. Res.*, **2009**, 42, 1152-1160.

9. Van Santen, R A.; Neurock, M. and Shetty, S G. Reactivity theory of transition-metal surfaces: a Brønsted-Evans-Polanyi linear activation energy-free-energy analysis. *Che.m Rev.*, **2010**, 110, 2005-2048.

10. Zheng, Y H.; Cheng, Y.; Wang, Y.; Bao, F.; Zhou, L H.; Wei X F.; Zhang, Y Y. and Zheng, Q. Quasicubic α-Fe$_2$O$_3$ Nanoparticles with Excellent Catalytic Performance. *J. Phys. Chem. B*, **2006**, 110, 3093-3097.

11. Goniakowski, J.; Finocchi, F. and Noguera, C. First principles studies of complex oxide surfaces and interfaces. *J. Phys. Condens. Matter,* **2000**, 12 R367.

12. Goniakowski, J.; Finocchi, F. and Noguera, C. Polarity of oxide surfaces and nanostructures. *Rep.Prog. Phys.,* **2008**, 71, 1. 016501.

13. Yang, Q.; Fu, X.; Jia, C.; Ma, C.; Wang, X.; Zeng, J.; Si, R.; Zhang, Y.; Yan, C. Structural determination of catalytically active subnanometer iron oxide clusters. *ACS Catal.,* **2016**, 6, 3072−3082.

14. Wang, S.; Zhao, L.; Wang, W.; Zhao, Y.; Zhang, G.; Ma, X and Gong, J. Morphology control of ceria nanocrystals for catalytic conversion of CO2 with methanol. *Nanoscale*, **2013**, 5, 5582-5288.

15. Park, G.; Seo, T.; Park, C.; Lim, J. and Joo. J. Effects of calcination temperature on morphology, microstructure, and photocatalytic performance of TiO$_2$ mesocrystals. *Ind. Eng. Chem. Res.*, **2017**, *56*, 29, 8235–8240.

16. Mai, H. X.; Sun, L. D.; Zhang, Y. W.; Si, R.; Feng, W.; Zhang, H. P.; Liu, H. C. and Yan, C. H. Shape-selective synthesis and oxygen storage behavior of ceria nanopolyhedra, nanorods, and nanocubes. *J. Phys. Chem. B.*, **2005,** 109, 24380–24385.

17. Wang, R. and Dangerfield, R. Seed-mediated synthesis of shape-controlled CeO$_2$ nanocrystals. *RSC Adv.,* **2014**, 4, 3615-3620.

18. Sayle. T.; Parker, C. and Catlow, A. The role of oxygen vacancies on ceria surfaces in the oxidation of carbon monoxide. *Surf. Sci.,* **1994**, 316, 329-336.

19. Trovarelli A. Catalysis by ceria and related materials. In: Hutchings G. J. ed. Catalytic Science Series. London: Imperial College Press, **2002.**

20. Lee, Y.; He, G.; Akey, J.; Si, R.; Flytzani-Stephanopoulos, M. and Herman, I. Analysis of mode softening in nanoparticle $CeO_{2-\delta}$ and $Au-CeO_{2-\delta}$ during CO oxidation. *J. Am. Chem. Soc.,* **2011.** 133, 12952-12955.

21. Mai, H. X.; Sun, L. D.; Zhang, Y. W.; Si, R.; Feng, W.; Zhang, H. P.; Liu, H. C. and Yan, C. H. Shape-selective synthesis and oxygen storage behavior of ceria nanopolyhedra, nanorods, and nanocubes. *J. Phys. Chem. B.*, **2005,** 109, 24380–24385.

22. Binet, C.; Badri, A.; Lavalley, J. A Spectroscopic characterization of the reduction of ceria from electronic transitions of intrinsic point defects. *J. Phys. Chem.,* **1994**, 98, 6392–6398.

23. Perrichon, V.; Laachir, A.; Bergeret, G.; Fréty, R.; Tournayan L. and Touret, O. Reduction of cerias with different textures by hydrogen and their reoxidation by oxygen. *J. Chem. Soc., Faraday Trans.*, **1994**, 90, 773-781.

Chapter 4: Effects of Catalyst Loading Amount and Support Shape on CO Oxidation in CeO$_2$ Supported CuO$_x$ Catalysts.

The results presented in this chapter will focus on the second objective of this dissertation. The specific plan is to investigate the effects of various percentages of CuO$_x$ (0 ≤ x ≤ 1) loading on CeO$_2$ nano-octahedra, nanocubes and nanorods in order to correlate the support shape effect and surface defects with catalytic activity for increased catalytic behaviors. The size/shape controlled CeO$_2$ nanostructures were impregnated using wet incipient method with varying percentages of 1 wt.%, 5 wt.% and 10 wt.% copper content. A comparative study was conducted on shape controlled, highly reducible CeO$_2$ nano-octahedral, nanocube and nanorod supported CuO$_x$ (0 ≤ x ≤ 1) catalysts, to understand the effect of support reducibility on the catalytic activity of CO oxidation. The results will further advance the depths of our knowledge on the interfacial interactions between catalyst and support. The influence of CuO$_x$ loading amounts and CuO$_x$-CeO$_2$ interactions due to variable CeO$_2$ shapes on CO oxidation were characterized using powder XRD, Raman spectroscopy, XPS, TEM, BET surface area, H$_2$-TPR, TPR-TPO cycling, CO-TPD, and CO conversion.

4.1. Introduction

The surface structure of the CeO$_2$ support helps enhance the catalytic activity of a metal or metal oxide catalyst, such as Al$_2$O$_3$, SiO$_2$, ZrO$_2$ and CuO.[1] Reducible CeO$_2$ acts as an active support due to having the ability to release or hold oxygen, depending on oxygen-lean or - rich conditions, respectively.the unique property of CeO$_2$ aids in decreasing the conversion temperature in the application of CO oxidation.[2,3,4] The ease of

oxidation states switch between Ce^{4+} and Ce^{3+} in CeO_{2-x} ($0 \leq x \leq 0.5$) aids in the formation of oxygen vacancies and contributes to the oxygen storage capacity (OSC).[5] Subsurface oxygen vacancies can form more readily on reactive surfaces, and this is due to the surface structure which causes lattice oxygen to diffuse or migrate, increasing oxygen mobility.[6] Some reactive crystal planes are thought to be responsible for the low temperature surface reducibility and significant oxygen vacancies creation in CeO_2.[7,8] The well-known low-index exposed crystal planes of CeO_2 are (111), (110) and (100), and the (110) and (100) represent a higher catalytic activity due to lower activation energy for oxygen vacancy formation.[9] Since the OSC reversibility is thought to be affected by the interaction of the catalyst and catalyst support at the interface, the (110) and (100) planes are more favorable for the increase of both oxygen vacancies and surface defects. These defects enhance the catalytic activity through superior oxygen mobility because oxygen migrates toward the surface of CeO_2 and this oxygen can be thermally reduced at lower temperature allowing for the release of oxygen ($CeO_2 \rightarrow CeO_{2-\delta} + \frac{\delta}{2}O_2$) easily.[10] In the application of automotive catalytic converters, this ultimately aids in the conversion of carbon monoxide and unburned hydrocarbons to carbon dioxide and water in exhaust emissions.

Zheng et al. has studied preparation, characterization and catalytic properties of CuO/CeO_2 systems.[11] They have supported their experimental results by TPR, which showed low temperature reducibility of the catalysts due to the interaction between the finely dispersed Cu species and CeO_2. Kundakovic and Flytzani-Stephanopoulos suggested that small copper clusters were more active than highly dispersed copper species, and bulk CuO made a little contribution to the catalytic activity.[12] Tang et al.

who investigated the influence of copper loading in the CuO/CeO_2 catalyst using H_2-TPR and CO oxidation showed lower reduction temperatures and discovered that copper and ceria nanoparticles have a strong synergetic effect which results in good catalytic performance.[13] Cui et al noted that it only takes minute amounts of Cu to promote the CeO_2 catalytic activity.[14] Cui et al experimented with their CuO/CeO_2 catalysts by the same preparation method used in this study and the results showed there is relationship between activity and loading amount and this was attributed to the strong metal-support interactions. Therefore, the intention of this work is to further examine the relationship between the structural properties and the catalytic activities of CuO_x ($0 \leq x \leq 1$) with varying loading amount supported on shape-controlled CeO_2 supports. Hence, we prepared 1 wt.%, 5 wt.%, and 10 wt.% CuO_x supported on CeO_2 nanorods, nanocubes and nano-octahedra with various exposed crystal planes by incipient impregnation and oxidation/reduction treatments.

4.2. Experimental Section

4.2.1. Catalyst and Catalyst Support Synthesis

From the objective one, it was discovered that CeO_2 nanocubes and nanorods synthesized through the hydrothermal method with a dwell time of 48 h and temperatures of 90 °C and 150 °C for nanorods and nanocubes respectively, were the best candidates for the second portion of this study. In addition, the volume ratios, of 11:1 ($V_{NaOH}:V_{Ce(NO3)3 \cdot 6H2O}$) and the molarity at 0.1 M $Ce(NO_3)_3 \cdot 6H_2O$ (99.9% purity, Alfa Aesar) for the Ce precursor had also proven to be the best parameters for the investigation of catalytic activities. Finally, the concentration of NaOH (>98% purity and obtained from Sigma–Aldrich) was held constant at 6 M to provide the optimum catalyst

support. All samples, including the co-precipitation of CeO_2 nano-octahedra, were synthesized as stated in the previous chapter. Where the samples were slight stirred and then placed in a Teflon-lined stainless-steel autoclaves. Again, it must be noted that, the CeO_2 nano-octahedra samples, a co-precipitation method was used. All samples were washed thoroughly with distilled water to remove any co-precipitated salts and residual ions, then washed with ethanol to avoid hard agglomeration in the nanoparticles, and dried in air at 60 °C for 12 h. Except for the nano-octahedra samples, these samples were calcined at 400 °C for 2 h before impregnation of the catalyst. For the catalyst loading, a wet incipient method was used to impregnate the copper catalyst. Copper carbonate was the Cu precursor used for all samples ($CuCO_3$ purchased from Fisher Scientific). For this comparative study, the Cu loading was done by varying the weight percentages of copper by 1 wt.%, 5 wt.% and 10 wt.%. After impregnation all samples were filtered and dried at 60 °C for 12 h. Then all the samples were oxidized in air at 400 °C for 5 h. The samples were equally divided and half of the samples were subjected to a reduction treatment. The reduction was done in 5 vol.%H_2/95 vol.% He atmosphere at 400 °C for 5 h and will be discussed later.

All techniques for characterization of the catalysts and catalytic activity, such as; X-ray diffraction (XRD), Raman spectroscopy, X-ray photoelectron spectroscopy (XPS), transmission electron microscopy (TEM), BET surface area measurement, temperature programmed reduction (TPR), temperature programmed oxidation (TPO), temperature programmed desorption (TPD), pulse chemisorption to calculate oxygen storage capacity (OSC), and CO oxidation can be found in Chapter 2.

4.2.2. Catalytic Experiments

4.3. Results

4.3.1. The effect of oxidation temperature

4.3.1.1. XRD and BET analysis

In Figures 4.1- 4.3, it can be seen that the X-ray diffraction (XRD) patterns for all of the as-synthesized 1 wt.%, 5 wt.%, and 10 wt.% of CuO/CeO_2 samples (nano-octahedra, nanorods, nanocubes) showed typical reflections which were observed at 2θ of 28.85°, 33.08°, 47.48°, 56.34°, 59.09°, 69.41°, 76.70° and 79.07°. These reflections can be indexed to (111), (200), (220), (311), (222), (331), (400), and (420) crystal planes which correspond to the pure cubic phase of CeO_2 (fluorite structure, JCPDS 81-0792, space group Fm3m). Figures 4.1 – 4.3, also showed two weak typical reflections at 35.54° and 38.72° (JCPDS, CuO file No. 80-1917) corresponding to CuO.[15] In Figure 4.3, the CuO/CeO_2 nanorod samples show broadened diffraction peaks which represent small crystallite sizes. Whereas, the CuO/CeO_2 nanocubes and octahedra samples have sharper peaks indicating of larger crystallite sizes. In addition, the presence of CuO peaks indicated that a phase separation of CuO from Cu-O-Ce solid solution occurred in some of these samples.[16] CuO is not only forming solid solution within the ceria (CeO_2) but also CuO is in the form of highly-dispersed species onto CeO_2 and bulk CuO clusters. As the Cu concentration was increased there is an increase in the relative intensity of the peaks. All 1 wt.% samples (Figures 4.1-4.3) do not show the CuO diffraction peaks due to the presence of mostly Cu-O-Ce solid solution and/or small CuO nanoclusters which are harder to be detectable in XRD analysis. This hypothesis becomes more evident with analysis of the Raman and TPR data.
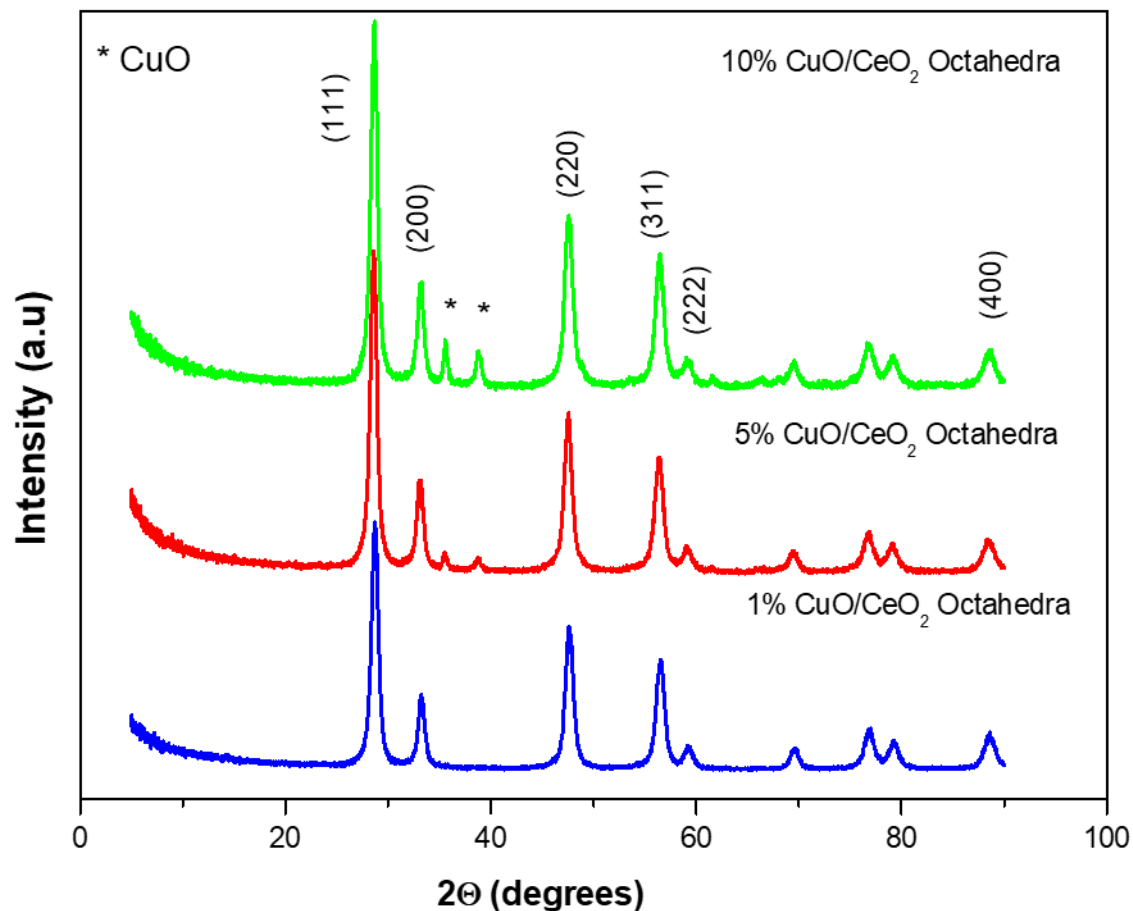
Figure 4.1. XRD patterns of 1 wt.%, 5 wt.% and 10 wt.% CuO/CeO$_2$ nano-octahedra.

BET surface areas for all samples of CuO/CeO$_2$ are tabulated in Table 4.1. When small amounts of CuO were added to CeO$_2$ nano-octahedra, nanocubes and nanorods, an obvious change in surface area for the CuO/CeO$_2$ samples can be seen. The surface areas of CuO/CeO$_2$ nano-octahedra and nanocubes decreased from 54.7 to 33.7 m^2/g for nano-octahedra and from 37.1 to 34.9 m^2/g for nanocubes with increasing the amount of CuO loading. The surface area of pure CuO is 4.6 m^2/g. However, the addition of CuO enhanced the surface area. The CuO/CeO$_2$ nanorod sample showed an increase in regard to surface area, due to the chance of forming higher amounts of Cu-O-Ce solution.[17]
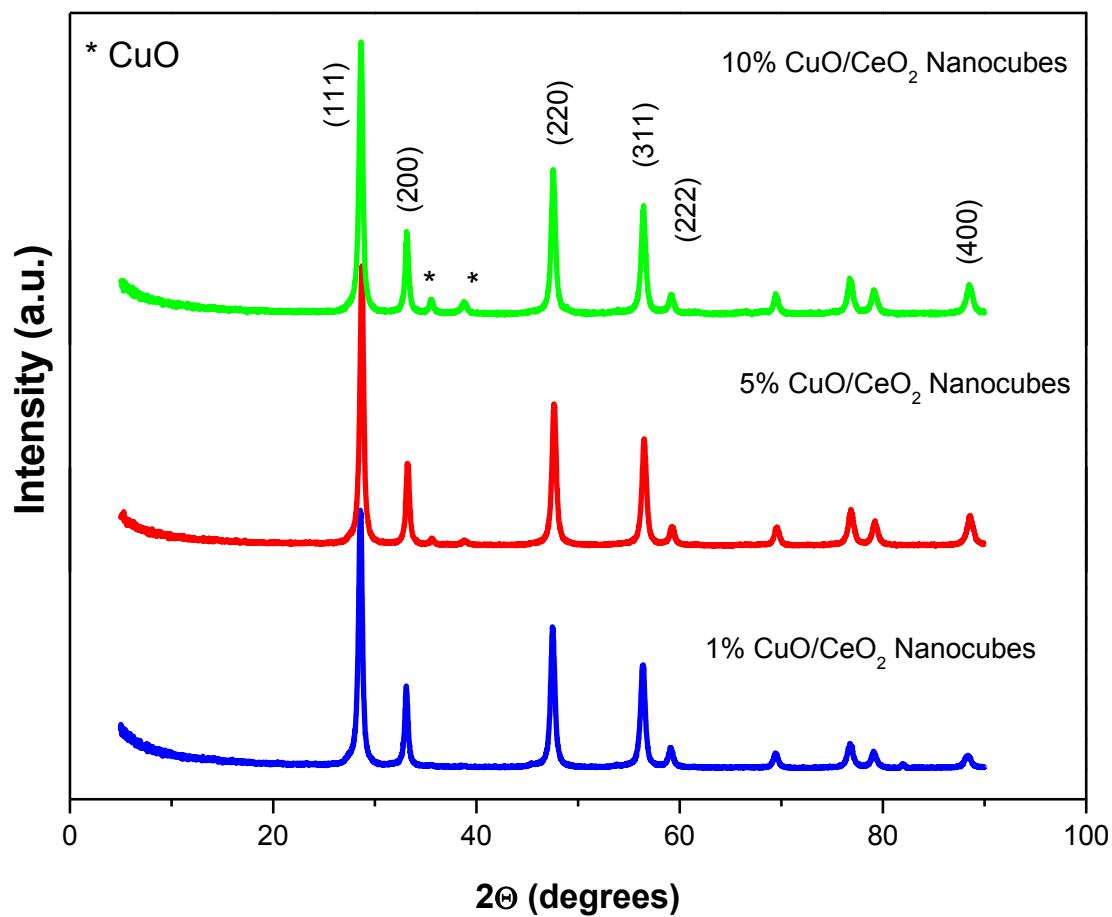
Figure 4.2. XRD pattern of 1 wt.%, 5 wt.% and 10 wt.% CuO/CeO₂ nanocubes.

Table 4.1. BET surface area of CuO/CeO₂.

BET surface area (m^2/g)			
CuO %	Nano-Octahedra	Nanocubes	Nanorods
1 wt.%	54.7	37.1	49.0
5 wt.%	47.1	36.8	54.9
10 wt.%	33.7	34.9	70.1
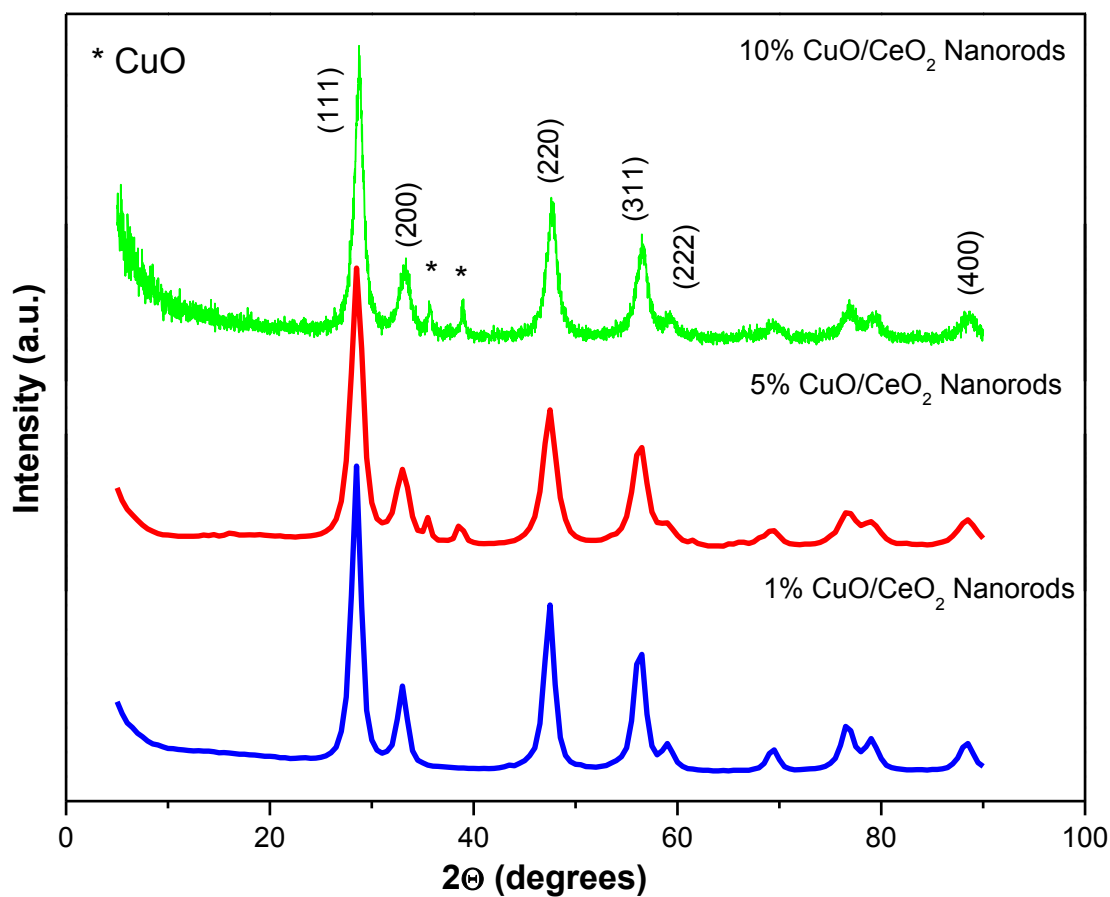
Figure 4.3. XRD pattern of 1 wt.%, 5 wt.% and 10 wt.% CuO/CeO₂ nanorods

4.3.1.2. Raman analysis

CeO$_2$ has a peak that is typically observed at 460 cm^{-1} and corresponds to the strong F$_{2g}$ vibrational mode which is representative of the Ce-O stretch vibrational mode.[18] As seen in the Figures 4.4-4.6, two peaks are on high and low energy sides of F$_{2g}$ peak, observed at ~276 cm^{-1} and ~605 cm^{-1} which demonstrates the existence of the oxygen vacancy in CeO$_2$.[19]
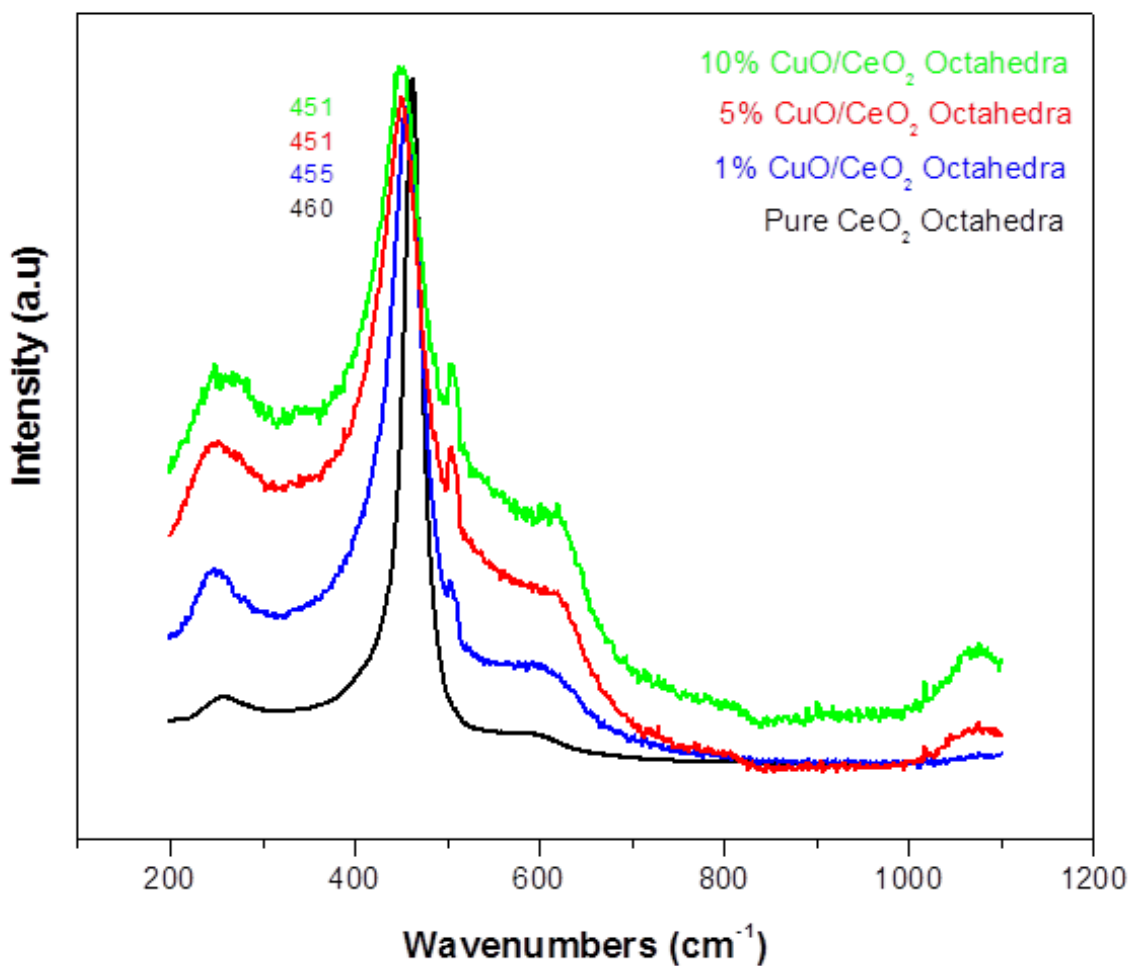
Figure 4.4. Raman spectra of 1 wt.%, 5wt.% and 10 wt.% CuO/CeO$_2$ nano-octahedra.

The high and low peaks correlate to oxygen vacancies in the pure CeO$_2$ lattice. In the CuO/CeO$_2$ samples, these two additional peaks at ~261 and ~624 cm^{-1} can be observed and account for the effect of CuO addition in the samples as well as oxygen vacancies. During Cu incorporation into CeO$_2$ lattice, Ce^{4+} ions are replaced by Cu^{2+} and thus, oxygen vacancy is formed in order to compensate the electronic charge.[20] It is well documented that increased catalytic activities are imparted from the high energy facets that contain a high concentration of surface defects e.g. voids. Raman peak shifts can be attributed to the increased lattice alterations e.g. particle size, oxygen vacancies, solid

solution and/or surface defects, such as: distortions, bending, steps, twinning.[21] Nevertheless, these catalytically beneficial surface defects rapidly diminish during the crystal growth process to balance the surface energy of the crystals.[22] However, if more unsaturated coordination atoms cerium atoms occur, (such as CeO_{2-x}) the peaks around ~261 cm^{-1} and ~605 cm^{-1} will become more intense and a broadening of the F_{2g} peak will occur.[23] This is more evident within the nanorod samples and suggests a possible explanation for superior catalytic activity. In Figure 4.4, the CuO/CeO_2 nano-octahedra samples showed small deviations in peak shift, much like the CuO/CeO_2 nanocubes samples and thus, CuO/CeO_2 nano-octahedra sample may have a small amount of Cu-O-Ce solid solution. In Figure 4.5, the CuO/CeO_2 nanocube samples show no shift in the F_{2g} peak position and consequently may be due to the absence of Cu-O-Ce solid solution and/or less surface defects on CeO_2. Figure 4.6 shows a gradual shift to the left for the F_{2g} peak of CeO_2 nanorods samples. As discussed above, this can be attributed to oxygen vacancies and the amount of solid solution formed in the nanorods samples, which cause changes in the vibrational bond length of Ce-O.
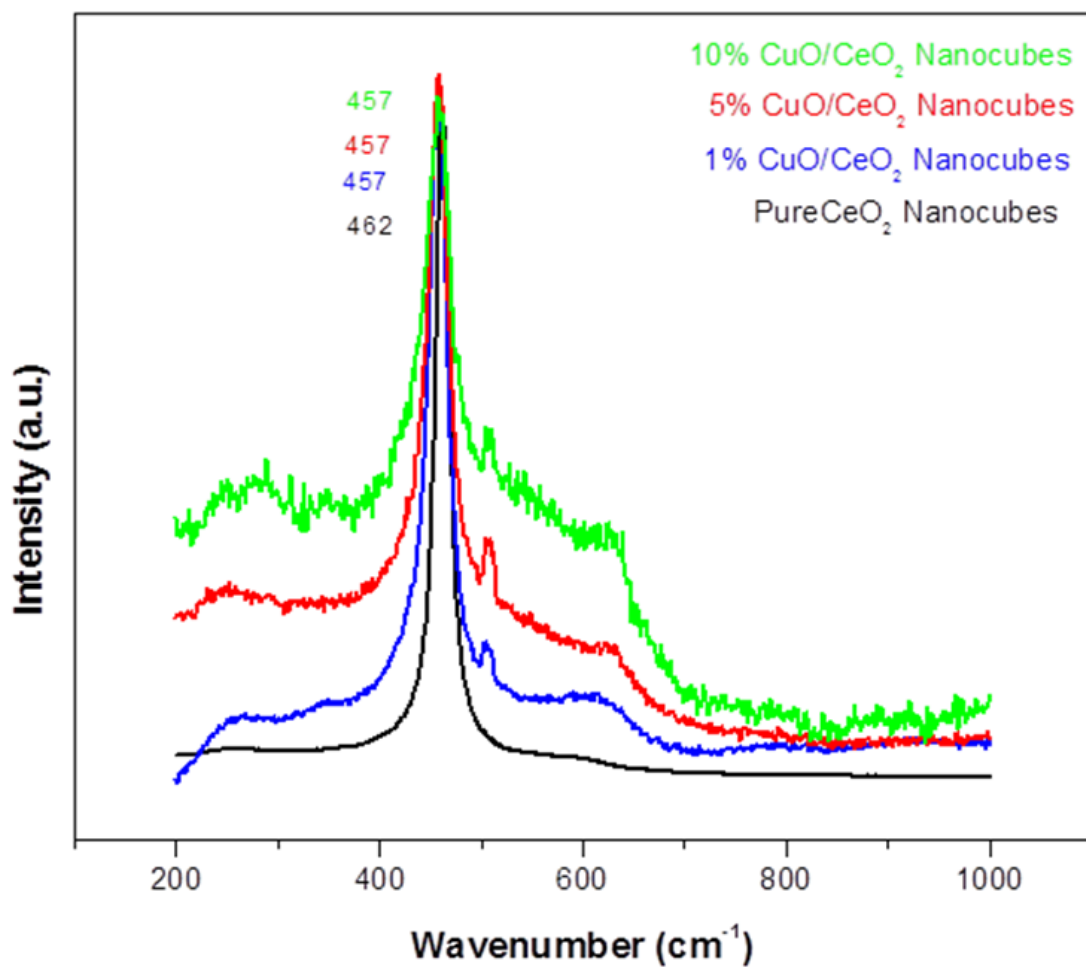
Figure 4.5. Raman spectra of 1 wt.%, 5 wt.% and 10 wt.% CuO/CeO₂ nanocubes.

.
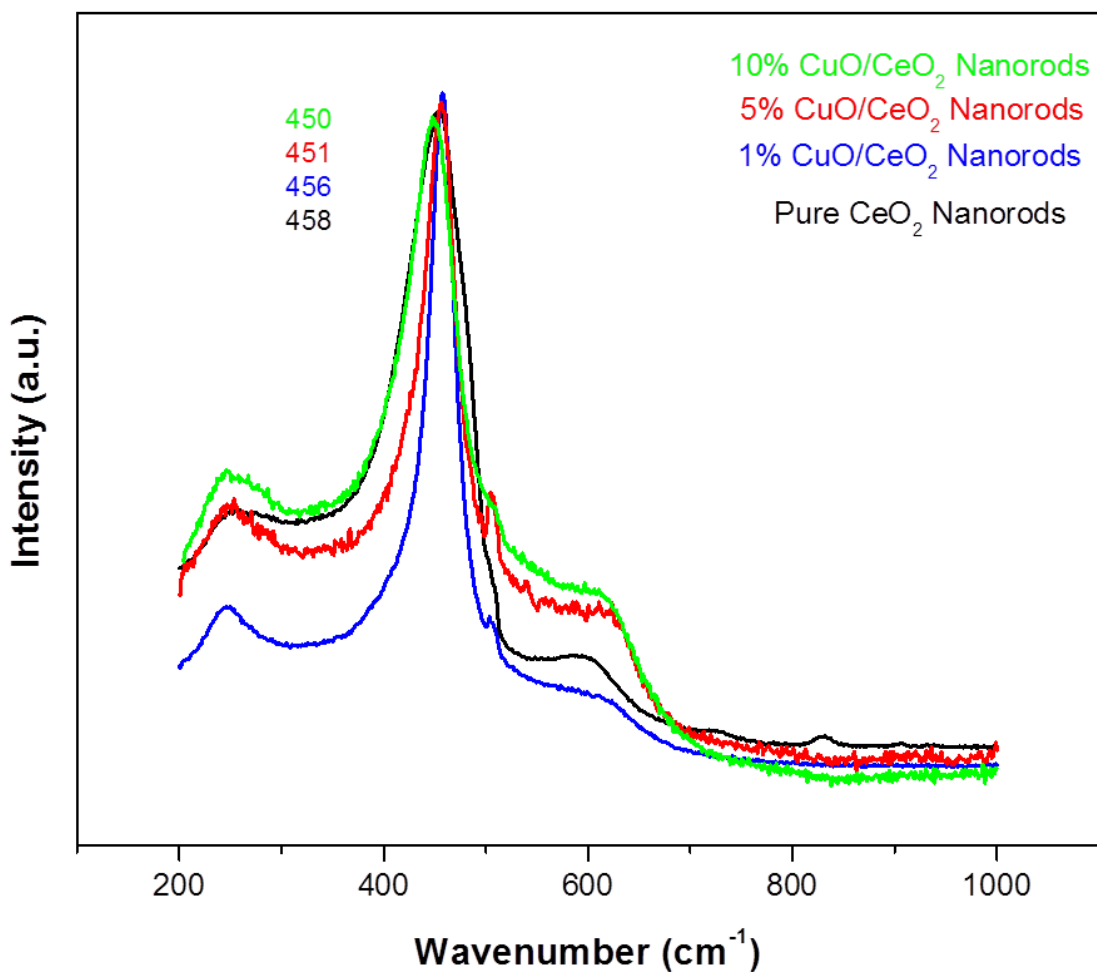
Figure 4.6. Raman spectra of 1 wt.%, 5wt.% and 10 wt.% CuO/CeO$_2$ nanorods.

4.3.1.3. *H$_2$-TPR, CO-TPD and TPR/TPO Cycling Analysis.*

H$_2$-TPR was performed to compare the differences in the reduction properties of the varying percentages of CuO impregnated onto shape-controlled CeO$_2$. As outlined in the experimental section, CuO/CeO$_2$ samples were prepared with a typical oxidation treatment at 400 ^{o}C for 5h. Figures 4.9-4.11 illustrated the hydrogen temperature programmed reduction (H$_2$-TPR) profiles of 1 wt.%, 5 wt.% and 10 wt.% CuO/CeO$_2$ nano-octahedra, nanocubes and nanorods. Figure 4.7 showed the proposed mechanism

that explained the results from the H$_2$-TPR data. The α peak, correlates to the first peak and represents CuO interacting strongly with CeO$_2$. This means CuO is incorporated into the lattice of CeO$_2$ and the interfacial structure is considered as a solid solution of Cu-O-Ce. The β peak, representing the second peak, is due to the reduction of the highly dispersed copper oxide species, which includes isolated copper ions and small two and three-dimensional clusters.[24] The γ peak denotes the third peak and has been ascribed to the reduction of bulk CuO phases.[25] Figure 4.8 included the TPR profiles of pure CeO$_2$ and pure CuO which have characteristic reduction peaks. The reduction peak of CeO$_2$ at ~475 °C corresponds to the reduction of the surface shell. The high temperature profile peak at ~825 °C for pure CeO$_2$ can be attributed to the reduction of bulk CeO$_2$ to Ce$_2$O$_3$.[26] Also seen in Figure 4.8, a single reduction peak of CuO nanoparticle appeared at about ~299 °C.
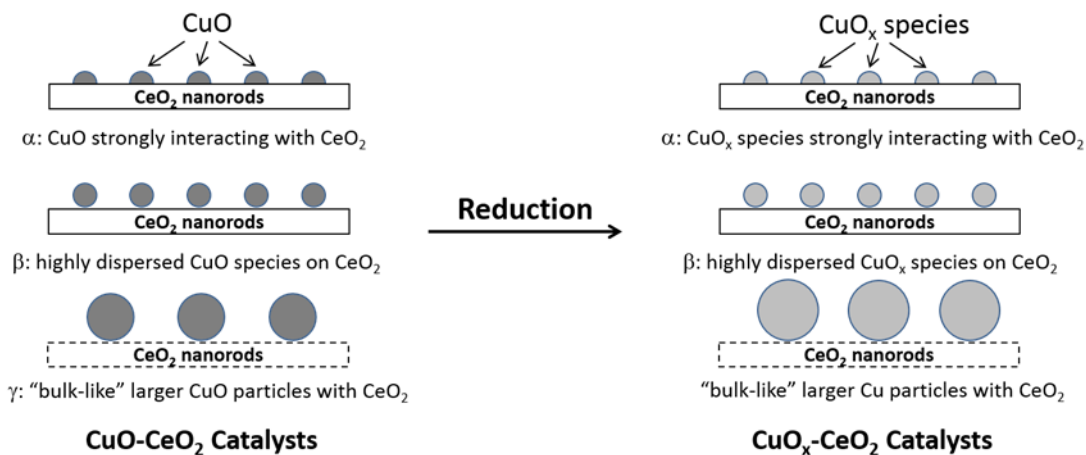
Figure 4.7. Proposed mechanism for CuO/ CeO$_2$ and CuO$_x$/CeO$_2$ nanorod catalysts to explain the H$_2$-TPR results. [27]
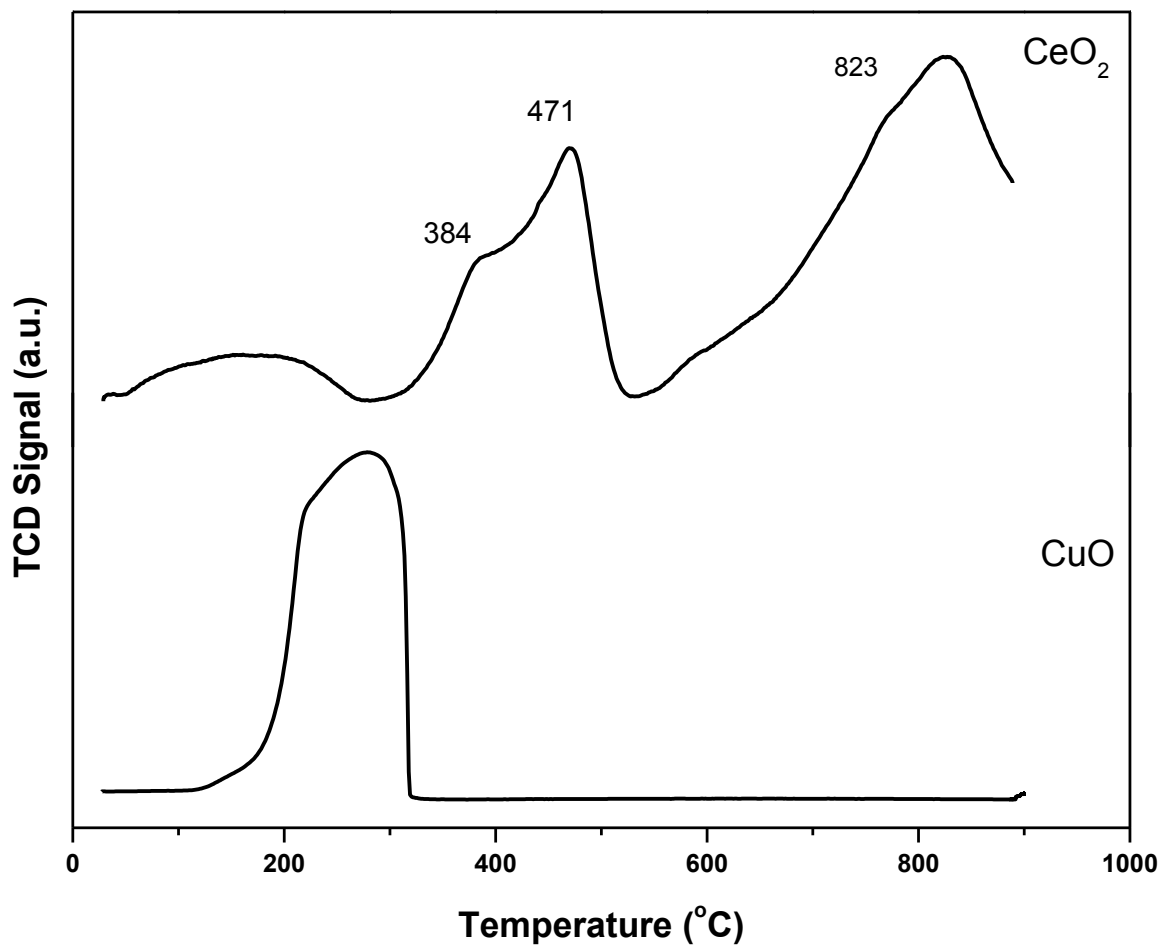
Figure 4.8. H$_2$-TPR profiles of pure CeO$_2$ nanorods and pure CuO.

In this study, all the maxima for the α, β and γ peaks of CuO/CeO$_2$ are noticeably higher than the reduction peaks in pure CeO$_2$ and lower than the single reduction peak of pure CuO. The α and β reduction peaks are partially controlled by the release of surface oxygen as well as the interfacial oxygen of CeO$_2$ stimulated by metallic copper ions.[28]

Figures 4.12, 4.13 and 4.14 documented are the total H$_2$ consumption for all samples. In the H$_2$-TPR data, CuO/CeO$_2$ nano-octahedra and nanocubes exhibited the highest levels of hydrogen consumption for the bulk CuO, γ peak, in both 10 wt.% samples. Whereas, the nanorods samples observed the highest consumption for α and β peaks where the hydrogen consumption is 0.77 mmol/g and 1.07 mmol/g respectively, for the

10 wt.% CuO/CeO_2 samples. In addition to comparing the reduction temperature and H_2 consumption, there are several differences in the H_2-TPR data among CuO/CeO_2 nano-octahedra, nanocubes and nanorods samples.
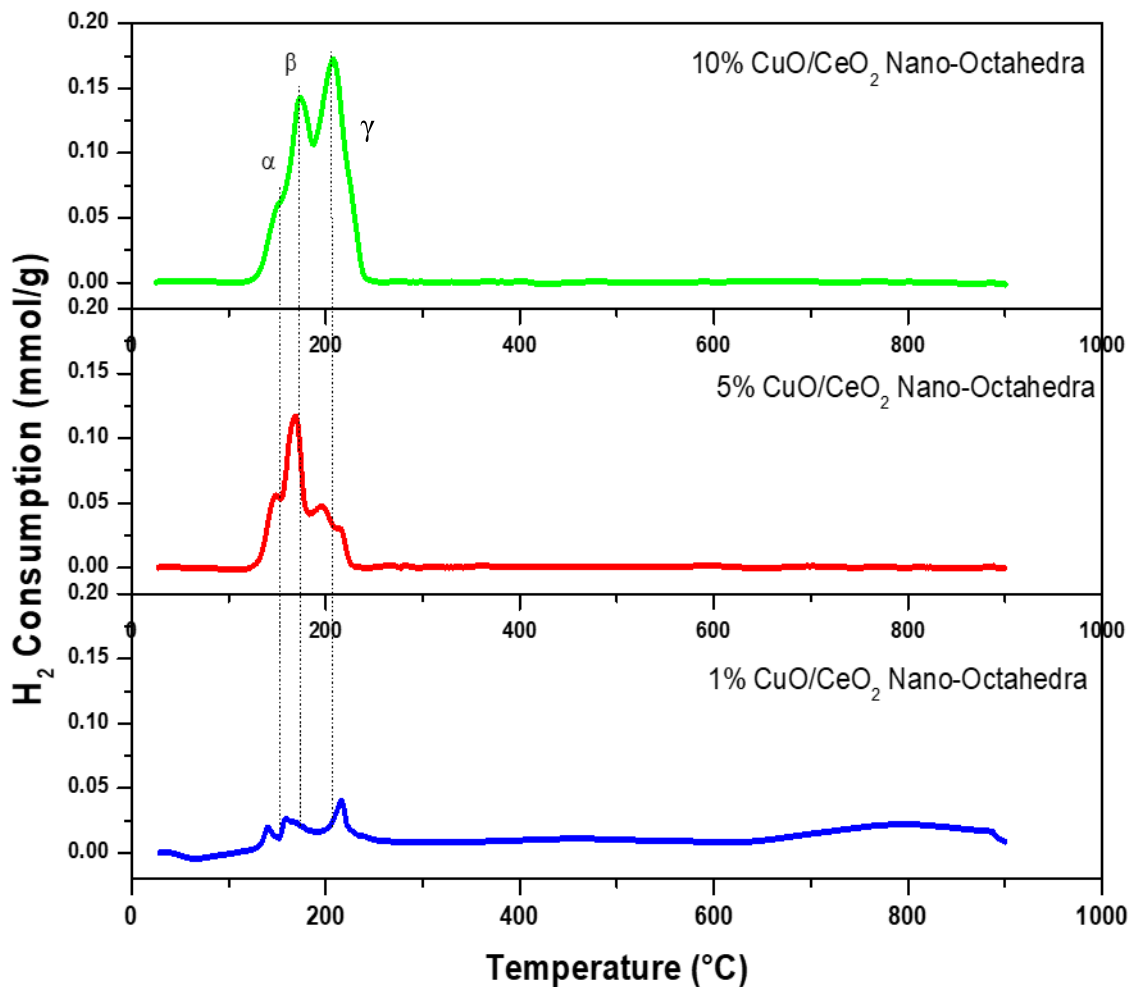
Figure 4.9. H_2-TPR of 1 wt.%, 5 wt.% and 10 wt.% CuO/CeO_2 nano-octahedra.
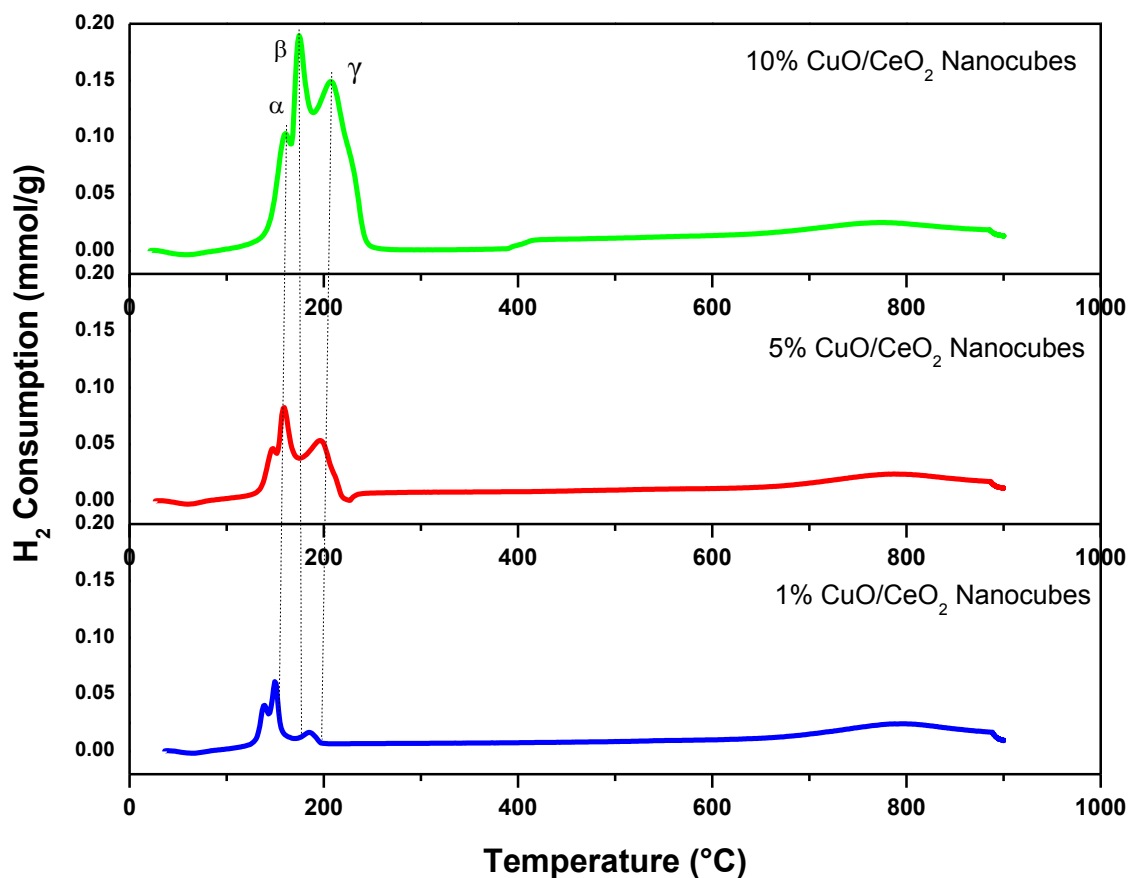
Figure 4.10. H₂-TPR of 1 wt.%, 5 wt.% and 10 wt.% CuO/CeO₂ nanocubes.

Importantly, for all samples the same TCD scales and similar sample weights (~80 mg) were maintained for comparison of hydrogen consumption amounts. Figure 4.9 showed the H_2-TPR profiles of 1 wt.%, 5 wt. % and 10 wt.% CuO/CeO_2 nano-octahedra. While 1 wt.% and 10 wt.% nano-octahedra samples present three reduction peaks, there are four reduction peaks in the 5 wt.% CuO/CeO_2 nano-octahedra sample seen with maxima at 140, 161, 197 and 210 °C. These peaks are very similar to those reported by Avgouropoulos, who identify them as peaks α, β^1, β^2 and γ.[29] The β^1 and β^2 peaks would correspond to larger CuO particles, less associated with CeO_2. Shown in Figure 4.10, the

1 wt.%, 5 wt.% and 10 wt.% CuO/CeO$_2$ nanocubes samples correlate to a three-step reduction profile.
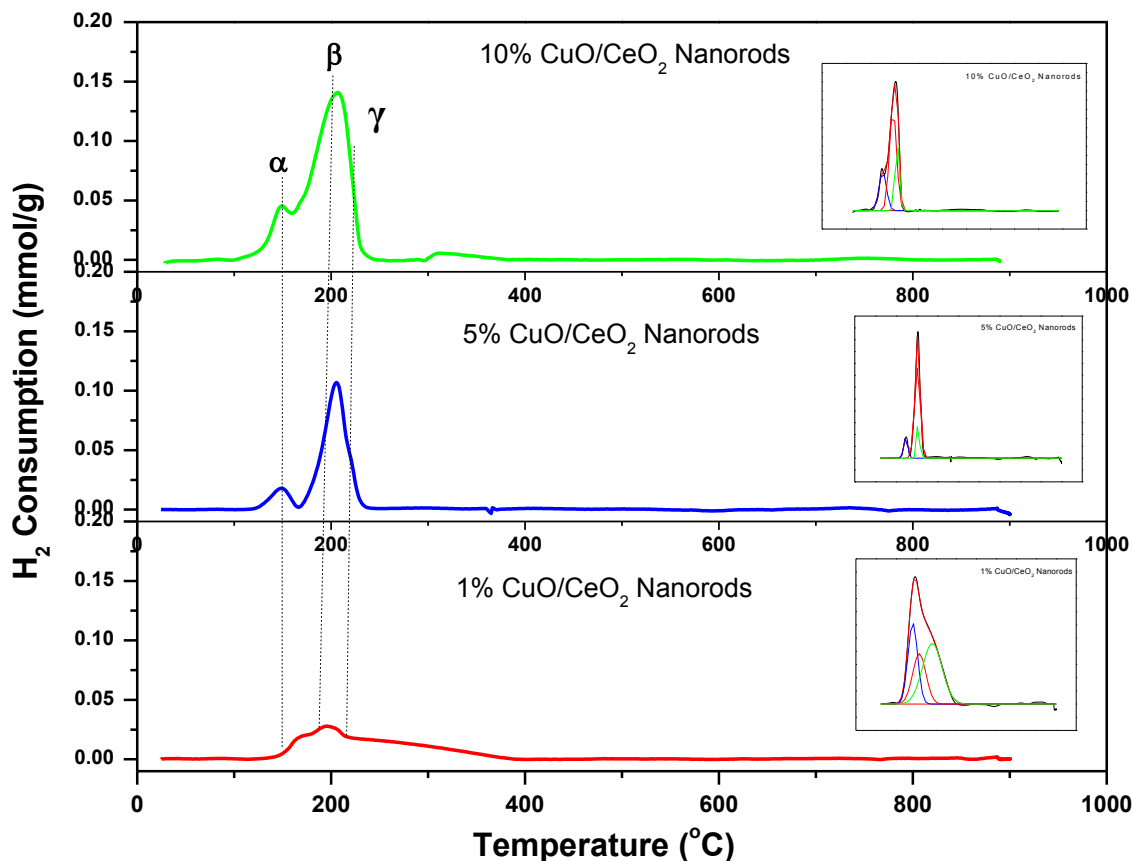
Figure 4.11. H$_2$-TPR of 1wt.%, 5wt.% and 10wt.% CuO/CeO$_2$ nanorods.

In Figure 4.11, the typical three-step reduction temperature profile is clearly observed for all the CuO/CeO$_2$ nanorods samples. The first peak is found ~150-170 °C, and is attributed to the strongly interacting CuO particles with the surface of CeO$_2$ nanorods. This may be due to their exposed crystal planes. It is known that the CuO/CeO$_2$ nano-octahedra mainly expose the crystal plane (111), which is the most stable index plane of ceria and the nanocubes have (100) exposed crystal plane. However, CeO$_2$ nanorods' exposed surface crystal planes are (110) and (100), and partial (111) reported here. As

seen in Figure 3.9, the HRTEM images clearly showed the exposed crystal planes of CeO_2 nanorods. The (110) and (100) are not the stable planes, and they are more reactive than the other low index planes. However, the stable (111) plane on CeO_2 nanorods showed high concentrations of surface defects, including steps, voids, and lattice distortions.[30] Shown in Table 4.2 are all the hydrogen consumption amounts and temperature maxima for all temperature reduction profile peaks. There is a noticeable correlation and significant trend between the hydrogen consumption and the BET surface area. With increased surface area, there is an increase in hydrogen consumption. The increased catalytic performance from CuO/CeO_2 nanorod samples indicate a synergetic effect between ceria and copper, where the copper ions favor the weakened Ce-O bond which also increases surface defects.[31]

Table 4.2. Hydrogen consumption α, β and γ peak (mmol/g) with maxima temperature of each oxidized CuO/CeO₂ samples.

Octahedra			H_2 (mmol/g)	Cubes			H_2 (mmol/g)	Rods			H_2 (mmol/g)
	Temp	PA	H_2		Temp	PA	H_2		Temp	PA	H_2
1% CuO α	142	0.09	0.02	1% CuO α	139	0.30	0.08	1% CuO α	165	0.48	0.12
1% CuO β	165	0.90	0.23	1% CuO β	149	0.34	0.08	1% CuO β	192	0.37	0.10
1% CuO γ	215	0.65	0.16	1% CuO γ	184	0.11	0.03	1% CuO γ	256	0.25	0.06
5% CuO α	151	1.06	0.26	5% CuO α	146	0.32	0.08	5% CuO α	146	1.45	0.36
5% CuO β	171	1.90	0.46	5% CuO β	161	1.26	0.32	5% CuO β	202	2.58	0.66
5% CuO γ	195	1.88	0.49	5% CuO γ	195	1.74	0.43	5% CuO γ	206	0.58	0.14
10% CuO α	151	1.40	0.36	10% CuO α	161	1.80	0.46	10% CuO α	152	3.01	0.77
10% CuO β	175	2.82	0.71	10% CuO β	178	1.71	0.46	10% CuO β	194	4.12	1.07
10% CuO γ	208	6.01	1.55	10% CuO γ	208	7.21	1.88	10% CuO γ	212	1.67	0.43

Figure 4.12. H₂ consumption of CuO/CeO₂ nano-octahedra after oxidation treatment.

Also, the correlation of increased hydrogen consumption and reactive crystal planes may be due to small amounts of surface oxygen that are present within the reactive planes of (110) and (100) and small amounts from (111). It is possible that tiny amounts of these surface O^{2-} ions become positioned at different sites. This may be the cause for many of the defects seen on the nanorods and why there is a lower number of defects present within the nano-octahedra and nanocubes.[32]
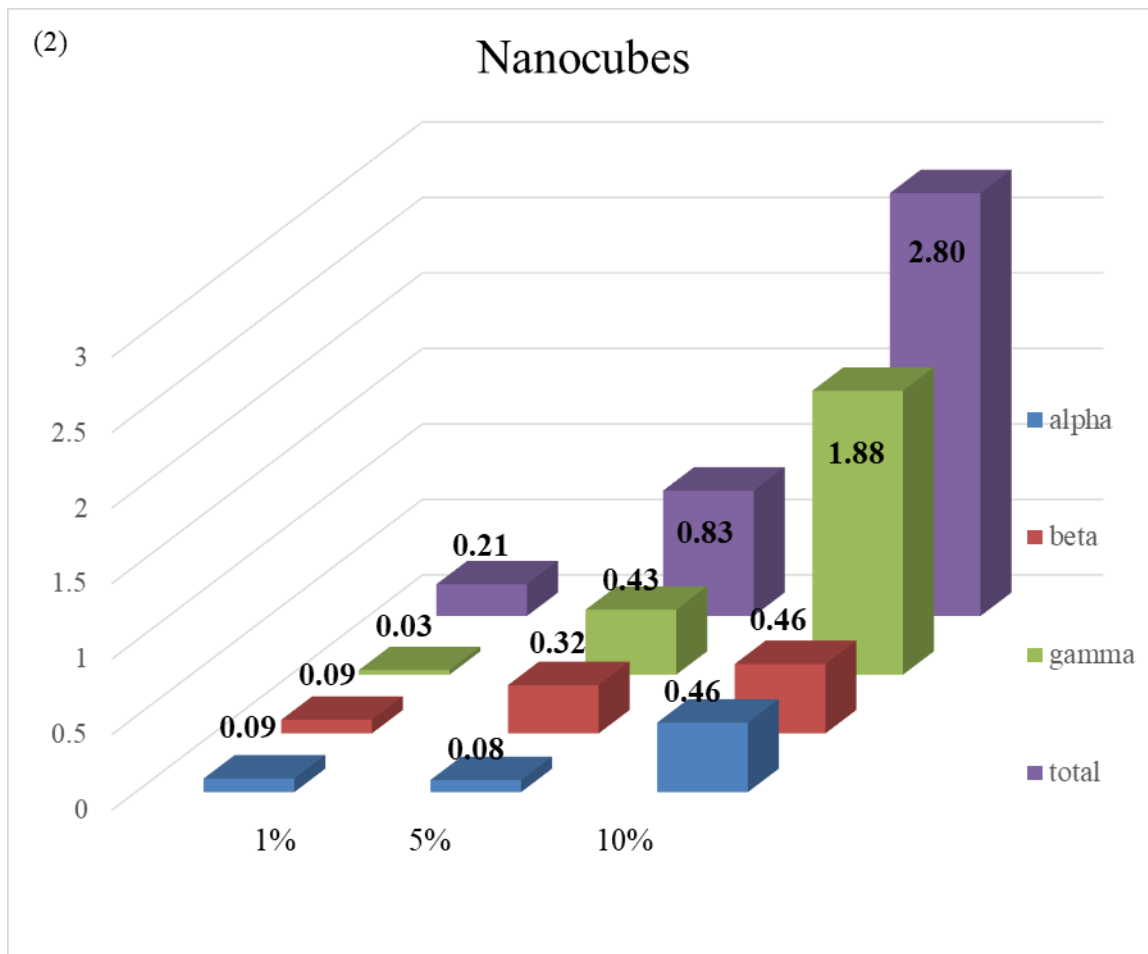
Figure 4.13. H₂ consumption of CuO/CeO₂ nanocubes after oxidation treatment.
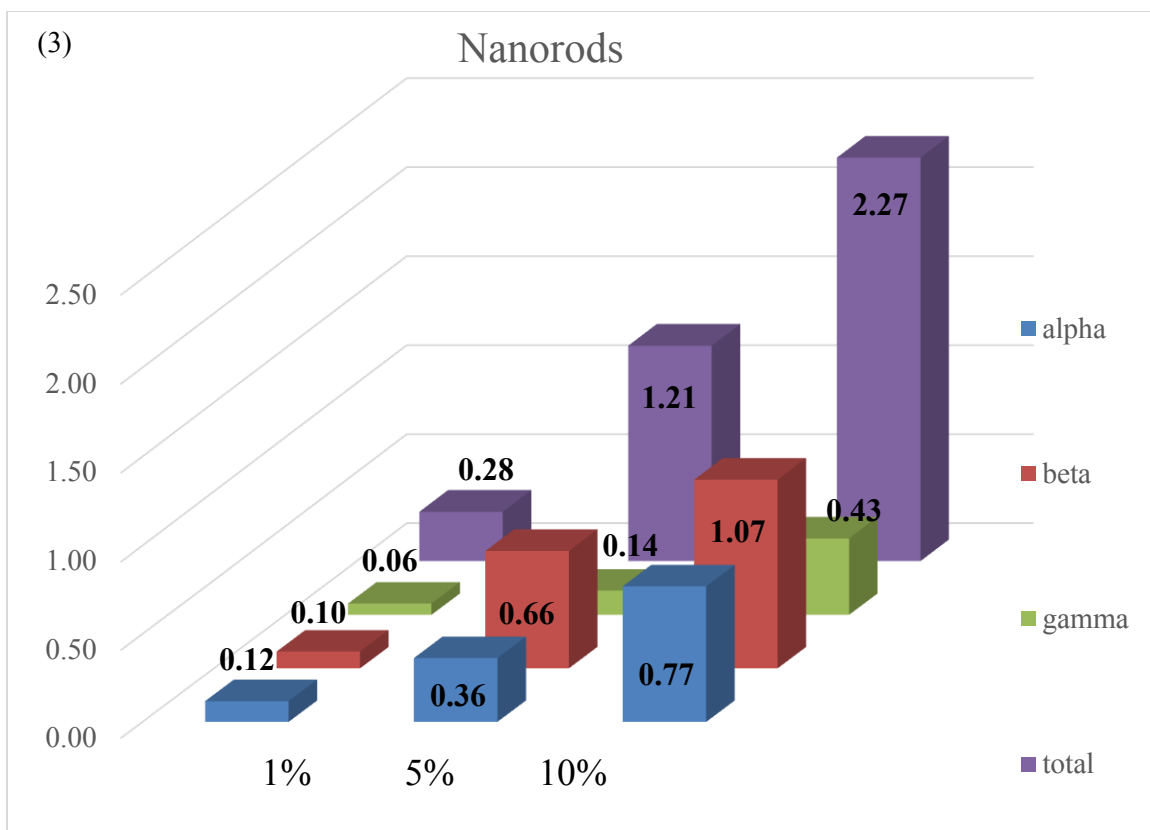
Figure 4.14. H₂ consumption of CuO/CeO₂ nanorods after oxidation treatment.
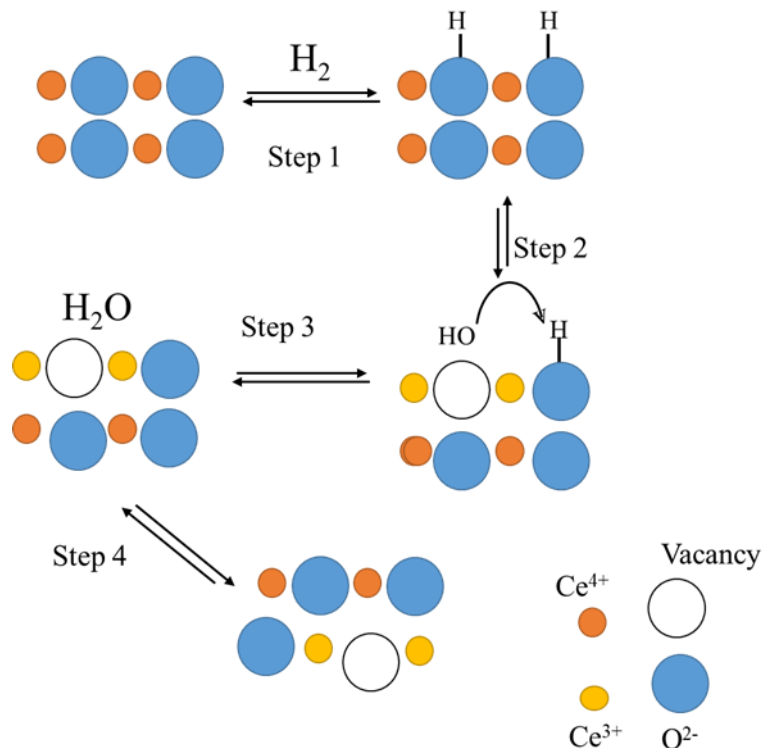
Figure 4.15. A schematic showing ceria reduction mechanism in H_2.

In Figure 4.15, Rao shows a mechanism, using H_2-TPR, for the reduction of ceria which will further help our understanding of the various kinetic rates for CeO_2.[32] There are four steps in this model, first the dissociation of chemisorbed hydrogen forms hydroxyl groups, second step is the formation of anionic vacancies and reduction of neighboring Ce^{4+} ions, third step desorption of water occurs by the recombination of hydrogen and hydroxyl groups and finally the diffusion of surface anionic vacancies into the bulk material.[32]

Figure 4.15, is a pictorial representation of each step within the model. It was demonstrated that reduction at the surface of ceria will occurs initially. Next it was documented that the bulk reduction will not start until the completion of all reduction of surface sites. Laachir et al. used FT-IR spectroscopy to explain that hydroxyl groups are

formed when surface ceria is reduced.[33] Noted within this research by Laachir a variety of hydroxyl groups were observed in different coordination environments on the surface of ceria. Intensity of the OH stretching bands increased proportionally with temperature. Finally, Laachir noted that at increased temperatures these bands will no longer exist and this was due to the formation of oxygen vacancies at the surface.[32] Therefore, examining the CO-TPD patterns of each 10 wt.% CuO/CeO_2 of varying morphologies is an important characterization to explore.
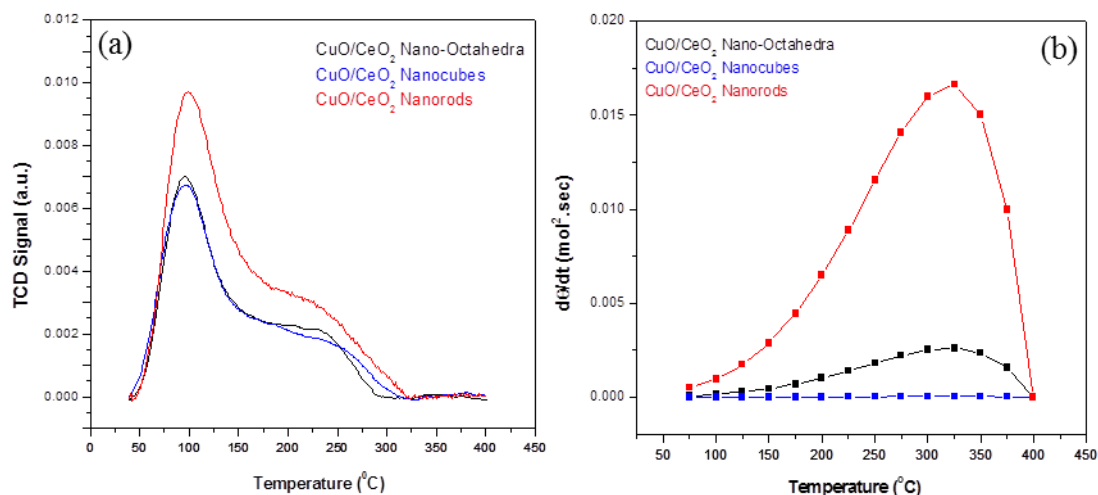
Figure 4.16. (a) CO-TPD curves of 10 wt.% CuO/CeO_2 nano-octahedra, vs. 10 wt.% CuO/CeO_2 nanocubes vs. 10 wt.% CuO/CeO_2 nanorods oxidized at 400^oC (b) Rate of desorption peaks (ROD).

In Figure 4.16 (a), it is seen that there is a broad CO desorption peak from 50-150 ^oC and a second peak at ~200-300 ^oC due to different CO adsorption approaches: a fraction of CO probably reacts with CeO_2 surface and adsorbs as carbonate, and desorbs as CO_2 at lower temperatures. The first peak was attributed to desorption of CO_2 produced from the reaction of adsorbed CO with CeO_2 surface.[34,35] The second peak was assigned to desorption of CO_2 which was formed by adsorbed CO developing into bidentate

118

carbonate species on the reactive sites.[35-36] It is evident that the intensity of CO and CO_2 desorption peaks differs with the varying morphologies, suggesting that the produced carbonate species can desorb more easily on the nanorod sample. This result would indicate that the ceria nanorods have the largest number of active sites for CO adsorption.[36] This is in good agreement with the above Raman and TPR results. Figure 4.16 (b), disclosed the rate of desorption (ROD) of CO_2 for all samples. The ROD for 10 wt.% CuO/CeO_2 sample increased from the nanocubes and nano-octahedra samples to the nanorods sample. A maximum ROD (~ 0.017 $mol.m^{-2}s^{-1}$) for 10 wt.% CuO/CeO_2 nanorods sample was achieved at ~ 345 ^{o}C. The rapid decrease of the adsorbed CO took place after reaching the maxima, due to the adsorbed CO already desorbed away from the surface. This may suggest, that the CuO/CeO_2 nanorod samples promoted CO_2 desorption more easily by creating more available CO oxidation sites.

To garner more information on the thermal stability of the different types of copper species on CuO/CeO_2 nanorods, TPR thermal cycling and TPR/TPO thermal cycling experiments were conducted on 10 wt% CuO/CeO_2 nanorods. The experiment consisted of six consecutive TPR cycles; the sample was placed in a U-tube and was not removed during cooling, as to not expose the sample to air oxidation. The TPR/TPO experiments were also consecutively run to eliminate any air oxidation. Throughout the experiment and in between each TPR and TPO run, the system was flushed by using 5% O_2/95% He or 5% H_2/95 % Ar for 2 h at 50 °C to remove any residual gases from the previous run. In addition, to avoid thermal deactivation, each H_2-TPR or H_2-TPR/O_2-TPO was only run up to 350°C. Figure 4.17 showed the TPR cycling profiles of the 10 wt.% CuO/CeO_2 nanorods, and it can be seen that there are two reduction peaks, consistent with the

reduction profile mentioned earlier. These two peaks represent the α and β copper species of the reduced 10 wt.% CuO_x/CeO_2 nanorods sample. In the Figure 4.17 (a), for all cycles of TPR, it can be seen that of both α and β peaks shifted gradually to the lower temperatures. Figure 4.17 (a) no β reduction peak was observed for the sixth TPR cycling experiment. Since, there is a strong interaction with copper species and CeO_2 nanorods support, we hypothesize that the oxygen used to reoxidize the system is coming from within the copper/CeO_2 system, meaning the interfacial area between copper and CeO_2. Since CeO_2 redox ability is well documented, this is the primary source for the sustainable H_2 consumption in the reduced 10 wt.% CuO_x/CeO_2 nanorods samples during these H_2-TPR cycling experiments.[37] In the TPR cycling it can be seen that both α and β peaks shifted to the lower temperatures. It is hypothesized that the copper species at the interface can aid in the early release of lattice oxygen in CeO_2, meaning lower reduction temperature. This may due to the production of oxygen vacancies. It is noted that there is a synergistic effect between Cu-O vacancy interactions. This may be due to the effects that the interaction has on copper, which enables the formation of oxygen vacancies in ceria under reaction conditions. Previously discussion, there is an ease of oxygen vacancy formation on highly defected ceria nanorods. The process occurs because of Ce^{4+} reduction and Cu^{2+} takes its place in the ceria lattice.[38] Since Ce^{3+} ion is larger and when Ce^{4+} is reduced there is an expansion within the ceria lattice.[39] However, this is not the same as the reduction of Ce^{4+} and Ce^{3+}. The reduction of two Ce^{4+} cations creates two Ce^{3+} cations with one oxygen vacancy formed.

$$2Ce^{4+} + O_{2-} \rightarrow 2Ce^{3+} + O_{vac} \qquad (4.2)$$

It was discovered if one Cu^{2+} cation replaces one Ce^{4+} cation with one oxygen vacancy.[39]

$$Ce^{4+} + O^{2-} \rightarrow Ce^{4+} + Cu^{2+} + O_{vac} \tag{4.3}$$

The H_2-TPR/O_2-TPO cycling experiments caused little change in the hydrogen consumption and reduction temperature of α and β copper species; however, the α peak seem to merge together with the increased cycling number, shown in Figure 4.17 (b). The cycling results indicate, the α and β copper species demonstrates good thermal stability on CeO_2 nanorods under reductive and oxidative conditions and retained most of all the hydrogen consumed throughout the cycling process.

(a)   (b)
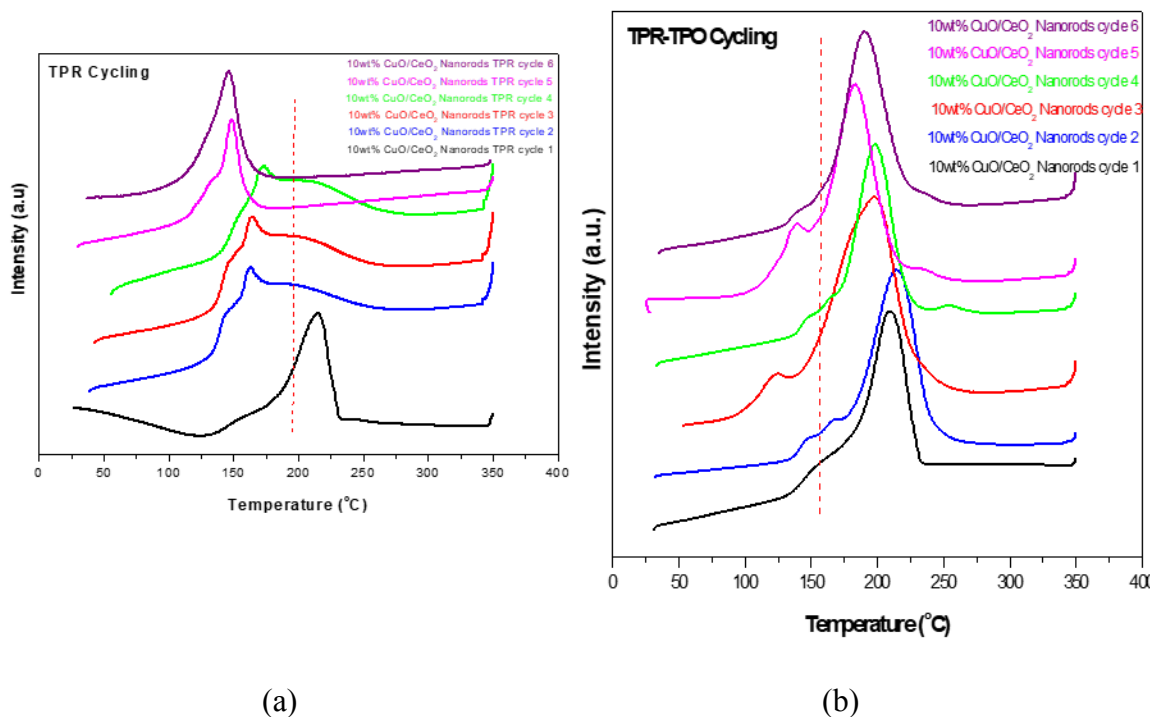
Figure 4.17. H_2-TPR cycling profiles for (a) six consecutive H_2-TPR (b) six H_2-TPR/ TPO cycling for 10wt% CuO/CeO$_2$ nanorods (oxidized) sample.

Table 4.3. Hydrogen consumption after TPR cycling and TPR/TPO cycling for 10 wt.% CuO$_x$/CeO$_2$.

Hydrogen Consumption TPR	Hydrogen Consumption TPR/TPO
Peak 1: α = 0.77 mmol/g; β = 1.02 mmol/g	Peak 1: α = 0.64 mmol/g; β = 0.93 mmol/g
Peak 2: α = 0.183 mmol/g; β = 0.39 mmol/g	Peak 2: α = 0.44 mmol/g; β = 1.73 mmol/g
Peak 3: α = 0.19 mmol/g; β = 0.38 mmol/g	Peak 3: α = 0.23 mmol/g; β = 1.32 mmol/g
Peak 4: α = 0.17 mmol/g; β = 0.40 mmol/g	Peak 4: α = 0.19 mmol/g; β = 1.29 mmol/g
Peak 5: α = 0.19 mmol/g; β = 0.064 mmol/g	Peak 5: α = 0.39 mmol/g; β = 1.48 mmol/g
Peak 6: α = 0.17 mmol/g	Peak 6: α = 0.11 mmol/g; β = 1.5 mmol/g

4.3.1.4. Oxygen Storage Capacity (OSC)

OSC is also strongly dependent on the exposed planes of the ceria. Oxygen at the surface and within the lattice in ceria (CeO$_2$) has been known to be easily stored and released from the (100) and (110) exposed crystal planes. These planes in ceria are responsible for the morphological shape of ceria nanoparticles. However, it has been demonstrated that restrictions to the plane of nano-octahedra ceria for OSC exists.[40] Recall, that oxygen vacancies are created more readily on highly defected nanorods as compared to nano-octahedra and nanocubes. This is possible because of lattice oxygen is highly mobile from the bulk to the surface on the more reactive planes.[41,42] Flytzani-Stephanopoulos determined that the morphology effect of CeO$_2$ particles when the system is used as a support for metal particles and that surface properties of ceria is governed by the dispersion of the metal particles and aids in the metal-support interaction.[43] In this study, OSC of the catalysts calculations were measured by H$_2$ pulse chemisorption using Micromeritics Autochem™ II 2920. Before sample measurements were taken the samples were loaded in U-tube and a temperature pre-treatment at 350 °C in 5%O$_2$-95%He environment for 30 min. After cooling down to room temperature, He

gas was flowed for 30 min to take excess oxygen out of the system. Then the sample tube was again raised to 350 ^{o}C and 5%H_2-95%He gas was injected into the sample tube every 3 min until the intensity of the hydrogen consumption peaks were nearly equal. The OSC was expressed as μmol of O_2 per gram catalyst sample. The OSC was tabulated are shown in Figure 4.18. The OSC for 10 wt.% CuO/CeO_2 nano-octahedra, 10 wt.% CuO/CeO_2 nanocubes, and 10 wt% CuO/CeO_2 nanorods samples were calculated at 0.679 μmol/g, 0.4427 μmol/g, and 4.32 μmol/g, respectively. The finely dispersed copper and the Cu-O-Ce solid solution that is present is thought to contribute to OSC on the CuO/CeO_2 nanorods and the metal-support interaction is directly associated with the presence of the oxygen vacancies on the surfaces of the ceria nanorod.
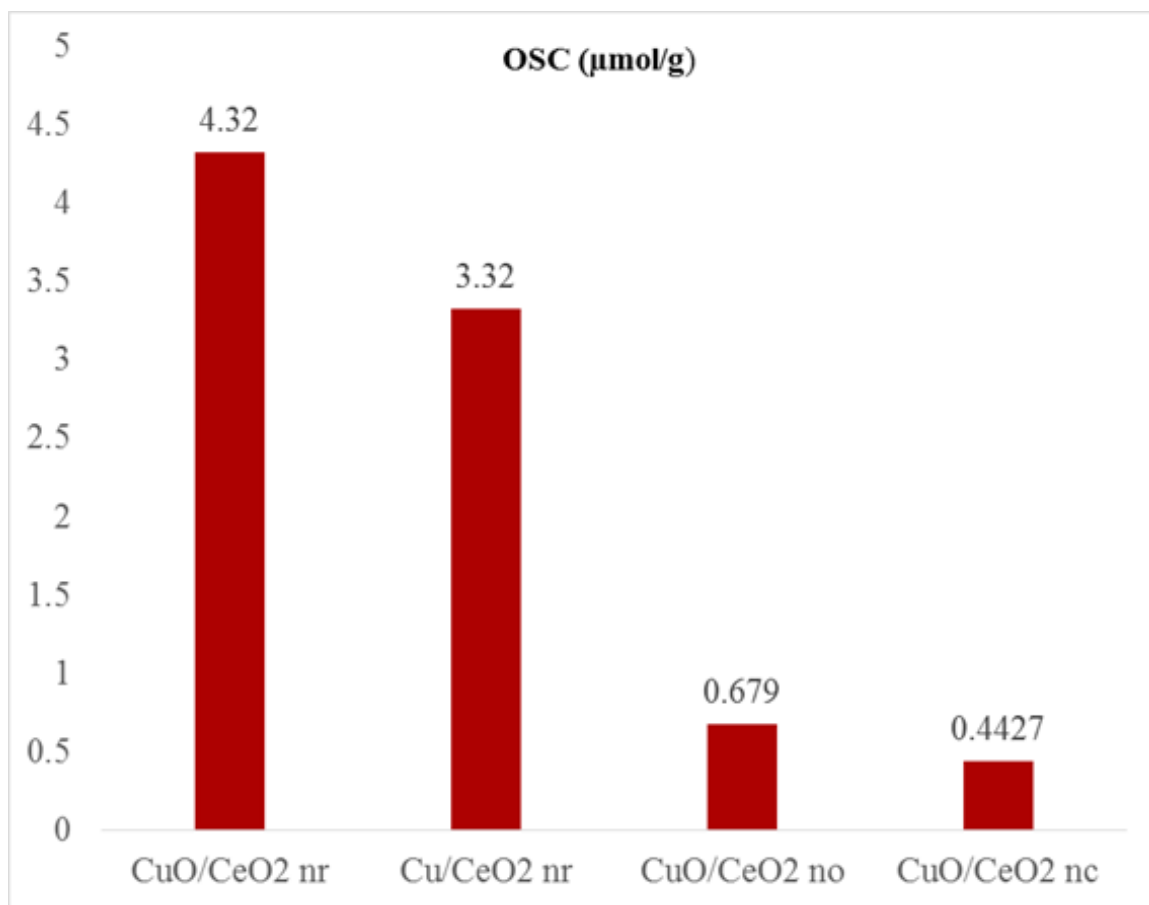
Figure 4.18. Oxygen Storage Capacity of oxidized 10% wt.% CuOₓ/CeO₂ nanorods, nanocubes and nano-octahedra and for nanorod comparison the 10 wt.% reduced Cu/CeO₂ sample was included.

4.3.1.5 CO conversion.

For all 10 wt.% CuO/CeO_2 nano-octahedra, nanocubes and nanorods after oxidation, the light-off curves of CO conversion as a function of temperature are shown in Figure 4.19. Observed in the CO conversion data is that the CuO/CeO_2 nano-octahedra and CuO/CeO_2 nanocube samples are unable to convert 100% CO up to 350 ^{o}C. The temperature (T_{50}) where 50% CO conversion occurred for 10wt% CuO/CeO_2 nanorods sample occurred at 91 ^{o}C and 100% CO conversion was obtained. For 10 wt.% CuO/CeO_2 nanocubes, temperature (T_{50}) at 50% CO conversion occurred at 107 ^{o}C and ~96% conversion was obtained. However, the 10 wt.% CuO/CeO_2 nano-octahedra,

temperature (T_{50}) where 50% CO conversion occurred at 117 ^oC and conversion was approximately 95% conversion. Evidently, this indicates that the CuO/CeO$_2$ nanorods show superior catalytic activity over CuO/CeO$_2$ nano-octahedra and CuO/CeO$_2$ nanocubes
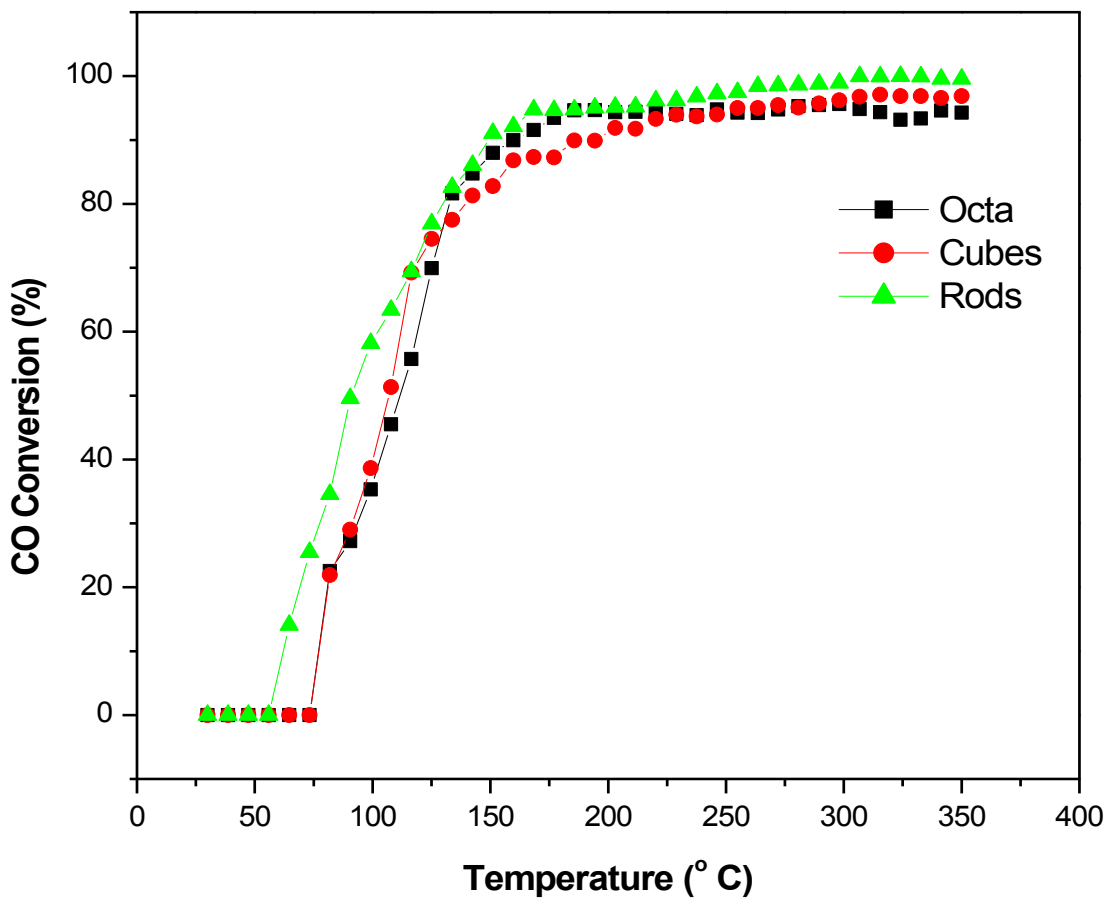
Figure 4.19. CO conversion curves of 10 wt.% CuO/CeO$_2$ nano-octahedra, vs. 10 wt.% CuO/CeO$_2$ nanocubes vs. 10 wt.% CuO/CeO$_2$ nanorods oxidized at 400 ^oC.
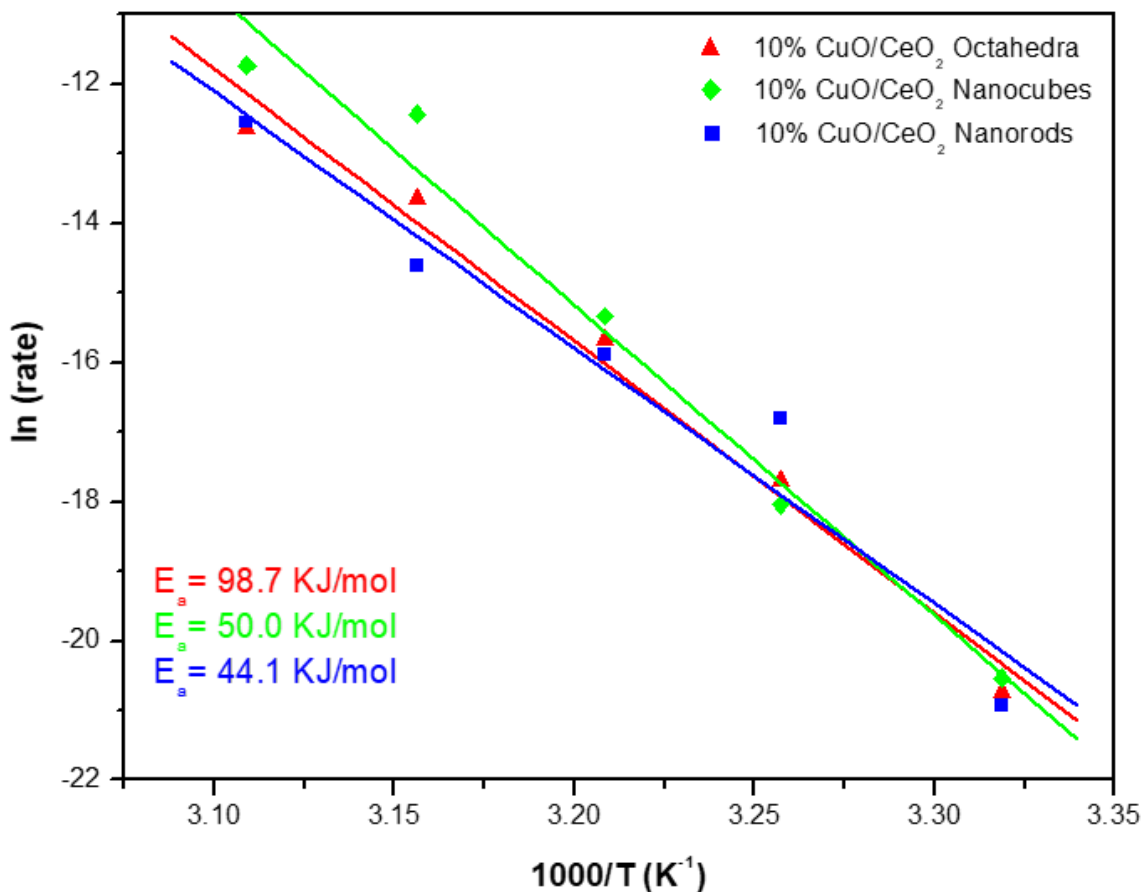
Figure 4.20. Activation energies calculated from CO oxidation data.

Shown in Figure 4.20, the activation energy can be derived from the linear regions of each CO oxidation curve. In using the Arrhenius equation, there is a relationship between slope and activation energy, these energies were calculated to as 98.7 kJ mol^{-1}, 50.0 kJ mol^{-1} and 44.1 kJ mol^{-1} for 10 wt.% CuO/CeO$_2$ nano-octahedra, CuO/CeO$_2$ nanocubes and CuO/CeO$_2$ nanorods, respectively. The difference in defects and oxygen vacancy formation is the main reason that 10 wt.% CeO$_2$ nanorods with well-defined (100), (110) and partial (111) planes show higher catalytic activity than the CeO$_2$ nano-octahedra sample with the thermodynamically stable (111) planes. The CuO/CeO$_2$ nanorods have lower activation energy and higher conversion rates over the same temperature range

126

when compared to 10 wt.% CuO/CeO_2 nano-octahedral and CuO/CeO_2 nanocube samples.

4.3.1.6. XPS and HRTEM Analysis.
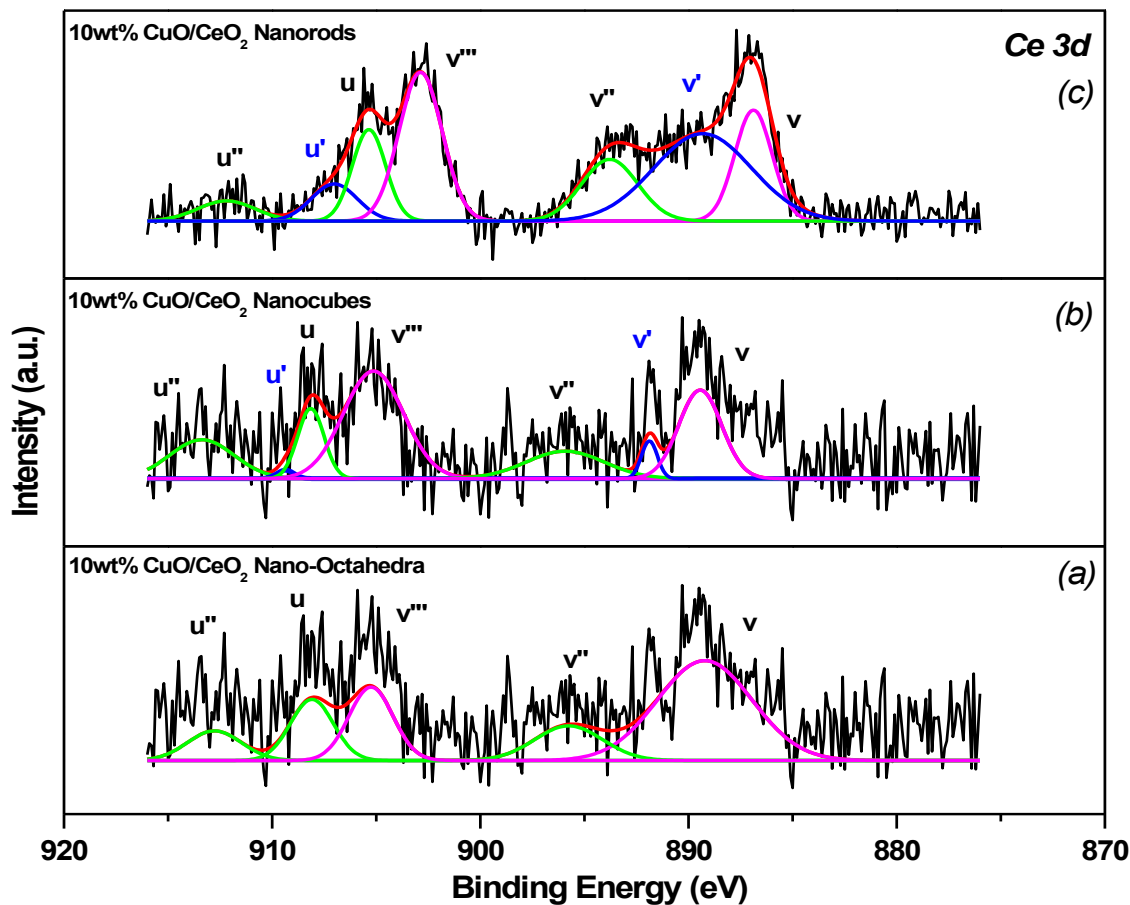
Figure 4.21. (a-c), Ce 3d XPS of 10 wt.% CuO/CeO₂ nano-octahedra, vs. 10 wt.% CuO/CeO₂ nanocubes vs. 10 wt.% CuO/CeO₂ nanorods oxidized at 400 °C before reduction treatment.

XPS experiments were run by Dr. Balaz. The XPS was employed to understand the chemical state of various elements at the catalyst surface. The Ce 3d spectra of 10 wt.% CuO/CeO_2 nano-octahedra, 10 wt.% CuO/CeO_2 nanocubes and 10 wt.% CuO/CeO_2 nanorods oxidized at 400 °C are shown in Figure 4.21 (a-c). The $3d_{3/2}$ and $3d_{5/2}$ peaks are

represented as u and v, respectively. For the CuO/CeO$_2$ nano-octahedra sample only five peaks could be distinguished: u (905.3), u' (N/A), u" (912.9), v (889.8), v' (N/A) and v" (895.9) of Ce 3d in 10 wt% CuO/CeO$_2$ nano-octahedra. Peaks u, u", v, v" and v"' are assigned to Ce^{4+} and peaks u' and v' are assigned to Ce^{3+}. [44] The presence of Ce^{3+} is necessary for improved performance in CO oxidation and it is noticeably non-existent in the CuO/CeO$_2$ nano-octahedra sample. For the CuO/CeO$_2$ nanocube samples all seven known peaks are observed: u (908.2), u' (908.2), u" (912.9), v (888.4), v' (891.8) and v" (893.8) of Ce 3d in 10 wt.% CuO/CeO$_2$ nanocubes. Recall Ce^{3+} which is needed to enhance catalytic activities, small amounts of Ce^{3+} are observed in the CuO/CeO$_2$ nanocube sample. For the CuO/CeO$_2$ nanorods sample all seven known peaks are observed: u (905.4), u' (907.1), u" (912.1), v (886.9), v' (889.4) and v" (893.8) of Ce 3d in 10 wt% CuO/CeO$_2$ nanorods. The presence of Ce^{3+} is increased significantly and the surface elemental XPS data showed key components to the increased catalytic activity that is seen in the CuO/CeO$_2$ nanorods samples.
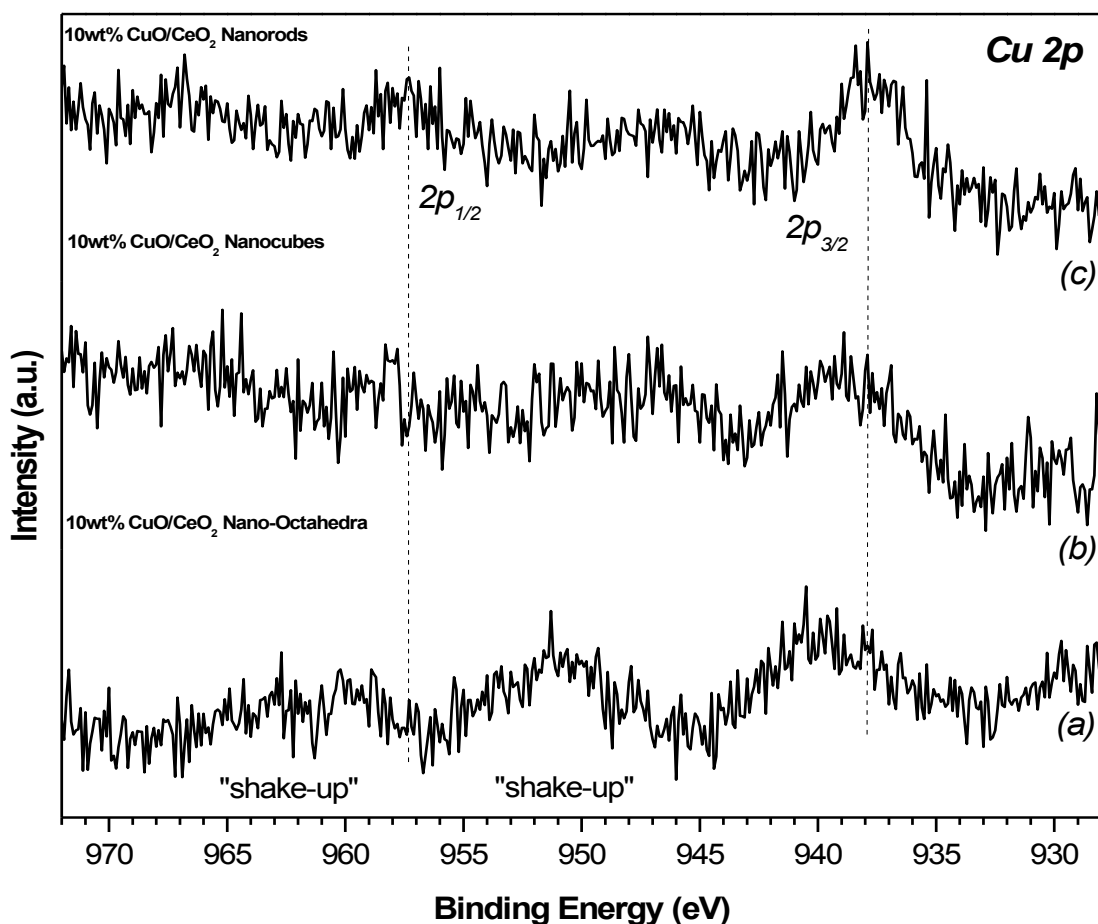
Figure 4.22. (a-c), Cu 2p XPS of 10 wt.% CuO/CeO₂ nano-octahedra, vs. 10 wt% CuO/CeO₂ nanocubes vs. 10 wt.% CuO/CeO₂ nanorods oxidized at 400 °C before reduction treatment.

Cu 2p XPS spectra can be seen in Figure 4.22 (a-c). Observed is the Cu 2p peaks, $2p_{3/2}$ and the $2p_{1/2}$. The $2p_{1/2}$ which represents Cu^{2+} is not present in the CuO/CeO₂ nano-octahedra and is present in the nanocube sample at 957.2 eV.[45] The nanorod sample observes the $2p_{1/2}$ at 956.9 eV. The most notable $2p_{3/2}$ represents the Cu^+, which is significant for its role in its ability to have a strong interaction between CeO₂ and copper species, and is observed at 940.2 eV 939.5 eV and 937.9 eV for CuO/CeO₂ nano-octahedra, CuO/CeO₂ nanocubes and CuO/CeO₂ nanorods, respectively.[46]

129

Typical O 1s XPS spectrum for CuO/CeO_2 have two peaks where the higher energy peak represents the adsorbed oxygen at the surface, denoted as O_{ads} and lower energy peak to represent lattice oxygen of metal oxides, denoted as O_{lat}.[47,48] In Figure 4.23 (a-c), 10 wt% CuO/CeO_2 nano-octahedra observed is only one peak at 536.3 eV. This suggests that only the lattice oxygen is being utilized in the catalytic conversion of CO to CO_2. The two peaks are observed for the 10 wt.% CuO/CeO_2 nanocube and CuO/CeO_2 nanorod samples where the observed peak is 536.7 eVand 534.2 eV and 535.9 eV and 533.8 eV, respectively. This O 1s XPS data is in agreement with Raman where it can be seen that the higher level of adsorbed oxygen is indicative of higher levels of oxygen vacancies.
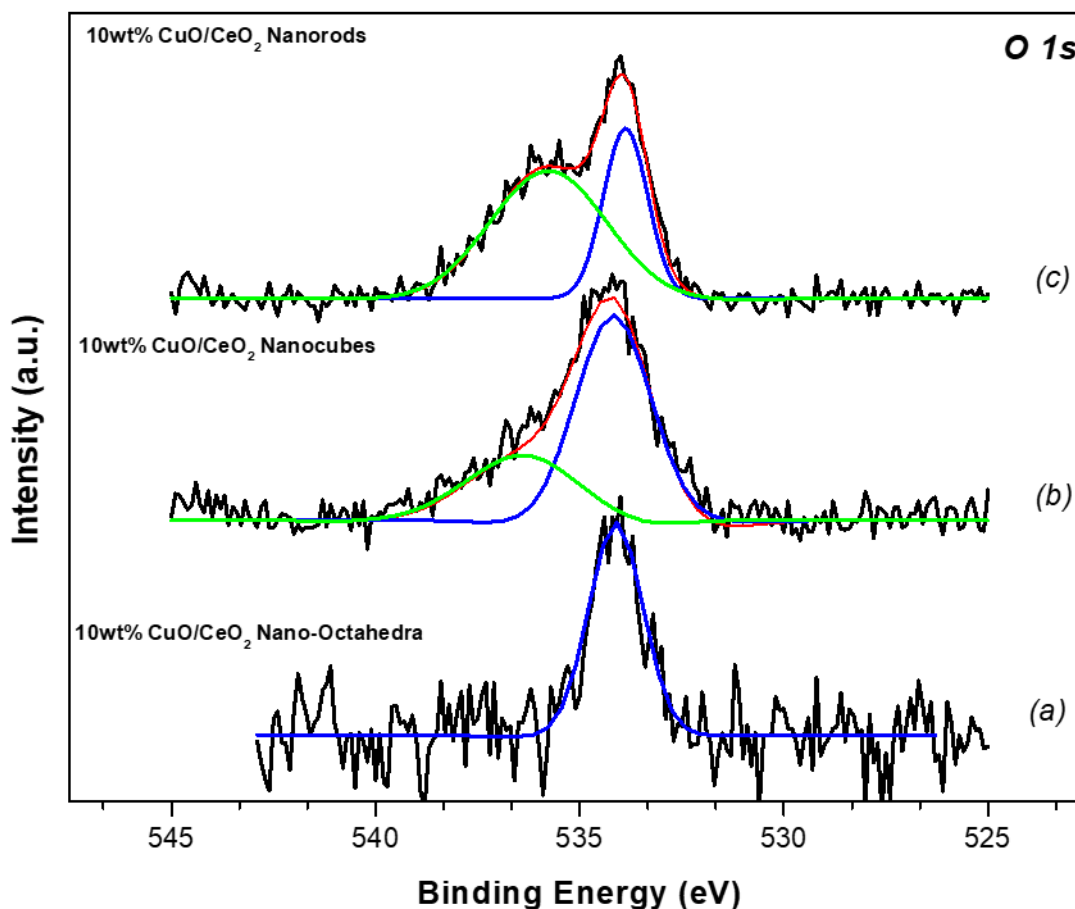
Figure 4.23. (a-c), O 1s XPS of 10 wt.% CuO/CeO₂ nano-octahedra, vs.10wt% CuO/CeO₂ nanocubes vs. 10 wt.% CuO/CeO₂ nanorods oxidized at 400 °C before reduction treatment

4.3.1.6. TEM

High resolution TEM images shown in Figures 4.24-4.26 represents the as synthesized 10 wt.% CuO/CeO₂ nanocubes and CuO/CeO₂ nanorods samples which are typically ~20-100 nm in length and 5–20 nm in diameter. Figure 4.24 (a) represents the CuO/CeO₂ nano-octahedra sample, where the (111) plane can be seen for each side shown. 4.24 (b) is HRTEM of 10 wt.% CuO/CeO₂ nanocube sample. Where it can be seen that the CuO/CeO₂ nanocube samples showed a lower concentration of surface defects which may be due to the Ce layer underneath is inaccessible, restricting oxygen

131

vacancy formation.[41] The H$_2$-TPR profile data and the HRTEM data for the CuO/CeO$_2$ nanorod samples are in agreement, indicating that small amounts of CuO are incorporated into the lattice of CeO$_2$ and well dispersed CuO is in high concentration aiding in increased catalytic activities. In Figure 4.25, the HRTEM images of the CuO/CeO$_2$ nanorod samples showed defects such as voids, lattice distortion, and steps.
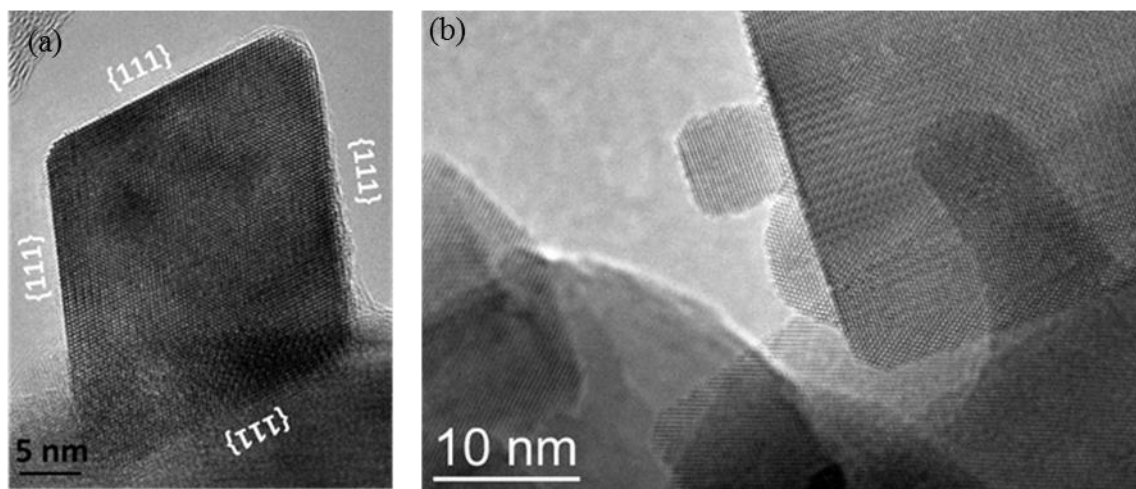
Figure 4.24. HRTEM images of (a) CeO$_2$ nano-octahedra (b) 10 wt% CuO/CeO$_2$ nanocubes.
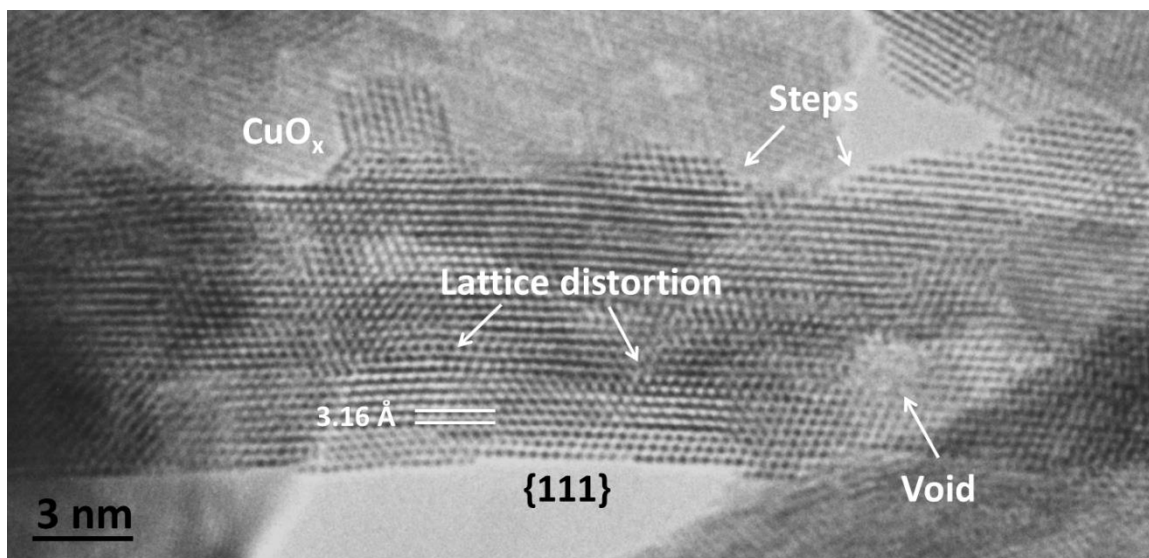
Figure 4.25. HRTEM images of 10 wt.% CuO/CeO$_2$ nanorods w/ (111) exposed plane and surface defect.
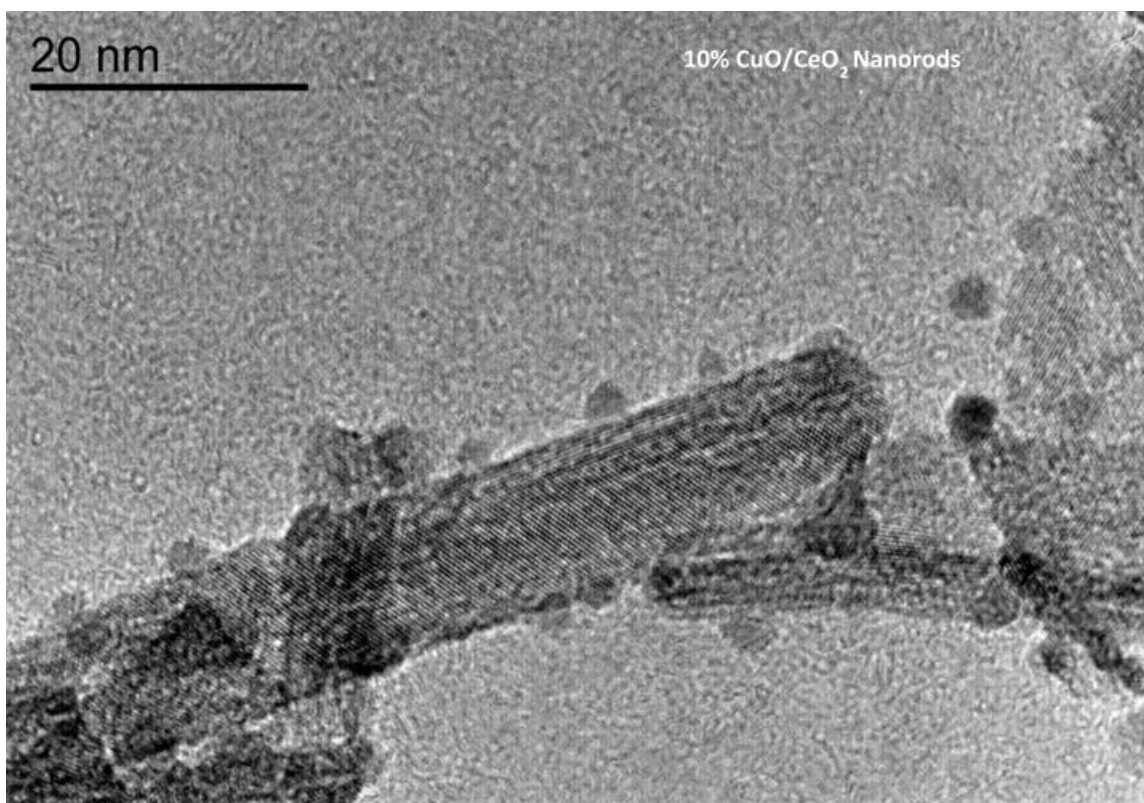
Figure 4.26. HRTEM image of highly dispersed CuO on the CeO$_2$ nanorod surface.

TEM was also used to offer information about spatial distribution and interaction of CuO$_x$ ($0 \leq x \leq 1$) species with the CeO$_2$ nanorod support. Figure 4.26, HRTEM image aids in the ability to distinguish the β copper species on CeO$_2$ nanorods. These images were obtained by tilting the x and y along the z axis in order to determine that β copper is just loosely dispersed over the CeO$_2$ nanorods. It is apparent that the nanorod with the more reactive and exposed (110), (100) and represented here the (111) planes represent highly defected planes and suggests this is the primary reason for the strong interactions of CuO$_x$ and CeO$_2$.

4.3.2. Reduction treatment effect

The reduced 10 wt.% CuO$_x$/CeO$_2$ nanorods catalysts were prepared by incipient wetness impregnation by using Cu$_2$(OH)$_2$CO$_3 \cdot$H$_2$O (copper(II) carbonate) as the copper

source followed by oxidation at 400 °C in air and reduction treatment at 400 °C in 5 vol% H_2/95 vol% He.

4.3.2.1. XRD and H_2- TPR

Denoted in Figure 4.27, is the XRD pattern of the reduced 10 wt% CuO_x/CeO_2 nanorods sample with metallic Cu^0 which was prepared with the aforementioned reduction treatment at 400 °C for 5 h in 5 vol% H_2/95 vol% He. The XRD patterns of two samples before and after the reduction treatment are shown in Figure 4.27, where the marked diffraction peaks are indexed and correspond to CuO (JCPDS 45-0937) and Cu (JCPDS 04-0836); each were identified after the oxidation and reduction treatments. Data from the XRD analysis showed that the reduced 10 wt.% CuO_x/CeO_2 nanorods sample, although exposed to air, exhibited no CuO peaks. The sharper metallic Cu peaks in Figure 4.27 indicates a larger particle size and a more crystalline nature of Cu compared with those of CuO particles before the reduction treatment.

Figure 4.28 and Figure 4.29 (a) and (b) showed the H_2-TPR profiles and H_2 consumption analysis of the reduced 10 wt.% CuO_x/CeO_2 nanorods and 10 wt.% CuO/CeO_2 nanorods using the same TCD signal scale and similar sample weight (~90 mg). Recall the H_2-TPR profile for CeO_2 nanorods shown in Figure 4.8, it was demonstrated that there are two reduction peaks for the surface and bulk reductions, with a relatively higher surface reduction peak at 467 °C. A larger amount of surface reduction occurs on the CeO_2 nanorods, with the (110), (100) and also (111) exposed planes as opposed to the CeO_2 nano-octahedra with dominant (111) and nanocube with (100) samples. Figure 4.25 illustrates the H_2-TPR profiles of the 10 wt.% CuO/CeO_2 nanorods and reduced 10 wt% CuO_x/CeO_2 nanorods, which correlated to two-step reduction

profiles. It is well established that two-step and three-step H_2-TPR reduction profiles have been reported for CuO/CeO_2 catalysts. Shown in schematic of Figure 4.7, the low-temperature peak from the two-step reduction profile is assigned to the smaller crystalline CuO, which is well-dispersed and strongly interacting with the CeO_2 support. The high-temperature peak is attributed to "bulk-like" larger CuO particles that interact weakly with the CeO_2 support.[49] The larger size CuO particles are a result of the decomposition of copper (II) carbonate. The H_2-TPR profile of the oxidized 10 wt.% CuO/CeO_2 nanorods sample, records the two reduction peak positions at 147 °C and 205 °C and the reduced 10 wt.% CuO_x/CeO_2 nanorods profile peaks are recorded at 143 °C and 198 °C. These peaks profiles are drastically similar, the α and β peaks for the low-temperature peaks that are assigned to CuO strongly interacting with the CeO_2 support and the intermediate temperature peak is attributed to highly dispersed CuO_x weakly interacting with the CeO_2 support. No assignment of TPR peak for bulk CuO was present in the samples. This was confirmed by XRD, and it is proposed that the bulk size metallic copper on CeO_2 was not oxidized, even though the sample was not protected from air oxidation. Recall the surface reduction temperature of the CeO_2 nanorods starts around 300 ˚C and is centered at 425 ˚C (Figure 3.8). It is then possible to state that since the two reduction peaks at 143 ˚C and 198 ˚C shown in Figure 4.28 are due to the CuO_x/CeO_2 areas where the CuO_x species interacts with the CeO_2. To quantify the amount of hydrogen consumed by each sample a peak fitting analysis was done. H_2-TPR profiles are shown in Figure 4.29, and document the peak area for the CuO/CeO_2 α peak 1.65 and the β peak was 6.25, which equivalent to 36.30 mmol/g and 137.50 mmol/g, respectively. The CuO_x/CeO_2 peak area for the α peak was 1.44 and the β peak was 2.54, which

equivalated to 31.68 mmol/g and 55.88 mmol/g. These results for the reduced samples were not expected and possibly due to small amounts of well-dispersed β copper particles converted to α copper particles by incorporating with the CeO_2 support during the reduction treatment at 400 ˚C and α particles forming a solid solution.
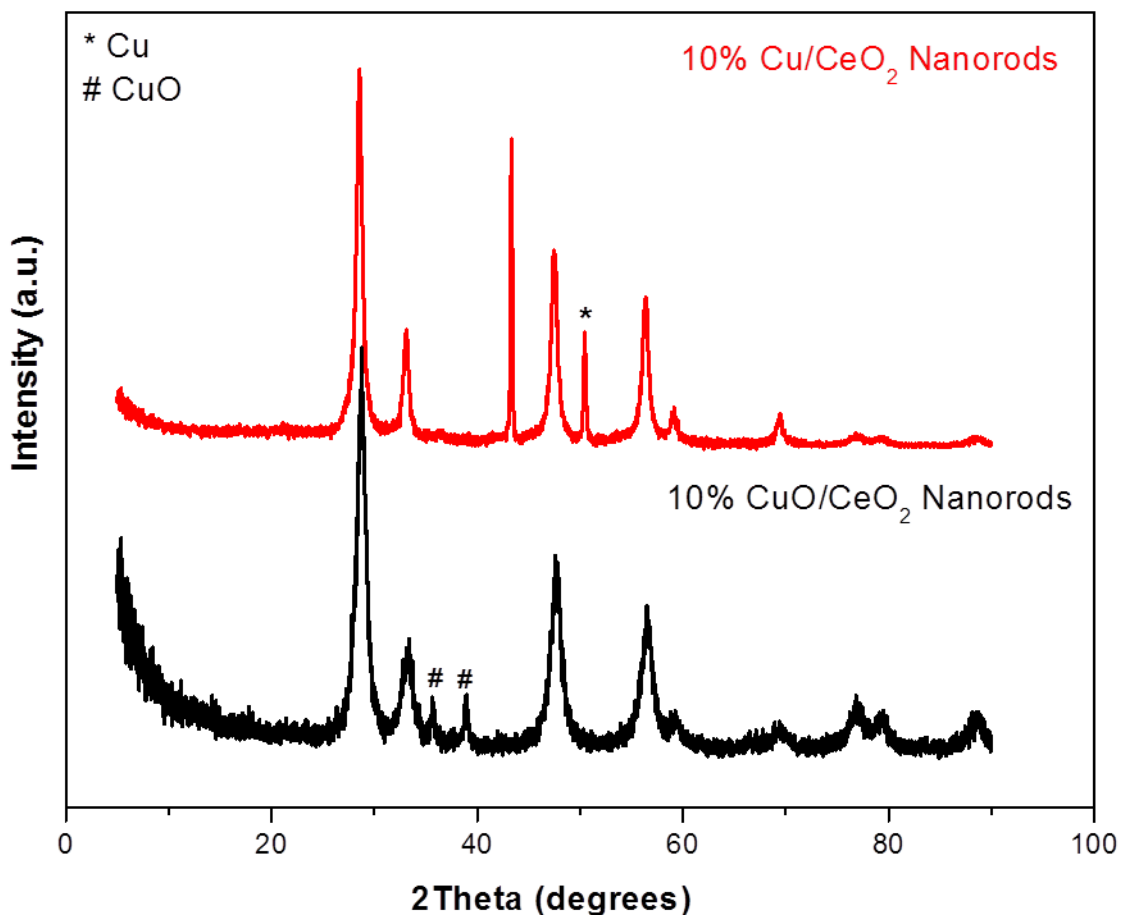
Figure 4.27. XRD data of 10 wt.% CuO/CeO₂ vs. 10 wt.% CuOₓ/CeO₂ nanorods.
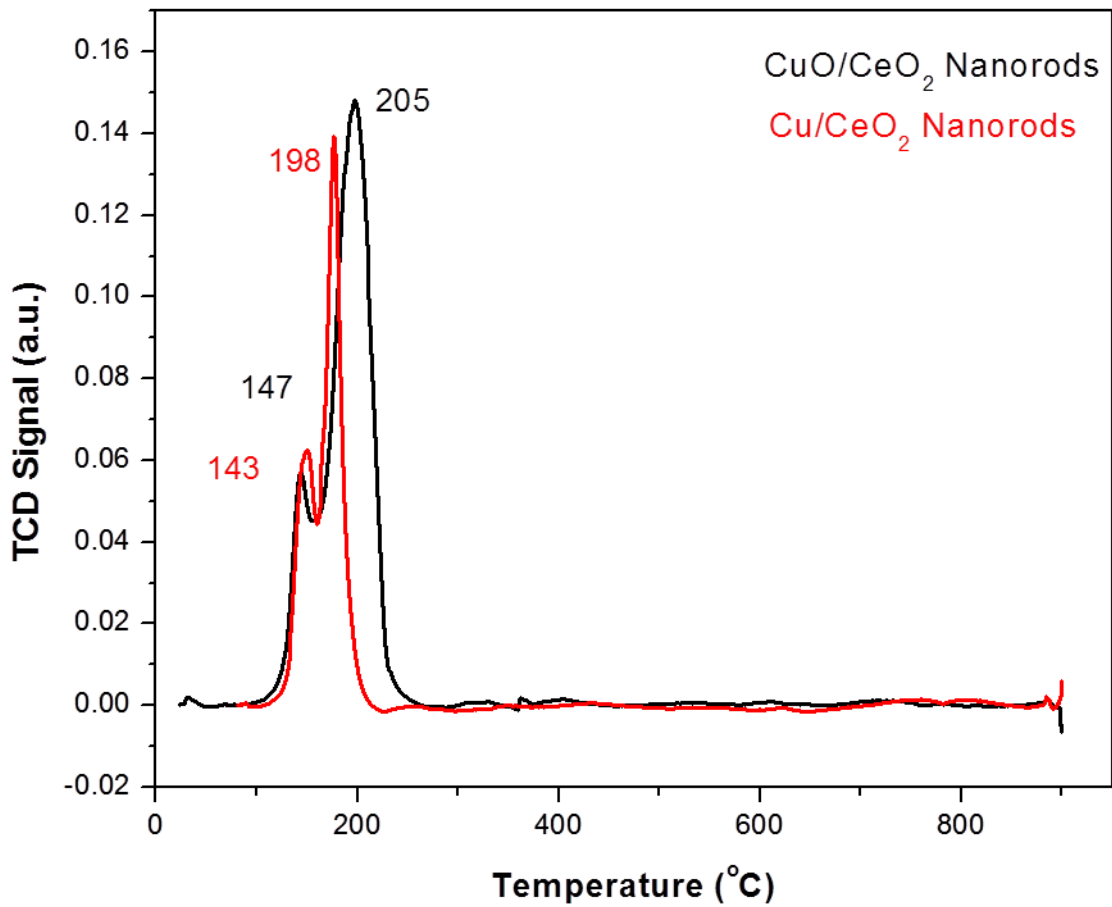
Figure 4.28. H₂-TPR data 10 wt.% CuO/CeO₂ vs.10 wt.% CuOₓ/CeO₂ nanorods.
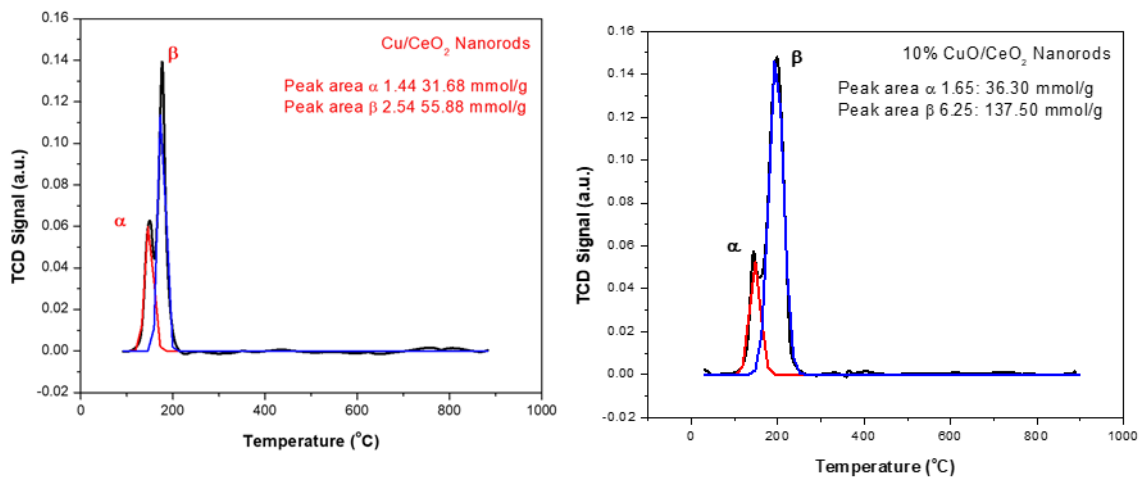
Figure 4.29. (a) Peak area used to calculate H₂-consumption of 10 wt.% CuOₓ/CeO₂ nanorods (b) Peak area used to calculate H₂-consumption of 10 wt.% CuO/CeO₂ nanorods.

137

4.3.2.2. Raman

In Figure 4.30, a comparison of Raman data sets of CuO/CeO_2, and CuO_x/CeO_2 are shown. Typically, CeO_2 nanorods exhibit the first-order F_{2g} peak near 460 cm^{-1}. Learning from the H_2-TPR experiments α, β and γ peaks CuO can be reduced at temperatures below 250 °C, meaning that all reduction peaks should be reduced to the metallic copper phase. Since, metallic copper is not Raman active all the Raman peaks are accredited to CeO_{2-x} (0≤x≤0.5) and CuO_x (0≤x≤1). Recall earlier, that the high and low energy Raman peaks for pure CeO_2 nanorods are documented at ~262 and ~602 cm^{-1} which have been well documented to contributed to the presence of oxygen vacancies in CeO_2.[50] When these two samples are compared with the pure CeO_2 sample, there is an unmistakable peak shift for the F_{2g} band. This is generally assigned to oxygen vacancy formation and to a lesser extent solid solution creation.[51] The first order F_{2g} peak shift correlates with the reactivity for CO oxidation due to the large number of defects and surface oxygen present on the nanorod sample.
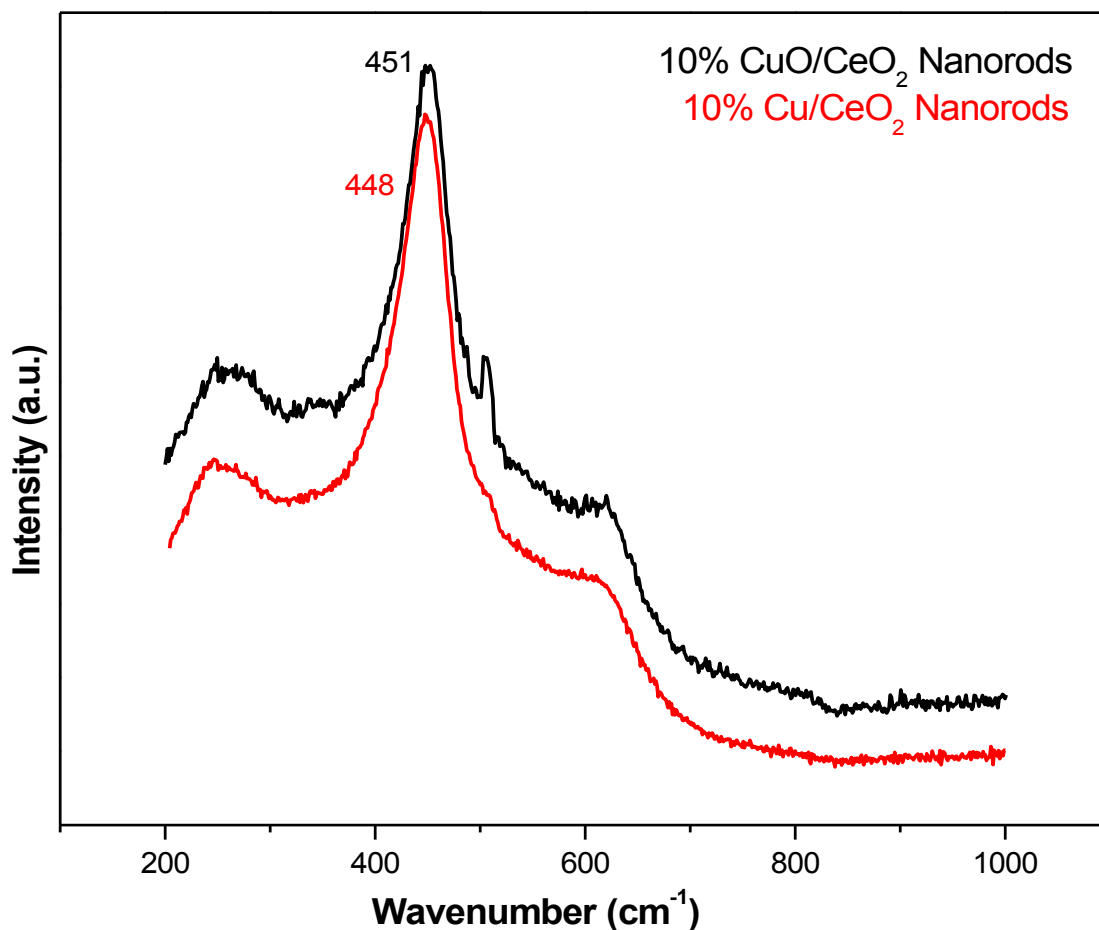
Figure 4.30. Raman data 10 wt% CuO/CeO$_2$ vs.10 wt% CuO$_x$/CeO$_2$ nanorods.

4.3.2.3. CO-TPD

In Figure 4.31, it is seen for both 10 wt% CuO$_x$/CeO$_2$ nanorods and 10wt.% CuO/CeO$_2$ nanorods that there is a broad CO desorption peak from 50-150 ^{o}C and a second peak at ~200-300 ^{o}C due to different CO adsorption approaches: a fraction of CO probably reacts with CeO$_2$ surface and adsorbs as carbonate, and desorbs as CO$_2$ at lower temperatures. Well documented that the first peak is attributed to desorption of CO$_2$ produced from the reaction of adsorbed CO with CeO$_2$ surface.[52,53] The second peak is assigned to desorption of CO$_2$ which was formed by adsorbed CO developing into

bidentate carbonate species on the reactive sites.[36] The produced carbonate species can desorb more easily on the nanorod samples, as indicated in the study comparing the various morphologies, the results indicate that the nanorod supports will assist in the number of active sites for CO adsorption.[54] Based on the Raman and H_2-TPR results are in good agreement and reinforce that the CeO_2 nanorods are the preferred morphology for increased catalytic activities.
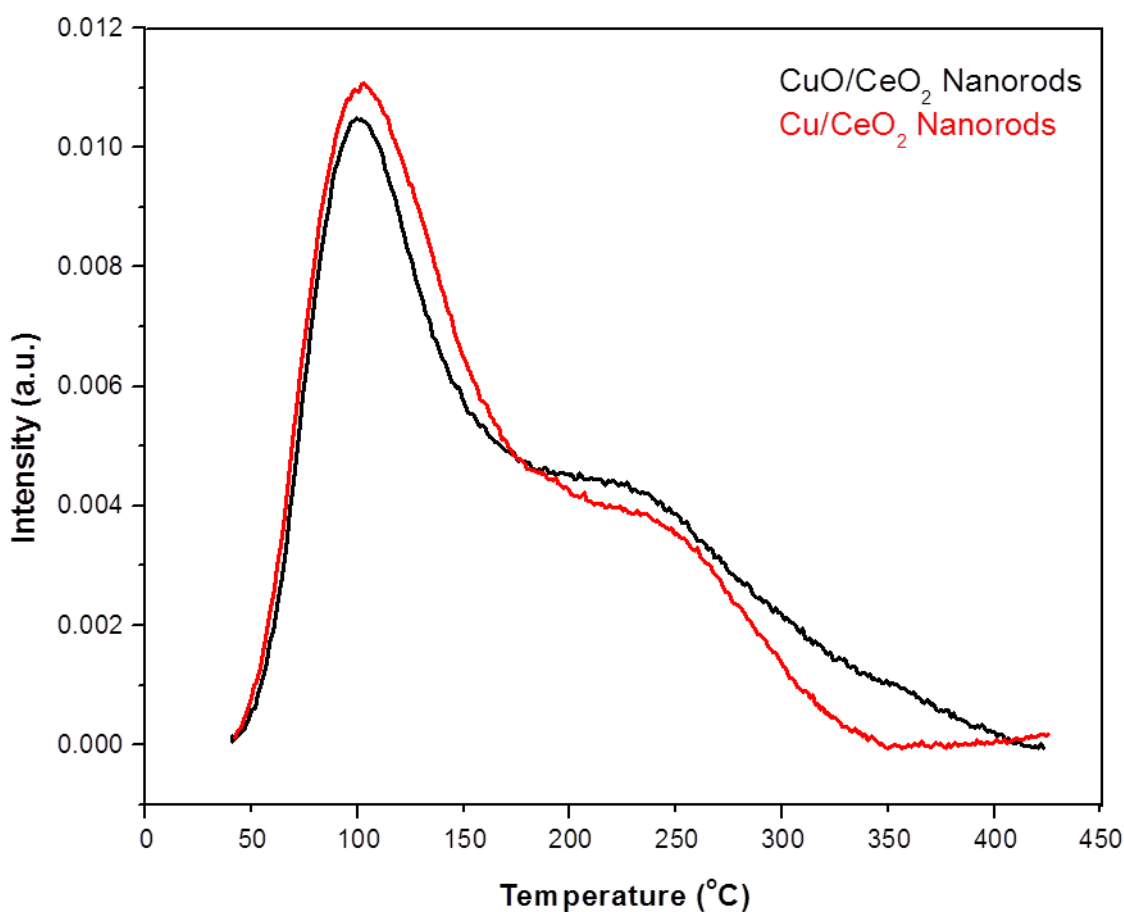
Figure 4.31. CO-TPD data 10 wt.% CuO/CeO_2 vs. 10 wt.% CuO_x/CeO_2 nanorods.

4.3.2.4. CO Oxidation

Figure 4.32, compares the catalytic activity of the 10 wt% CuO/CeO_2 nanorods and 10 wt% CuO_x/CeO_2 nanorods for CO oxidation. The samples were compared at different temperatures, up to 350 °C. The conversion activities of the catalysts are compared based on the T_{50} and T_{100} temperatures under which 50% CO and 100 % conversion are achieved: T_{50}: 10 wt.% CuO_x/CeO_2 (73 °C) and 10 wt.% CuO/CeO_2 (99 °C); T_{Max}: 10 wt.% CuO/CeO_2 (259 °C) and 10 wt.% CuO_x/CeO_2 (314 °C). Recall Figure 3.11, the CO oxidation for pure CeO_2 nanorods showed a T_{50}: occurred at 155 °C and never reached 100% conversion. The CO conversions for the oxidized and reduced samples are very similar. This is an indication that the exposing the more reactive planes on nanorods aids in an increased catalytic efficiency, possibly due to the strong metal-oxide interaction at the surface of the CeO_2 nanorods.
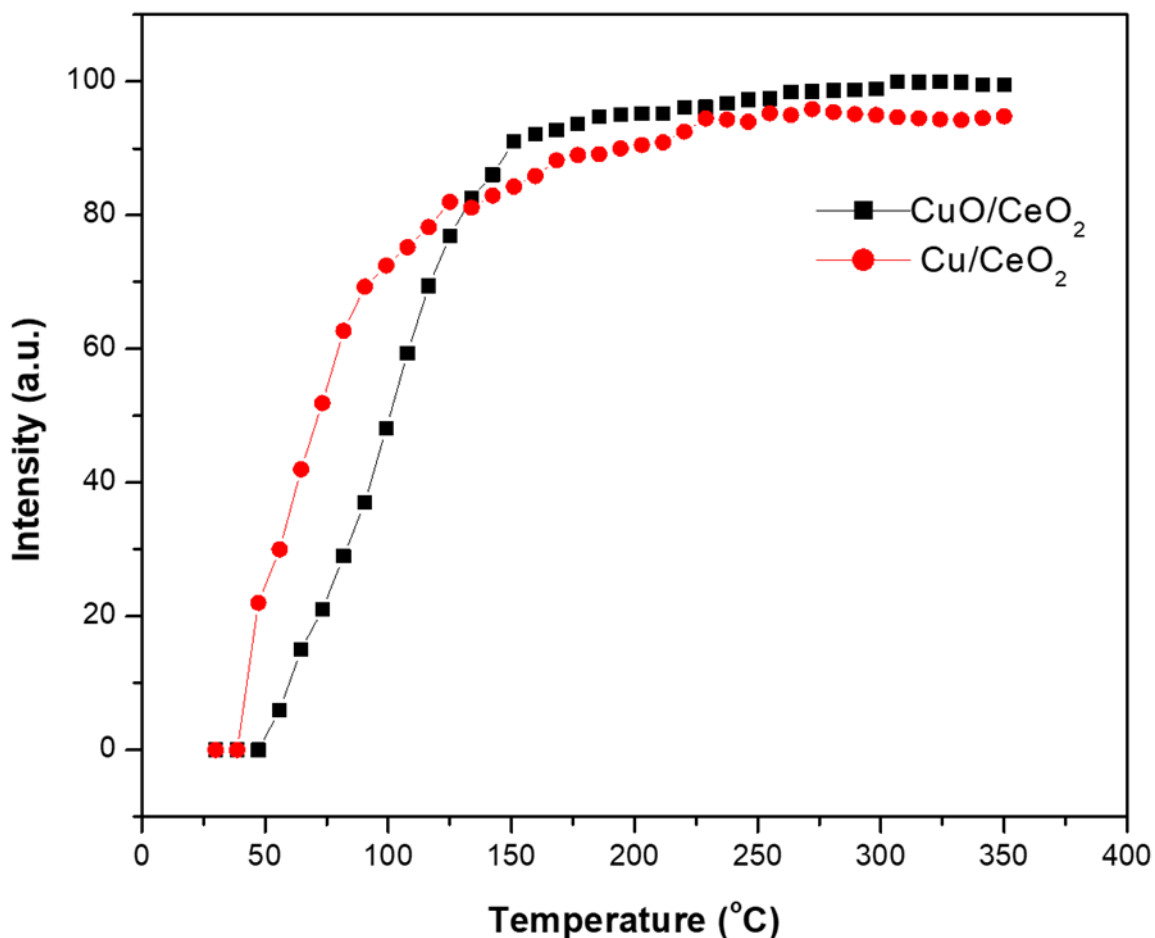
Figure 4.32. CO Oxidation data 10 wt% CuO/CeO₂ vs.10 wt% CuOₓ/CeO₂ nanorods.

4.3.2.5. TEM

TEM images were obtained to garner a better understanding of the interfacial interaction of CuO_x ($0 \leq x \leq 1$) and CeO_2 nanorod support. Figure 4.33 represents an in-depth TEM study of the CuO/CeO_2 nanorod and CuO_x/CeO_2 nanorod catalysts. As indicated earlier, two and three step reduction profiles have been well documented. As stated the peak is representative of the copper species interacting strongly, in fact becoming part of the CeO_2 lattice, a solid solution is created. The β peak is indicative of highly dispersed copper and finally the γ peak exposed that the bulk copper species are present. Figure 4.33 showed that there is a strong interfacial interaction between the α

particles and the support. The β copper species are highly dispersed on top of the CeO_2 nanorods, which can be seen in Figure 4.26. Then seen in Figure 4.25, various defects were distinguishable and documented as voids, lattice distortion, and steps. D-spacing calculations were done to determine the interplanar distances along the lattice fringes. The HRTEM image of an individual CeO_2 nanorod shown in Figure 3.9, correspond to the (111) and (100), with a d-spacing at about 3.1Å and 2.7Å, respectively. The nano-octahedra samples do not represent increased catalytic activities which may be due to the eight less reactive (111) planes however, the more reactive nanorods with (111) exposed planes, do represent an increase. This implies that surface defects may be the main factor responsible for the strong interactions between the CuO_x and CeO_2. This results in enhanced catalytic activity and lower reduction temperatures.
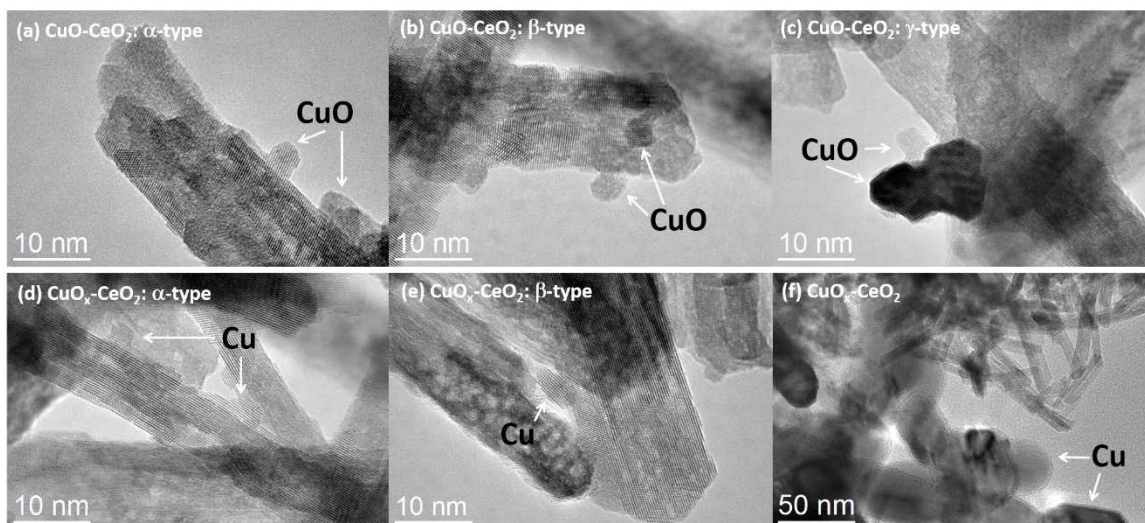
Figure 4.33. HRTEM images of 10 wt.% CuO/CeO₂ nanorods and 10 wt.% CuOₓ/CeO₂ nanorods.

4.4. Conclusion

In this chapter, the controlled shape morphologies and their role in the redox properties of the catalyst were compared. Observed was the interaction between CuO_x/CeO_2 and its synergetic effect for CO oxidation and reduction temperature. CuO/CeO_2 nanorods showed significantly lower reduction temperatures and these samples have the ability to oxidize CO to CO_2. This may be due to the more reactive exposed crystal planes (110) and (100) of CuO/CeO_2 nanorods. Based on Raman analysis, H_2-TPR and HRTEM the interfacial structure and defects of CuO_x-CeO_2 nanorods contributes greater to oxygen mobility and low-temperature catalytic activities than the nano-octahedra and nanocube samples due to nanorods ability to the create of oxygen vacancies more readily due to highly dispersed copper species on CeO_2 and a small amount solid solution forming at the metal-oxide interface. Along with the XPS data that unequivocally demonstrates that adsorbed oxygen and Ce^{3+} are more prevalent on the nanorod samples. The varying percentages of copper onto the various morphologies indicate that increased catalytic performance increase with the increased copper content, in all samples. In addition, the Ce 3d XPS data confirms that Ce^{3+} which necessary for improved performance in CO oxidation. As seen in the comparison between CuO_x and CuO, the reduction treatment further assists in the formation of active states which aids in the interaction between CuO_x and CeO_{2-x} support. With an increase in active sites more gas adsorption can occur and prevent migration of the metal species during thermal treatments, which thermally stabilizes the samples, making these support catalyst pairs a prime candidate for low temperature reducibility.

Acknowledgements

4.6. References

1. Trovarelli, A. Structural and Oxygen Storage/Release Properties of CeO_2-Based Solid Solutions. *Comments Inorg. Chem.,* **1999**, 20, 263-284.

2. Kundakovic, L. and Flytzani-Stephanopoulos, M. Reduction characteristics of copper oxide in cerium and zirconium oxide systems. *Appl. Catal. A.,* **1998**, 171, 13-29.

3. Mock, S.; Sharp, S.; Stoner, T.; Radetic, M.; Zell, E. and Wang, R. CeO_2 nanorods-supported transition metal catalysts for CO oxidation. *J. Colloid Interface Sci*., **2016**, 466, 261-267.

4. Song, W.; Jansen, J. and Hensen, M. A computational study of the influence of the ceria surface termination on the mechanism of CO oxidation of isolated Rh atoms., *Faraday Discuss*, **2013**, 162, 281.

5. Trovarelli, A. (Ed.), Catalysis by Ceria and Related Materials in: Catalytic Science Series. vol. 2, Imperial College Press, London, **2002**.

6. Wang, D.; Kang, Y.; Doan-Nguyen, V.; Chen, J.; Küngas, R., Wieder, N. L.; Bakhmutsky, K.; Gorte, J. and Murray, B. Synthesis and oxygen storage capacity of two-dimensional ceria nanocrystals. *Angew. Chem. Int. Ed*., **2011**, 50, 4378–4381.

7. Henrich, E. and Cox, A. The Surface Science of Metal Oxides, Cambridge University Press, Cambridge, **1994**.

8. Ivoning, J. and Van Santen, A. Electrostatic potential calculations on crystalline TiO_2: The surface reducibility of rutile and anatase. *Chem. Phys. Lett.,* **1983**, 101, 541-547.

9. Yang, Z.; Woo, K.; Baudin, M. and Hermansson, K. Atomic and electronic structure of unreduced and reduced CeO_2 surfaces: a first-principles study. *J. Chem. Phys.,* **2004**, 120, 7741-7749.

10. Kaspar, J.; Fornasiero, P.; Graziani, M. Use of CeO_2-based oxides in the three-way catalysis. *Catal. Today.,* **1999**, 50, 285.

11. Zheng, Y.; Mao, D.; Sun, S. and Fu, G. CO oxidation on CuO/CeO_2 catalyst prepared by solvothermal synthesis: influence of catalyst activation temperature *J. Nanopart. Res.,* **2015**, 17, 471 1-12.

12. Yang, W.; Li, D.; Xu, D. and Wang, X. Effect of CeO_2 preparation method and Cu loading on CuO/CeO_2 catalysts for methane combustion. *Nat. Gas Chem.,* **2009,** 18, 4, 458-466.

13. Tang, X.; Zhang, B.; Li, Y.; Xu, Y.; Xin, Q. and Shen, W. CuO/CeO_2 catalysts: Redox features and catalytic behaviors. *Appl Catal. A.,* **2005**, 288, 116–125.

14. Cui, S.; Yang, D.; He, S.; Song, J.; Huang, W. and Chen, F. Effect of CuO/CeO_2 Catalyst on Methane Combustion. *J Chin. Rare Earth Soc.,* **2004**, 22, 605-608.

15. Bello, A.; Dodoo-Arhin, D.; Makgopa, K.; Fabiane, M. and Manyala, N. Surfactant assisted synthesis of copper oxide (CuO) leaf-like nanostructures for electrochemical applications. *J. Mater. Sci.,* **2014**, 4, 64-73.

16. Hossain, S.T.; Almesned, Y.; Zhang, K.; Zell, E.; Bernard, D.; Balaz, S.; and Wang, R. Support Structure Effect on CO Oxidation: a comparative study on SiO_2 nanospheres and CeO_2 nanorods supported CuO_x catalysts. *Appl. Surf. Sci.,* **2018**. 428, 598-608.

17. Djinović, P.; Batista, J. and Pintar, A. Calcination temperature and CuO loading dependence on CuO-CeO$_2$ catalyst activity for water-gas shift reaction. *Applied Catalysis A*., **2008,** 347, 1, 23-33.

18. Liu, L.; Yao, Z.; Deng, Y.; Gao, F.; Liu, B. and Dong, L. Morphology and crystal-plane effects of nanoscale ceria on the activity of CuO/CeO$_2$ for NO reduction by CO. *Chem. Cat. Chem.* **2011**, 3, 978 – 989.

19. Lin, Y.; Wu Z.; Wen J.; Poeppelmeier, R. and Marks, D. Imaging the atomic surface structures of CeO$_2$ nanoparticles. *Nano Lett.,* **2013**, 14, 191–196.

20. Fotopoulos, A. One pot synthesis and characterization of ultrafine CeO$_2$ and Cu/CeO$_2$ nanoparticles: application for low temperature CO Oxidation, *J. Nanosci. Nanotechnol.* **2011**, 11, 8593–8598.

21. Mock, S.; Zell, E.; Hossain, S.T. and Wang, R.; Effect of reduction treatment on CO oxidation in CeO$_2$ nanorods supported CuO$_x$ catalysts. *Chem.Cat.Chem.*, **2017**,10,1, 311-319.

22. Lee, Y.; He, G.; Akey, A.; Si, R.; Flytzani-Stephanopoulos, M. and Herman, I. Raman analysis of mode softening in nanoparticle CeO$_{2-\delta}$ and Au-CeO$_{2-\delta}$ during CO oxidation *J. Am. Chem. Soc.,* **2011**, 133, 12952–12955.

23. Wang, X.; Rodriguez, J.; Hanson, J.; Gamarra, D.; Martínez-Arias, A. and Fernández-García, M. Unusual physical and chemical properties of Cu in Ce$_{1-x}$Cu$_x$O$_2$ oxides. *J. Phys. Chem. B.,* **2005**, 109, 19595–19603.

24. Chen, S.; Li, L.; Hu, W.; Huang, X.; Li, Q.; Xu, Y.; Zuo, Y. and Li, G. Anchoring high-concentration oxygen vacancies at interfaces of CeO$_{2-x}$/Cu toward enhanced

activity for preferential CO oxidation. *ACS Appl. Mater. Interfaces,* **2015**, 7, 22999–23007.

25. De Leitenburg C.; Trovarelli, A.; Zamar, F.; Maschio, S.; Dolcetti, G. and Llorca, J. A novel and simple route to catalysts with a high oxygen storage capacity: the direct room-temperature synthesis of CeO_2–ZrO_2 solid solutions. *J. Chem. Soc. Chem. Commun.,* **1995**, 0, 2181-2182.

26. Fornasiero, P.; Di Monte, R.; Rao, G.; Kaspar, L.; Meriani, Trovarelli, A. and Graziani, M. Rh-loaded CeO_2-ZrO_2 solid-solutions as highly efficient oxygen exchangers: dependence of the reduction behavior and the oxygen storage capacity on the structural-properties. *J. Catal.,* **1995**, 151, 168-177.

27. Wang, R.and Dangerfield, R.; Seed-mediated synthesis of shape-controlled CeO_2 nanocrystals. *RSC Adv.,* **2014**, 4, 7, 3615-3620.

28. Liu, W. and Flytzani-Stephanopoulos, M. Transition metal-promoted oxidation catalysis by fluorite oxides: a study of CO oxidation over Cu-CeO_2. *J. Chem. Eng.,* **1996**, 64, 283-294.

29. Trovarelli, A. Catalytic properties of ceria and CeO_2-containing materials. *Catal. Rev. Sci. Eng.,* **1996**, 38, 439-520.

30. Yang, Q.; Fu, X.; Jia, C.; Ma, C.; Wang, X.; Zeng, J.; Si, R.; Zhang, Y. and Yan, C. Structural determination of catalytically active subnanometer iron oxide clusters *ACS Catal.,* **2016**, 6, 3072−3082.

31. Zabilskiy, M.; Djinović, P.; Tchernychova, T.; Tkachenko, O.; Kustov, L. and Pintar, A. Nanoshaped CuO/CeO_2 materials: effect of the exposed ceria surfaces on catalytic activity in N_2O decomposition reaction. *ACS Catal.,* **2015**, 5, 5357–5365.

32. Laachir, A.; Perrichon, V.; Badri, A.; Lamotte, J.; Catherine, E.; Lavalley J.C.; Fallah, E.; Hilaire, L.; Normand, F.; Quemere, E.; Sauvion G.N. and Touret, O. *J. Chem. Soc. Faraday Trans*. **1991,** 87, 1601-1609.

33. Binet, C.; Badri, A. and Lavalley, J.C. Spectroscopic characterization of the reduction of ceria from electronic transitions of intrinsic point defects. J. Phys. Chem., 1994, 98, 6392–6398.

34. Shen, W.; Mao, D.; Luo, Z. and Yu, J. CO oxidation on mesoporous SBA-15 supported $CuO–CeO_2$ catalyst prepared by a surfactant-assisted impregnation method. *RSC. Adv.,* **2017**, 7, 27689-27698.

35. Zheng, Y.; Mao, D.; Sun, S. and Fu, G. CO oxidation on CuO/CeO_2 catalyst prepared by solvothermal synthesis: influence of catalyst activation temperature *J. Nanopart. Res.,* **2015**, 17, 471 1-12.

36. Li, J.; Zhu, P.; Zuo, S.; Huang, Q. and Zhou, R. Influence of Mn doping on the performance of $CuO-CeO_2$ catalysts for selective oxidation of CO in hydrogen-rich streams. *Appl. Catal. A.,* **2010**, 381, 261–266.

37. Wang, X.; Rodriguez, J. A.; Hanson, J. C.; Gamarra, D.; Martinez-Arias, A. and Fernandez-Garcia, A. M. In situ studies of the active sites for the water gas shift reaction over $Cu−CeO_2$ catalysts: Complex interaction between metallic copper and oxygen vacancies of ceria. *J. Phys. Chem. B.,* **2006**, 110, 428–434.

38. Wang, X. Q.; Hanson, J. C.; Liu, G.; Rodriguez, J. A.; Iglesias-Juez, A. and Fernandez-Garcıa, M. The behavior of mixed-metal oxides: physical and chemical properties of bulk $Ce_{1−x}Tb_xO_2$ and nanoparticles of $Ce_{1−x}Tb_xO_y$. *J. Chem. Phys.,* **2004**, 121, 5434.

39. Wang, X.; Rodriguez, J. A.; Hanson, J. C.; Gamarra, D.; Fernandez Garcia, M. and Martinez-Arias, A. Unusual physical and chemical properties of Cu in $Ce_{1-x}Cu_xO_2$ Oxides. *J. Phys. Chem. B.,* **2005**, 109, 19595.

40. Sayle. T.; Parker, C. and Catlow, A. The role of oxygen vacancies on ceria surfaces in the oxidation of carbon monoxide. *Surf Sci.,* **1994**, 316, 329-336.

41. Tasker, P.W. The stability of ionic crystal surfaces. *J. Phys. C: Solid State Phys.* **1979**, 12, 4977.

42. Bertaut, F. *Comp. Rendu.,* **1958**, 246, 3447.

43. Si, R. and Flytzani-Stephanopoulos, M. *Angew. Chem. Int. Ed*. **2008**, 47, 2884– 2887.

44. Holgado, J.P.; Alvarez, R. and Munuera, G. Study of CeO_2 XPS spectra by factor analysis: reduction of CeO_2. *Appl Surf Sci*., **2000,** 161, 3 and 4, 301-315.

45. Avgouropoulos, G.; Ioannides, T. Effect of synthesis parameters on catalytic properties of CuO-CeO_2. *Appl. Catal. B Environ.*, **2006**, 67, 1-11.

46. Hu, C.; Zhu, Q.; Chen, L. and Wu, R. CuO–CeO_2 binary oxide nanoplates: Synthesis, characterization, and catalytic performance for benzene oxidation. *Mater. Res. Bull.,* **2009**, 44: 2174–2180.

47. Sun, X.; Gong, C.; Lv, G.; Bin, F. and Song, C. Effect of Ce/Zr molar ratio on the performance of Cu–Cex–Zr_{1-x}/TiO_2 catalyst for selective catalytic reduction of NO_x with NH_3 in diesel exhaust. *Mater. Res. Bull.,* **2014**, 60, 341–347

48. Zhou, K.; Wang, X.; Sun, X.; Peng, Q. and Li, Y. Enhanced catalytic activity of ceria nanorods from well-defined reactive crystal planes. *J. Catal.,* **2005**, 229, 206–212.

49. Luo, M. F.; Zhong, Y. J.; Yuan, X. X. and Zheng, X. M. *Appl. Catal. A* **1997**, 162, 121–131.

50. Guo, M.; Lu, J.; Wu, Y.; Wang, Y. and Luo, M. *Langmuir,* **2011**, 27, 3872–3877.

51. Lee, Y.; He,G.; Akey, A.J.; Si, R. Flytzani-Stephanopoulos, M. and Herman, I. P. *J. Am. Chem. Soc.,* **2011**, 133, 12952–12955.

52. Shen, W.; Mao, D.; Luo, Z. and Yu, J. CO oxidation on mesoporous SBA-15 supported CuO–CeO2 catalyst prepared by a surfactant-assisted impregnation method. *RSC. Adv.,* **2017**, 7, 27689-27698.

53. Zheng, Y.; Mao, D.; Sun, S. and Fu, G. CO oxidation on CuO/CeO_2 catalyst prepared by solvothermal synthesis: influence of catalyst activation temperature *J. Nanopart. Res.,* **2015**, 17, 471 1-12.

54. Li, J.; Zhu, P.; Zuo, S.; Huang, Q. and Zhou, R. Influence of Mn doping on the performance of $CuO-CeO_2$ catalysts for selective oxidation of CO in hydrogen-rich streams. *Appl. Catal. A.,* **2010**, 381, 261–266.

Chapter 5: Facile Synthesis and Characterization of Bimetal Oxides Fe-CuO/CeO$_2$, Mn-CuO/CeO$_2$ and Ni-CuO/CeO $_2$and Bimetallic Catalyst Ag-CuO$_x$/CeO$_2$ nanorods.

The results presented in this chapter focus on synthesizing and characterizing various bimetal oxide and bimetallic nano-catalysts using shape-controlled CeO$_2$ supports. The synthesis was performed using a wet impregnation method and the supports were synthesized using the hydrothermal method, as stated in earlier chapters. There is limited research conducted on shape-controlled supports used in bimetal oxides and bimetallic nano-catalyst systems. No support or supports like alumino-silicate are used, which are inactive and do not contribute to lowering reduction temperatures or increasing hydrogen consumption and CO conversion. CeO$_2$ nanorods, an active support, were chosen because of its outstanding ability to contribute to these catalytic activities.

5.1. Introduction

Single metal nano-catalysts, such as Pd, Pt, Rh and Ru can be used for the reduction of harmful emissions from manufacturing and transportation fields. These catalysts are selective and are less effective due to a shortened life span.[1] Unique quantum mechanical properties occur on the nanoscale therefore, the bimetal oxides and bimetallic nanomaterials are extremely effective as catalysts and can be used in other fields of chemical industry.[2,3,4,5] An example of the synergy between nanoparticles is found in a study done by Rana et al, on Pd–Au nano bimetallic materials. Rana showed that catalytic activities increased in the bimetallic system compared to the monometallic nano-catalysts towards the oxidation of CO, alcohols and C–H bonds, and in the synthesis of H$_2$O$_2$ from H$_2$ and O$_2$.[6,7,8] In addition, there are disadvantages that cannot be overcome using

unsupported precious metal catalysts. The catalyst requires a support system in order to be reusable. Therefore, using CeO_2 nanorods as an active support not only lends to continued use but, the redox properties of CeO_2 found in earlier chapters, aids in increased catalytic efficiencies.[9,10,11] Take for example, in a work done by Nagy et al, Au–Ag nanoparticles supported SiO_2, an inactive support, were prepared by the adsorption of bimetallic colloids.[12] In the study by Nagy, successive heat treatments were performed and after a reduction the sample was deactivated. Nagy was able to show that the Ag23/Au77 nano-catalyst supported on SiO_2 decreased CO conversion temperatures to 125 °C. In a study by Mirzaei et al, they showed 5Ni/10CoMgO catalysts provided active and stable catalytic performance.[13] In their research, the 5Ni/10CoMgO H_2-TPR profiles had two main peaks at around 350–400 °C and a broad peak at above 500 °C. In addition, the BET surface areas for various wt.% of Ni-Co were documented in a range of 51.42-68.88 m^2/g.

Typical methods in synthesizing bimetallic nano-catalysts may constitute of a few dozen to hundreds of atoms. However, there are some obstacles arise in traditional synthetic routes. For example, small specific surface areas, low adsorption abilities, and homogenous surface layer of bimetallic catalysts are common disadvantage.[14] Figure 5.1 (a-c) shows three well-known configurations for bimetallic catalysts. Figure 5.1 (b) presents the core-shell bimetallic nanoparticle, where the outer shell consists of only one element and the inner core is the second element. Typically, demonstrated in this type is a mixture of bimetallic and monometallic properties. Then another configuration shown in Figure 5.1(c), is the cluster in cluster. This is where a group of one atom is located and

the second atom is also grouped in clusters. Figure 5.1 (a) depicts the purely bimetallic nanoparticles and this type is colloquial known as an alloy.

Transition metals like Cu, Ag, Fe, Mn and Ni are less-expensive and readily available, compared to the noble metals which are typical catalysts. Therefore, in this portion I will present a facile synthesis and examine a systematic study on bimetal oxides and a bimetallic nano-catalyst impregnated onto active shape-controlled CeO_2 nanorods. CeO_2 nanorods support material possess high surface area, which enhanced the catalytic activity as well aids in the CO oxidation at lower reduction temperatures.
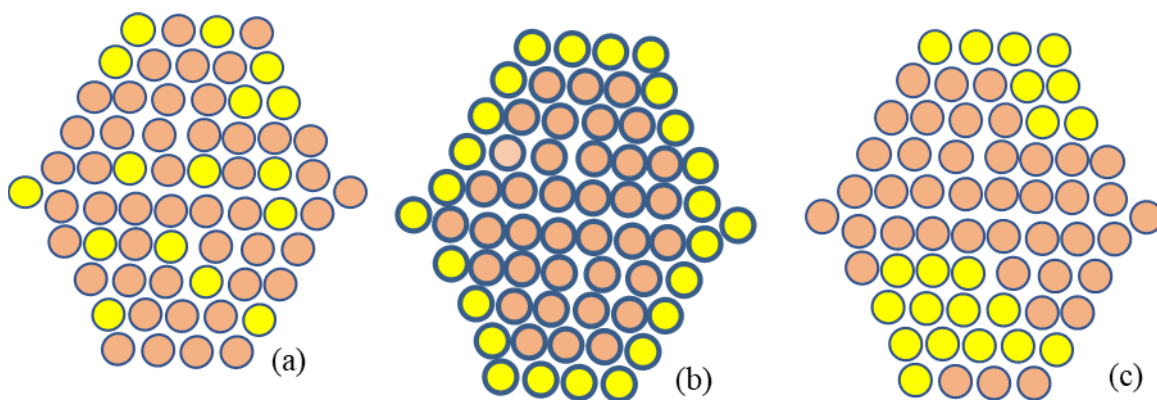
Figure 5.1. Schematic of the bimetallic nanoparticles configuration (a) alloy, (b) core-shell, and (c) cluster in cluster.

5.2. Experimental

5.2.1. Catalyst and Support Synthesis

CeO$_2$ nanorods were synthesized using hydrothermal synthesis method, at 90 °C and 48 hr dwell time as described in Chapter 3. All nano-catalysts were synthesized using the same parameters for all samples: mixed in small beakers with ~ 40 ml DI water, 5 wt.% of each transition metal nitrate (Ag, Fe, Mn and Ni) and the other 5 wt.% was Cu, using copper nitrate for all samples. Next, concentrated NH_4OH was delivered dropwise until the solution fully reacted (dark blue color). Then the samples were heated at ~120 ^{o}C

with constant stirring for approximately 30 min and two to three drops of H_6N_2O was added to reduce the oxides to their zero oxidation states. Finally, continued stirring with heat for an additional 15 min to ensure the reduction was complete. The samples were all filtered and dried at 60 ^{o}C 12 h. Wet incipient impregnation of 90 wt.% CeO_2 nanorods were added to each 10 wt.% bimetal oxides and bimetallic system, each containing 5 wt.% of the two metals, one being Cu. No high temperature calcination was conducted that could alter the morphology or surface area and surfactants were not used that could hinder catalytic activities.

All techniques for characterization of the catalysts and catalytic activity, such as; X-ray diffraction (XRD), Raman spectroscopy, X-ray photoelectron spectroscopy (XPS), transmission electron microscopy (TEM), BET surface area measurement, temperature programmed reduction (TPR), temperature programmed oxidation (TPO), temperature programmed desorption (TPD), pulse chemisorption to calculate oxygen storage capacity (OSC), and CO oxidation can be found in Chapter 2.

2.2. Results and Discussion

5.2.2. Characterization of the Bimetal Oxides and Bimetallic Nano-catalysts.

5.2.2.1. XRD and BET

In Figure 5.2, seen is the X-ray diffraction (XRD) data for all the as-synthesized supported bimetal oxides nano-catalysts: Ni-CuO/CeO_2, Mn-CuO/CeO_2, Fe-CuO/CeO_2 and the bimetallic nano-catalyst Ag-CuO$_x$/CeO_2 samples. All CeO_2 reflections were indexed and correspond to the pure cubic phase of CeO_2 fluorite structure (JCPDS 81-0792). Figure 5.1 also showed two weak typical reflections at 35.54° and 38.72° (JCPDS, CuO file No. 80-1917) corresponding to CuO.[15] Shown in Figure 5.2, all the samples

showed broadening of the diffraction peaks, which represent small crystallite sizes. Interestingly, when we look at the second metal in the system there are no diffraction peaks pertaining to the second metal except for Ag (silver) sample. This is evidence of the systems creating a type of core-shell configuration and cluster in cluster for the Ag sample. The hypothesis is that the metal reduction potentials determine the end configuration. In this case, the transition metals (Mn:-1.18 eV, Fe:+.-41eV, and Ni:-.25 eV) possess different reduction potentials to (Cu:+.52 eV). This allows the reduction to occur in a sequential order and form a core–shell assignment.[16] A better explanation would be that the (Ni, Fe and Mn) may be attributed to the formation solid solution: Ni-Ce, Fe-Ce and Mn-Ce are possible.[17] Whereas, Ag (Ag:+.80 eV) has a similar reduction potential to Cu and when the reduction potentials are in proximity with one another the metals will reduce at the same time and form the cluster in cluster configuration.[16] The XRD reflections for silver in the Ag-CuO$_x$/CeO$_2$ sample are observed at 27.8˚, 38.1˚, 44.1˚ and 78.1˚ corresponding to (220), (111), (200) and (311), respectively and represent a bimetallic nano-catalyst system. However, the (Ni, Mn and Fe) form a bimetal oxide, where CuO passivates the metal forming core-shell system.

Recall CeO$_2$ nanorods sample has a BET surface area, 56.4 m^2/g. Several of the bimetal oxides and bimetallic nano-catalyst's BET surface area has changed significantly. This may be due to the possible incorporation of the inner constituent of the system with CeO$_2$ lattice. In Table 5.1, the BET surface areas are documented. For Ni-CuO/CeO$_2$ the BET surface area is recorded at 106.68 m^2/g. For Fe-CuO/CeO$_2$ the BET surface area is 71.445 m^2/g. For Mn-CuO/CeO$_2$ the BET surface area is 124.16 m^2/g and For Ag-CuO$_x$/CeO$_2$ the BET surface area is 53.30 m^2/g. When compared to the BET surface

areas of the CuO/CeO$_2$ systems (noted in Chapter 4), the surface area increases for all samples except the Ag-CuO$_x$ sample. This information provides substantiating evidence for the hypothesis that the bimetal oxide nano-catalysts have a core-shell configuration and/or a solid solution formation with CeO$_2$, and therefore increasing the surface area dramatically.

Table 5.1. BET Surface area CeO$_2$ nanorods supported bimetal oxides and bimetallic catalysts compared to CeO$_2$ nanorods.

BET Surface area	m^2/g
CeO$_2$ nanorods	56.4
CuO/CeO$_2$	70.1
Fe-CuO/CeO$_2$	71.45
Ag-CuO$_x$/CeO$_2$	53.30
Mn-CuO/CeO$_2$	124.16
Ni-CuO/CeO$_2$	106.68
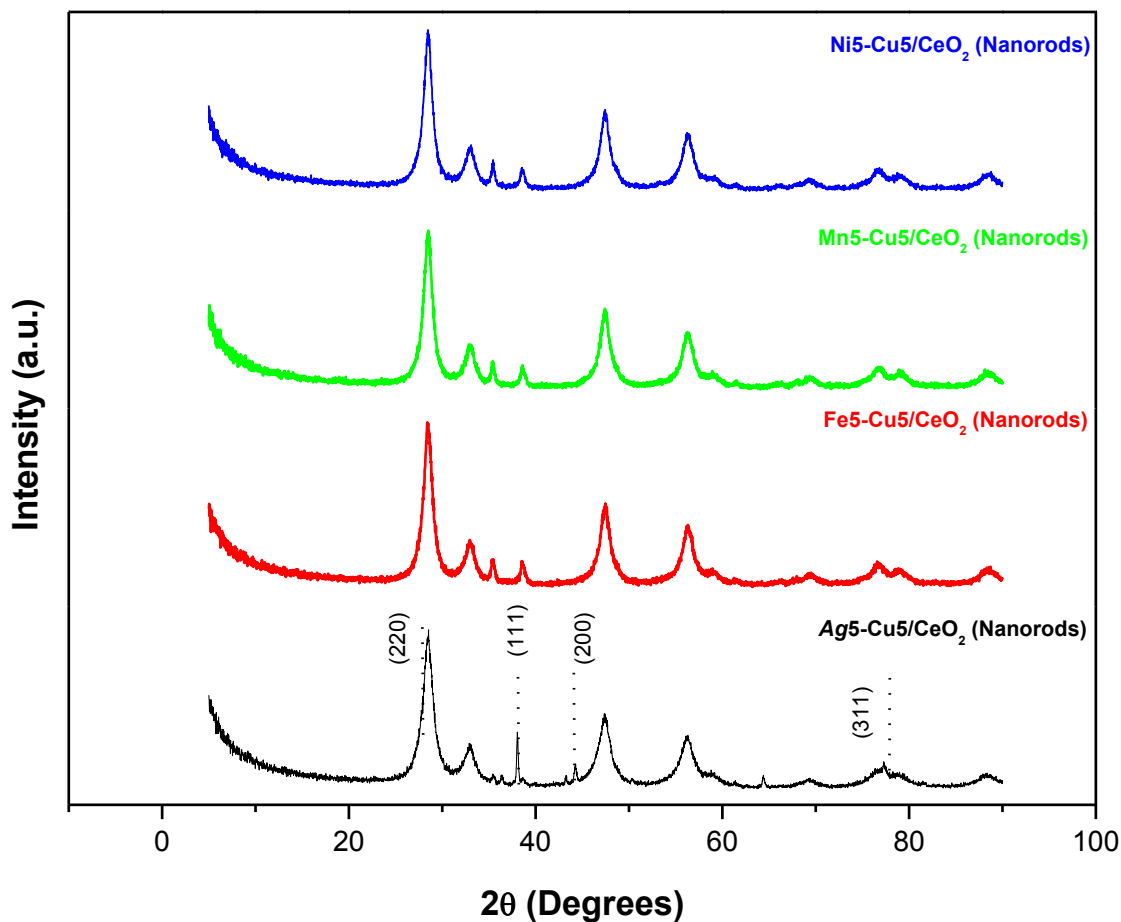
Figure 5.2. XRD patterns for Ni-CuO/CeO₂, Mn-CuO/CeO₂ Fe-CuO/CeO₂ and Ag-CuOₓ/CeO₂ samples.

5.2.2.2. H₂-TPR

It is well established that surface lattice oxygen of CeO_2 contributes significantly in CO oxidation reaction. For pure ceria the first reduction peak is representative of surface oxygen and the second reduction peak correlates to bulk oxygen.[18] Recall, that these peaks were at ~467°C and 826 °C. Therefore, H_2-TPR was performed to demonstrate the correlation with the surface size and catalytic activities. Figure 5.3 shows the H_2-TPR profile Ni-CuO/CeO₂, Mn-CuO/CeO₂ Fe-CuO/CeO₂ and Ag-CuOₓ/CeO₂ all uncalcinated. The two-step reduction profile shows that all reduction temperatures are significantly below pure CeO_2 nanorods' reduction temperatures.

159

The high surface area seems to be a major contributing factor in the increased hydrogen consumption.[19] Recall, that the BET surface area increased significantly for Ni-CuO/CeO$_2$ and Mn-CuO/CeO$_2$, these two catalysts had the highest H$_2$ consumption, Mn-CuO/CeO$_2$ was approximately 4.88 mmol/g and Ni-CuO/CeO$_2$ samples were at 11.34 mmol/g. Documented in Table 5.2 are the total consumptions of the bimetal oxides and bimetallic nano-catalyst systems, they show a large increase compared to the CuO/CeO$_2$ and CuO$_x$/CeO$_2$ samples. This increase in hydrogen consumption may be due to the increased surface area and possibly the solid solution.[20] Hence, small bimetallic particles are formed, resulting in improved reducibility. The samples with the core–shell type arrangement presented synergetic activity increase.
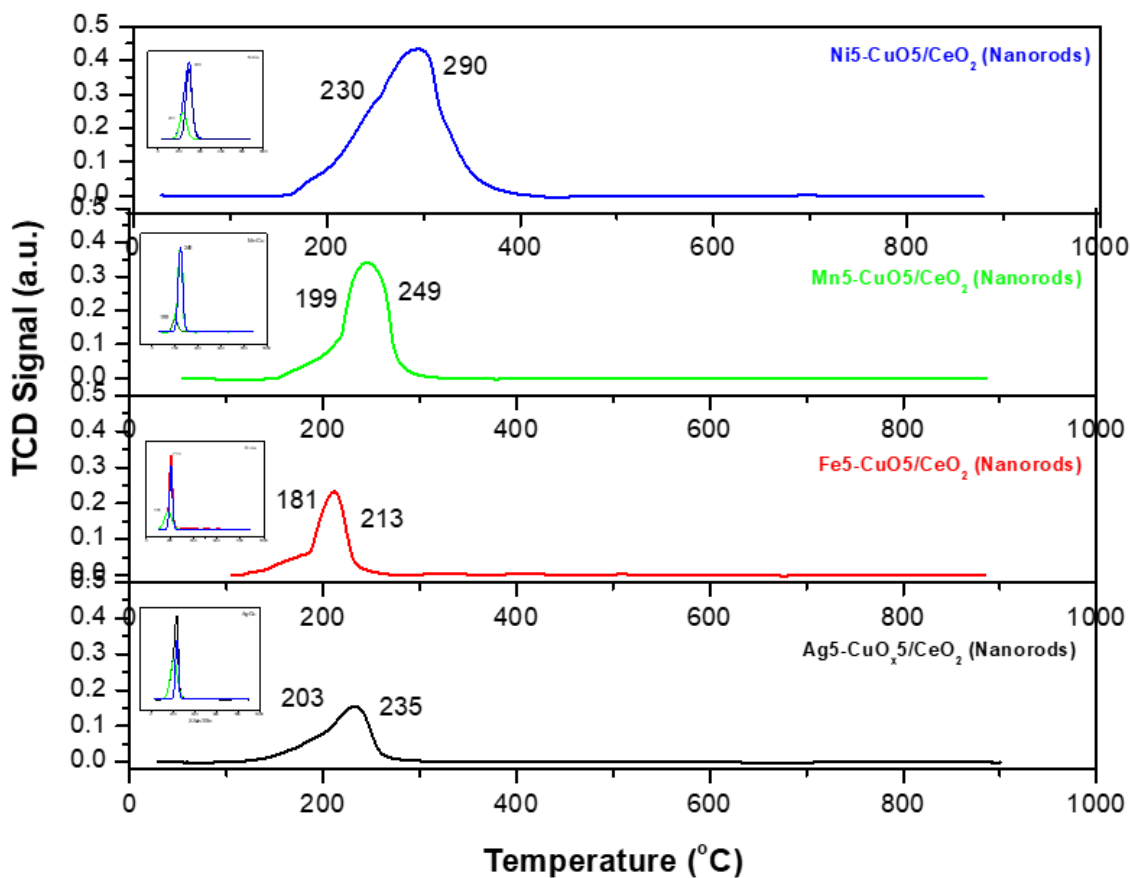
Figure 5.3. H$_2$-TPR reduction temperature profiles.

160

Table 5.2. Hydrogen consumption calculation in mmol/g and µmol/g.

Sample	Temp (°C)	PA	H_2 (mmol/g)
Ag5-Cu5	232	9.8	2.69
Fe5-CuO5	211	9.8	2.62
Mn5-CuO5	244	18.3	4.88
Ni5-CuO5	292	42.1	11.34

5.2.2.3. CO Oxidation

CO oxidation of heterogeneous catalysts are greatly determined by the active constituents within the system.[21,22] Figure 5.4 shows the CO conversion compared to the reaction temperature. The temperatures for T_{50} and T_{100} of each sample are tabulated in Table 5.3. It is noted, that the bimetal oxides and bimetallic catalyst have an affinity toward CO oxidation, as indicated by the T_{50} and T_{100} values. At 50% conversion Ag-CuO_x has a higher (T_{50}:162 °C) reaction temperature when compared to the other nano-catalysts and supports systems in this study; Fe-CuO system (T_{50}:125 °C), Ni-CuO (T_{50}:125 °C) and Mn-CuO (T_{50}:142 °C). At 50% conversion these temperatures are significantly lower than pure ceria which may be associated with the oxygen mobility of the CeO_2 support which is greatly improved with the bimetal oxides and bimetallic systems.[23]
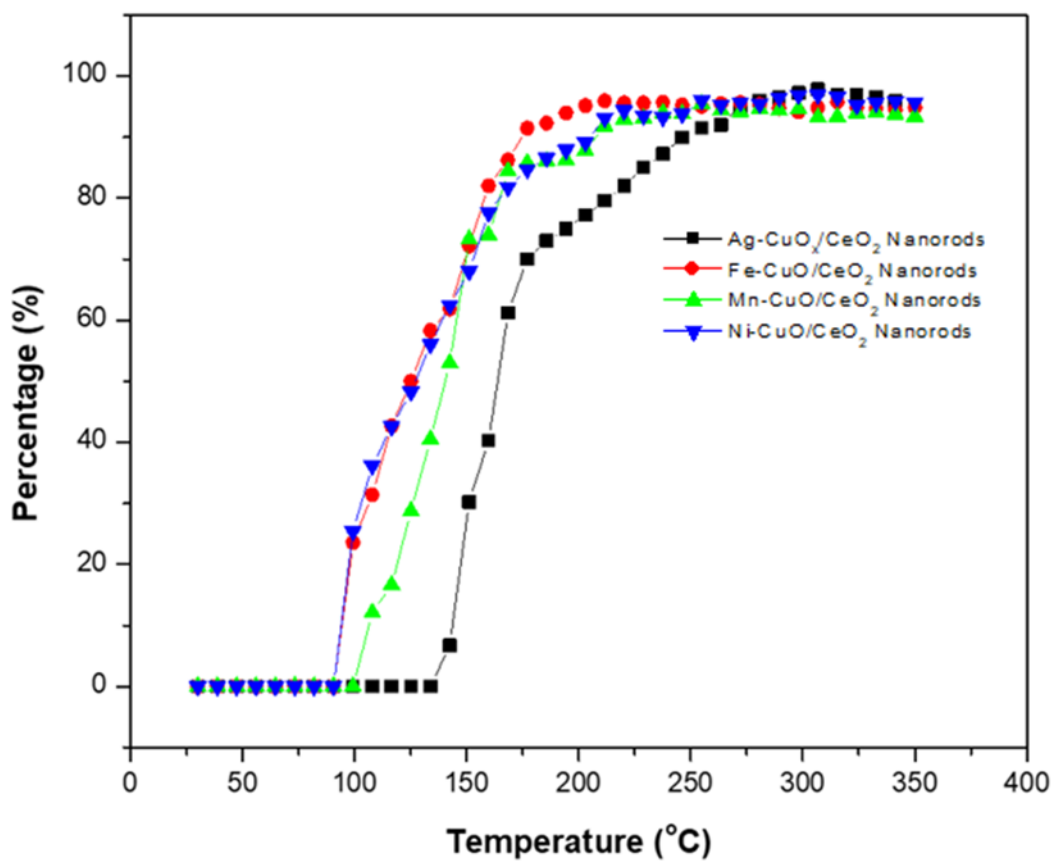
Figure 5.4. CO oxidation data for Ni-CuO/CeO$_2$, Mn-CuO/CeO$_2$ Fe-CuO/CeO$_2$ and Ag-CuO$_x$/CeO$_2$.

Table 5.3. CO conversion data of the Bimetal oxides and bimetallic nano-catalysts.

Bi Metallic Alloy	10BMNA/90CeO$_2$ Nanorods		
	T_{50} (^{o}C)	Max conversion (%)	T_{max} (^{o}C)
Ag-CuO$_x$	164	95	280
Fe-CuO	125	97	210
Mn-CuO	142	95	218
Ni-CuO	125	96	221

5.2.2.4. XPS

XPS experiments were run by Dr. Balaz, and the XPS was used to determine the composition and the oxidation state of catalyst surface species of samples Ni-CuO/CeO$_2$, Mn-CuO/CeO$_2$ Fe-CuO/CeO$_2$ and Ag-CuO$_x$/CeO$_2$. Figure 5.5 shows seven known peaks that are observed for Ce 3d. Figure 5.5 (d) shows the peak positions for Mn-CuO/CeO$_2$ sample at; u (900.2 eV), u' (905.8 eV), u" (911.9 eV), v (887.1 eV), v' (889.6 eV), v" (893.8 eV) and v''' (903.1 eV). Figure 5.5 (c) shows the peak positions for Fe-CuO/CeO$_2$ u (905.8 eV), u' (906.9 eV), u" (912.3 eV), v (887.3 eV), v' (886.2 eV), v" (893.4 eV), and v''' (903.1 eV). Figure 5.5 (b) shows the peak positions for Ag-CuO$_x$/CeO$_2$ CeO$_2$ u (905.1 eV), u' (906.8 eV), u" (911.2 eV), v (888.4 eV), v' (888.2 eV), v" (893.1 eV), and v''' (902.6 eV). Figure 5.5 (a) shows the peak positions for Ni-CuO/CeO$_2$ CeO$_2$ u (899.9 eV), u' (904.4 eV), u" (910.6 eV), v (886.9 eV), v' (888.4 eV), v" (891.6 eV), and v''' (901.6 eV). Qualitatively the larger u' and v' peaks indicate the sample is superior due to more Ce^{3+} present. The 3d$_{3/2}$ and 3d$_{5/2}$ peaks are represented as u and v, respectively, where peaks u, u", v, v" and v''' are assigned to Ce^{4+} and peaks u' and v' are assigned to Ce^{3+}.[24] Ce^{3+} is known to be a contributing factor involved for improved performance in CO oxidation. The presence of Ce^{3+} is significant in all samples but qualitatively decrease accordingly: Ni-CuO > Mn-CuO > Fe-CuO > Ag-CuO$_x$. The surface elemental XPS data shows key components to the increased catalytic activity.
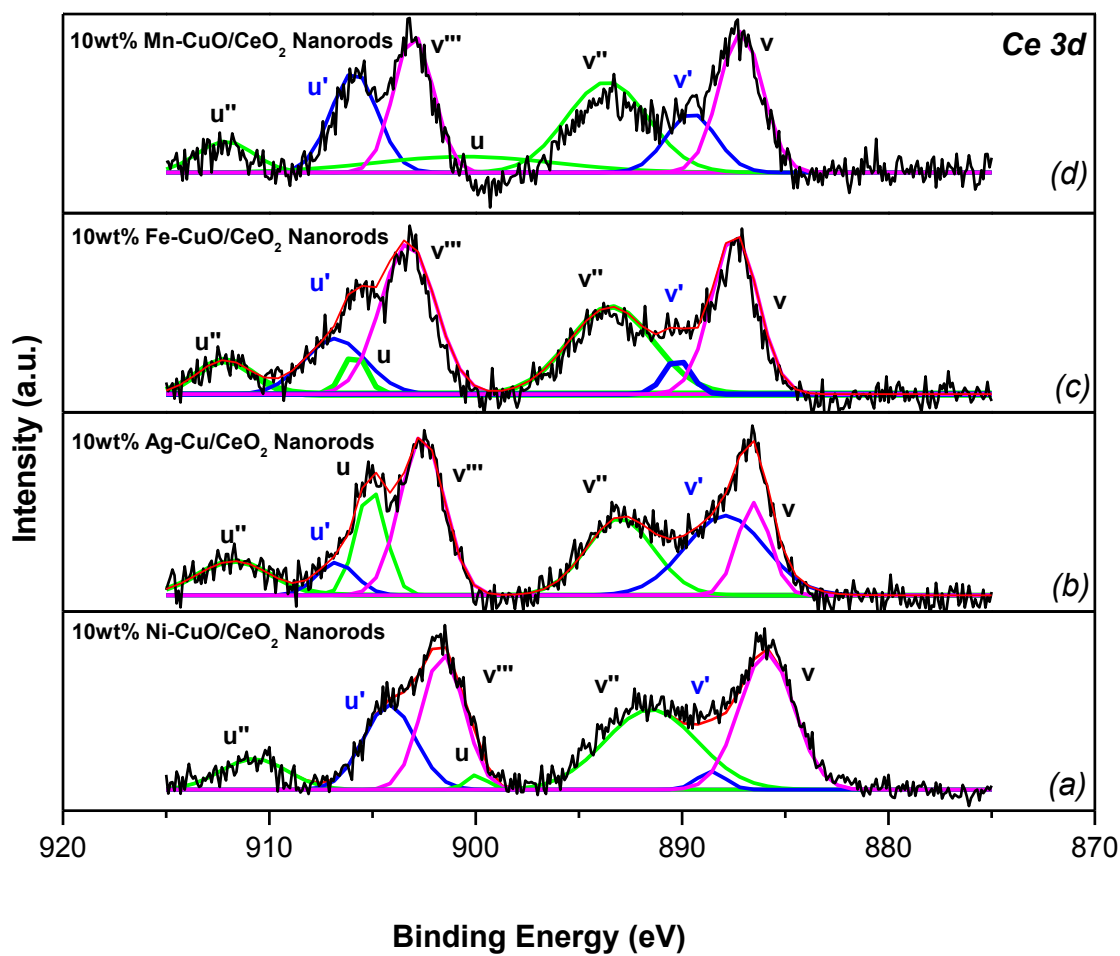
Figure 5.5. (a-d), Ce 3d XPS of Ni-CuO/CeO₂, Mn-CuO/CeO₂ Fe-CuO/CeO₂ and Ag-CuOₓ/CeO₂.

164
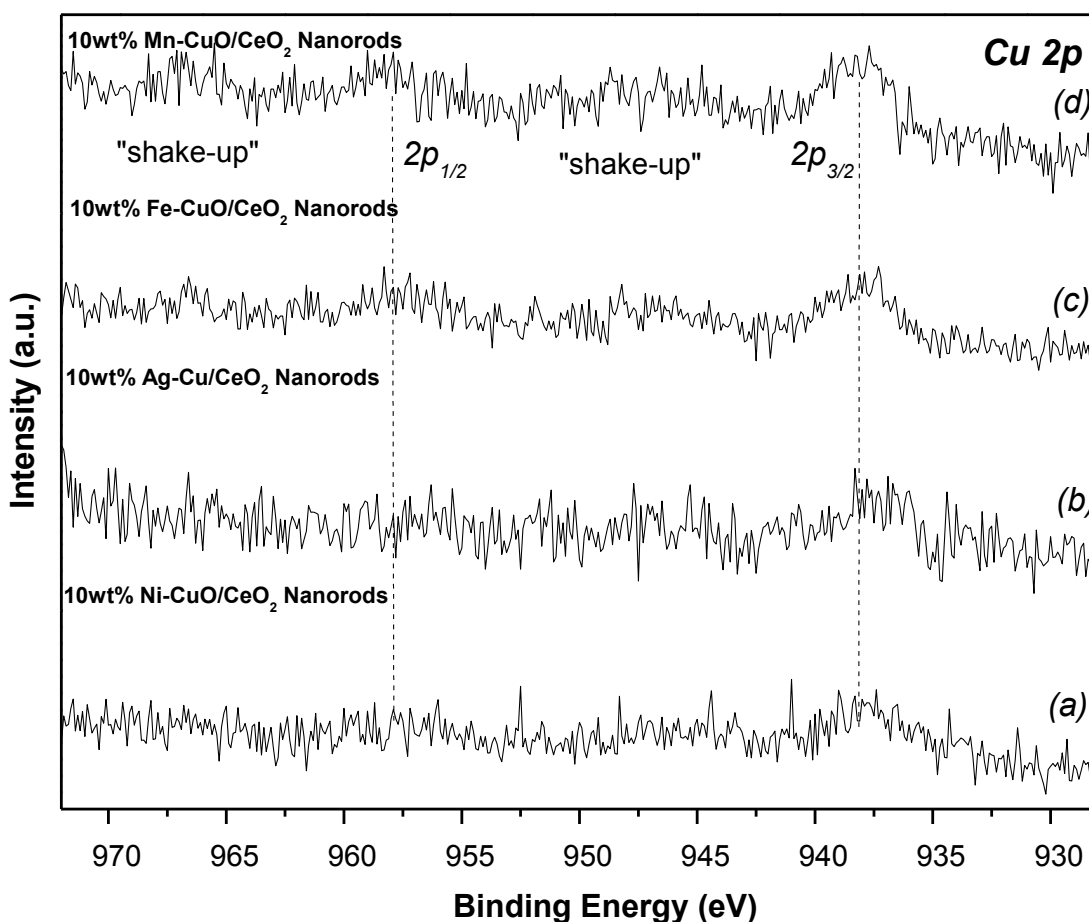
Figure 5.6. (a-d), Cu 2p of XPS of Ni-CuO/CeO₂, Mn-CuO/CeO₂ Fe-CuO/CeO₂ and Ag-CuOₓ/CeO₂.

Cu 2p XPS spectra can be seen in Figure 5.6 (a-d). Observed is the Cu 2p peaks, $2p_{3/2}$ and the $2p_{1/2}$. The $2p_{1/2}$ which represents Cu^{2+} is present for all samples at (958.1 eV).[25] The most notable $2p_{3/2}$ Cu^{+}, which is significant for its role in its ability to have a strong interaction between CeO_2 and copper species, is observed at (938.1 eV) for all samples.[26] There are two typical shake-up peaks found approximately at (943.2–952.5 eV) and (964.4-968.4 eV). Transition metals often times show shake-up peaks. Shake-up peaks can be explained from the interaction that occurs concurrently with the excitation of the outgoing photoelectron and a valence electron, that is excited to a higher-energy level.

Therefore, causing the binding energy of the core electron to get "shaken-up" and decreasing the energy slightly causing a shake-up a satellite feature at a lower binding energy position then the core level position.[27]
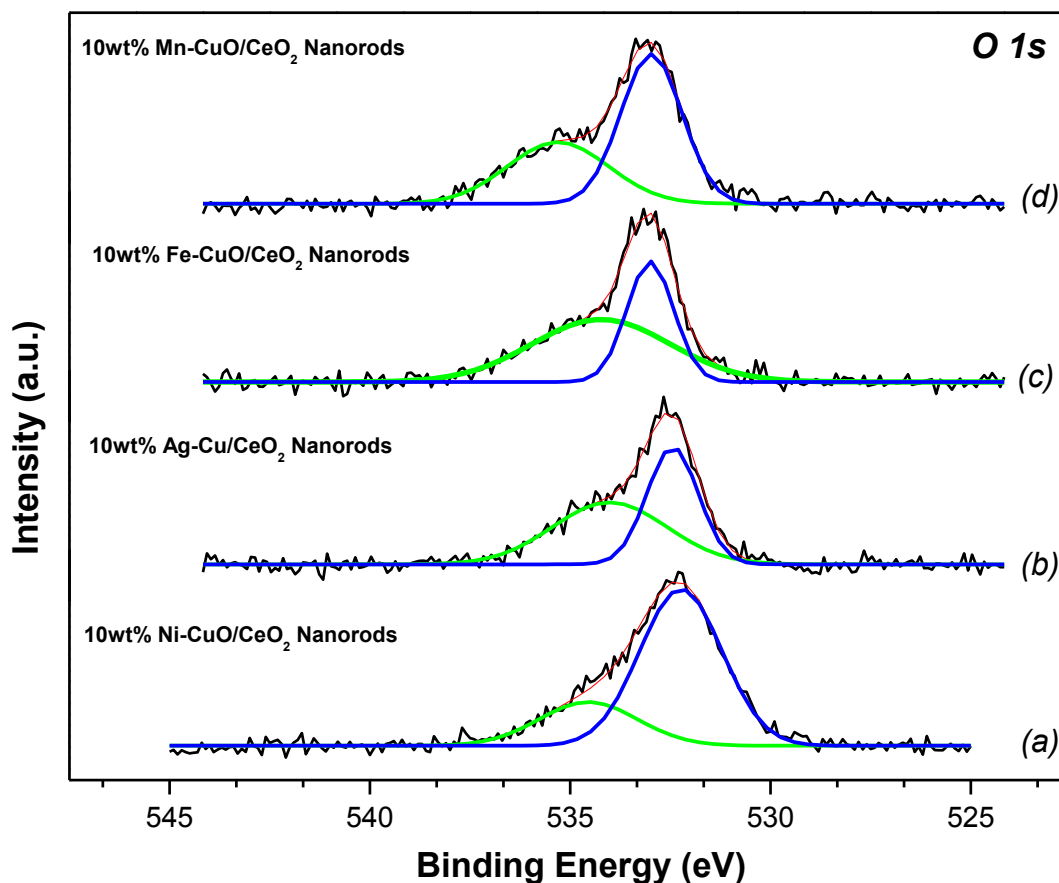
Figure 5.7. (a-d), O 1s of XPS of Ni-CuO/CeO₂, Mn-CuO/CeO₂ Fe-CuO/CeO₂ and Ag-CuOₓ/CeO₂.

Typical O 1s XPS spectrum for bimetal oxides and bimetallic systems have two peaks where the higher energy peak represents the adsorbed oxygen at the surface, denoted as O_{ads} and lower energy peak to represent lattice oxygen of metal oxides, denoted as O_{lat}.[28,29] Figure 5.7 (a-d) shows the lower energy peak at (~533.2 eV) and the higher

energy peak (~534.5 eV) for all samples. This O 1s XPS data shows that Ni-CuO and Mn-CuO samples have qualitatively, more lattice oxygen. This may be due to the increased surface area which aids in the lattice expansion of CeO_2 and increases oxygen vacancy formation. Also, the O 1s peak shows a broadening effect and a shift in binding energy, this broadened and shift to a higher energy can be linked to lattice oxygen formation.[30]
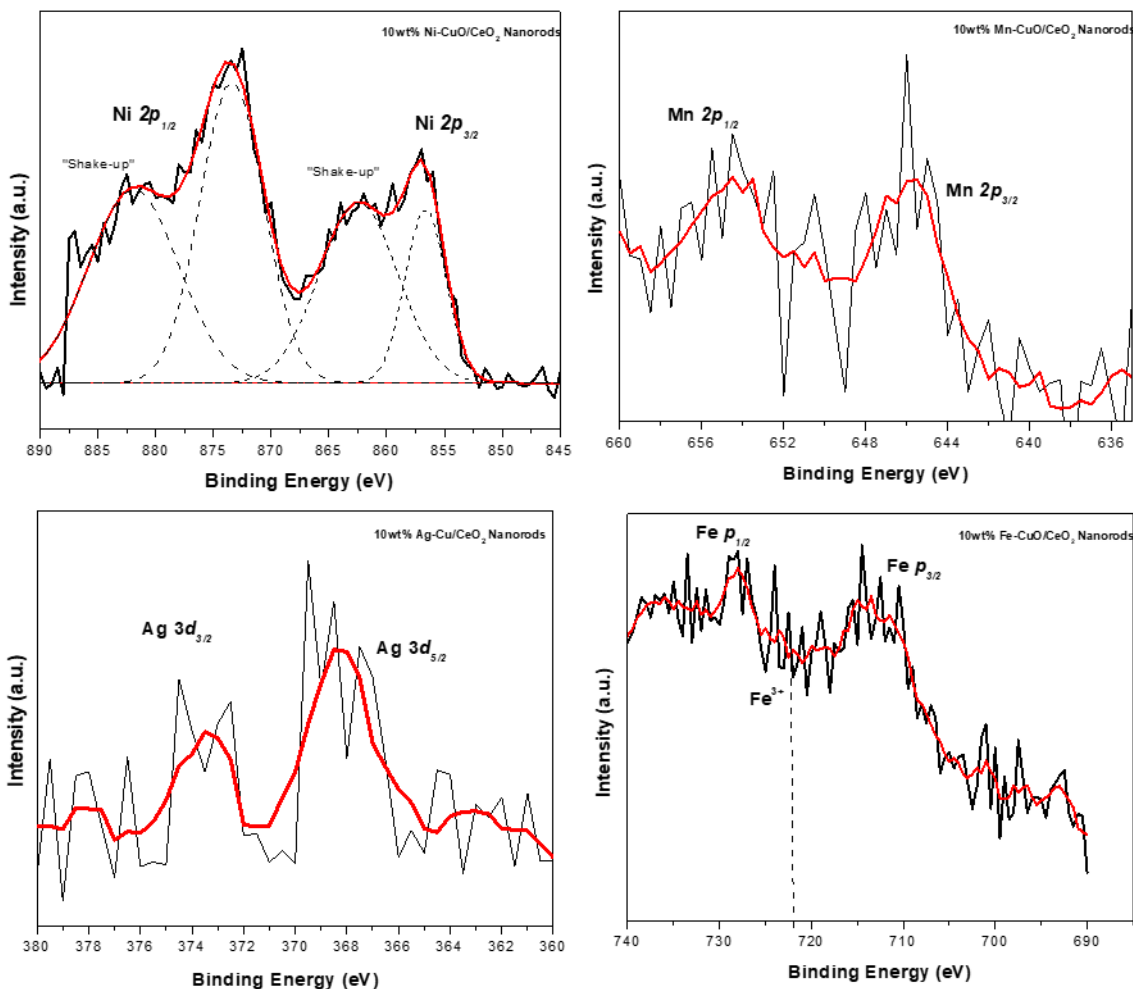
Figure 5.8. XPS (a) Ni-CuO/CeO$_2$, (b) Mn-CuO/CeO$_2$ (c) Fe-CuO/CeO$_2$ and (d) Ag-CuO$_x$/CeO$_2$ nanorods oxidized at 400°C before reduction treatment.

167

XPS spectrum for the metals; Ni, Fe Ag and Mn all have very low intensities on the surface. However, copper is present on the surface of each sample. Figure 5.8, shows the XPS spectrum for the bimetal oxides and bimetallic system, in (a) Ni's $2p_{1/2}$ peak is at (870 eV) and $2p_{3/2}$ is noted at (852 eV). A slight shift in binding energy is noticed and this is due to the lattice expansion of the ceria.[31] Ni and NiO have sophisticated spectra where satellite and core level features are intricate. In Figure 5.6 (b), the Mn $2p_{1/2}$ is located at (653.1 eV) and $2p_{3/2}$ is at (647.2 eV). These peaks coincide with MnO, this may be due to the Mn incorporating as solid solution where Ce–O–Mn is present.[32] In addition, with the addition CuO, there is a significant increase in surface area (124.16 m^2/g) and a lower reduction temperature, 199 ˚C, when compared to a study done by Venkataswamy et al, where reduction temperatures were above 250 ˚C. Venkataswamy's group determined that the incorporation of Mn to ceria would demonstrate a better performance of the catalyst due to larger surface area (>58 m^2/g), higher concentration of surface adsorbed oxygen, enhanced reducibility, and more oxygen vacancy sites.[33] The Fe $p_{1/2}$ and Fe $p_{3/2}$ peaks also coincide with FeO, where Ce-O-Fe solid solution is formed and possibly a core-shell configuration of the bimetal oxides model. Figure 5.6 (c) indicates two very weak peaks for the Ag, the typical $3d_{5/2}$ peak has a binding energy of (368.2 eV) and Ag $3d_{3/2}$ at (373.3 eV). It is unclear why these peaks are almost indistinguishable, but since XPS is a surface analysis, it could mean that the silver sample could have a one of the bimetallic configurations. The XRD analysis indicates that Ag crystals planes are indexed, suggesting the metal is present. In addition, H_2-consumption for Ag-CuO_x/CeO_2 differs significantly from Cu/CeO_2.

5.2.2.5. Energy Dispersion X-ray Spectroscopy (EDS)

Figures 5.9-5.14 shows some of the chemical analysis done using EDS for the bimetal oxides and bimetallic nano-catalysts systems, Ni grids were used in the analysis. Figure 5.8 and 5.9 shows a break-down of the Ag-CuO_x/CeO_2 sample. It is worth noting that at different areas in the sample concertation levels of the chemical make-up are varied. As in Figure 5.9, Ag has a wt.% of 1.3 and Cu has a wt.% of 16.3. However, in Figure 5.10, the wt.% of Ag is 13.4 and the wt.% of Cu is 18.8. Although, only 5 wt.% of each metal was used in the preparation of each sample. Ce totals are 74.1 wt.% and 62.5 wt.% respectively. In Figure 5.10 and Figure 5.11, the Mn elemental analysis is 2.3 wt.% and 1.5 wt.% at different locations on the sample. Figure 5.12 (a) shows the element composition spectrum of Ni-CuO/CeO_2 and 5.12 (b) shows the analysis for the Ni grid and 5.12 (c) shows the breakdown of the composition, where Ni has wt.% of 11.3 and 5.7 wt.% for Cu. The plain Ni grid was analyzed because the sample itself contains nickel. Figure 5.13, shows the EDS elemental analysis for the Fe samples. It can be seen that at different positions the wt.% is very different. A major advantage for using X-ray energy dispersion spectroscopy is it provides a greater depth evaluation regarding chemical composition. EDS depths are microns deep whereas, XPS is on tens of Angstroms. The low-level concentrations are indicative of the actual preparation and supports, where CuO passivates the Fe, Ni and Mn and form a type of core-shell bimetallic nano-catalyst or possibly a cluster in cluster configuration.

```
c:\edax32\genesis\genspc.spc
Label:AB-1_1_100kX_Dark
kV:200.0  X Tilt:0.0  Y Tilt:0.0 Det Type:SUTW+ Res:130 Amp.T:51.2
FS : 644   Lsec : 9                              9-Mar-2018 18:42:50
```
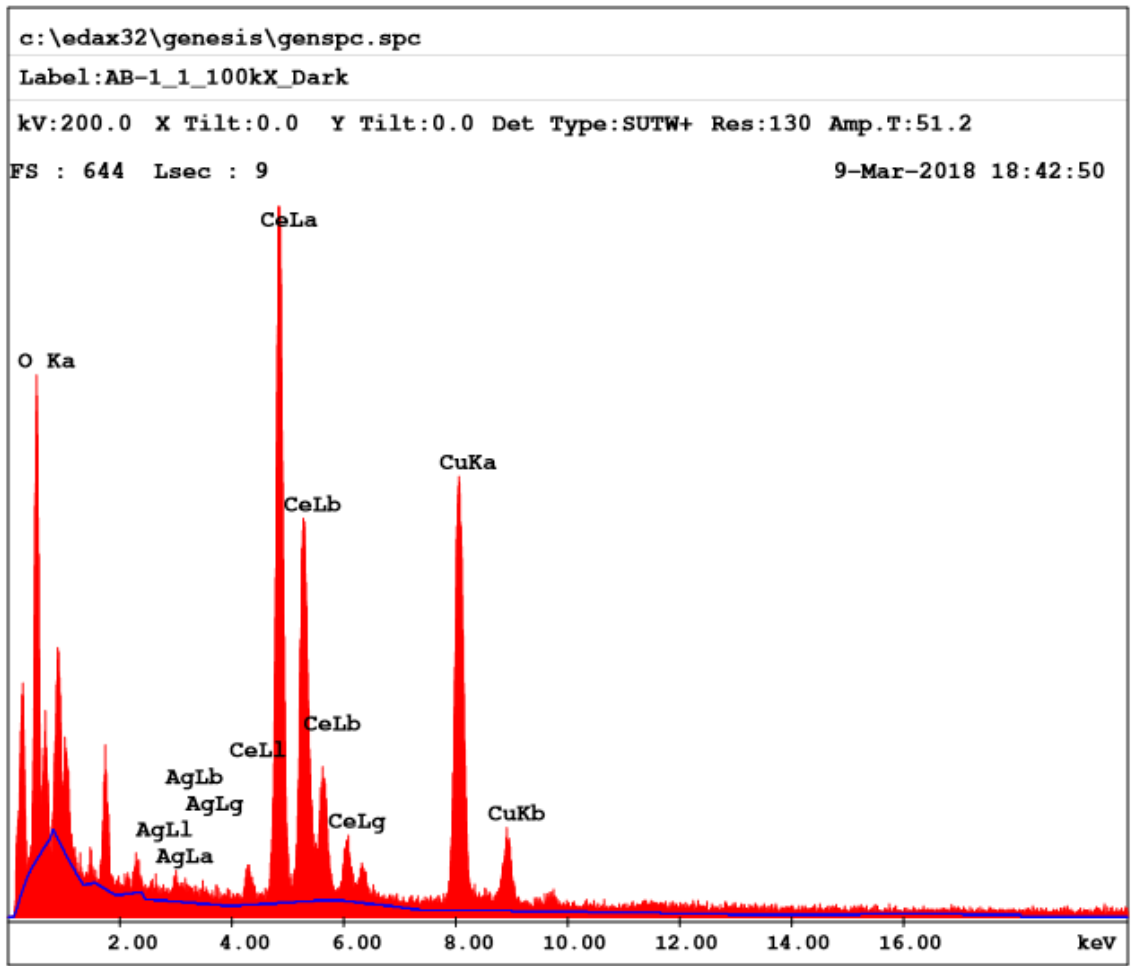


```
Thin Apx
Theoretical KAB, Elements, Model : Zaluzec

Element   Weight %  Atomic %

  O K        8.3      39.4
  AgL        1.3       0.9
  CeL       74.1      40.2
  CuK       16.3      19.5
 Total     100.0     100.0

Element  Net Inte.    Bkgd Inte.   Inte. Error     P/B

  O K     478.46        72.92        1.71         6.56
  AgL      33.79        29.94        9.37         1.13
  CeL    1314.66        32.93        0.92        39.92
  CuK    1030.15        19.89        1.04        51.80
```

Figure 5.9. Energy Dispersion X-ray Spectroscopy (EDS) spectrum of 5Ag-5Cu/CeO$_2$.

```
c:\edax32\genesis\genspc.spc
Label:AB-1_1_100kX_Dark
kV:200.0   X Tilt:0.0   Y Tilt:0.0  Det Type:SUTW+  Res:130  Amp.T:51.2
FS : 349   Lsec : 5                                    9-Mar-2018 18:46:06
```
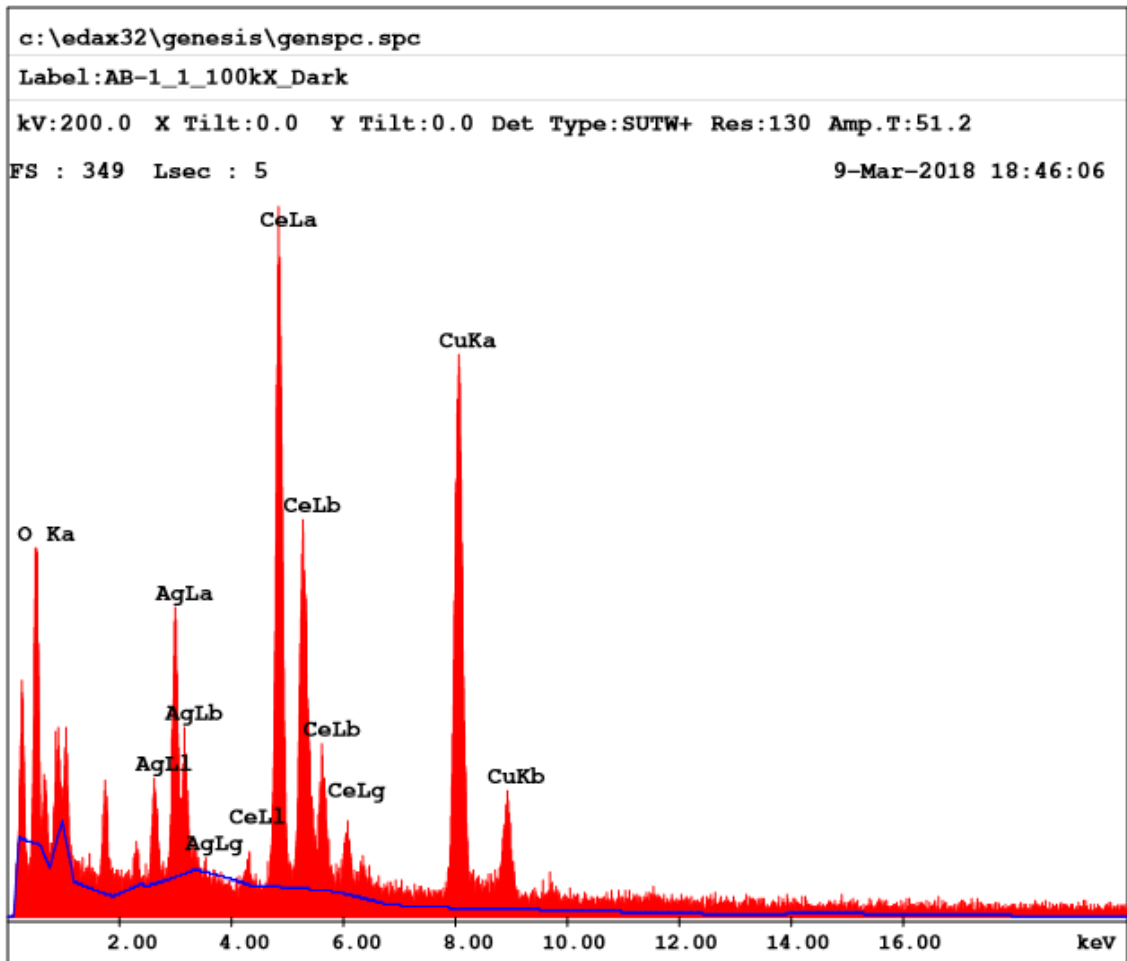
```
Thin Apx
Theoretical KAB, Elements, Model : Zaluzec

Element   Weight %   Atomic %

   O K       5.2       27.3
   AgL      13.4       10.4
   CeL      62.5       37.4
   CuK      18.8       24.8
  Total    100.0      100.0

Element   Net Inte.    Bkgd Inte.    Inte. Error      P/B

   O K      305.14        88.95         3.14         3.43
   AgL      366.10        73.90         2.70         4.95
   CeL     1125.90        67.43         1.38        16.70
   CuK     1207.05        23.62         1.28        51.10
```

Figure 5.10. Energy Dispersion X-ray Spectroscopy (EDS) spectrum of 5 Ag-CuO$_x$/CeO$_2$.

```
c:\edax32\genesis\genspc.spc
Label:AB-1_1_100kX_Dark
kV:200.0  X Tilt:0.0  Y Tilt:0.0 Det Type:SUTW+ Res:130 Amp.T:51.2
FS : 226  Lsec : 2                                9-Mar-2018 16:39:22
```

```
Thin Apx
Theoretical KAB, Elements, Model : Zaluzec

Element   Weight %   Atomic %

  O K       12.2       49.7
  CeL       71.8       33.5
  MnK        2.3        2.7
  CuK       13.7       14.1
 Total     100.0      100.0

Element   Net Inte.   Bkgd Inte.   Inte. Error    P/B

  O K      675.99        97.89        2.55        6.91
  CeL     1224.76        24.56        1.70       49.87
  MnK      166.78        70.26        6.14        2.37
  CuK      833.90        74.01        2.19       11.27
```

Figure 5.11. Energy Dispersion X-ray Spectroscopy (EDS) spectrum of 5Mn-CuO/CeO₂.

```
c:\edax32\genesis\genspc.spc
Label:AB-1_1_100kX_Dark
kV:200.0  X Tilt:0.0  Y Tilt:0.0 Det Type:SUTW+ Res:130 Amp.T:51.2
FS : 502  Lsec : 25                              9-Mar-2018 16:47:25
```
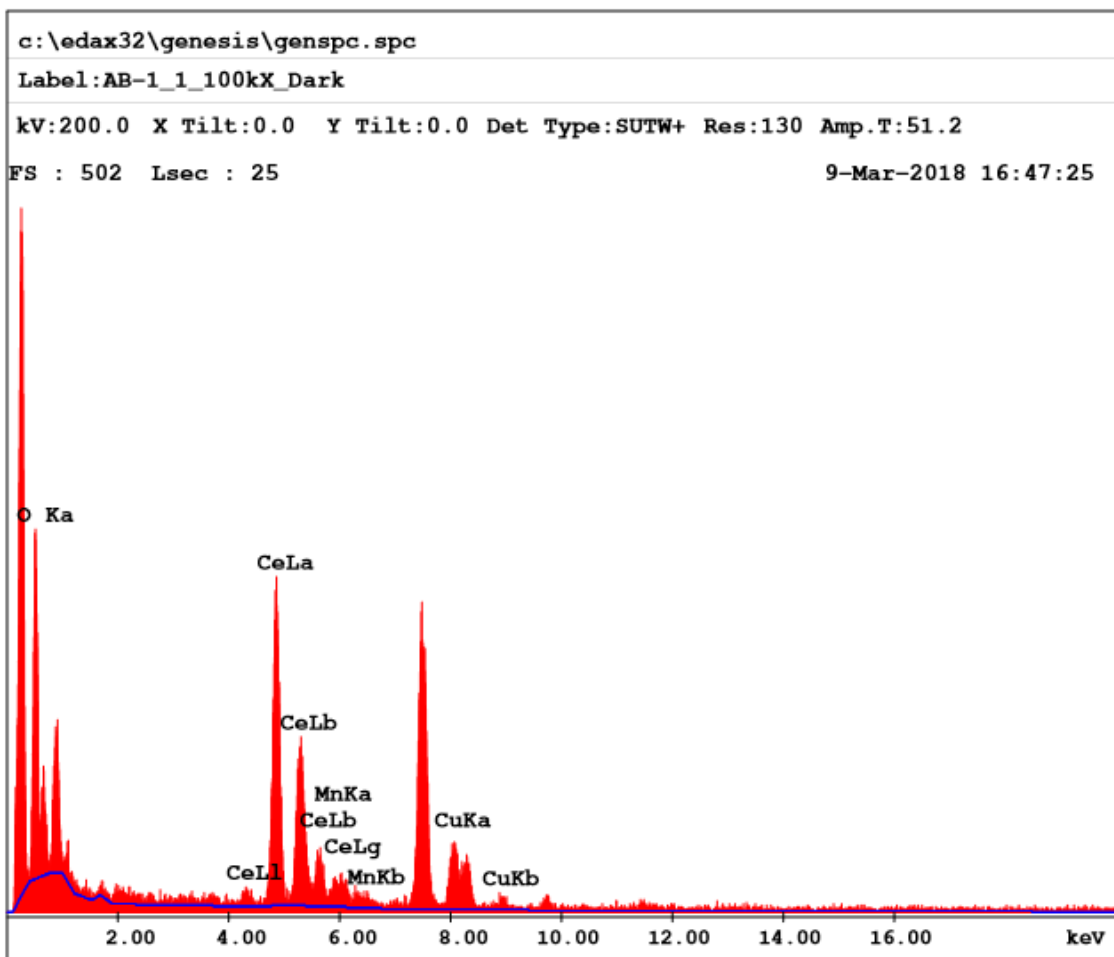
```
Thin Apx
Theoretical KAB, Elements, Model : Zaluzec

Element  Weight %  Atomic %

  O K      14.8      57.9
  CeL      77.9      34.8
  MnK       1.5       1.7
  CuK       5.7       5.6
 Total    100.0     100.0

Element  Net Inte.   Bkgd Inte.   Inte. Error    P/B

  O K     103.46       12.29         2.18        8.42
  CeL     167.25        4.79         1.59       34.93
  MnK      14.24        4.31         6.71        3.31
  CuK      43.49        2.47         3.20       17.58
```

Figure 5.12. Energy Dispersion X-ray Spectroscopy (EDS) spectrum of 5Mn-CuO/CeO₂.
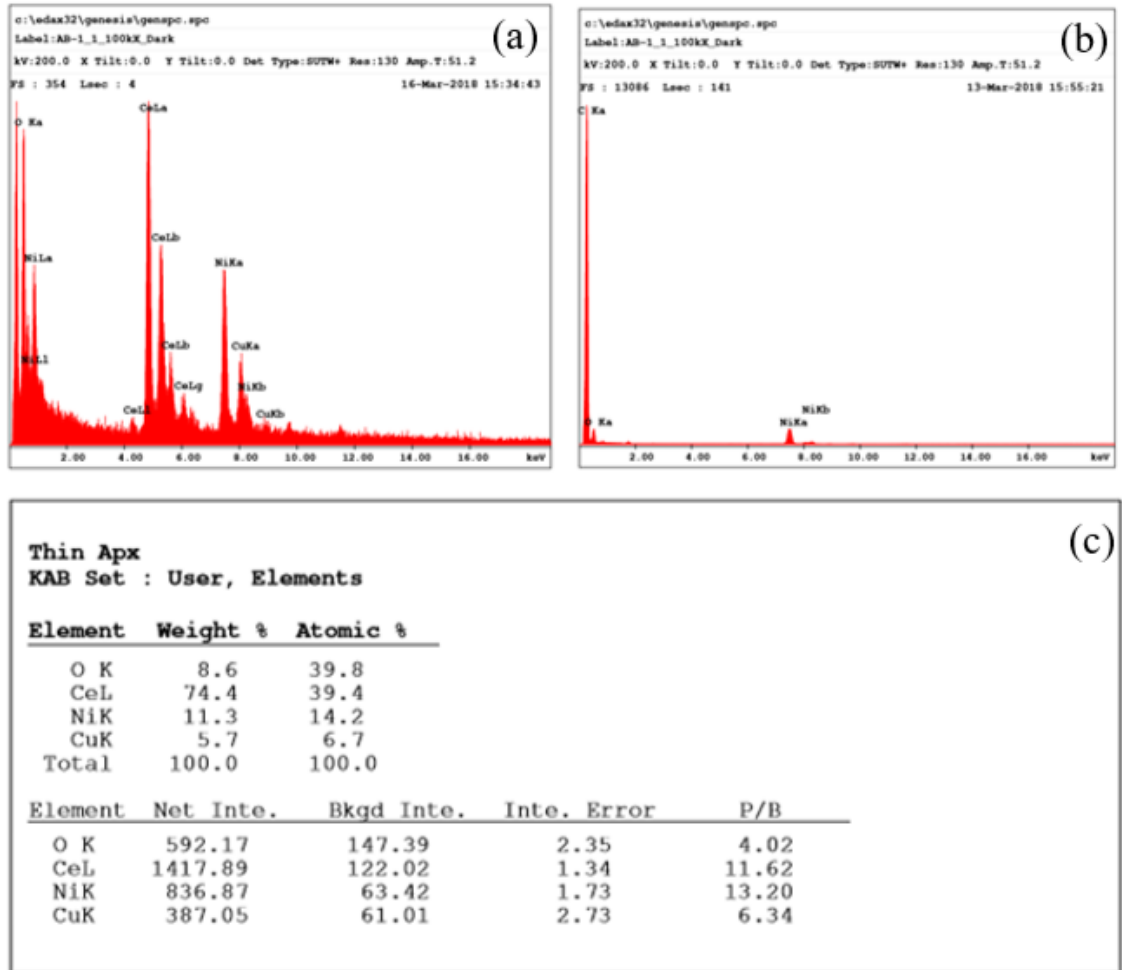
Figure 5.13. Energy Dispersion X-ray Spectroscopy (EDS) spectrum of 5Ni-5CuO/CeO₂ and the EDS of a blank Ni grid.

```
c:\edax32\genesis\genspc.spc
Label : AB-1_1_100kX_Dark                           (a)
Acquisition Time  : 19:54:01        Date:16-Mar-2018

kV : 200.00    Azimuth:45.00    Elevation:35.00    AmpT : 51.2
Detector Type:SUTW, Sapphire    Resolution:129.68   Lsec:56

Thin Apx
KAB Set : User, Elements

Element   Weight %   Atomic %

   CeL      10.6       4.9
   FeK      34.9      40.1
   CuK      54.4      55.0
 Total     100.0     100.0

Element   Net Inte.    Bkgd Inte.   Inte. Error      P/B

   CeL       2.48         4.44        18.16         0.56
   FeK      34.63         7.15         2.70         4.85
   CuK      45.10         9.39         2.37         4.80
```

```
c:\edax32\genesis\genspc.spc
Label : AB-1_1_100kX_Dark                           (b)
Acquisition Time  : 15:22:33        Date:16-Mar-2018

kV : 200.00    Azimuth:45.00    Elevation:35.00    AmpT : 51.2
Detector Type:SUTW, Sapphire    Resolution:129.68   Lsec:15

Thin Apx
KAB Set : User, Elements

Element   Weight %   Atomic %

   O K      10.7      48.8
   CeL      82.1      42.9
   FeK       0.2       0.2
   CuK       7.0       8.1
 Total     100.0     100.0

Element   Net Inte.    Bkgd Inte.   Inte. Error      P/B

   O K     604.42       137.03        1.27          4.41
   CeL    1284.26        64.62        0.76         19.87
   FeK      12.06        65.82       25.66          0.18
   CuK     392.58        39.24        1.43         10.01
```

Figure 5.14. Energy Dispersion X-ray Spectroscopy (EDS) spectrum of 5Fe-5Cu/CeO$_2$

5.3. Conclusion

A systematic study of CeO$_2$ nanorods supported bimetal oxides and bimetallic nano-catalyst were synthesized using hydrazine as a reducing agent and were characterized using XRD, BET surface area, H$_2$-TPR, XPS and CO-Oxidation. The result of Mn-CuO/CeO$_2$, Fe-CuO/CeO$_2$ and Ni-CuO /CeO$_2$ showed significantly higher catalytic

activities toward CO oxidation over the Ag-CuO$_x$/CeO$_2$ catalysts. With the addition of the bimetal oxide, there was a significant increase in catalytic activities compared to pure CeO$_2$. Venkataswamy's group determined that the incorporation of Mn to ceria would demonstrate a better performance of the catalyst due to larger surface area, higher concentration of surface adsorbed oxygen, enhanced reducibility, and more oxygen vacancy sites.[34] This synergetic effect of the bimetal oxides and bimetallic system had lower reduction temperatures (181-230 °C) compared to Mirzaei et al where reduction temperatures were in the range (300-500 °C). In addition, Mirzaei's best performing sample, 5Ni/10CoMgO, had a BET surface of 43.72 m^2/g which dwarfed the Mn-CuO/CeO$_2$ nanorods surface area 124.16 m^2/g synthesized in this research. The configuration of the bimetal oxides may be a contributing factor in the increased hydrogen consumption. Implying that the interaction at the interface of Ce and the other metals present, thereby increasing surface area. Whereas, it is may be deduced that the Ag-CuO$_x$ system is more of a cluster in cluster or even an alloy configuration. The Ce 3d XPS data indicates that the Mn-CuO, Fe-CuO and Ni-CuO showed greater amounts of Ce^{3+} compared to the Ag-CuO$_x$ sample. Recall, that Ce^{3+} aids in the formation of oxygen vacancies and which in turn increase the catalytic efficiencies. Recall, the CuO catalysts showed lower reduction temperatures, seen in Chapter 4. In addition, the bimetal oxides, the CuO possibly passivates the metal and there may be a solid solution with the ceria lattice and increases the surface area, thereby making room for surface lattice oxygen to be generated.[35]

5.4. References

1. Feng, Y.S.; Ma, J.J.; Kang Y.M. and. Xu, H.J. PdCu nanoparticles supported on graphene: an efficient and recyclable catalyst for reduction of nitroarenes. *Tetrahedron*, **2014**, 70, 6100–6105.

2. Rao, G. R. Chemistry of bimetallic surfaces. *Curr. Sci.,* **1998**, 75, 901–910.

3. Yamauchi, T.; Tsukahara, Y.; Sakata, T.; Mori, H.; Yanagida, T.; Kawai T. and Wada, Y. *Nanoscale*, **2010**, 2, 515–523.

4. Everett, B.; Boyle, G.; Peake, S. and Ramage, J. Energy Systems and Sustainability: Power for a Sustainable Future, Oxford University Press, 2nd ed, **2012**.

5. Li, D.; Atake, I.; Shishido, T.; Oumi, Y.; Sano T. and K. Takehira, *J. Catal*., **2007**, 250, 299–312.

6. Liao, F.; Lo, T. W. B. and Tsang, S. C. E. *ChemCatChem*, **2015**, 7, 1998–2014.

7. Dimitratos, N.; Lopez-Sanchez J. A. and Hutchings, G. J. Selective liquid phase oxidation with supported metal nanoparticles. *Chem. Sci*., **2012**, 3, 20–44.

8. Davis, S. E.; Ide M. S. and Davis, R. J. Selective oxidation of alcohols and aldehydes over supported metal nanoparticles. *Green Chem*., **2013**, 15, 17–45.

9. Koper, M. T. Fuel cell catalysis: a surface science approach. Hoboken: John Wiley. **2009.**

10. Zhanga H. and Toshima N., Glucose oxidation using Au-containing bimetallic and trimetallic nanoparticles. *Catal. Sci. Technol*., **2013**, 3, 268–278

11. Martin Alonso, D.; Wettsteina, S. G. and Dumesic, J. A. Bimetallic catalysts for upgrading of biomass to fuels and chemicals. *Chem. Soc. Rev*., **2012**, 41, 8075–8098.

12. Nagy, G.; Benkó, T.; Borkó, L.; Csay, T.; Horváth, A.; Frey, K. and Beck, A. Bimetallic Au–Ag/SiO$_2$ catalysts: comparison in glucose, benzyl alcohol and CO oxidation reactions. *Reac. Kinet. Mech. Cat.*, **2015,** 115, 45-65.

13. Mirzaei, F.; Rezaei, M. and Meshkani, F. Coprecipitated Ni- Co bimetallic nano-catalysts for methane dry reforming. *Chem Eng Techn.,* **2014**, 37, 6, 973-978.

14. Chaturvedi, S.; Dave, P. N. and Shah, N. K. Applications of nano-catalyst in new era. *J Saudi Chem. Soc.,* **2012**, 16, 3, 307–325.

15. Bello, A.; Dodoo-Arhin, D.; Makgopa, K.; Fabiane, M. and Manyala, N. Surfactant assisted synthesis of copper oxide (CuO) leaf-like nanostructures for electrochemical applications. *J. Mater. Sci.*, **2014**, 4, 64-73.

16. Surjyakanta, R. and Jonnalagadda, S.B. A facile synthesis of Cu–Ni bimetallic nanoparticle supported organo functionalized graphene oxide as a catalyst for selective hydrogenation of p-nitrophenol and cinnamaldehyde. *RSC Adv.*, **2017**,7, 2869-2879.

17. Teng, X. and Yang, H. Synthesis of magnetic nanocomposites and alloys from platinum-iron oxide core-shell nanoparticles. *Nanotechnology,* **2005**, 16, 554–561.

18. Xu, J.; Harmer, J.; Li, G.; Chapman, T.; Collier, P.; Longworth, S.; and Tsang, S.C. Size dependent oxygen buffering capacity of ceria nanocrystals. *Chem. Commun.*, **2010**, 46, 1887-1889.

19. Suryanarayana, C. Mechanical alloying and milling. *Prog. Mater. Sci.* **2001**, 46,1, 1-184.

20. Barcari, G. Metal. Nanoparticles and Nanoalloys; Wilcoxon, J., Johnston, R.L., Eds.; *Elsevier:* Amsterdam, The Netherland, **2012**, 213–247.

21. Yang, F.; Deng, D.; Pan, X.; Fu, Q. and Bao, X. Understanding nano effects in catalysis. *Natl. Sci. Rev.*, 2**015**, 2, 2, 183–201,

22. Bell A.T. The impact of nanoscience on heterogeneous catalysis. *Science,* **2003**, 299, 1688-1691.

23. DjinovićabIlj, P.; Črniveca, I.; Erjavecab, B. and Pintara, A. Influence of active metal loading and oxygen mobility on coke-free dry reforming of Ni-Co bimetallic catalysts. *Appl. Catal. B Environ.* **2012,** 125, 259-270.

24. Holgado, J.P.; Alvarez, R. and Munuera, G. Study of CeO_2 XPS spectra by factor analysis: reduction of CeO_2. *Appl Surf Sci*., **2000,** 161, 3 and 4, 301-315.

25. Avgouropoulos, G. and Ioannides, T. Effect of synthesis parameters on catalytic properties of CuO-CeO2. *Appl. Catal. B Environ.*, **2006**, 67, 1-11.

26. Hu, C.; Zhu, Q.; Chen, L. and Wu, R. CuO–CeO2 binary oxide nanoplates: Synthesis, characterization, and catalytic performance for benzene oxidation. *Mater. Res. Bull.,* **2009**, 44: 2174–2180.

27. de Groot, F. and Kotani A. Core level spectroscopy of solids, CRC Press, Boca Raton, **2008**, 147.

28. Sun, X.; Gong, C.; Lv, G.; Bin, F. and Song, C. Effect of Ce/Zr molar ratio on the performance of $Cu–Ce_x–Zr_{1-x}/TiO_2$ catalyst for selective catalytic reduction of NO_x with NH_3 in diesel exhaust. *Mater. Res. Bull.,* **2014**, 60, 341–347.

29. Zhou, K.; Wang, X.; Sun, X.; Peng, Q. and Li, Y. Enhanced catalytic activity of ceria nanorods from well-defined reactive crystal planes. *J. Catal.,* **2005**, 229, 206–212.

30. Rangel, R.; Bartolo-Pérez, P.; Martínez, E.; Trejo-Cruz, X.A.; Díaz, G. and Galván D. H. *Catal. Sci. Technol*., **2012**, 2, 847-852.

31. Jung, J. Ch.; Lee, H.; Kim, H.; Chung, Y. M.; Kim, T. J.; Lee, S. J.;. Oh, S. H.; Kim Y. S. and Song, I. K. *Catal. Lett.*, **2008**, 124, 262–267.

32. Arena, F.; Trunfio, G.; Fazio, B.; Negro, J. and Spadaro, L. *J Phys Chem C*. **2009,** 113, 2822–2829.

33. Venkataswamy, P.; Jampaiah, D.; Mukherjee, D.; Aniz, C. U. and Reddy, M. B. Mn-doped ceria solid solutions for CO oxidation at lower temperatures *Catal Lett.,* **2016**, 146, 2105–2118.

34. Venkataswamy, P.; Jampaiah, D.; Mukherjee, D.; Aniz, C. U. and Reddy, M. B. Mn-doped ceria solid solutions for CO oxidation at lower temperatures *Catal Lett.,* **2016**, 146, 2105–2118.

35. Camardese, J.; McCalla, E.; Abarbanel, D.W.; Dahn, J.R. Determination of shell thickness of spherical core-shell $Ni_xMn_{1-x}(OH)_2$ particles via absorption calculations of X-ray diffraction patterns. *J. Electrochem. Soc.* **2014**, 161, 814–820.

Chapter 6: Understand the Interfacial Interaction and Structure on CuO_x/CeO_2

Both CuO/CeO_2 and Cu/CeO_2 have been reported to have high catalytic activity to promote carbon monoxide oxidation, water-gas shift reaction, and methanol steam reforming. This can be attributed to the quick reversible Ce^{4+}/Ce^{3+} redox couple, $Cu^{2+}/Cu^{+}/Cu^{0}$ redox triple, and the $CuO_x(0{\leq}x{\leq}1)/CeO_{2-x}(0{\leq}x{\leq}0.5)$ interactions. The redox functionality of both catalyst and support are vital components for gas adsorption, oxygen migration at the metal-support interface and in the catalytic reactions. For CuO/CeO_2 catalyst, the strong metal-support interactions (SMSI) between CuO species and CeO_2 support provides a synergistic effect that causes the reduction of both CeO_2 support and CuO crystalline to occur at lower temperatures, resulting in the enhanced activity. However, for CuO/CeO_2 used as an oxidation catalyst, the superior activity suggests an oxygen transfer from CeO_2 to metallic Cu^{0} at the interface or with the presence of copper there is activation in lattice oxygen of CeO_2. In other words, the high catalytic activity is due to the interplay between $CeO_{2-x}(0{\leq}x{\leq}0.5)$ and $CuO_x(0{\leq}x{\leq}1)$ at their interface. From this result it follows that controlling the interfacial structure is an essential way to enhance the catalytic activity in both CuO/CeO_2 and CuO/CeO_2 catalysts.

This chapter will investigate the interfacial interaction and structure on CuO_x/CeO_2. TEM and HRTEM techniques were used in this section to characterize the interfacial structure and structural relationship of CuO_x/CeO_2 nanorods before and after thermal treatments. The H_2-TPR profiles were re-evaluated and offered information on the possible structural analysis as well as indicating reduction temperatures. Raman

181

spectroscopy provides information on elemental coordination environment and oxygen vacancy concentration. Although, the interaction between CuO_x and CeO_2 is still unclear, the information elucidated from this work should allow for a better understanding on structural characteristics and evolution during thermal treatments. Noted, some of the data was taken from Chapter 4 and used to help explain the interfacial interaction.

6.1. Introduction

Noble metals like Pt, Pd and Ru are typical catalysts used for CO oxidation. Finding a more abundant and cost-effective catalyst would be a benefit to many CO producing industries processes such as soot oxidation, steam reforming of methanol, preferential CO oxidation (PROX) and to aid in the remediation of toxic emissions such as NO_x, CO and unburned hydrocarbons.[1,2,3] Catalyst based on combinations between copper and ceria constitute a highly attractive alternative from an economical point of view. A recent report claimed that reducible CeO_2 supported metals also exhibit increased rates for reactions involving redox steps. A possible explanation for the increased reaction rates may involve highly mobile surface oxygen species in CeO_2, and/or the surface defect structures in partially reduced CeO_{2-x} at elevated temperature. It has been demonstrated that CeO_2 nanorods show superior low temperature surface reducibility and high oxygen storage capacity due to exposing {011} and {001} surfaces and/or rough surface with oxygen vacancy clusters, as compared to other morphologies e.g. nano-octaherda and nanocubes.

In a work done by Avgouropoulos et al, they reported that CuO as a catalyst with the active CeO_2 support can be equally as effective Pt/Al_2O_3 for CO oxidation.[4] Jia et al investigated the reactivity for different CuO species, where finely dispersed CuO

possessed the highest activities.[5] Liu and Stephanopoulos presented a reaction mechanism where Cu^+ would aid in interaction between CuO and CeO_2. Cu^+ provides active surface sites for CO to chemisorb and CeO_2 contributes through the outstanding redox property and provide oxygen for oxidation of CO to CO_2.[12] In this study, it was determined that CeO_2 nanorods supported CuO_x sample possess the highest levels of loosely dispersed CuO_x species (β particles). To further understand the $CuO_x(0 \leq x \leq 1)/CeO_{2-x}(0 \leq x \leq 0.5)$ interfacial effect, the research objectives proposed here undertake a detailed investigation to obtain a fundamental understanding of metal-support interactions at atomic level in CuO/CeO_2 and CuO/CeO_2 nanorods catalysts and their effect on low temperature carbon monoxide oxidation.

6.2. Experimental

CeO_2 nanorods were synthesized through the hydrothermal method with a dwell time of 48 h and temperatures of 90 °C nanorods. In addition, the volume ratios, of 11:1 (V_{NaOH}:$V_{Ce(NO3)3 \cdot 6H2O}$) and the molarity at 0.1 M $Ce(NO_3)_3 \cdot 6H_2O$ (99.9% purity, Alfa Aesar) for the Ce precursor which was proven to be the best parameters for the investigation of catalytic activities. Finally, the concentration of NaOH (>98% purity and obtained from Sigma–Aldrich) was held constant at 6 M to provide the optimum catalyst support. Where the samples were slight stirred and then placed in a Teflon-lined stainless-steel autoclaves. All samples were washed thoroughly with distilled water to remove any co-precipitated salts and residual ions, then washed with ethanol to avoid hard agglomeration in the nanoparticles, and dried in air at 60 °C for 12 h. For the catalyst loading, a wet incipient method was used to impregnate the copper catalyst. Copper carbonate was the Cu precursor used for all samples ($CuCO_3$ purchased from

Fisher Scientific). 10 wt.% copper loading was used for the evaluation of the interfacial interaction between CuO_x and CeO_2. After impregnation all samples were filtered and dried at 60 °C for 12 h. Then all the samples were oxidized in air at 400 °C for 5 h. The samples were equally divided and half of the samples were subjected to a reduction treatment. The reduction was done in 5 vol.%H_2/95 vol.% He atmosphere at 400 °C for 5 h.

All techniques for characterization of the catalysts and catalytic activity, such as; X-ray diffraction (XRD), Raman spectroscopy, X-ray photoelectron spectroscopy (XPS), transmission electron microscopy (TEM), BET surface area measurement, temperature programmed reduction (TPR), temperature programmed oxidation (TPO), temperature programmed desorption (TPD), pulse chemisorption to calculate oxygen storage capacity (OSC), and CO oxidation can be found in Chapter 2.

6.3. Results and Discussion
6.3.1. Raman and H_2-TPR

As stated earlier in Chapters 3 and 4, CeO_2 has a characteristic peak that is typically observed at ~460 cm^{-1} and corresponds to the strong F_{2g} vibrational mode which is representative of the Ce-O stretch vibrational mode, can be seen at 448 and 451 cm^{-1}.[6] Demonstrating a significant shift to the left indicates a disruption in the lattice. As seen in the Figure 6.1, two peaks are on high and low wavenumber sides of F_{2g} peak, observed at ~276 cm^{-1} and ~605 cm^{-1} which demonstrate the existence of the oxygen vacancy in CeO_2.[7] The peak areas of the bands at ~460 and 605 cm^{-1} are denoted as I_{F2g} and I_{Ov}. The area ratio of I_{F2g} to I_{Ov} was calculated and represents the concentration of oxygen vacancies in CuO_x/CeO_2.[8,9] For instance, the intensity of the Raman peak on the high

wavenumber side, ~605 cm^{-1}, of the F_{2g} peak, 460 cm^{-1}, is associated with oxygen vacancies in pure CeO_2 and impregnated CeO_2. The ratio of peak 605/460 was calculated as 0.224 and 0.118 for 10 wt% CuO/CeO_2 and 10 wt% CuO_x/CeO_2 nanorods, respectively. This indicates that the oxidized sample has a larger concentration of oxygen vacancies as opposed to the reduced sample.
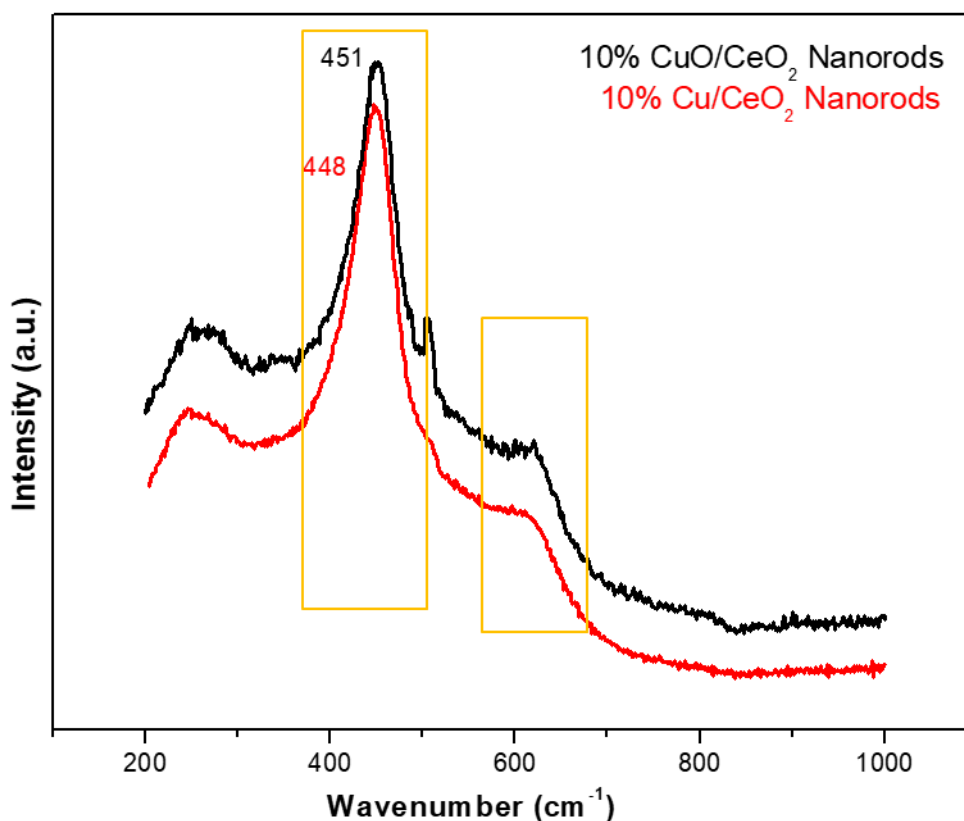
Figure 6.1. Raman data of 10 wt.% CuO/CeO$_2$ vs. 10 wt.% CuO$_x$/CeO$_2$ nanorods.

In Chapter 4, the H_2-TPR profiles and H_2 consumption data from the 10 wt.% CuO_x/CeO_2 nanorods and 10 wt.% CuO/CeO_2 nanorods samples were used to better explain the interfacial interaction between the catalyst and the support. As stated earlier, similar sample weights (~90 mg) were used. Figure 6.3 shows the reduction profile,

where the α peak represents the CuO or CuO$_x$, which are strongly interacting with the CeO$_2$ support. The β peak of CuO or CuO$_x$ is highly dispersed and loosely interacting with the CeO$_2$ support and then the γ peak which is the "bulk-like" peak is larger CuO or CuO$_x$ particles that interact weakly with the CeO$_2$ support.[10] The recall, that the H$_2$-TPR profile for the oxidized 10 wt.% CuO/CeO$_2$ nanorods sample, recorded the two reduction temperatures at 147 °C and 205 °C and the reduced 10 wt.% CuO$_x$/CeO$_2$ nanorods reduction temperatures were recorded at 143 °C and 198 °C. The area under the peak was calculated and represents that the oxidized sample contains larger amounts of the highly dispersed copper species and consumed more hydrogen at low reduction temperatures. Chapter 4 describes how the amounts were calculated. The H$_2$-TPR profiles for the oxidized and reduced sample of CuO and CuO$_x$/CeO$_2$ nanorods are shown in Figure 6.2. The α peak area for the CuO/CeO$_2$ is 1.65 and the β peak area was 6.25, which is equivalent to 36.30 mmol/g and 137.50 mmol/g, respectively. The CuO$_x$/CeO$_2$ peak area for the α peak was 1.44 and the β peak was 2.54, which equivalated to 31.68 mmol/g and 55.88 mmol/g, respectively.
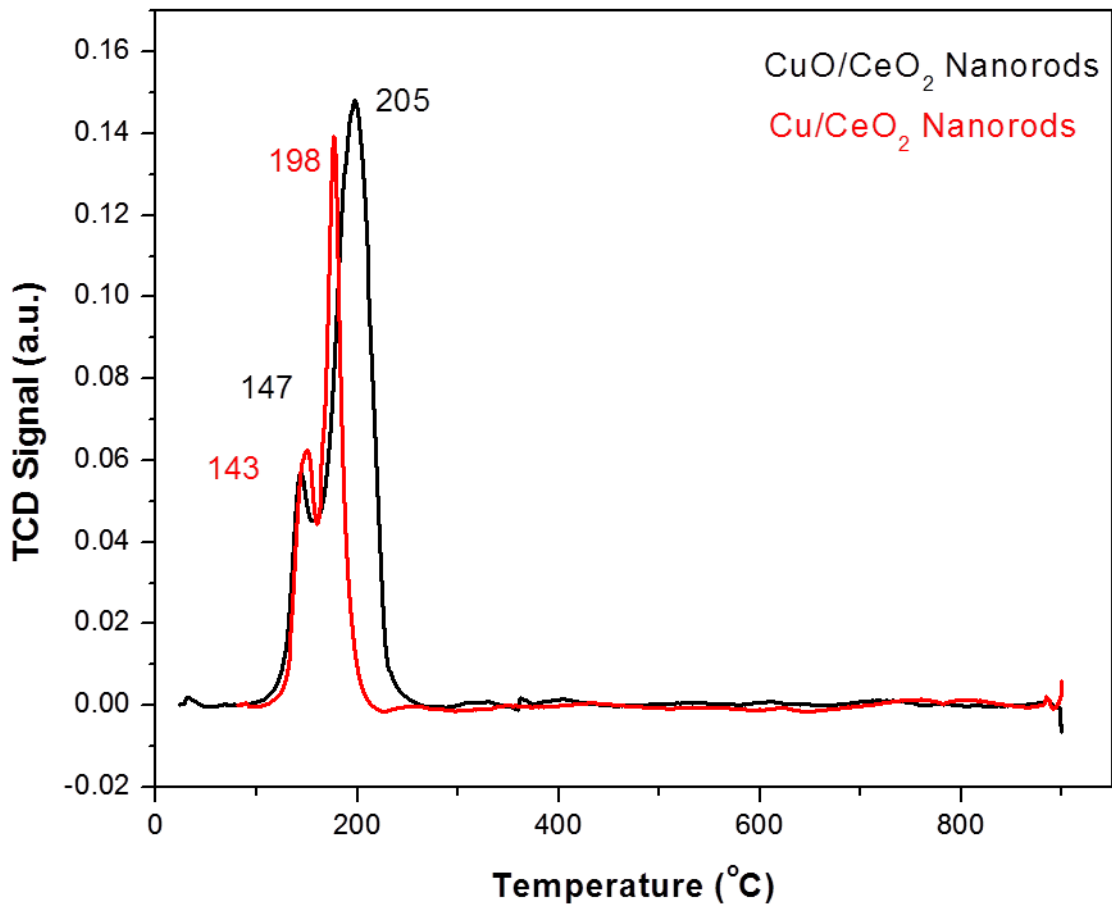
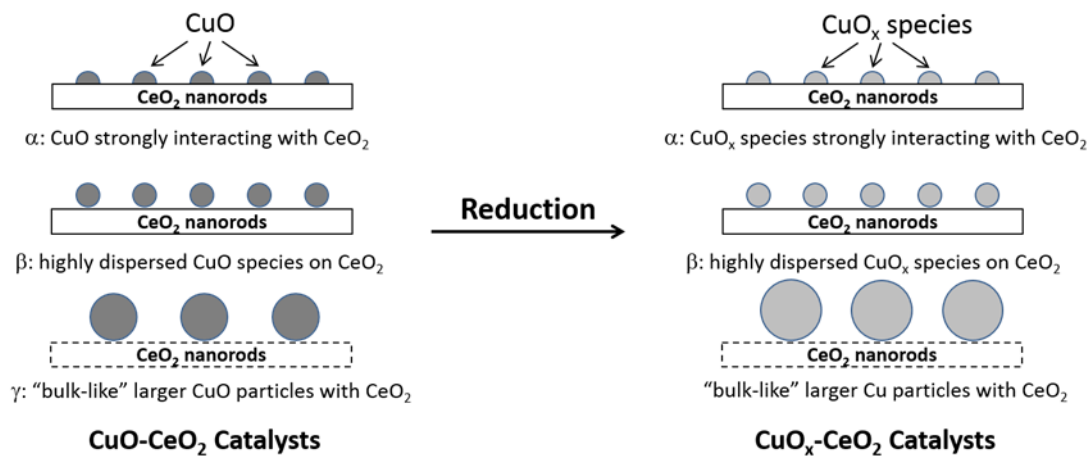*Figure 6.2. H$_2$-TPR data 10 wt.% CuO/CeO$_2$ and 10 wt.% CuO$_x$/CeO$_2$ nanorods.*

Figure 6.3. Proposed mechanism for CuO/ CeO$_2$ and CuO$_x$/CeO$_2$ nanorod catalysts to explain the H$_2$-TPR results. [11]

6.3.2. Interfacial Structure Investigation of CuO_x/CeO_2

6.3.2.1. High Resolution Transmission Electron Microscopy

It has been reported that a high ratio of Ce^{3+} and oxygen vacancy on the surface was observed on CeO_2 nanorods, so owing to incomplete oxidation or charge/oxygen interaction with CeO_2 support, it is possible to form a mixture of Cu^+ and Cu^{2+}, particularly at the CuO_x-CeO_2 interface. For the increased amount of finely dispersed CuO species, the effect of these interfacial structures could be critical for the activity of CuO_x-CeO_2 catalysts. Seen in Figure 6.4, there is a structure-interaction relationship with the β particles of CuO_x and CeO_2 for CO oxidation. Since β-type CuO_x is loosely interacting with the CeO_2, Cu^+ can be more readily reduced which acts as an active site for CO oxidation to occur. There is a synergetic relationship that occurs because more Cu-Ce interfacial sites can form. For example, the oxygen transfer could lead to oxidation of Ce^{3+} to Ce^{4+} and reduction of Cu^{2+} to Cu^+ at the interface. Raman analysis of the oxygen vacancies shows an increase when compare to pure CeO_2 nanorods, with a ratio of peak 605/460, 0.04. The oxygen vacancy peak ratio, 605/460, for 10 wt% CuO/CeO_2 and 10 wt% CuO_x/CeO_2 nanorods were calculated as: 0.224 and 0.118, respectively. This is indicative of an increase in surface and bulk oxygen vacancies, especially at the interface of CuO_x/CeO_2.
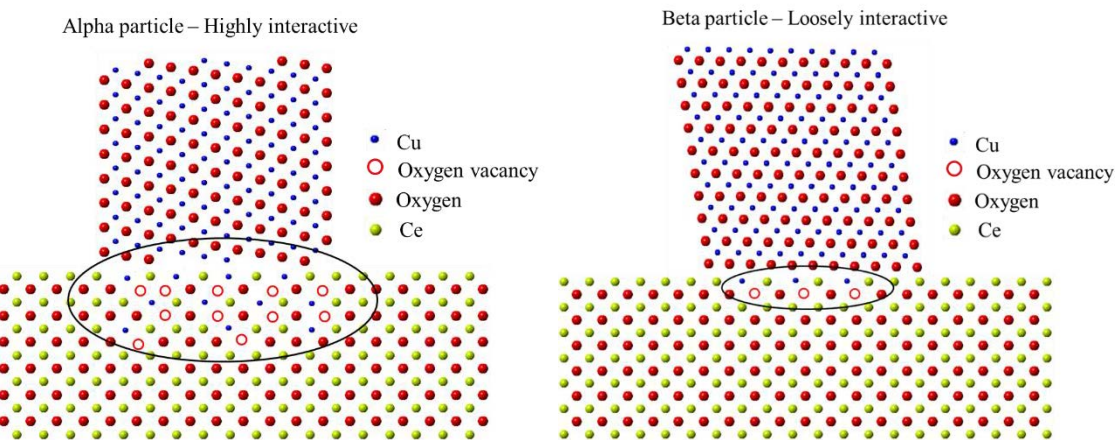
.

Figure 6.4 Model of the beta (β) particle on CuO$_x$/CeO$_2$ using Crystal Maker.

Among the various characterization techniques, high resolution TEM (HRTEM) imaging has the advantage to directly reveal the projected interfacial structure and allow to investigate atomic-level interfacial imperfection, such as disorder and defects etc. Depending on the particular catalyst–support system, various morphological changes resulting from a metal–support interaction have been reported, namely sintering, encapsulation, inter-diffusion, and alloy formation. In our previous study, we have found significant variations of interfacial structure and chemical composition between supported catalysts samples prepared through different methods and experimental conditions. This nano-heterogeneity provides us with an opportunity to identify the most active particles in the materials.

The state-of-the-art electron microscopy facility (JEOL 2100, 0.19 nm point resolution) is available at the Center of Excellence in Materials Science and Engineering at YSU to characterize the atomic-level structure and chemistry of the materials. Using atomic resolution imaging, the obtained structural and chemical information at the interface on the CeO$_2$ supported CuO$_x$ can be classified and correlated with the synthesis and thermal treatment conditions.

Visible in Figure 6.5 (a), the low magnification TEM image shows large amounts of highly dispersed β-type CuO_x particles on CuO_x/CeO_2 nanorods. In Figure 6.5 (b), the HRTEM image shows the strongly interacting α-type CuO_x particles. Figure 6.5 (c) is a HRTEM image of the loosely dispersed β-type CuO_x particles and in Figure 6.5 (d), shown is the HRTEM image of both α-type and β-type CuO_x particles present on CeO_2 nanorods.

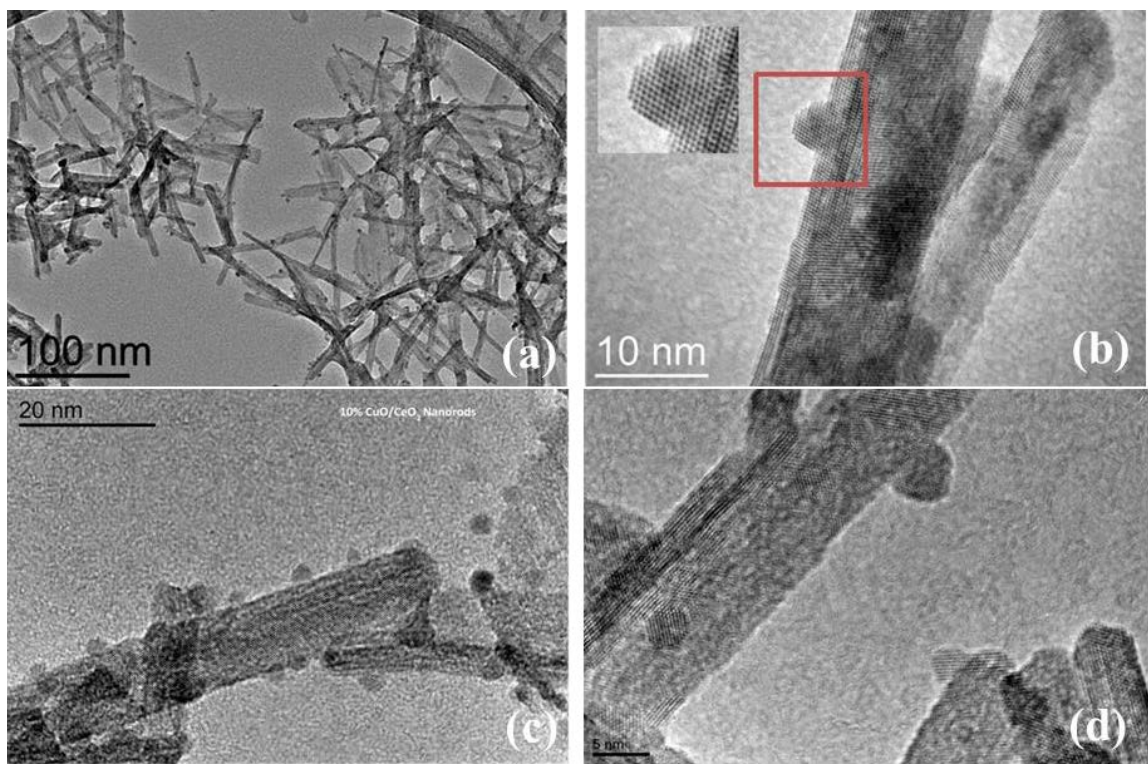*Figure 6.5. HRTEM images of CuO_x/CeO_2 nanorods (a) low magnification TEM image of highly dispersed β-type CuO_x particles (b) HRTEM image of strongly interacting α-type CuO_x particles. (c) HRTEM image of loosely dispersed β-type CuO_x particles. (d) HRTEM image of both α-type and β-type CuO_x particles on CeO_2 nanorods*

6.3.3. Oxygen Vacancy Formation and Its Effect on CO Oxidation.

The role of copper species at the interfacial areas may activate the lattice oxygen release of CeO_2 which can occur at a lower temperature.[12] In a study by Li et al, they concluded that copper may aid in the production of oxygen vacancies. Their conclusions illustrated the that CeO_2 mediated the CO process. It was reported that CO would adsorb on the metal, oxidize and then ceria would in turn be oxidized by water.[12] Therefore, the CO oxidation would occur in a two-steps process; oxygen is transferred from ceria to the interface of Cu and the re-oxidation of ceria.

Surface defects on CeO_2 nanorods are shown in Figure 6.6, the HRTEM revealed several types of defects, including steps, lattice disorder, and dislocation. The HR-TEM analysis allows a two-dimensional image of the catalyst and support to provide a visual of the surface defects present within the sample. As noted in Chapter 4, the (111) and (110) termination planes provided more surface defects which is good agreement with the Raman analysis. The catalyst characterization, concluded that the CuO_x/CeO_2 nanorods showed the lowest reduction temperature and improved catalytic activity.
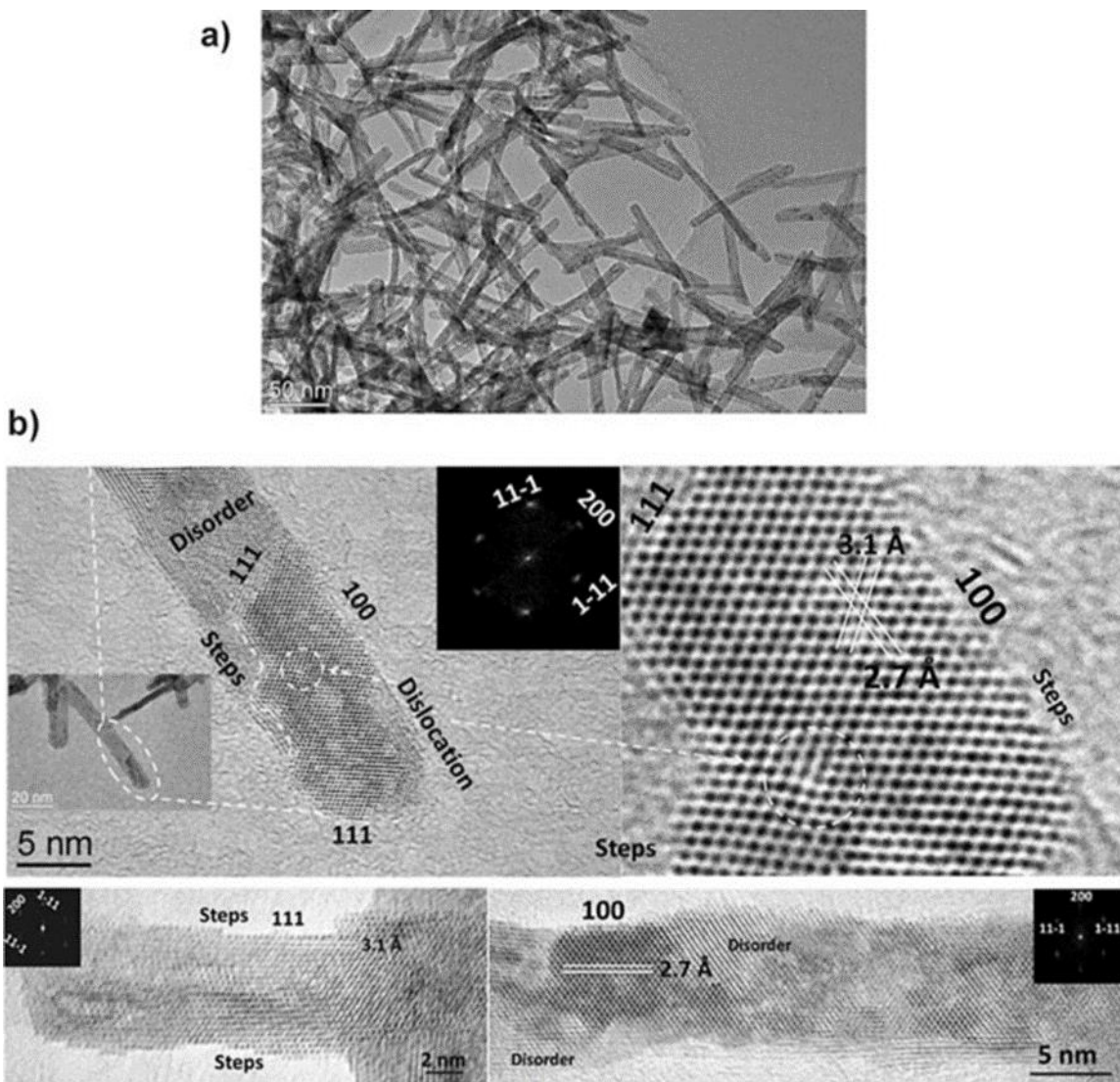
Figure 6.6. High Resolution TEM of CeO$_2$ nanorod sample. [14]

Surface oxygen is essential in the heterogeneous catalysis reactions where the gas-solid interaction occurs. Highly dispersed copper species and oxygen mobility allow the oxidation of Ce^{3+} to Ce^{4+} and reduction of Cu^{2+} to Cu$^+$ at the interface to occur more readily. In Figure 6.7, a proposed mechanism of CO oxidation with highly dispersed CuO$_x$/CeO$_2$ and CuO$_x$ strongly interacting is shown. Noted here XPS information from Chapter 4 was used, where the existing copper species, Cu$^+$ is generated from the involvement of Cu^{2+} and Ce^{3+} ions, this occurs through electron transfer. During this

process the formation of Cu^+-carbonyl group and CO_2 occurs simultaneously.[13] The lattice oxygen on the surface of CeO_2 allows CO to adsorb, which creates the formation of CO_2. Thereby creating an oxygen vacancy position as well as, Ce^{3+} and Cu^+ are generated. The open system would then allow O_2 molecules to fill the oxygen vacancy positions and re-oxidize Ce^{3+} and Cu^+ to Ce^{4+} and Cu^{2+}. In addition, the proposed mechanism demonstrates that solid solution would prohibit the increase in oxygen vacancy formation, although not eliminate the formation within the sample. Therefore, beta particles that are highly dispersed would increase oxygen formation, and hence increase the overall catalytic performance of the system.
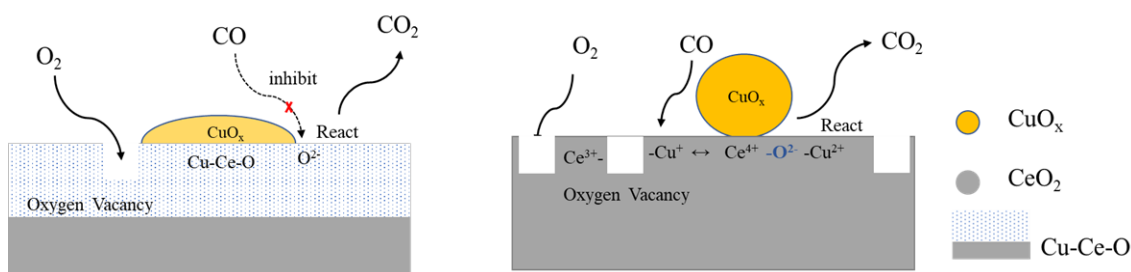

Figure 6.7 Proposed reaction mechanism CO oxidation of (α) particles strongly interacting with CeO₂ and (β) particles highly dispersed and loosely interacting with CeO₂.

6.4. Conclusion

A complete description of the high spatial resolution structure and chemistry at CuO/CeO_2 and CuO_x/CeO_2 interface is critical to identify the most active forms of the materials and pinpoint the origin of improved low-temperature catalytic activity. In this chapter HRTEM was used to reveal the surface and interfacial structure in CuO_x/CeO_2 and particular copper species were identified. For example, Figure 6.6 (b) shows 1D growth structure of CeO_2 nanorods with most of the termination surfaces planes are (111) and (100) planes. In addition, the presence of numerous defects can also be seen.

Examining the interfacial interaction between the catalyst and the support using HR-TEM was crucial for understanding visually what is occurring at the interface. Determining why there is an increase in catalytic activities was possible with the catalyst characterization and the HR-TEM. It is proposed that due to the formation of oxygen vacancies that were more energetically favored on the (100) and (110) surfaces.[14] This is possible because the oxygen vacancy formation energy is lower compared to the (111) surface.[15] Finally, a mechanism was proposed that would suggest that highly dispersed and loosely interactive CuO_x species on CeO_2 nanorods were superior for CO oxidation.

6.5. References

1. Xu, D.; Cheng, F.; Lu, Q. and Dai, P. Microwave enhanced catalytic degradation of methyl orange in aqueous solution over CuO/CeO_2 catalyst in the absence and presence of H_2O_2. *Ind. Eng. Chem. Res*., **2014**, 53, 7, 2625–2632.

2. Wet-oxidation of a model domestic wastewater on a Ru/Mn/Ce composite catalyst Ind. *Eng. Chem. Res.,* **1998**, 37, 3, 1136–1139.

3. Centeno, M.; Ramírez Reina, T.; Ivanova S.; Hernando Laguna, O. and Odriozola, J. A. Au/CeO_2 catalysts: structure and CO oxidation activity. *Catalysts*. **2016**, 6, 10, 158-188.

4. Avgouropoulos, G.; Ioannides, T.; Papadopoulou, C.; Batista, J.; Hocevar, S, and Matralis, H. K. A comparative study of $Pt/gamma-Al_2O_3$, Au/ alpha-Fe_2O_3 and CuO-CeO_2 catalysts for the selective oxidation of carbon monoxide in excess hydrogen. *Catalysis Today*, **2002**, 75, 14, 157–167.

5. Jia, A. P.; Hu, G. S.; Meng, L.; Xie, Y. L.; Lu, J. Q. and Luo, M. F; CO oxidation over $CuO/Ce_{1-x}CuxO_{2-\delta}$ and $Ce_{1-x}CuxO_{2-\delta}$ catalysts: Synergetic effects and kinetic study. *J Catal*, **2012**, 289, 199– 209.

6. Liu, L.; Yao, Z.; Deng, Y.; Gao, F.; Liu, B. and Dong, L. Morphology and crystal-plane effects of nanoscale ceria on the activity of CuO/CeO_2 for NO reduction by CO. *Chem. Cat. Chem.* **2011**, 3, 978 – 989.

7. Lin, Y.; Wu Z.; Wen J.; Poeppelmeier, R. and Marks, D. Imaging the atomic surface structures of CeO_2 nanoparticles. *Nano Lett.,* **2013**, 14, 191–196.

8. Wang, S. Y.; Li, N.; Luo, L. F; Huang, W. X.; Pu, Z. Y. Wang, Y. J. Hu, G. S. Luo, M. F. and Lu. J. Q. Probing different effects of surface MO_y and Mn^+ species (M= Cu, Ni,

Co, Fe) for $xMO_y/Ce_{0.9}M_{0.1-x}O_{2-\delta}$ catalysts in CO oxidation. *Applied Catalysis B: Environmental*, **2014**, 144, 325–332.

9. Pu, Z. Y.; Lu, J. Q.; Luo, M. F.; and Xie, Y. L. Study of oxygen vacancies in Ce0.9Pr0.1O2-δ solid solution by in situ X-ray diffraction and in situ Raman spectroscopy. *J Phys Chem C*, **2007**, 111, 50, 18695–18702.

10. Luo, M. F.; Zhong, Y. J.; Yuan, X. X. and Zheng, X. M. *App. Catal A.,* **1997**, 162, 121–131.

11. Wang, R. and Dangerfield, R.; Seed-mediated synthesis of shape-controlled CeO_2 nanocrystals. *RSC Adv.,* **2014**, 4, 7, 3615-3620.

12. Li, Y.; Fu, Q. and Flytzani-Stephanopoulos. Low-temperature water -gas shift reaction over Cu and Ni loaded cerium oxide catalysts. *Appl Catal B. Environ* **2000**, 27 179-191.

13. Ren, Z.; Peng, F.; Li, J.; Liang J. and Chen, B. Morphology-dependent properties of Cu/CeO_2 catalysts for the water-gas shift reaction. *Catalysts,* **2017**, 7, 48-60.

14. Mock, S.A.; Zell, E.T.; Hossain, S.T. and Wang, R. Effect of reduction treatment on CO oxidation with CeO_2 nanorod-supported CuO_x catalysts. *ChemCatChem.,* **2018**, 10, 311 –319.

15. Nolan, M.; Parker, S. C. and Watson, G. W. CeO_2 catalyzed conversion of CO, NO_2 and NO from first principles energetics. *Phys. Chem. Chem. Phys.* **2006**, 8, 216– 218.

Chapter 7: Summary and Future Work

7.1. Summary

In this dissertation, hydrothermal and precipitation methods, were the main routes of synthesis. Characterization and catalytic study of cerium oxide supports with an emphasis on gaining a deeper understanding of the catalyst support interface due to the exposed crystal planes and crystal defects, and discovering a correlation with their catalytic activities were the main focus. This research also investigated a systematic study of several bimetal oxides and bimetallic nano-catalysts for their reduction temperatures and CO oxidation. All samples were designed for improved catalytic performance and were fully characterized using techniques, such as X-ray diffraction, Raman Spectroscopy, electron microscopy, X-ray photoelectron spectroscopy, H_2-TPR, CO-TPD, oxygen storage capacity (OSC), and CO oxidation.

Chapter 3 presented the various synthesis routes to prepare different morphologies of pure cerium oxide. Using NaOH for the synthesis of ceria and varying the temperatures and dwell times showed a myriad of results in relation to morphology, particle size, and specific surface area as well as OSC. Ceria nanorods, nanocubes, and nano-octahedra had BET surface area of 56.4 m^2/g, 48.5 m^2/g, and 38.2 m^2/g, respectively. These surface areas are directly proportional to the hydrogen consumption and CO conversion. With the addition of CuO catalyst, seen in Chapter 4, these surface areas increased significantly for the nanorod samples. On the other hand, the surface area of nanocubes decreased, and that of nano-octahedra samples increased at first and then decreased, with increasing the catalyst loading. The increase in surface area and further investigation into the nanorod

samples helped to gain a clearer understanding why the nanorods showed superior activity.

In Chapter 4, the controlled shape morphologies and their role in the redox properties of the catalyst were compared. The observation was focused on the interaction between CuO_x and CeO_2 and its synergetic effect on CO oxidation. CuO/CeO_2 nanorods showed a significant enhancement of lowering the reduction temperature due to the presence of highly reactive exposed crystal planes (110) and (100) in addition of (111). Furthermore, the synergistic effect of CuO_x/CeO_2 catalysts depended on the shape and size of CeO_2 due to the formation of different amounts of solid solutions at the interface and highly dispersed β particles that are loosely interacting with CeO_2 surface planes. Thus, CuO/CeO_2 nanorods, CuO/CeO_2 nanocubes and CuO/CeO_2 nano-octahedra achieved 100% CO conversion at different temperatures (298, 315 and 272 °C, respectively).

Chapter 5 demonstrated that the configuration of Fe-CuO, Ni-CuO, Mn-CuO and Ag-CuO_x bimetal oxides and bimetallic catalytic systems significantly increased hydrogen consumption. The interaction at the interface of CeO_2 and the reduced metal may have created a solid solution which increased oxygen vacancy formation, leading to increased oxygen mobility and enhanced catalytic performance.

In Chapter 6, HRTEM displayed the interfacial relationship between the catalyst (CuO) and the support (CeO_2). The images clearly demonstrated the presence of three species of CuO on CeO_2 surfaces: α, β, and γ. Each CuO species reacts with CO in different ways as mentioned in previous chapters. These species helped in increasing the amount of oxygen vacancies in CeO_2 depending on their position on the more energetically favored (100), (100) and (111) planes. The highly defected nanorods also

198

aided in the formation of oxygen vacancies as desirable to enhance the catalytic performance

7.2. Future Work

In this research, we looked at mono-metallic and bimetal oxides and bimetallic nano-catalyst systems on shape-controlled CeO_2 supports and their catalytic activity. The main focus was to gain a better understand of the interfacial interaction of the catalyst and support. Future work would focus on the interfacial structure of the catalyst support using STEM and EELS analysis, which would provide information on the presence of Ce^{3+} at interfacial regions. Recall, that with increased amounts of Ce^{3+} more oxygen vacancies form. The defects, such as oxygen vacancies, voids, bending and steps of CeO_2 play a major role in increasing the catalytic efficiencies. Therefore, investigating the interfacial structure of various defects would contribute to a better understanding of how to synthesize an improved catalyst. Diverse bimetallic systems, such as Ag-Fe, Ag-Ni, Ag-Mn, Fe-Ni, Fe-Mn, and Ni-Mn, with varying the amounts in the catalysts would be helpful in finding an enhanced catalyst.